Formation of organic and inorganic thin films at the aqueous solution-gas interface

Dissertation

zur Erlangung des Doktorgrades der Naturwissenschaften

der Fakultät Physik der Technischen Universität Dortmund

vorgelegt von

D.C. Florian Wieland

Februar 2012

Contents

1. Introduction

Interfaces are subject to many investigations as they hold interesting characteristics which are important for fundamental research and applications alike. An interface always defines the border between two particular phases with different properties. Chemical and physical processes are influenced by the properties of the two phases and can alter significantly from the corresponding process in the bulk of the media. At the liquid-air interface, e.g., adsorption processes occur due to the interaction of the liquid phase with molecules from the gas phase. Such events result in the formation of thin films at the interface and can effect the interfacial roughness.[1] Furthermore, the presence of surfactants might decrease the surface tension of a liquid-air interface.

X-ray reflectivity (XRR) and grazing incidence diffraction (GID) are well established tools for the investigation of interfaces and allow to monitor in-situ changes in the interfacial structure with Angstrom resolution.[2] With these techniques, detailed information on the lateral and vertical structure can be obtained and a comprehensive picture of the interface structure may be drawn. Further X-ray absorption spectroscopy (XAS) in a surface sensitive way allow to gain information on inter-atomic structural properties of interfaces.[3] This technique is sensitive to the local ordering of the probed atoms and gives insight into the structure of samples lacking long range order. By the combination of these techniques different length scales can be addressed yielding information on the long range structure, vertical film thickness, and short range arrangement of the interface under consideration.

An advantage of these techniques is the possibility to examine processes at interfaces in-situ. Oftentimes, experiments can only be performed ex-situ. Ex-situ experiments, however, can be problematic as it cannot be ruled out that sample treatment, such as drying, can have significant influence on the samples' structure. If samples are removed from their "natural" aqueous environment, conditions are altered and further changes are possible. This uncertainty renders in-situ experiments essential.

In this thesis, research on the structure of thin films at the liquid-air interface by in-situ X-ray scattering techniques is presented. The growth of thin films was studied using solutions of two different types of iron salts and the formation process and ordering of the structure of these films was investigated. Furthermore, the formation of thin films by adsorption of nanoparticles to the interface was examined.

This thesis is structured in the following way. The theoretical framework of nucleation and adsorption processes along with chemical aspects important within the scope of this work are given in **chapter 2**. Here, also the description of the theoretical background of the used X-ray scattering methods is summarized.

Chapter 3 describes the experimental procedures and details used. A short description of the beamline end-stations as well as the data handling is given.

Examinations of interfaces modified with surfactants are presented in **chapter 4**. Special attention is payed to the influence of the pH value on the interfacial structure. Surfactants can have a tremendous effect on the interfacial structure which in turn governs e.g. structural or diffusional properties. For example, the presence of these films can inhibit the diffusion of molecules between the neighboring phases or can enhance the concentration of ions in the interfacial region. Surfactants forming films of molecular thickness can be composed of single molecules joined by either van der Waals forces or by covalent bonds. The properties of these films depend strongly on these joining forces which influence the elastic properties and the lateral homogeneity. This chapter is a basis for the investigation reported in the following chapter.

The subsequent **chapter 5** deals with the formation of inorganic thin films from solutions containing iron chloride salts investigating the influence of different interfacial compositions on the formation process. These investigations tend to explore the influence of such modified interfaces on the thin film formation process in natural systems. During the evolution organisms were caught in the crossfire of influences which continuously required significant development and change in their habit and survival strategies.[4] For protection or stabilization, rigid structures with high durability are needed but cannot be provided by organic tissue alone. Therefore, organisms had to develop strategies to form resistant structures by the incorporation of inorganic parts. One prominent structure which was developed by nature is the human bone. This mineral structure is five times stronger than steel and has a tensile load two times bigger than that of concrete. By further comparing the artificially constructed materials with the ones by nature, more advantages of the natural materials can be found. Bone not only rearranges during the lifetime to account for varying exposures, but also self-healing occurs in these entities. In these days, a further point of view is the low amount of energy and CO_2 emission which is needed for the growth of biominerals. These highly robust structures are formed under ambient conditions in aqueous environments where no high temperatures or toxic reagents are employed. The mimicking of these processes could, thus, help to develop low cost and efficient materials, which in the case of iron could have magnetic properties or high durability.

The fundamentals which direct the nucleation can be identified as a templating effect by membranes of vesicles or cells containing proteins.[5] Secondly, the shape, phase and texture of the inorganic compounds is a function of ions and organic molecules in the growth environment. The growth is managed in intracellular spaces or organic scaffolds.[5] The self-assembly processes, which are the key mechanisms for the nucleating minerals, are controlled on a molecular level. This allows to control the habit, shape, size and polymorph of the forming crystals precisely. The access to the influence of organic molecules on the growth process is therefore crucial as these interactions determine the basic influences of membranes and proteins on the growth process.

As the experiments are conducted under a biomimetic point of view, meaning that processes in nature are tried to emulate, templates are necessary in order to investigate their influence on the biomineralization and to explore the different factors. The ideal template, which can be used

to investigate the mineralization process at the solution-air interface are Langmuir layers. These mono molecular films represent one half of a cellular membrane's bilayer.[6] Furthermore, different molecules can be used which allow tweaking of the interfacial properties. Such a sample system gives valuable insight into processes taking place at organic interfaces. The investigation of the Langmuir layer composition upon film formation of iron compounds are performed in order to explore the responsible factors for the nucleation at membrane structures. Langmuir layers with different functional groups were employed to probe the effect of the chemical nature and interface charge on the formation process. Furthermore, the effect of the oxidation state of iron ions in solution and the concentration is questioned in the course of the study.

The study of the formation of inorganic thin films from solution containing nanoparticles is summarized in **chapter 6**. Nanoparticles are used in many applications, e.g. in sun protection and food purposes, and hold promising properties for future task.[7] Because of their small size these particles exhibit different properties compared to their bulk counterparts showing higher chemical reactivity, smaller influence of mass forces for the benefit of surface forces, special optical characteristics, increased importance of the surface potential and thermodynamic properties.

The stabilization of foam or emulsions e.g. pickering emulsion, can be performed by nanoparticles which adsorb at the interface.[8] The adsorption properties depend on the wettability, the size and the material. However, the wettability properties can be changed using surfactants which adsorb to interfaces. The structure of such composite surfactant nanoparticle films was investigated to gain information on the vertical structure of the forming films. For this, solutions combining nanometer sized particles of different surface potentials with different surfactants of varied composition were investigated. The adsorption process was investigated for different evolution times by XRR experiments in order to get access to the vertical film structure.

The **chapter 7** gives a summary and outlook of this thesis.

The last **chapter 8** is dedicated to projects which were performed collaterally to the here presented experiments.

2. Theory

In-situ investigations with Angstrom resolution can be performed with X-ray scattering techniques. These allow for instance the investigation of buried interfaces and matter under extreme conditions without disturbing the sample itself.[9, 10] Other methods need vacuum conditions, like scanning electron microscopy (SEM), or have no resolution on sub nanometer length-scales, like atomic force microscopy (AFM) and Brewster angle microscopy (BAM). X-ray techniques like X-ray reflectivity (XRR) and grazing incidence diffraction (GID) allow to address questions regarding the interface structure and adsorption processes on sub nanometer length scales.

Amorphous as well as periodic structures are present at liquid-air interfaces. Thus, the use of different techniques is necessary to draw a comprehensive picture of the events taking place. In the case of samples exhibiting long range order X-ray diffraction techniques were used, which give information on the periodic arrangement within the sample. Other techniques like X-ray absorption spectroscopy were used to explore the short range order of amorphous samples present at the interface.

A further challenge was the sample system itself as the chemistry of iron ions in aqueous solutions is very complex. The growth of thin inorganic films was investigated under biomimetic aspects where special interest lies on the interaction of inorganic ions and amphiphilic molecules. This includes crystal nucleation and growth from solutions and the modification due to the presence of organic molecules forming so called Langmuir layers.

This chapter is subdivided in different sections describing first the principles of biomineralization (see chapter 2.1) and the nucleation of minerals from solutions (see chapter 2.2). The adsorption of nanoparticles to interfaces is described in chapter 2.3 and the iron species forming in solution are mentioned in chapter 2.4. Further, Langmuir layers are described in chapter 2.5 which organize in two-dimensional periodic structures. These were used as organic templates as they can mimic biological membranes. In the end of this chapter, the X-ray techniques are described which were used to study the interface and the adsorption processes.

2.1. Biomineralization

During evolution living organisms have developed composite materials with fascinating properties. Such composite materials are composed of organic and inorganic components which are structured on the nanometer length scale.[11, 12] By this composites are obtained with high hardness and advanced elastic behavior or reduced crack propagation properties compared

to single component systems.[11] Nature controls the production of these materials by self-organization. For this purpose the control of the nucleation and growth conditions of crystals is an essential step in order to reach the desired composite.[5, 13] The minerals forming the inorganic part vary from calcium carbonate, iron oxide, silica to apatite depending on the requested properties.[13–16] The composition and shape are adapted for functions like stabilization in the case of bones, storage of iron in the protein ferritin, sensing of the magnetic field in magnetotactic bacteria or in the avian magnetometer system of birds.[16–25] Even specific types of bacteria are capable of nucleating ice with the aid of specialized proteins.[26]

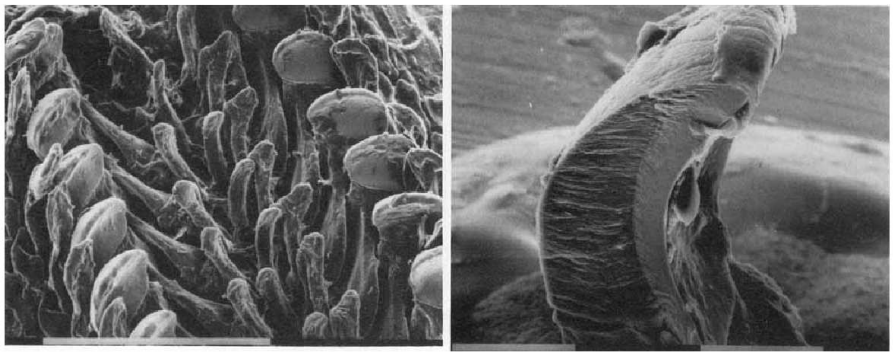

Figure 2.1.: Left: Mature portion of the radula of chiton. Rows of teeth are visible. Right: Fractured cross section of an individual mineralized tooth. The images are taken from [20].

Iron is used in nature for different aspects from which one example is the radula of the teeth of chiton which are shown in figure 2.1. These structures are extremely resistant against abrasion allowing these mollusks to erode rock on which they reside.[27] These teeth have the largest hardness and stiffness of any biomineral reported on. This property is the consequence of an anisotropic construction organized by specially distinct organic and inorganic phases. The immature teeth only consist of a few ferric compounds which undergo a transformation to magnetite in the mature teeth.[28]

Another example is bacterial magnetite which is composed of well ordered single domain particles with a morphology connected to a hexagonal prism with truncated (011) faces by low index planes.[24] The crystallization seems to start from an amorphous phase composed of hydrated iron(III) oxide.

The iron storage protein ferritin, which is composed of 24 apoferritin subunits forming the outer shell of the protein, is capable of performing site specific catalytic oxidation of Fe(II) and the accumulation of Fe(III) in the inner core which is composed of ferrihydrite.[19] A modification of ferritin also results in the controlled growth of magnetite in the inner core.[21]

The generation of such composite structures is guided on a molecular level by complex combinations of different macromolecules like proteins, or interfaces directing the structure and composition of the particles.[5, 29–31] The influence of the control mechanism can be very specific. For example, only the growth of aragonite or calcite from supersaturated calcium hydrogen carbonate solution was reported when using proteins extracted from organisms forming either aragonite or calcite, respectively.[32, 33] Structured organic interfaces are examined in detail as they are thought to be one important aspect for matrix mediated crystal growth. At

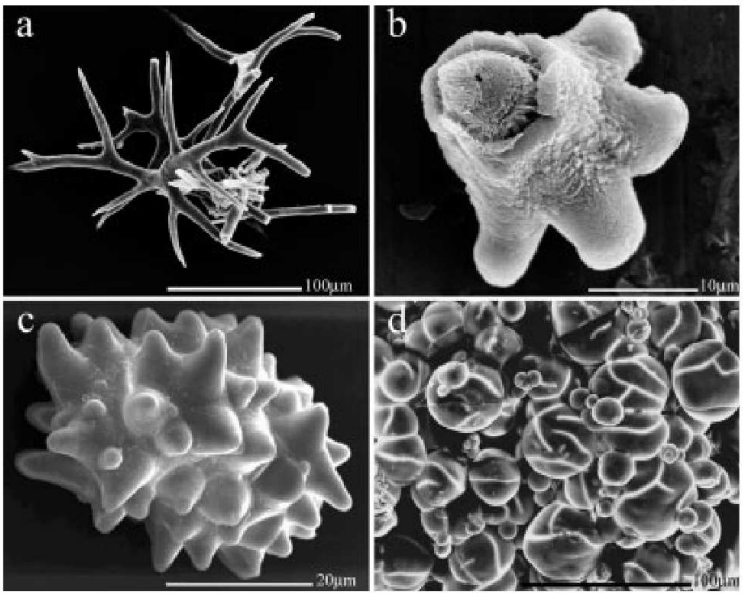

Figure 2.2.: SEM images from different structures made of ACC: a) Body spicules from pyura pachydermatina. b) Cross section of a broken tunic spicule from pyura pachydermatina. c) Cystolith from leaves of ficus microarpa. d) Granule from storage structures of orchestia cavimana. The image is taken from [57].

such interfaces the nucleation of particular crystal faces or the nucleation of certain polymorphs may be promoted by interfacial recognition.[30]

It was shown that inorganic ions tend to accumulate at charged interfaces increasing the interfacial concentration by a factor of two over the bulk concentration as well as a lateral ordering might appear at structured organic interfaces.[34–37] Studies reported on complex formation and strong bindings between the inorganic ions and the functional motif of a Langmuir layer.[38, 39] The growth of oriented crystals under Langmuir layers was explained by the match between the inorganic crystal lattice and the lateral order of the organic boundary.[40, 41] From this an epitaxial growth mechanism was proposed.[4, 30, 41–47] However, this process is highly disputed in literature. Another proposed growth mechanism in biological tissue is stereochemical matching controlling the nature of the crystals.[48] This growth mechanism requires rigid and highly specific interaction sides with a complementary periodic arrangement of the organic interface with an array of ions in the crystal lattice.[5, 13, 49] Further a stereochemical correspondence between the organic interface and the crystal is required e.g. a correspondence between a carboxylate group of an organic motif and a carbonate group of a calcium carbonate crystal.[5, 13, 49] In contradiction to this, recent studies report on the dominance of electrostatic interactions influencing the crystallization by which periodic arrangement can be neglected.[50, 51] These studies show mainly the interaction of acidic residues of proteins with the crystal faces.[52] The interacting residues lack a periodic arrangements and, thus, the interaction with the crystals occurs due to unspecific and flexible sites. The mineral phase may be controlled by the surface charge density.[53] Also experiments report on the stabilization of different polymorphs depending on the surface pressure of Langmuir layers which is directly linked to the surface charge density.[45, 54–56]

The observations made regarding the surface charge are in accordance with reports from the

appearance of amorphous particles providing the first nucleation step for biomineralization in biological samples as well as in in-vitro investigations.[43, 55, 56, 58–61] A well studied example is amorphous calcium carbonate (ACC). Different structures which are composed of (ACC) are shown in figure 2.2. Clusters of ACC nucleate and are transformed subsequently into crystalline material. However, the stabilization of the amorphous phase and the transformation towards a crystalline polymorph are subject of different investigations.[57, 62–64] These studies show the existence of various biogenic ACC which offer a different ordering in the near structure. It could be shown that the transformation of this ACC can be influenced by the surface pressure of Langmuir layers, the pH value, or magnesium ions.[64] The formation of ACC happens at phospholipid monolayers which subsequently cause the transformation to calcite via vaterite where the stability of the metastable vaterite was influenced by the surface pressure.[54, 65] High surface pressure inhibits the transformation thus stabilizing vaterite. Similar observations could be made for macromolecules like ovalbumine where first ACC was stabilized which transformed to vaterite and calcite.[66] However, the stability of the vaterite phase was also increased as the ovalbumine concentration increased hinting a stabilizing effect. By combining soluble process-directing agents and a Langmuir monolayer the growth of tablets of aragonite at the interface could be induced.[67]

2.2. Nucleation and growth

The nucleation of minerals from solution can be described by a spontaneous formation of small seeds throughout the solution with size-dependent free energies.[68–71] These seeds dissolve again if the condition for a stable cluster is not fulfilled. The nucleation process is induced if a two phase system is energetically more favorable than a sole single phase system. The free Gibbs energy ΔG of such seeds is composed of the strain energy ΔG_S of the cluster per unit volume and the free energy ΔG_V of the cluster per unit volume. The initial seeds are stable if the decrease in energy by creating the bulk volume overcomes the energy increase due to interfacial free energy. From this condition the critical radius r_s can be derived which defines a stable cluster

$$r_s = -\frac{3\sigma}{\Delta G_V - \Delta G_S}. \tag{2.1}$$

The interfacial tension of the cluster is described by σ and the difference of the Gibbs free energies by $\Delta G_V - \Delta G_S$. If the radius of the cluster is bigger than this critical radius the clusters are stable and continue to grow whereas for smaller values the seeds dissolve again. This radius depends on the temperature, the level of supersaturation, and the energy of the accruing interfaces of the two phase system.

The mentioned situation accounts for homogeneous nucleation, meaning the spontaneous nucleation in solutions by statistically controlled fusion of small seeds. If the nucleation takes place at an interface, a so called heterogeneous nucleation occurs. If the interaction between the seed and the interface lowers the Gibbs free energy, the critical radius for a cluster is lowered. It can happen that the concentration is high enough to achieve a supersaturation at the interface

and only the heterogeneous nucleation sets in, as the limit for homogeneous nucleation is not surpassed. However, by ongoing mineralization the saturation level decreases again stopping the film growth process. The heterogeneous nucleation mostly results in the formation of thin films.

The final morphology of the crystals can be understood in the framework of thermodynamical and kinetic growth mechanism. Regarding the thermodynamic picture of thef crystal growth process, the difference of the surface energy and the growth environment is influencing the forming structure. The evolution from the initial seed to the final crystalline phase proceeds by a single step. The final shape can be described by the rule of Wulff which states that the equilibrium morphology is determined by the minimum of the sum of the products of all exposed faces with the relative surface energies.[72] Fast growing faces have a high surface energy whereas slow growing faces have a low one. By this, the slow growing faces determine the shape of the crystal. The thermodynamic treatment can not always predict the final morphology as defect structures and kinetic aspects have to be considered, too. However, it can be used as a basis for the explanation of additive mediated crystal growth. These additives are composed of ions, polymers, and proteins which influence the surface energy of a crystal face.[73–80] Thereby the surface energy of the according face is changed, thus, influencing the growth speed of the crystal face and with this the overall shape.[5] The formation of anisotropic structures like needles, spheres, or tubes can be explained by this route.

The kinetic controlled growth relies on the modification of activation energy barriers of metastable states of the nucleation cluster.[5] The crystallization proceeds by a step by step process via metastable phases until a stable polymorph is reached. This mechanism includes the modification of the composition and the crystal structure by kinetic effective reaction pathways. The phase transformation normally proceeds by a dissolution-recrystallization process. The stability of each metastable state is a function of the solubility of the present phase and activation energy for a further transformation step. These transformations can be described by the Oswald rule.[81] However, the stability of each metastable state can be changed by additives as the transformation mainly relies on recrystallization of the intermediate phase.

In biomineralization processes a high relevance is allocated to the evolution of amorphous pre-cursor phases. These phases allow an effective material transport but also enable the generation of complex structures like the skeletal of corals.[5, 28, 82–86] The concentration needed for the formation of amorphous phases is low compared to a direct nucleation of a crystal.[5] The transformation process is speculated to proceed by a solid state transformation of the amorphous structure resulting in a crystalline ordered compound and not via an anew solution and recrystallization process.[87]

The crystallization in organisms will not only proceed by one single mechanism but rather all different ways might be present in order to achieve the best result. At organic interfaces, for which Langmuir layers are used in the following studies, the crystallization can proceed via different ways. A sketch of the different mechanisms is depicted in figure 2.3. A templating effect could be exerted by the regular arrangement of a Langmuir layer as single ions accumulate at the functional group of the mono molecular film.[41] As this layer mimics a regular

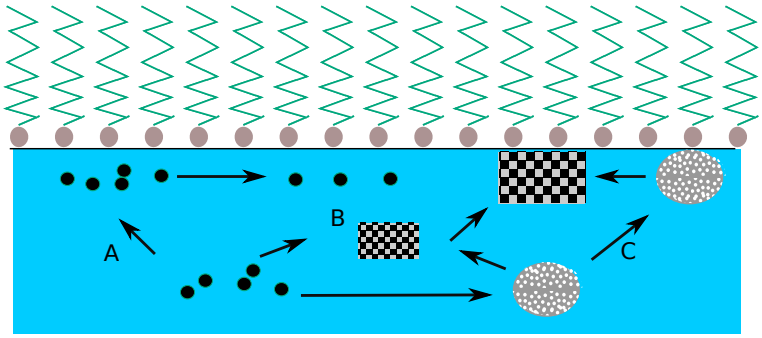

Figure 2.3.: Crystallization pathways at an organic interface. A) Cluster formation directly occurs at the monolayer. B) Cluster form in the solution and enrich at the interface. C) Amorphous pre-cursor form. The scheme was adapted from [88].

arrangement similar to a crystal lattice an ordered growth might occur. Also the homogeneous nucleation of small crystallites could occur which subsequently adsorb to the interface with a certain orientation. This would induce the growth of a crystalline layer with preferred crystal orientation.[5, 13] A further pathway includes amorphous pre-cursors. Such structures might be formed in the bulk solution or at an interface. In all of these processes the Langmuir layer can influence the inorganic film but also the ongoing mineralization could induce changes in the organic matrix itself as such systems are not rigid and exhibit some flexibility.

2.3. Nanoparticle adsorption

Particles are able to adsorb to an interface dividing hydrophilic and hydrophobic media. If the particles are regarded as single spheres the adsorption behavior is determined by the surface tension and the contact angle of the particle to the interface. From this it follows that particles with a finite contact angle and sufficient small mass can adsorb to an interface.[89, 90] If the contact angle is equal to $90°$ the particles are preferred to be at the interface whereas for a contact angle which is smaller than $90°$ the particles are favored to be present in the hydrophilic phase. If the contact angle is bigger than $90°$ the particles like to be in the hydrophobic phase. However, the bulk concentration seems to have also a significant influence as an adsorption was observed if the particle concentrations in the solution was raised to higher concentrations.[91]

2.4. Iron species in aqueous solution

The chemical compounds which are encountered in an aqueous solution containing iron species can differ significantly. The Fe(III) ion has sixfold coordination and a strong tendency for hydrolysation in aqueous media which is the source for a variety of different iron species e.g. $(Fe(OH)_y^{3-y}, y \leq 4)$ and dimers with the composition $Fe_2(OH)_2^{4+}$ under strong acidic conditions.[92, 93] Further, compounds may be observed if other ions are present in the solution. For example at elevated chlorine concentration chloro-complexes like $[FeCl(H_2O)_5]^{2+}$ may be present as well.[94] Table 2.1 renders an overview of the different species of Fe(III) in

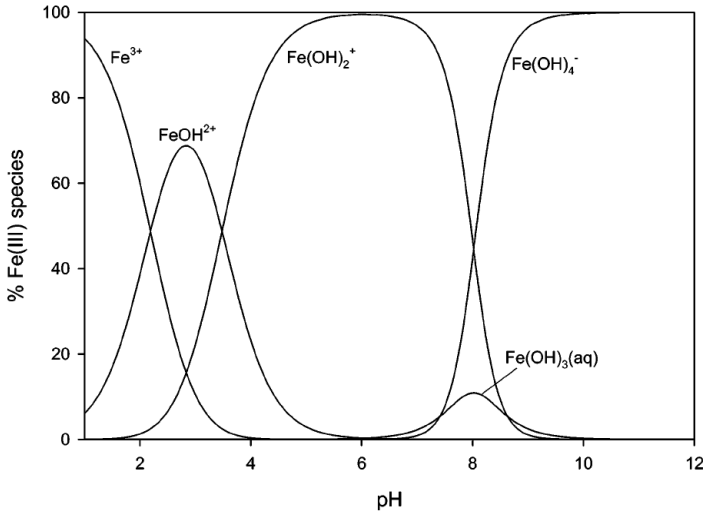

Figure 2.4.: Speciation of iron(III) as function of the pH value at an iron concentration of totality c(Fe)=10 μmol. The graph is taken from [92].

aqueous solutions along with the hydrolysis constants. Figure 2.4 shows a graph depicting the fraction of different iron(III) species in an aqueous solution as function of the pH value.[92] It is obvious that depending on the pH value a distinct compound is dominating. Thus, the observations which are made for iron(III) chloride solutions and Langmuir layers cannot be explained by sole interactions of iron(III) ions with the monolayer film.

A hydrolysis reaction can be formulated as

$$Fe^{3+} + H_2O \rightleftharpoons [FeOH]^{2+} + H^+. \tag{2.2}$$

This balance can be characterized by the hydrolysis constant

$$K = \frac{c[FeOH^{2+}]c[H^+]}{c[Fe^{3+}]}. \tag{2.3}$$

For solutions containing iron(II) species the situation is much simpler as only the compounds $FeOH^+$, $Fe(OH)_2$, and $FeCl^+$ can be present. The hydrolysis constants are summarized in table 2.2. The amount of each compound was calculated for different initial iron(II) chloride concentration and is given in table 2.3.

The calculated values show that mainly iron(II) ions are present and the contribution from other iron compounds can be neglected in contrast to iron(III) chloride solutions.

The formation of insoluble iron hydroxides or iron oxides is a process depending on different factors like the pH value, the temperature, or the presence of different ions, organic molecules and oxidation agents.[99] Different nucleation and growth steps occur from soluble iron species towards a solid state material. On the addition of iron salts to aqueous solutions small colloidal particles form by the aggregation of pre-cursors composed of aqueous $Fe(OH)^0_{3,(aq)}$ species.[100–102] The colloidal particles formed by the fusion of monomeric $Fe(OH)_3$ subsequently transform

species	log(K)	reference
$[FeCl(H_2O)_5]^{2+}$	1.16 ± 0.20	[94, 95]
$[FeCl_2(H_2O)_4]^{+}$	1.28 ± 0.25	[94, 96]
$[FeCl_3(H_2O)]_{(aq)}$/ $[FeCl_3(H_2O)_2]_{(aq)}$	0.77 ± 0.25	[94, 95]
$FeCl_4^-$	-1.26 ± 0.45	[94]
$Fe(OH)^{2+}$	-2.19	[92, 97]
$Fe(OH)_2^+$	-5.76	[92, 97]
$Fe(OH)_3^0$	-11.8	[92, 97]
$Fe(OH)_4^-$	-21.8	[97]
$Fe_2(OH)_2^{4+}$	-2.92	[97]

Table 2.1.: Hydrolysis constant of different ion complexes formed by iron(III) aqueous species.

species	log(K)
$Fe(OH)^+$	4.5
$Fe(OH)_2$	-6.5
$FeCl^+$	1.5

Table 2.2.: Stability constant of different iron species formed by iron(II) aqueous species.[98]

species	concentration [$\mathrm{mmol/L}$]	concentration [$\mathrm{mmol/L}$]
$FeCl_2$	0.1	100
c(Fe)	0.61	95
$c(FeOH^+)$	0.039	3.9
$c(FeCl)^+$	10^{-7}	10^{-4}
$c(Fe(OH)_2)$	10^{-16}	10^{-10}

Table 2.3.: Speciation of iron(II) for different iron(II) chloride concentration values calculated by the stability product.

to crystalline material.[102] The following transformation route can be established [100, 101]

$$Fe^{2+} \rightarrow Fe^{3+} \rightarrow Fe(OH)_n^{3-n} \rightarrow \text{amorphous particles} \rightarrow \text{crystalline phase.} \tag{2.4}$$

The rate of crystallization strongly depends on the solution condition and can be very slow lasting months.[99] However, the initial formation of the amorphous colloidal particles proceeds very quickly.[100, 102] After this first step the formation of crystalline species proceeds by a transformation reaction yielding e.g. goethite (γ-FeOOH) or maghemite (Fe_2O_3).[101] The last step is a precipitation reaction where the insoluble species are dropped out. This can also be described by a stability constant K. However, the determination of K is extremely difficult. Factors like the composition, pH value, and temperature are influencing the equilibrium. For the experiments presented here, the equilibrium is shifted by a change of the pH value in the interfacial region. By this the precipitation reaction is triggered and unsoluble products are formed. The different formation and transformation pathways are depicted in figure 2.5 showing the complexity of the system.

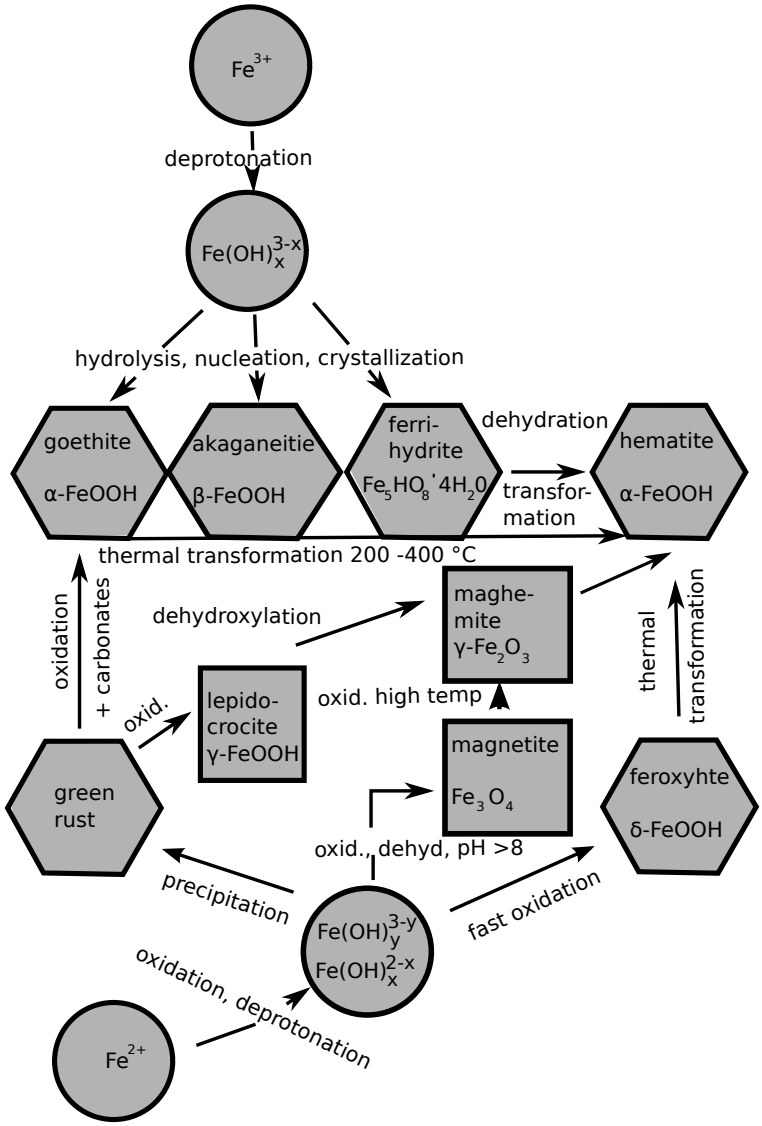

Figure 2.5.: Transformation and formation pathways of iron compounds. The graph is adapted from [103].

2.5. Langmuir layers

This section describes the structure and properties of mono molecular films of amphiphilic molecules called Langmuir layers. First, the effects which drive the formation of a Langmuir layer will be discussed. Then, the structural phase transitions will be shortly outlined together with a description of the surface pressure-area isotherms. The different amphiphiles will be specified in the end.

Langmuir layers are mono molecular films composed of amphiphilic molecules which are oriented at specific interfaces, e.g. the water-air interface. These molecules are composed of hydrophilic (polar) and hydrophobic (non-polar) parts. The polar part is denoted as the headgroup and the unpolar alkyl chain as the tailgroup. Amphiphilic molecules vary in the headgroup composition having e.g. carboxylate or amide headgroups. Also, the tailgroup varies as the length of the alkyl chain or the number of chains can differ. Thus, Langmuir layers have diverse properties with respect to the observable phases they form.

sufficiently low, the formation of a monolayer at the interface is favorable compared to the formation of such complex structures. A further impact on the formation of a monolayer comes from the hydrophobicity of the single amphiphiles, which is directly influenced by the length of the alkyl chain.For chains shorter than 12 carbon atoms mostly water soluble micelles are formed. However, if the carbon group is too long no monolayer can be formed either because crystallization occurs.

Normally, Langmuir layers are formed by solving the amphiphiles in unpolar volatile solvents like tert-butyl-methyl ether (TBME) or trichlormethan (chloroform). If such a solution is spread on the water subphase, the solvent evaporates leaving the amphiphilic molecules at the interface and a monolayer is formed. The amphiphiles orient themselves with the polar headgroup towards the water subphase, whereas the tailgroup is oriented towards the air.

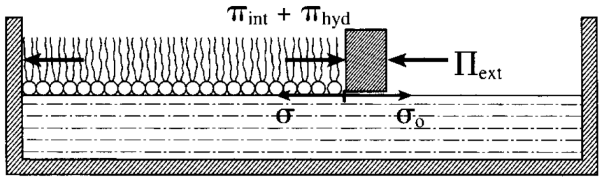

Figure 2.6.: Langmuir trough with compressed Langmuir layer. The surface pressure of the pure water surface and with lipid layer is represented by σ_0 and σ, respectively. The lateral pressure Π_{ext} is exerted by the surface barrier with counter force $\pi_{\text{int}} + \pi_{\text{hyd}}$.[6]

Figure 2.6 depicts a Langmuir layer at a water-air interface. The film is compressed by a surface barrier with the pressure Π_{ext} to a smaller area. The film is strained and a force $\pi_{\text{int}}+\pi_{\text{hyd}}$ exerts on the surface barrier and the surface pressure Π increases to

$$\Pi = \sigma_0 - \sigma. \tag{2.5}$$

The surface pressure can be calculated by considering the free energy F_{m} of a monolayer at a

water interface by [6]

$$F_{\mathrm{m}} = n_{\mathrm{m}}[\Phi_{\mathrm{hyd}}(A_{\mathrm{m}}) + \Phi_{\mathrm{int}}(A_{\mathrm{m}}) + \Phi_{\text{m-u}}(A_{\mathrm{m}})]. \tag{2.6}$$

The number of molecules in the film is denoted by n_{m} and the area occupied by each molecule as A_{m}. The hydration of the headgroup, the interaction of the molecules between each other, and the interaction between the hydrocarbon chains with the atmosphere are denoted by $\Phi_{\mathrm{hyd}}(A_{\mathrm{m}})$, $\Phi_{\mathrm{int}}(A_{\mathrm{m}})$ and $\Phi_{\text{m-u}}(A_{\mathrm{m}})$.

The surface pressure results from the derivative of the free energy with respect to the area A$_m$

$$\Pi_{\mathrm{m}}(A_{\mathrm{m}}) = -\left(\frac{\Delta F_{\mathrm{m}}}{\Delta A_{\mathrm{m}}}\right)_{n_{\mathrm{m}}} = \pi_{int}(A_{\mathrm{m}}) + \pi_{\mathrm{hyd}}(A_{\mathrm{m}}) - \phi'_{\text{m-u}}(A_{\mathrm{m}}). \tag{2.7}$$

The last term $\phi'_{\text{m-u}}(A_{\mathrm{m}})$ can be neglected as the interaction between the air and the carbon chain is weak. In case of the derivative of the free energy for a double layer, it can be shown that the mono and double layers are in a corresponding state as the molecules adopt the same area A_{m} and the surface pressure of the monolayer corresponds to the density of the hydrophobic free energy of a double layer.[6] Monolayers can, thus, be regarded as good model system for lipid double layers of biomembranes.

The surface pressure Π of a Langmuir layer can be measured using a Wilhelmy balance. Such a Wilhelmy balance consist of a test pad, called Wilhelmy plate, and a force sensor. The Wilhelmy plate is dipped into the water surface and a force pulls on this pad proportional to the surface tension. The force F_{W} which is observed by the force sensor can be calculated as [104]

$$F_{\mathrm{W}} = g(\rho_{\mathrm{p}} l_{\mathrm{p}} W_{\mathrm{p}} t_{\mathrm{p}} - \rho_{\mathrm{f}} h_p W_{\mathrm{p}} t_{\mathrm{p}}) + 2\sigma t_{\mathrm{p}} W_{\mathrm{p}} \cos\theta_{\mathrm{B}}. \tag{2.8}$$

The first term describes the flotation of the Wilhelmy plate which depends on the volume of the plate, given by the length l_{p}, width W_{p}, and thickness t_{p}, the height being immersed in the water subphase h_p and the density of the plate and water subphase ρ_{p} and ρ_{f}, respectively. The second term describes the force due to wetting of the plate as a function of the surface

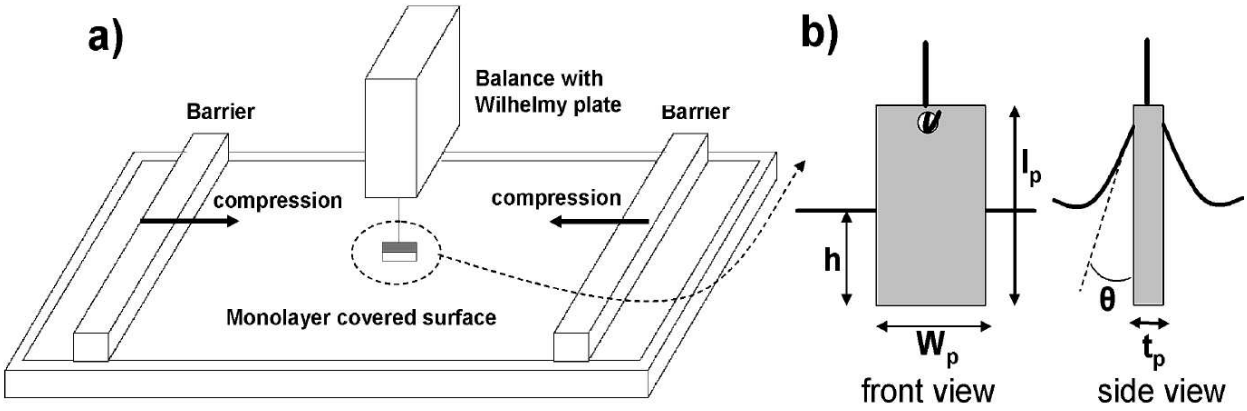

Figure 2.7.: a) Langmuir trough with two adjustable barriers for compression of the Langmuir layer. b) Front and side view of the Wilhelmy plate. The picture was taken from [105]

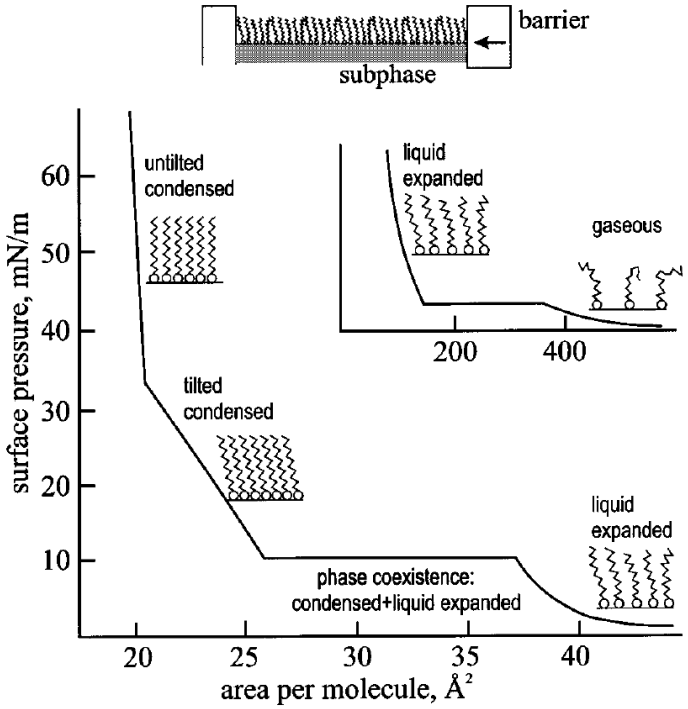

Figure 2.8.: Top: Compressed Langmuir layer. Bottom: Sketch of a Π-A isotherm of a Langmuir layer and a scheme showing the structure of the amphiphiles in the corresponding phase.[106]

tension σ and the contact angle θ_{B}. Wilhelmy plates with high surface energies, like platinum or iridium, have contact angles of $0°$ and the force depends linearly on the surface tension. Thus, the difference of the force exerted by a pure water subphase and a subphase with Langmuir layer on the Wilhelmy plate gives information on the surface pressure yielding

$$\Pi = \sigma_0 - \sigma = \frac{\Delta F_{\mathrm{W}}}{2(t_{\mathrm{p}} + w_{\mathrm{p}})}. \tag{2.9}$$

Langmuir films exhibit different phases which depend on the temperature of the subphase and surface pressure.[106] The compression of a Langmuir layer by reducing the accessible area at constant temperature yields a surface pressure-area (Π-A) isotherm. A sketch of such an isotherm is shown in figure 2.8. For a large area per molecule, a huge space is available for every molecule and the monolayer is in a gaseous state. The interactions between the lipids are low and the Langmuir layer can be regarded as an ideal two-dimensional gas. The surface pressure can be approximated by [107]

$$\Pi = \frac{k_{\mathrm{B}} T}{A_{\mathrm{m}}}. \tag{2.10}$$

If the film is compressed, a transition to the liquid expanded phase can be observed. This phase can be described by the van der Waals equation for a non-ideal gas [6]

$$\left(\Pi + \frac{A_{\mathrm{int}}}{A_{\mathrm{m}}^2}\right)(A_{\mathrm{m}} - A_{\mathrm{e}}) = k_{\mathrm{B}} T \tag{2.11}$$

lipid	molecular formula	headgroup	l_c	N_{chain}	M_w [g mol^{-1}]
DPPC	$C_{40}H_{80}NO_8P$	zwitter-ionic	C_{16}	2	734
DPPA	$C_{35}H_{68}NO_8PNa$	anionic	C_{16}	2	670.9
EPC	$C_{42}H_{85}NO_8PCl$	cationic	C_{16}	2	797.5
stearic acid	$C_{18}H_{36}O_2$	anionic	C_{18}	1	284.4
stearyl amide	$C_{18}H_{37}ON$	non-ionic	C_{18}	1	283.50
stearyl alcohol	$C_{18}H_{38}O$	non-ionic	C_{18}	1	270.49

Table 2.4.: Summarized properties of the used amphiphiles in the presented studies. The number of the alkyl chains is denoted by N_{chain} and the length of this chain by l_c in terms of carbon atoms.

A repulsion correction is accounted by A_{int} and the area A_e which is excluded by amphiphiles itself. The single lipids start to interact but still no long range ordering occurs. This region is followed by a coexistence region of the condensed and liquid expanded phase. The liquid expanded phase normally exhibits a phase transition of first order with a horizontal curve in the isotherm. Most systems show a positive slope which can be attributed to impurities. The Gibb's phase rule allows the coexistence of two phases for the increased number of components over a larger surface pressure range.[108] Upon further compression, the so called tilted condensed phase is reached. In this phase, the headgroups are arranged regularly and the tailgroup exhibits a tilt with respect to the interface. This tilt reduces as the surface area is decreased further until all tailgroups are in the upright position and the untilted condensed phase is obtained. Further compression results in a collapse of the film structure. The tilted and untilted condensed phase both exhibit a lateral periodic arrangement.[106]

Langmuir layers form well ordered lateral structures with crystalline domains which can be investigated by X-ray diffraction experiments. In the investigations performed in the framework of this study six different amphiphiles varying in the headgroup composition and the length and number of the hydrocarbon chains were used. The amphiphiles along with their properties are listed in table 2.4. The phospholipids consist of a glycerol backbone which links the headgroup with the two alkyl chains each consisting of 16 carbon atoms. Stock solutions with a concentration of $0.5\ \mathrm{mmol/L}$ were prepared by using chloroform. Anionic, cationic, and zwitter-ionic molecules were used in order to change the charge properties of the interface systematically. The second class of amphiphiles has an alkyl chain with a length of 18 carbon atoms. However, these amphiphiles only have a single chain. Two of the used headgroups were non-ionic and one was anionic, being a carbonyl-, an amide- and a carboxylate headgroup, respectively. For these amphiphiles, stock solutions with a higher concentration of $1\ \mathrm{mmol/L}$ were used. In order to control the surface pressure with good accuracy while spreading the amphiphiles at the interface, these different concentration had to be used.

2.6. X-ray scattering from interfaces

In the framework of this thesis, experiments utilizing different X-ray techniques were employed in order to investigate adsorption processes at interfaces. In the following chapter the methods of X-ray reflectivity (XRR), grazing incidence diffraction (GID), and X-ray absorption spec-

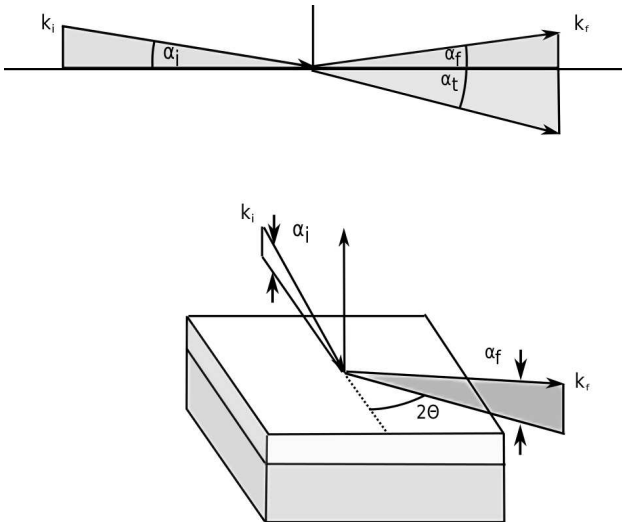

Figure 2.9.: Sketch of the in-plane and out-of-plane scattering geometry

troscopy (XAS) are described briefly. The mentioned techniques complement each other and, thus, allow to draw a comprehensive picture of the sample system under investigation.

2.6.1. Scattering geometry

The following paragraph deals with the geometry of X-ray scattering experiments in general. A sketch of the scattering layout is shown in figure 2.9. The X-ray beam hits the sample under an angle denoted α_i and is scattered under an angle α_f into the space above the sample surface. A part of the incoming X-ray beam is refracted into the medium under the angle α_t. The so called in-plane geometry is defined by the plane which is oriented perpendicular to the sample surface and which accommodates the incoming and the reflected beam. A further out-of-plane angle 2θ has to be defined if scattering contributions are investigated which lie outside of this plane.

The incoming and scattered X-rays are described by plane waves $\vec{E_\mathrm{i}}(\vec{k_\mathrm{i}})$, $\vec{E_\mathrm{f}}(\vec{k_\mathrm{f}})$, and $\vec{E_\mathrm{t}}(\vec{k_\mathrm{t}})$ with the wave vectors $\vec{k_\mathrm{i}}$, $\vec{k_\mathrm{f}}$ and $\vec{k_\mathrm{t}}$, respectively. In the following only elastic scattering is considered and the wavelength λ of the photons is preserved. In X-ray scattering experiments the intensity is monitored as function of the wave vector transfer $\vec{q} = \vec{k_\mathrm{f}} - \vec{k_\mathrm{i}}$. The correlation of the wave vector transfer to the incident angle and the scattering angle can be deduced from the sketched geometry depicted in figure 2.9 as

$$\vec{q} = \vec{k_\mathrm{f}} - \vec{k_\mathrm{i}} = |\vec{k_\mathrm{i}}| \begin{pmatrix} \cos\alpha_\mathrm{f}\cos 2\theta - \cos\alpha_\mathrm{i} \\ \sin\alpha_\mathrm{f}\sin 2\theta \\ \sin\alpha_\mathrm{f} + \sin\alpha_\mathrm{i} \end{pmatrix}. \tag{2.12}$$

X-ray reflectivity measurements investigate the specular reflected intensity and with this, the

incident and exit angle are equal ($\alpha_\mathrm{i} = \alpha_\mathrm{f}$ and $2\theta = 0$). Insofar, the expression simplifies to

$$\vec{q} = \begin{pmatrix} 0 \\ 0 \\ q_z \end{pmatrix} = |\vec{k_\mathrm{i}}| \begin{pmatrix} 0 \\ 0 \\ 2\sin\alpha_\mathrm{i} \end{pmatrix} = \frac{4\pi}{\lambda} \begin{pmatrix} 0 \\ 0 \\ \sin\alpha_\mathrm{i} \end{pmatrix}. \tag{2.13}$$

In XRR measurements, only a wave vector transfer perpendicular to the sample surface occurs. Consequently, such experiments only give information on the laterally averaged vertical structure of the sample.

A further special case is a so called out-of-plane measurement; in these measurements, the experimental conditions are chosen to be: $\alpha_i \approx \alpha_f \approx 0$ and $2\theta \neq 0$. By this, the wave vector transfer only has lateral components

$$\vec{q} = \begin{pmatrix} q_x \\ q_y \\ 0 \end{pmatrix} = \frac{2\pi}{\lambda} \begin{pmatrix} \cos(2\theta) - 1 \\ \sin(2\theta) \\ 0 \end{pmatrix}. \tag{2.14}$$

Thus, these measurements supply only information on the lateral structure of the sample surface.

The lateral component $|\vec{q}_{||}|$ is given by

$$|\vec{q}_{||}| = |k_\mathrm{i}|\sqrt{1 + \cos^2\alpha_f - 2\cos\alpha_f\cos 2\theta} \approx 2k\sin\frac{2\theta}{2}. \tag{2.15}$$

It is obvious that, depending on the kind of information which is of interest, the optimal scattering geometry has to be used.

2.6.2. X-ray reflectivity from smooth surfaces

The following section briefly describes the theory of X-ray reflectivity measurements in terms of optics at smooth interfaces. For a detailed description the reader is referred to [109].

One relevant parameter in an X-ray reflectivity measurement is the index of refraction n of the sample. Under the assumption that N atoms per unit volume can be described by harmonic oscillators with the respective resonance frequencies ω_j the index of refraction can be expressed as [109]

$$n^2(r) = 1 + N\frac{e^2}{\epsilon_0 m_\mathrm{e}} \sum_{j=1}^{N} \frac{f_i}{\omega_j^2 - \omega^2 - 2i\omega\eta_j}, \tag{2.16}$$

where ω is the frequency of an electromagnetic wave propagating through the medium, e the elementary charge, m_e the electron mass and ϵ_0 the electrical field constant. The factors f_i denote the forced oscillation strength of each single atom and η_j are damping factors. The oscillation strength f_j is, in general, a complex number:

$$f_j = f_j^0 + f_j'(\omega) + if_j''(\omega). \tag{2.17}$$

Dispersion and absorption corrections are taken into account by $f_j'(\omega)$ and $f_j''(\omega)$. If the oscillation frequency of the electromagnetic wave field is much higher than optical frequencies and far away from resonance frequencies of inner atomic shells, equation 2.16 simplifies to

$$n = 1 - \delta + i\beta, \tag{2.18}$$

with $\delta = \frac{\lambda^2}{2\pi} r_\mathrm{e} \rho$ being the dispersion, where r_e is the classical electron radius and ρ the electron density, and the absorption $\beta = \frac{\lambda}{4\pi}\mu$, where μ represents the linear absorption coefficient.[2] Scattering at smooth surfaces can be described by the Fresnel formulas[1] which are given by

[110]

$$\begin{aligned} r =& \frac{k_{\mathrm{i},z} - k_{\mathrm{t},z}}{k_{\mathrm{i},z} + k_{\mathrm{t},z}}, \\ t =& \frac{2k_{\mathrm{i},z}}{k_{\mathrm{i},z} + k_{\mathrm{i},z}}, \end{aligned} \tag{2.19}$$

where the index z denotes the z component of the corresponding wave vector.

Since the real part $\Re(n)$ is always smaller than one in matter, vacuum is the medium with the higher optical density. The consequence is the occurrence of total external reflection. As the incident angle of the X-rays gets smaller than the critical angle α_c, the X-rays are totally reflected. The value of the critical angle α_c can be deduced from Snell's law and it follows $\alpha_c = \sqrt{2\delta}$.

For smaller angles $\alpha_i < \alpha_c$ the wave field can no longer penetrate the sample and an evanescence wave propagates parallel to the interface.

This wave field infiltrates the medium with a penetration depth [109]

$$\Lambda = \frac{1}{2k_i \Im(\alpha_t)}. \tag{2.20}$$

As the incident angle tends to zero, the penetration depth gets independent of the wavelength yielding $\Lambda = \frac{1}{\sqrt{4\pi r_\mathrm{e}\rho}}$.[109] For most materials, a penetration depth of $\Lambda \approx 50$ Å exists which shows that for very shallow angles the scattering mainly originates from the near surface region. As the angle α_i is increased, the penetration depth increases rapidly and is then only limited by the absorption of the material.

The square of the transmission function $|t|^2 = T$ and reflection function $|r|^2 = R_\mathrm{F}$ (called the Fresnel reflectivity) are depicted in figures 2.10 and 2.11. The incident angle α_i is normalized by the critical angle α_c. The transmission function shows a maximum for $\alpha_\mathrm{i} = \alpha_\mathrm{c}$ which originates from a constructive interference of the reflected and transmitted waves increasing the intensity by a factor of two.[109] As the angle α_c is passed T tends to unity. This angle dependence of the transmission coefficient may result in the observation of the so called Vineyard peak.[111]

[1] In case of X-rays the Fresnel formulas for p-polarized and s-polarized waves are practically the same. Hence, for simplification only the s-polarized waves are considered.

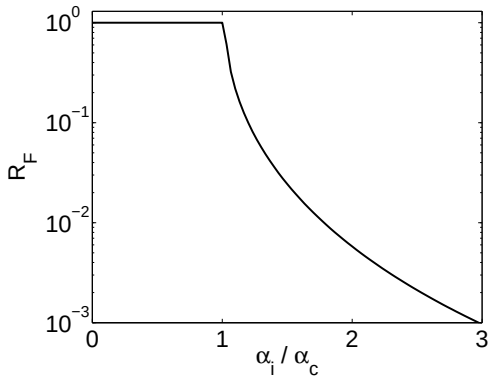

Figure 2.10.: Fresnel reflectivity R_F as function of the incident angle α_i normalized by the critical angle α_c.

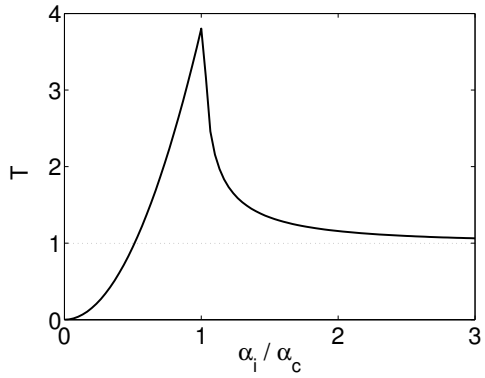

Figure 2.11.: T as function of the incident angle α_i normalized by the critical angle α_c.

Figure 2.10 shows that the reflected signal $R_\mathrm{F} = |r^2|$ is unity as the incident angle is smaller then α_c and exhibits a strong decay as this angle is passed.

In case of stratified media with j layers where every layer has a different refractive index n_j multiple reflections occur at the interfaces. The electromagnetic waves interfere with each other and a modulation of the reflected signal is observed. This can be described by the recursive approach of Parratt [112]

$$X_\mathrm{j} = R_\mathrm{j}/T_\mathrm{j} = \exp(-2ik_\mathrm{z,j}z_\mathrm{j})\frac{r_\mathrm{j,j+1} + X_\mathrm{j+1}\exp(2ik_\mathrm{z,j+1}z_\mathrm{j})}{1 + r_\mathrm{j,j+1}X_\mathrm{j+1}\exp(2ik_\mathrm{z,j+1}z_\mathrm{j})} \tag{2.21}$$

where $X_\mathrm{j+1}$ denotes the ratio of $R_\mathrm{j+1}$ and $T_\mathrm{j+1}$ in the j-th layer. The Fresnel-coefficient $r_\mathrm{j,j+1}$ is defined as

$$r_\mathrm{j,j+1} = \frac{k_\mathrm{z,j} - k_\mathrm{z,j+1}}{k_\mathrm{z,j} + k_\mathrm{z,j+1}} \tag{2.22}$$

with $k_\mathrm{z,j} = k(n_\mathrm{j}^2 - \cos^2\alpha_i)^{1/2}$ being the z-component in the j-th layer. The substrate is in general much thicker than the penetration depth of the X-rays and no reflection from the substrate occurs. This condition serves as a starting point for the recursion. The reflected intensity is thus given as

$$R_\mathrm{j+1} = \frac{1}{t_\mathrm{j+1,j}}\left(T_\mathrm{j}r_\mathrm{j+1,j}\exp(-i(k_\mathrm{z,j+1} + k_\mathrm{z,j})z_\mathrm{j}) + R_\mathrm{j}exp(-i(k_\mathrm{z,j+1} - k_\mathrm{z,j})z_\mathrm{j})\right) \tag{2.23}$$

$$T_\mathrm{j+1} = \frac{1}{t_\mathrm{j+1,j}}\left(T_\mathrm{j}\exp(i(k_\mathrm{z,j+1} - k_\mathrm{z,j})z_\mathrm{j}) + R_\mathrm{j}r_\mathrm{j+1,j}exp(i(k_\mathrm{z,j+1} + k_\mathrm{z,j})z_\mathrm{j})\right) \tag{2.24}$$

with the Fresnel coefficient $t_\mathrm{j+1,j} = 1 + r_\mathrm{j+1,j}$.

Real interfaces are not perfectly smooth and offer always roughness. Due to this the specular reflected intensity is damped compared to the Fresnel reflectivity. The interface of such a system is no longer sharp and has to be replaced by a continuous variation of the laterally averaged refractive index $n_\mathrm{j}(z)$. If the variation between two media can be described by an error function

profile new Fresnel-coefficients are obtained

$$\tilde{r}_{\mathrm{j,j+1}} = r_{\mathrm{j,j+1}} \exp(-2k_{\mathrm{z,j}}k_{\mathrm{z,j+1}}\sigma_j^2) \tag{2.25}$$

$$\tilde{t}_{\mathrm{j,j+1}} = r_{\mathrm{j,j+1}} \exp((k_{\mathrm{z,j}} - k_{\mathrm{z,j+1}})^2\sigma_j^2/2) \tag{2.26}$$

where σ is root-mean-square (rms) roughness of the interface.

Figure 2.12 shows the calculated reflectivity of a single layer system. The figure also shows the Fresnel reflectivity from the bare substrate. Due to the presence of the layer, oscillation occur, the so called Kiessing fringes.[113] These fringes originate from interference of the X-rays scattered at the interface.s The thickness of the layer can be deduced from the period of the oscillation by $l = 2\pi/\Delta q_z$ where Δq_z is the difference of two subsequent minima. The figure also shows the increased decay of the reflectivity induced by the roughness.

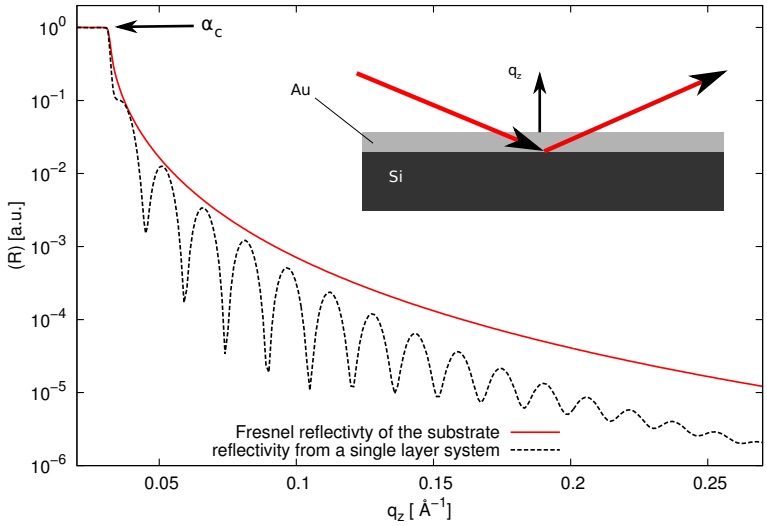

Figure 2.12.: Calculated reflectivity of a silicon wafer covered by a 400 Å thick polystyrene layer for a wavelength of 8 keV. Also the Fresnel reflectivity from a smooth silicon substrate without layer is shown. In case of a stratified sample Kiessing fringes can be seen.

2.6.3. Diffraction experiments

The following section illustrates the grazing incidence diffraction (GID) technique which probes the long range order of the sample's interface under consideration. The scattering geometry is described in chapter 2.6.1. Here, a general description of diffraction experiments is given at first. Then the conditions of grazing incidence diffraction experiments are discussed more closely. Furthermore, theoretical considerations important for scattering from two-dimensional systems such as Langmuir layers are made.

Crystals are composed of a periodic arrangement of atoms or molecules. Therefore, a crystal can be defined by a combination of a point lattice and a basis, which resides on the lattice points. The unit cell of a crystal contents information on the structure and symmetry. It is completely defined in three dimensions by the length of the translation vectors a_i $(i = 1, 2, 3)$ and the angles α, β and γ between them. If these lattice vectors are chosen in a way, that the unit cell has the

smallest possible volume this cell is called primitive. In three dimensions 14 Bravais lattices with 230 space groups describing the symmetry of the crystal structures exist. This number reduces for a two-dimensional system to 5 Bravais lattices with 14 space groups.[114]

The point lattice of a crystal can be described by a set of translation vectors

$$\overrightarrow{R_n} = \sum_{i=1}^{N} n_i \vec{a_i}, \tag{2.27}$$

with $n \in \mathbb{Z}$, the lattice vectors $\vec{a_i}$, and the dimension N of the periodic structure.[2]

The basis is described by the translation vectors $\vec{a}_i$ and the position of the k constituents of the basis in real space are given by

$$\overrightarrow{r_n} = \sum_{i=1}^{N} x_{i,j} \vec{a_i},\ j = 1, .., k \tag{2.28}$$

with $x_{i,j} \neq 1$. This crystal lattice is further connected to an equivalent lattice in the reciprocal space via a Fourier transformation. The translation vectors of the reciprocal lattice can be calculated from the lattice vectors via

$$b_1 = \frac{2\pi \vec{a}_2 \times \vec{a}_3}{V_\mathrm{U}}, \tag{2.29}$$

$$b_2 = \frac{2\pi \vec{a}_3 \times \vec{a}_1}{V_\mathrm{U}}, \tag{2.30}$$

$$b_3 = \frac{2\pi \vec{a}_1 \times \vec{a}_2}{V_\mathrm{U}}. \tag{2.31}$$

V_U denotes the volume of the unit cell. Thus, every point in the reciprocal lattice can be reached by the vector

$$\vec{G}_{hkl} = (h\,\vec{b}_1 + k\,\vec{b}_2 + l\,\vec{b}_3), \quad h, k, l \in \mathbb{Z}. \tag{2.32}$$

In the framework of the first-order Born approximation, the scattering amplitude, which is generated by the interaction of the X-rays with matter, can be described by [2]

$$A(\vec{q}) = -r_\mathrm{e} \int_V \rho(\vec{r}) e^{i\,\vec{q}\,\cdot\,\vec{r}} d^3r, \tag{2.33}$$

where $\rho(\vec{r})$ describes the electron distribution in the media and r_e the classical electron radius. By using $\vec{r} = \overrightarrow{R_n} + \overrightarrow{r_n} + \vec{r}'$ to describe the position of every electron at the relative position $\vec{r'}$ in the electronic shell of the atoms, it follows for the scattering amplitude of periodic structures

$$A(\vec{q}) \propto F_{\text{str}}(\vec{q}) \cdot \tilde{G}(\vec{q}) \tag{2.34}$$

with

$$\begin{aligned}\tilde{G}(\vec{q}) &= \sum_{n_1=0}^{N_1} \sum_{n_2=0}^{N_2} \sum_{n_3=0}^{N_3} e^{(i\vec{q}\cdot\vec{R}_n)} \\ &= S_{N_1}(\vec{q}\cdot\vec{a_1}) S_{N_2}(\vec{q}\cdot\vec{a_2}) S_{N_3}(\vec{q}\cdot\vec{a_3})\end{aligned} \tag{2.35}$$

and

$$F_{\text{str}}(\vec{q}) = \sum_{j=i}^{N} f_j(\vec{q}) e^{(i\vec{q}\cdot\vec{r_n})}, \tag{2.36}$$

$$f_j(\vec{q}) = \int_{-\infty}^{\infty} \rho(\vec{r}') e^{i\vec{q}\cdot\vec{r}'} d^3\vec{r}'. \tag{2.37}$$

The scattering amplitude can be split into parts: the structure factor $F_{\text{str}}(\vec{q})$ and the lattice sum $\tilde{G}(\vec{q})$. The structure factor $F_{\text{str}}(\vec{q})$ describes the scattering originating from each unit cell and depends on the atoms in it. The summation is performed over all atoms N residing in the unit cell. Further, the atomic form factor $f_j(\vec{q})$ is included which represents the scattering amplitude of a single atom and is defined as the Fourier transformation of the electron distribution $\rho(\vec{r}')$ of the electron shell. However, this term might be altered if the X-ray energy is in the range of an absorption edge. Then, the effect of the dispersion correction and resonant scattering has to be taken into account. The lattice sum $\tilde{G}$ accounts for required phase factors and between the scattered waves. This term only depends on the translation vectors defining the crystal lattice and the wave vector transfer. By summing up this term, the interference functions S_{N_i} are obtained. These functions have a maximum at the position $|\vec{q}| = \frac{2\pi n}{|\vec{a}_i|}$ and their width correlates with the number of unit cells as

$$\Delta_{\text{FWHM}} \approx \frac{1}{N_i}, \tag{2.38}$$

and, thus, with the size of the crystalline structure. As the size of the crystal tends to infinity ($N_i \to \infty$), the interference function transforms into a δ-distribution. A scattering signal can only be observed if the conditions

$$\vec{q}\cdot\vec{a_1} = 2\pi h, \tag{2.39}$$

$$\vec{q}\cdot\vec{a_2} = 2\pi k, \tag{2.40}$$

$$\vec{q}\cdot\vec{a_3} = 2\pi l, \tag{2.41}$$

are fulfilled simultaneously. In this case the lattice sum $\tilde{G}$ has a maximum value. Using the relation $\vec{a_i}\cdot\vec{b}_j = 2\pi\delta_{i,j}$ it follows that this occurs if the wave vector transfer is equal to a reciprocal lattice vector

$$\vec{q} = \vec{G}, \tag{2.42}$$

thus, resulting in a constructive interference of the scattered waves. This equation, also known as the Laue condition, represents the scattering condition in the reciprocal space. An equivalent equation to this is the Bragg condition

$$n\lambda = 2d\sin(\theta). \tag{2.43}$$

Here denotes d the distance between two lattice planes in real space and θ the observed angular position of the Bragg reflection. The order of the integer n is equal to the length of G_{hkl} divided by the shortest reciprocal lattice vector parallel to G_{hkl}.

Hence, the total differential cross section $\frac{d\sigma}{d\Omega}$, which is defined as the square of the scattering amplitude per solid angle $d\Omega$, is

$$\left(\frac{d\sigma}{d\Omega}\right)_{\text{diffraction}} = r_0^2 PL|F_{\text{str}}|^2 M V_{\text{U}} \delta(\vec{q} - \vec{G}_{hkl}), \tag{2.44}$$

for a diffraction experiment at a three-dimensional periodic structure. Here r_0 denotes the Thompson scattering length, P the polarization factor, L the Lorentz factor and M the number of unit cells.[2] For small deviations from the scattering conditions, also scattered intensity can be observed which is accounted by the Lorentz factor.

In case of a lower dimensional system, e.g. two-dimensions, the lattice sum can only converge in two directions, and the total differential cross section changes to

$$\left(\frac{d\sigma}{d\Omega}\right)_{\text{diffraction,2D}} = r_0^2 P|F_{hk}|^2 N_x N_y \frac{\lambda^2}{A_{\text{U}}} \frac{1}{\sin 2\theta} \left(\frac{\Delta q_z}{k_i}\right) \tag{2.45}$$

with a modified Lorentz factor which is in the case of powder diffraction given as
$L = \frac{1}{\sin 2\theta \sin\theta}$.[2]

As shown by equation (2.38) the widths of the diffraction maxima are influenced by the number of unit cell and the size of the crystal, respectively. However, if the line broadening is mainly due to size effects of the crystallites, their size can be estimated using the Scherrer formula [115]

$$\Delta\theta_{\text{FWHM}} = \frac{K \cdot \lambda}{l\cos(2\theta/2)}. \tag{2.46}$$

The scattering angle of the observed peak is denoted as θ, the length of crystal is marked with l and the full width at half maximum of the diffraction peak by $\Delta\theta_{\text{FWHM}}$. The constant K is a factor which includes different contributions and can vary between 0.7 and 1.2.[116] For a crystal with a cubic lattice the factor was calculated to 0.94.[117]

A two-dimensional system is a special case of a three-dimensional structure having only periodicity in the $q_{||}$ direction. For a two-dimensional array of point-like scatterers a so called Bragg rod would develop at G_{hk} which is extended infinitely perpendicular to the lattice plane. In real systems, atoms or molecules with finite extension are present and broad maxima are obtained in the direction perpendicular to the restricted plane. These rods have no uniform intensity distribution as the form factor of the unit cell induces a modulation of the intensity. This will be

described later in more detail.

If the diffraction pattern of a single crystal is inspected, isolated maxima can be observed, each of which corresponding to a single reciprocal lattice vector. If diffraction experiments are performed on powder samples, this assignment changes showing a maximum in the scattered intensity as the magnitude of the wave vector transfer is equal to the magnitude of a reciprocal lattice vector. In powders, small crystals are present with the crystal axis orientated randomly. The diffraction patterns for all possible orientations of a single crystal are obtained simultaneously. In two-dimensional powder samples, the crystallites are all oriented randomly in one single plane. This is equivalent to a single crystal which is rotated in the plane around one crystal axis.

2.6.4. Grazing incidence diffraction

In grazing incidence diffraction (GID) measurements, the incoming X-ray beam is adjusted to hit the sample under a shallow angle $\alpha_{\mathrm{i,g}}$. This angle is in the range of 60%-80% of the value of the critical angle α_{c} for total external reflection (see chapter 2.6.2). Thus, an evanescence wave propagates along the interface. This wave has a penetration depth of roughly 50 Å and therefore the wave is scattered predominantly from the interfacial region.[109] The direction of the incident beam is fixed in experiments investigating Langmuir layers as the Bragg condition is always fulfilled since the samples form two-dimensional powders at the interface. For these measurements usually a position sensitive detector is employed. This detector is oriented perpendicular to the sample surface and is rotated by the angle 2θ around the sample. By using this setup, a two-dimensional scattering map is obtained. This map has a lateral and vertical wave vector transfer component. In case of lipids, information about the orientation can be obtained from the Bragg rods.

The combined scattering amplitudes of a Langmuir film and forming crystals below are not superimposed coherently, as the crystalline domains of the amphiphiles and crystals have a random orientation with respect to each other. Thus, the different scattering signals can be treated independently and the observed signal can be just described by a summation of the scattered intensity.

In GID patterns the formation of the Vineyard peak can be observed. For shallow angles the approximations which are made in the Born approximation are not valid anymore, as multiple scattering has to be considered. Here the distorted wave Born approximation (DWBA) has to be used. If the diffusely scattered intensity is calculated one obtains [109]

$$I \approx |t_i(\alpha_i)|^2 F^2_{\mathrm{str}}(\vec{q}) |t_f(\alpha_f)|^2. \tag{2.47}$$

As the incident angle α_i or the exit angle α_f are close to the critical angle α_c maxima are observed. These maxima are caused by the transmission functions $t_i(\alpha_i)$ and $t_i(\alpha_f)$ of the incoming and outgoing X-ray beam. For GID scans the incident angle is kept fixed, thus, $t_i(\alpha_f)$ reduces to a constant and the transmission function $t_i(\alpha_i)$ leads to the observation of the Vineyard peak.

2.6.5. The two-dimensional unit cell of a Langmuir layer

Langmuir monolayers at liquid interfaces form a two-dimensional periodic structure where every lattice point hosts one amphiphilic molecule. The observed diffraction pattern originates from the periodic arrangement of the tailgroups; no diffraction pattern from the headgroup itself has been observed so far.[108] The structure factor $F_{\text{str}}(\vec{q})$ bears the information on the composition of the amphiphilic molecules and thus determines the intensity of the diffraction pattern. For diffraction experiments on Langmuir layers usually only the lowest order peaks can be observed. Anyhow, the two-dimensional structure can be extracted from the position of the out-of-plane Bragg peaks by taking geometric considerations into account.

The structure factor (see equation (2.36)) can be separated in two parts

$$F_{\text{str}}(\vec{q}) = \sum_j e^{i\vec{q_{||}} \cdot \vec{r}_j} f_j^0(\vec{q}) e^{iq_z z_j} = F_{\text{p}}(\vec{q}_{||}) F_{\text{mol}}(q_z, q_{||}), \tag{2.48}$$

yielding the structure factor $F_{\text{p}}(\vec{q}_{||})$ and the molecular form factor $F_{\text{mol}}(q_x, q_{||})$. Due to this, the lattice structure and the alignment of the molecules in the unit cell can be regarded independently for a Langmuir layer.

For a closely packed two-dimensional lattice, each molecule is surrounded by six neighboring molecules. This limits the number of two-dimensional unit cells which can be formed. The possible unit cells differ further in the number of lattice spacings d_{hk}, which are directly related to the wave vector transfer $q_{||}$ via

$$d_{hk} = \frac{2\pi}{q_{||}}. \tag{2.49}$$

The symmetry of the unit cell has an influence on the number of detectable Bragg reflections. A sketch of an oblique unit cell, which has the lowest symmetry, is shown in figure 2.13. For this lattice type, three different spacings can be observed. If the symmetry of the lattice increases and the lattice spacings become equal, the unit cell changes to a (centered) rectangular geometry with two degenerated lattice spacings and to a hexagonal one if all lattice spacings are degenerated. [2] The rectangular, the oblique and hexagonal lattice are primitive ones, only the centered rectangular is not primitive.

A sketch of the different lattice types is shown in figure 2.14. For the oblique lattice, the low order reflections are the $(0,1)$,$(0,\bar{1})$ (first reflection), $(1,0)$,$(\bar{1},0)$ (second reflection) and $(1,\bar{1})$,$(\bar{1},1)$ (third reflection) reflections. A centered rectangular and a rectangular lattice exhibits two Bragg reflections, being the (11) (first reflection) and (02) (second reflection) reflection. For this type of lattice extinction occurs and only peaks with $(k+h=2n)$ are observable. In the hexagonal lattice all spacings are degenerated and the first reflection is indexed as $(0,1),(1,0),(1,\bar{1}),(\bar{1},1),(\bar{1},0),(0,\bar{1})$.

The unit cell construction is normally carried out by constructing the reciprocal lattice via equation 2.49. However, a consequence of the limited number of lattice types is the ability to

[2] The cubic lattice is not mentioned, but it is the fifth lattice type. Is is also a primitive lattice.

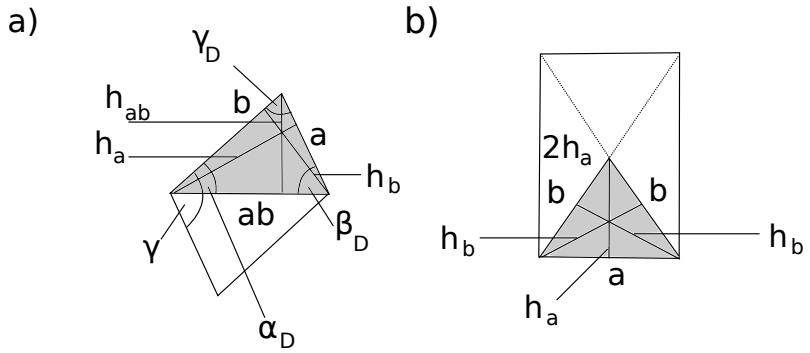

Figure 2.13.: a) Primitive unit cell of an oblique lattice. The sketch shows the heights, sides, and angles of the cell. b) Non-primitive unit cell of an orthorhombic lattice. Heights and sides are marked. The picture was adapted from [105].

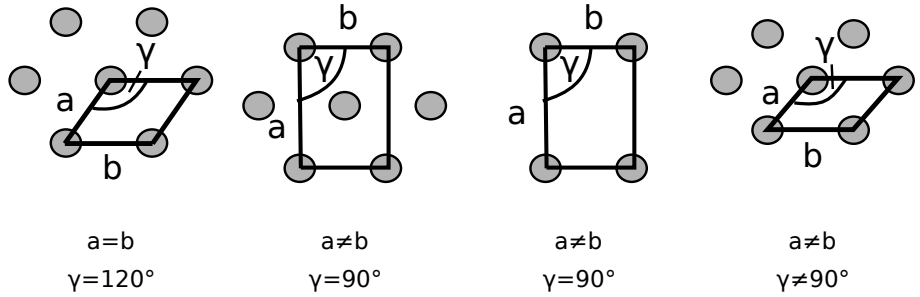

Figure 2.14.: Scheme of two-dimensional unit cells. The sequence of the cells from left to right is as followed: hexagonal, centered rectangular, rectangular, oblique.

calculate the parameters of the unit cell by the lowest order Bragg peak positions alone.

The heights of an oblique unit cell (see figure 2.13) can be calculated by equation 2.49 to

$$h_{a,b,ab} = \frac{2\pi}{q_{||}^{a,b,ab}}, \tag{2.50}$$

where the crystallographic convention is made $q_{||}^{a} \leq q_{||}^{b} \leq q_{||}^{ab}$. The important correlation for the angles of an oblique lattice are

$$\sin\alpha_D = \frac{h_{ab}}{b} = \frac{h_b}{ab}, \tag{2.51}$$

$$\sin\beta_D = \frac{h_{ab}}{a} = \frac{h_a}{ab}, \tag{2.52}$$

$$\sin\gamma_D = \frac{h_b}{a} = \frac{h_a}{b}. \tag{2.53}$$

The heights and sides are related by

$$ab = \frac{h_a}{h_{ab}}a, \tag{2.54}$$

$$b = \frac{h_a}{h_b}a, \tag{2.55}$$

$$a = \frac{h_a}{h_b}b. \tag{2.56}$$

by using equation eqs. (2.53) to (2.56) in combination with the law of cosines the angle γ_D can

be calculated to

$$\gamma_D = arccos\left[\frac{h_b}{2h_a} + \frac{h_a}{2h_b} - \frac{h_a h_b}{2h_{ab}^2}\right]. \tag{2.57}$$

Further are the angles between the vectors $\vec{a}$ and $\vec{b}$ connected by

$$\gamma = \alpha_D + \beta_D = 180 - \gamma_D. \tag{2.58}$$

2.6.6. Intensity distribution along a single Bragg rod

In a two-dimensional crystal system, the appearance of a Bragg rod can observed. This Bragg rod is a direct consequence of the finite crystalline size perpendicular to the crystal axis. As molecules are placed on the point lattice a modulation of the rod occurs due to the form factor of these molecules. The intensity distribution along the Bragg rod at the position $q_{||} = G_{hk}$ is a function of q_z and is determined by the mentioned form factor as shown by the decomposition in equation (2.48). Thus, an analysis of the intensity distribution along the Bragg rod yields information on the structure of the unit cell.

The primitive unit cell resides one molecule which is titled with respect to the water phase by an angle τ. The angle Ψ describes the angle between the projection of the tailgroup onto the lattice plane and the lattice vector, see figure 2.15. If the tilt angle τ is zero, the maxima of the Bragg peaks lie in the horizontal plane. As a tilt angle $\tau \neq 0$ is realized, the maximum moves out of this plane and has a $q_z \neq 0$ component. Hence, the content of the unit cell does not change the position of the Bragg peak with respect to $q_{||}$ but changes the position with respect to q_z. It has to be noted that the peaks are not only shifting to a positive $q_z$cell of position but also a shift to negative q_z position may occur. As a consequence, some peaks lie beneath the horizontal scattering plane and can no longer be observed. For a hexagonal structure the $(1, \bar{1})$ and $(\bar{1}, 1)$ reflections would remain in the horizontal plane as the hydrocarbon groups are titled. The (0,1) and (1,0) reflections shift to a position with $q_z > 0$ and the $(0, \bar{1})$ and $(\bar{1}, 0)$ reflections to a position with $q_z < 0$. A scheme showing the tilt of the alkyl chains towards the nearest neighbor (NN) and next nearest neighbors (NNN) is shown in figure 2.16.

A coordinate system can be chosen where the hydrocarbon groups are not tilted. The tilt direction is chosen to be along the q_x axis. By this new coordinates q'_z and $q'_{||}$ can be obtained which are connected to the laboratory system via [118]

$$\vec{q}'_z = (q_z \cos\tau - q_x \cos(\pi/2 - \tau))\,\vec{e}'_z \tag{2.59}$$

$$\rightarrow q'_z = q_z \cos\tau - q_x \sin\tau \tag{2.60}$$

$$\vec{q}'_{||} = (q_x \cos\tau + q_z \cos(\pi/2 - \tau))\,\vec{e}'_x + q_y \vec{e}'_y \tag{2.61}$$

$$\rightarrow q'_{||} = \sqrt{q_y^2 + (q_x \cos\tau + q_z \sin\tau)^2}. \tag{2.62}$$

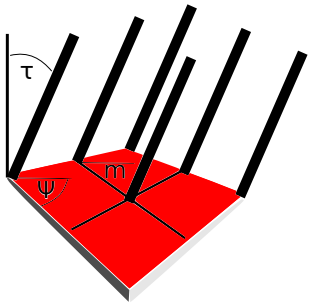

Figure 2.15.: Scheme of a two-dimensional lipid network. The lipids are titled by the angle τ from the surface normal in the unit cell. The angle between the lattice vector and the projection m is denoted by Ψ.

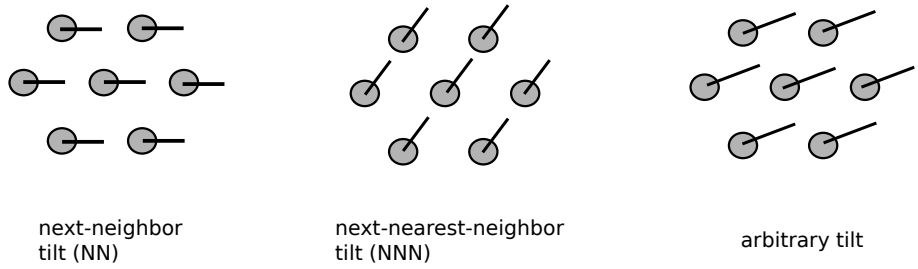

Figure 2.16.: Scheme for the tilt along different directions.

By this, the components of the in-plane wave vector transfer can be calculated as

$$q_x = G_{hk} \cos \Psi^*_{hk} \tag{2.63}$$

and

$$q_y = G_{hk} \sin \Psi^*_{hk}, \tag{2.64}$$

respectively. The magnitude of the reciprocal lattice vector of the Bragg reflection is denoted as G_{hk} and the angle between the reciprocal lattice vector and tilt direction as Ψ^*_{hk}. If the tilt direction of the chains is chosen as the reference point for the decomposition of the wave vector transfer the derived components are valid independently of the chosen lattice.

The construction of the alkyl chain by a molecular model is too static as e.g. for phospholipids a free rotator phase can be assumed, which introduces a degree of freedom.[119, 120] A better model allowing rotation of the lipids around their longitudinal axis is the approximation of the chain by a stiff cylinder.[118, 121, 122] The model assumes a free rotation of the lipid chain which results in a smearing of the electron density over the shell of the cylinder. The diameter of the cylinder can be estimated by the length of the CH_2-CH_2 bond distance of 1.54 Å and the angle between the single CH_2 groups which is $110°$, yielding a radius of 0.44 Å. The length L of the cylinder can be calculated in a similar way under the assumption that the chain is in the all-trans configuration using the number n_{CH_2} of CH_2 groups to $L = (n_{CH} + \frac{9}{8}) \cdot 1.265$ Å. The second term in the bracket takes into account the slightly longer methyl (CH_3) group at the end of the chain. The form factor can then be expressed as

$$F_{mol}(\vec{q}) = f^0(\vec{q}) \int dV \cos(\vec{q} \cdot \vec{r}), \tag{2.65}$$

where the integration is performed over the volume of the lipid chain. This form factor can be further split into

$$S(q_z') = \int_{-L/2}^{L/2} dz \cos(q_z' \cdot z) = 2\frac{\sin(\frac{1}{2}Lq_z')}{q_z'}, \tag{2.66}$$

and

$$R(\vec{q}'_{xy}) = \int_0^{2\pi} d\phi \int_0^R dr \langle \cos(\vec{q}'_{xy} \cdot \vec{r}) \rangle_{2\mathrm{d}} = 2\pi \frac{R \cdot J_1(R \cdot q'_{||})}{q'_{||}} \tag{2.67}$$

with J_1 being the first order Bessel function. The prime indicates that the actual coordinate system is titled by the angle τ with respect to the sample surface. Thus, the Bragg rod for a given Bragg reflection is influenced by the tilt angle τ and the angle Ψ^*_{hk} of the lipid chains.

By this, the intensity along a Bragg rod as a function of q_z is given by

$$I(q_z) = |F_{\mathrm{lipid}}|^2 \cdot |t_f(q_z)|^2 \cdot A + b. \tag{2.68}$$

Here, A is a scaling amplitude which accounts for the fact, that neither the calculations nor the measurements are performed using absolute intensities. The factor b is a constant background and $t_f(q_z)$ describes the transmission function which defines the Vineyard peak, see equation 2.47.

The tilt direction Ψ^* in reciprocal space and the tilt angle τ can be computed if the q_z and $q_{||}$ values of the maxima are known. By using the relation $q_z = q_{||} \cos\Psi^* \tan\tau$ a set of equations is obtained for an oblique lattice [118, 123, 124]

$$q_z^a = q_{||}^a \cos\Psi_a^* \tan\tau, \tag{2.69}$$

$$q_z^b = q_{||}^a \cos\Psi_a^* \tan\tau, \tag{2.70}$$

$$q_z^{ab} = q_{||}^{ab} \cos\Psi_{ab}^* \tan\tau, \tag{2.71}$$

with the boundary condition $q_z^a = q_z^b + q_z^{ab}$.

For the angle Ψ_b^* one obtains (see [105])

$$\Psi_b^* = \arctan\left(\frac{1}{\sin\gamma_D} \cdot \left(\cos\gamma_D - \frac{q_z^a q_{||}^b}{q_z^b q_{||}^a}\right)\right). \tag{2.72}$$

By the combination of equation 2.69 and 2.70 the angle Ψ_{ab}^* can be computed to

$$\Psi_{ab}^* = \arccos\left(\frac{q_z^{ab} q_{||}^b \cdot \cos\Psi_b^*}{q_z^b q_{||}^{ab}}\right). \tag{2.73}$$

Using the relation $\Psi_a^* = \gamma^* + \Psi_b^*$ all angles between the reciprocal lattice vectors are known

along with the tilt direction. Finally the tilt angle τ can be calculated via

$$\tau = \arctan\left(\frac{q_z^i}{q_{||}^i \cdot \cos\Psi_i^*}\right), i = a, b, ab. \tag{2.74}$$

The angles of the reciprocal lattice are linked to the angle of the tilt directions by

$$\Psi_b = \Psi_a^* - \pi/2 \tag{2.75}$$

$$\Psi_a = \Psi_b + \gamma = \Psi_a^* - \pi/2 + \gamma \tag{2.76}$$

$$\Psi_{ab} = \Psi_b + \alpha_d = \Psi_a - \beta_D. \tag{2.77}$$

with $\gamma = \gamma_D$.

2.6.7. X-ray absorption spectroscopy

In the following section the X-ray absorption spectroscopy (XAS) method will be outlined. So far, X-ray techniques were discussed with the constrain for preservation of the value of the X-ray energy (elastic scattering). The scattered intensity in these experiments was monitored as function of the wave vector transfer. However, in XAS experiments the absorption coefficient $\mu(E)$ is the quantity to be measured as a function of the X-ray energy. The technique is described briefly and the interested reader is directed to the book of Koningsberger.[3]

The intensity of X-rays is attenuated when passing matter. This process is represented by the law of Lambert-Beer [2]

$$I = I_0 \cdot e^{-\mu(E)d}. \tag{2.78}$$

The intensity of the incoming X-ray beam with an energy E is denoted with I_0, the energy depended absorption coefficient is given by $\mu(E)$, the sample thickness by d and the transmitted intensity by I. The absorption coefficient of a specific element shows a strong modulation if the X-ray energy is in the range of the binding energy of core-electrons. The reason is a successful removal of a core electron from the inner shell resulting in a sudden increase in the absorption, the so called absorption edge. This energy dependent modulation of the absorption coefficient, called the X-ray absorption fine structure (XAFS), yields information on the physical and chemical properties of the absorbing atom. Informations like the coordination number, oxidation state, the distance and type of next neighbor atoms can be obtained on crystalline as well as on amorphous or distorted structures. This technique is sensitive to the local environment of the absorbing atom.[125]

If strongly bound core electrons from K and L shells are investigated which require X-ray energies between $1\ \mathrm{keV}$ and $10\ \mathrm{keV}$ this technique is highly sensitive to bulk material as a strong penetration depth exists in this energy range. Furthermore are these absorption edges well separated and the signal of interest can be extracted because no overlap from other edges occur.

If the X-ray energy E of the incoming photons is larger than the binding energy E_b of the core electron the photons excite a core electron to an unoccupied state. This process, called

photoabsorption, is accompanied by other mechanisms such as elastic scattering (e.g. Thompson scattering) and inelastic scattering (e.g. Compton scattering). Nevertheless, these processes can be neglected for the used energies in the presented experiments. The scattering contributions have only weak energy dependence and can be regarded as a constant background. So far photoabsorption alone has to be accounted.

If the X-ray energy is far away from an absorption edge, the absorption coefficient can be described by the Victoreen polynomial

$$\mu(E) = \frac{Z^4 \rho}{A} \left(\frac{C}{E^3} - \frac{D}{E^4} \right) \tag{2.79}$$

where Z is the atomic number of the element, ρ the particle density, A the atomic mass, C and D element specific factors.[126] If the energy of the photons is smaller than the binding energy of the core electrons, no excitation can occur. As the energy of the X-rays is equal to the binding energy E_b the absorption suddenly increases as the electrons are now able to reach an unoccupied state. Above this absorption edge the difference of the photon energy E and the binding Energy E_b is carried away as kinetic energy E_kin by the photoelectron. The absorber atom is afterwards in an excited state composed of an atom having a core hole. Because the electron hole left behind belongs to a strongly bound state, the atom relaxes during a short period of time. This can proceed by the emission of a photon which is called fluorescence or by the radiation free emission of a weakly bound electron called Auger-Effect. This last process is dominant at photon energies of the incoming beam lower than $1\ \mathrm{keV}$ and can therefore be neglected for the experiments which will be presented.[2]

For samples which allow the transmission of the X-ray's the experiments can be performed by monitoring the incident X-ray intensity I_0 and the transmitted intensity I. The absorption coefficient is received by calculating the logarithm of the ratio of the intensities and by dividing it by the sample thickness d

$$\mu(E) = \ln\left(\frac{I}{I_0}\right)/d. \tag{2.80}$$

Many experiments and also the experiments presented herein do not allow this geometry. In

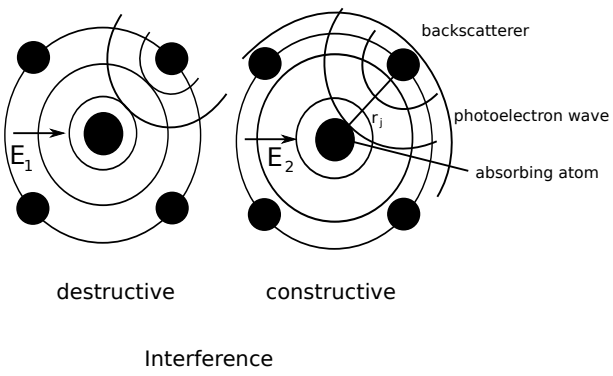

Figure 2.17.: Sketch of a destructive and constructive interference of a photoelectron wave after backscattering from the neighboring atoms. The sketch was adapted from [127].

order to achieve surface sensitivity the samples were illuminated in the total external reflection mode. The X-rays hit the sample under a grazing angle which is smaller than the angle of total external reflection. Thus, the penetration depth is lowered to approximately 50 Å. This sample geometry allows one to monitor two different signals which give information on the absorption coefficient. The first one is the totally reflected beam. If the energy is increased to the energy of the absorption edge, the intensity of the reflected beam decreases due to absorption. The second signal, which can be used is the fluorescence emission. The advantage of this signal is that no smooth surface is needed. The absorption coefficient is determined by the ratio of the fluorescence and the incident intensity

$$\mu(E) \propto \frac{I_f}{I}. \tag{2.81}$$

As mentioned in the beginning of this section the modulation in the absorption edge depends strongly on the local environment of the absorbing atom. This can be understood by quantum mechanical interference effects. If an atom is excited a photoelectron with the impulse p is emitted, which can be described by a spherical wave with the wavelength $(\lambda = h/p)$, where h is the Planck constant, see figure 2.17. This spherical wave is scattered back to the emitting atom along different scattering paths by the surrounding atoms. During this process, the photoelectron suffers a phase shift. The backscattered wave interferes with the spherical wave of the photoelectron as a function of the photoelectron wavelength and the surrounding geometry. By this, the probability for photoabsorption is modified and, thus, the absorption coefficient is modulated.

The absorption edge can be divided into two parts, the so called X-ray absorption near edge structure (XANES) and the extended X-ray absorption fine structure (EXAFS). Figure 2.18 depicts the absorption K-edge of goethite. The XANES and EXAFS region are sketched for clarity. The boundary between these regions is usually chosen to be approximately $40\,\mathrm{eV}$ above the absorption edge. The segmentation is reasonable because the regions differ in the analysis procedure and in the information which can be gained. In the XANES region the photoelectron is subject to strong interaction with the surrounding which results in multiple scattering. Due to this, an analytical calculation is difficult because not all effects which modulate the structure of the absorption edge can be described successfully.[125] Often, XANES spectra are simulated by ab-initio calculations, which rely on multiple scattering approaches e.g. FEFF, and are compared to the measured data.[125] Other approaches for data analysis use experimentally obtained reference spectra or combination of references which are fitted to the spectra. By this, information on the radial distribution of the neighboring atoms, interatomic distances or the electronic structure like the oxidation state can be deduced.

For some elements, a so called pre-peak can be observed at energies which are below the energy of the absorption edge. Such pre-peaks originate by a transition of a core-electron into a weakly bounded state. The pre-peak gives information on the oxidation state and the coordination to the next neighborhood. In the energy range of the absorption edge such transitions to unoccupied states are also possible. If the density of these states is bigger than the density of the unbound states the height of the absorption edge can be enhanced further.

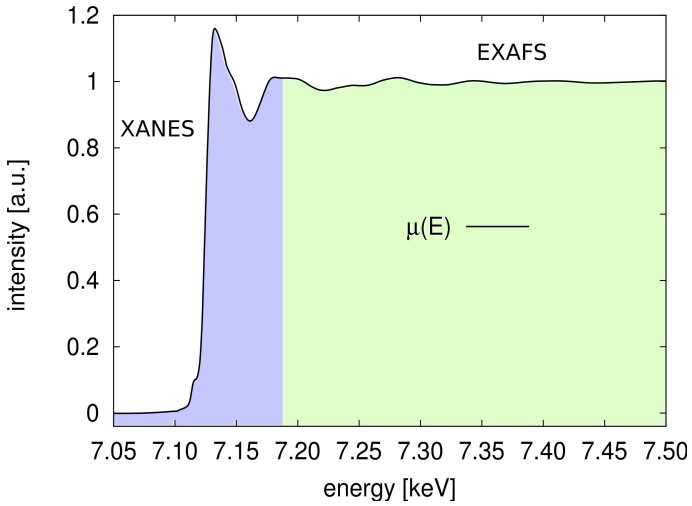

Figure 2.18.: Experimentally obtained absorption spectrum $\mu(E)$ of iron K-edge in goethite. The onset of the absorption edge can clearly be seen at $7.112\ \mathrm{keV}$. The spectrum is divided into two parts the XANES and the EXAFS region.

A change in the charge distribution around the absorbing atom has an impact on the position of the absorption edge. If, for example, the oxidation state of the central atom changes the position of the absorption edge shifts. The lack of a valence electron decreases the screening of the core potential thus increasing the binding strength of the core-electron and with this the absorption edge shifts to higher energies.[125]

In the EXAFS region, photoelectrons with a higher kinetic energy are generated which are not subject to strong interactions with the surrounding atomic potentials. A theoretical treatment is possible as only single scattering events have to be considered. As a result, only information on the geometrical properties around the absorbing atoms can be obtained. The oscillatory part $\chi(E)$ of the absorption coefficient $\mu(E)$ is extracted by subtracting the absorption coefficient $\mu_0(E)$ of an isolated atom and is normalized by this

$$\chi(E) = \frac{\mu(E) - \mu_0(E)}{\mu_0(E)}. \tag{2.82}$$

Here, an isolated atom is to be understood as an atom in the same electronic environment which is not influenced by the back scattered photoelectron wave. Based on the difficulty to calculate $\mu_0(E)$, this absorption coefficient is mostly approximated by a spline or polynomial μ_b. This approximated absorption coefficient $\mu_\mathrm{b}(E)$ is subtracted and the data is normalized by a value of the absorption coefficient $\mu(E)$ at a constant energy E_i.[125] Furthermore, the energy range is normally converted to the wave number k of the photoelectron: $k = \sqrt{\frac{2m_0(E-E_0)}{\hbar^2}}$.

A semi-phenomenological expression for the EXAFS oscillation at the K-edge is given by [127–129]

$$\chi(k) = \frac{m_0}{2\pi\hbar^2 k^2} \sum_i N_i s_0^2 \frac{t_i(2k)}{R_i^2} e^{-2k^2\sigma_i^2} e^{-2R_i/\lambda(k)} \sin(2kr_i + \delta_i(k)). \tag{2.83}$$

The summation is performed over all neighboring atoms in the same coordination shell with the

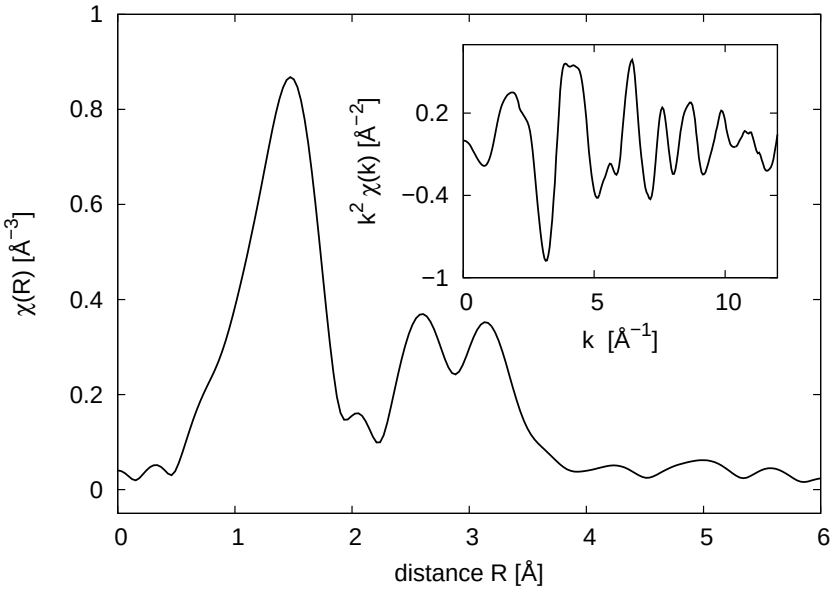

Figure 2.19.: The Fourier transformed $\chi(R)$ of the EXAFS oscillations. The $\chi(k)$ is shown in the inset. The data was extracted from the spectrum of goethite shown in figure 2.18.

mean distance R_i to the absorbing atom. The backscattering amplitude is denoted by $t_i(2k)$ and the lifetime of a photoelectron by $e^{-2R_i/\lambda(k)}$ with the energy dependent mean free path $\lambda(k)$. The coefficient σ accounts for structural and thermal disorder and N_i describes the number of the same atoms in the coordination shell. The factor s_0^2 accounts for the reduction in the oscillations due to many-body effects. For a calculation of $\chi(k)$, the backscattering amplitude $t_i(2k)$, the mean free path $\lambda(k)$, and the phase shift $\delta_i(k)$, which is experienced by the photoelectron wave due to the potential of the absorbing atom and the backscattering at the neighboring atoms, must be known. Because $\chi(k)$ depend on $\lambda(k)$ and R_i^2 only the local environment up to a distance of approximately 10 Å can be investigated.[125]

As a result every coordination shell generates a frequency in the EXAFS signal which depends on its distance. In order to get information about the distances of the coordination shells, the k-weighted EXAFS signal is Fourier transformed:

$$\chi(R) = \mathrm{FT}(\chi(k)) = \frac{1}{\sqrt{2\pi}} \int_{k_{\mathrm{min}}}^{k_{\mathrm{max}}} k^n \chi(k) e^{2ikR} dk. \tag{2.84}$$

The applied power of the k value depends on the atomic number and varies between one and three. The $\chi(R)$ of the goethite sample is shown in figure 2.19. The result is a radial distribution of atoms from which the distances of the coordination shells can be extracted after performing a phase correction.

The EXAFS signal gives information on the distances of the coordination shells, the disorder around the absorbing atom, and coordination number N_i.

3. Experimental setup

In the framework of this thesis, experiments were performed at different synchrotron radiation facilities and experimental end-stations. In this chapter, these end-stations will be specified. A description of the sample system and data handling will be given. The chapter starts with the characterization of the sample system and will carry on with the requirements needed for the investigation of liquid interfaces in general. The different end-stations will be sketched briefly in the following. This chapter ends with a description of the general data handling.

3.1. Sample system

The sample system, which is utilized, consists of a pure water or an aqueous solution containing either iron chloride salts or nanoparticles with different concentrations. On top of the aqueous surface different Langmuir layers were placed in order to influence interfacial properties. A sketch of the sample system is shown in figure 3.1. As described in chapter 2.4 the formation of insoluble precipitates is induced by a change in the pH value of the solution. As a part of this study aims for the investigation of the growth of inorganic thin films at the liquid air interface, the interfacial pH value was controlled in the regarding experiments using gaseous ammonia. For this purpose, vials containing ammonia solution were placed inside the sample trough in order to generate an ammonia containing atmosphere. The ammonia diffuses first into the air volume in the sample cell and then, into the interfacial region of the sample.

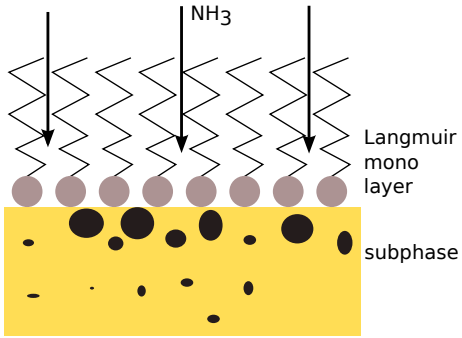

Figure 3.1.: Sketch of the investigated sample system. On top of the iron salt containing subphase (yellow) the Langmuir monolayer is spread. Small particles start to nucleate as ammonia diffuses from the gas phase into the interfacial region.

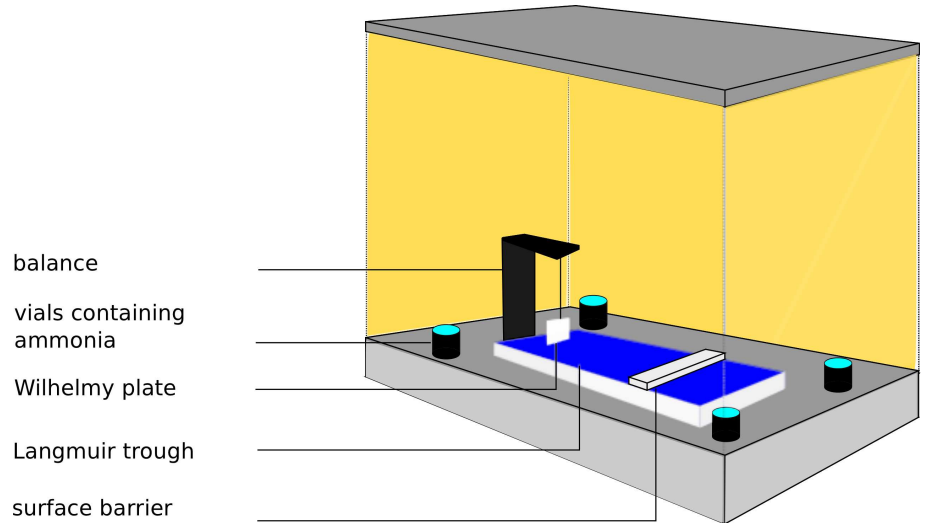

Figure 3.2.: Sketch of a typically used sample cell. The sample cell contains a Langmuir trough and a Wilhelmy balance. The surface pressure is adjusted by controlling the surface area via a computer controlled surface barrier. Vials with an ammonia solution were distributed around the trough.

3.2. General setup

For the experiments, a Langmuir trough made of teflon (PTFE) equipped with a Wilhelmy balance and a computer controlled surface barrier was used. A sketch of a typically used sample cell is shown in figure 3.2. The surface pressure of the sample system can be altered by adjusting the geometrical area of the trough. For this, the surface barrier is moved to decrease the accessible area for the amphiphiles. The single amphiphiles were pushed closer together, thus, increasing the surface pressure. In the trough itself the aqueous subphase is filled. This assembly is enclosed by a sample cell providing a controllable air phase above the sample. The sample cell possesses windows made of kapton which can be passed by the X-rays with a low amount of absorption. Air scattering was reduced by flushing the cell with helium. This setup also allowed to generate an ammonia containing atmosphere above the sample surface in a controlled way. The extrusion of air was monitored by an oxygen sensor and the ammonia content was measured by diffusion tubes (ISO 9001, Dräger). Because the concentrations of ammonia were only in the ppm regime no suitable electronic device which is sensitive to the concentrations and small enough to be mounted on the inside of the cell, could be found.

As already mentioned in chapter 2.6, the experiments had to be performed under a grazing angle for the incoming X-rays in order to achieve surface sensitivity.[130, 131] For fluid samples, the beam has to be bent down on the sample surface, which makes the use of additional optical elements necessary. A sketch of a typical beamline setup is shown in figure 3.3. The beamlines used for the experiments were equipped with deflection stages for beam tilting or have specialized monochromators capable of changing the incident angle. For XAS and GID measurements, a constant incident angle is utilized, whereas for XRR measurements the angle has to be changed continuously in order to fulfill the condition for specular reflection.

For detecting the X-rays, point detectors, one dimensionally sensitive detectors (PSD) and fluorescence detectors were employed in the different experiments. The point detectors were

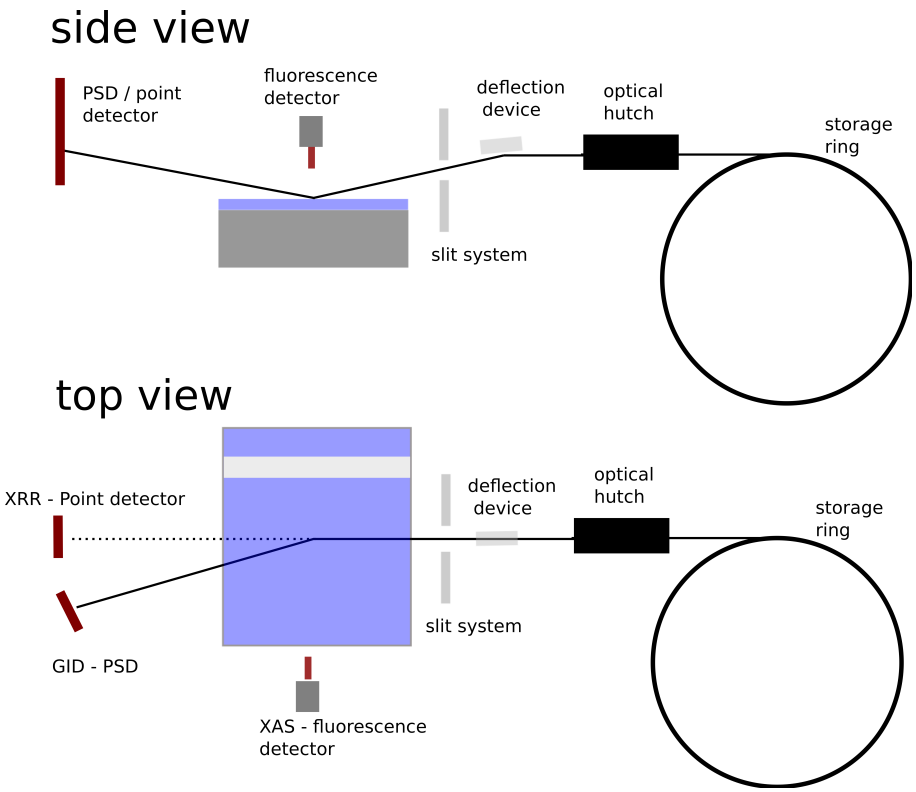

Figure 3.3.: Sketch of a typical experimental setup used for the experiments, showing the most important components.

used for reflectivity measurements where the resolution is defined by a slit system in front of the detector and the size of the X-ray beam. The GID measurements took advantage of a PSD detector in combination with a soller slit. Depending on the orientation of the soller slit, the resolution along a distinct direction is enhanced. The loss of intensity for a soller slit is much smaller than for a single slit. This makes it favorable for GID experiments in order to detect also scattering contributions with weak intensity. Energy dispersive detectors were used in the XAS experiments to measure the fluorescence signal emitted by the sample.

3.3. Beamline BW1, DORIS III

XRR and GID measurements were performed at the beamline BW1 of the synchrotron light source DORIS III, HASYLAB, Hamburg. In the experimental hutch, a liquid surface diffractometer with a custom made Langmuir trough is available. The white beam emitted by a wiggler is monochromized by a beryllium crystal which is also responsible for adjusting the incident angle.[132] The beamline utilizes an X-ray energy of 9.51 keV or a wavelength of $\lambda = 1.297$ Å, respectively. The size of the incident X-ray beam was adjusted by a slit system to a size of (0.2×2) mm^2 (v $\times$ h). For the GID experiments the incident angle of the X-ray beam was adjusted to $0.1°$ which is 85 % of the critical angle of water. A typical XRR experiment was performed up to a wave vector transfer of $q_z = 0.8$ Å^{-1}. GID measurements were performed in the angular regime of $2\theta = 15°$ to $2\theta = 20°$ in order to detect the scattering reflection from Langmuir layers. This range was extended when scattering signals from crystalline minerals were sought.

3.4. Beamline A1, DORIS III

At the beamline A1 of the synchrotron radiation source DORIS III, HASYLAB, Hamburg, XAFS experiments were performed. The beamline uses X-rays emitted by a bending magnet with accessible X-ray energies from $2.4\ \mathrm{keV}$ up to $8.3\ \mathrm{keV}$ by using a silicon (111) double crystal monochromator.[133] Furthermore, the beamline is equipped with a toroidal mirror to focus the incident beam. In fact, the beamline is not designed for probing liquid samples and an additional mirror for manipulating the X-ray beam had to be mounted. The incident angle was adjusted to $0.1°$ by a silicon mirror of $20\ \mathrm{cm}$ length using total external reflection for deflection of the primary beam. A KSV mini trough along with a sample cell was installed into the experimental end-station. In these experiments, an energy dispersive X-ray detector was used in order to observe the fluorescence signal emitted by the sample. The size of the incident X-ray beam was defined by a slit system to a size of $(0.8\ \mathrm{x}\ 3)\ \mathrm{mm}^2$ (v $\times$ h). The energy range from $7.05\ \mathrm{keV}$ to $7.21\ \mathrm{keV}$ was scanned for XANES spectra. For EXAFS measurements, the energy range was extended from $6.9\ \mathrm{keV}$ up to $7.6\ \mathrm{keV}$. For each sample several scans were recorded which were summed up afterwards.

3.5. Beamline ID10B, ESRF

Experiments were further performed at the beamline ID10B of the European synchrotron radiation facility (ESRF), Grenoble, France. The end-station is designed for surface diffraction on liquid and solid interfaces.[134] The beamline is capable of performing GID, XRR and grazing incidence small angle X-ray scattering (GiSAXS) experiments. The energy of the incoming X-rays can be changed between $8\ \mathrm{keV}$ to $22\ \mathrm{keV}$ using diamond crystal monochromators. The beamline is equipped with a deflection mirror made of a germanium crystal for tilting the X-ray beam. The XRR and GID experiments were performed using an energy of $22\ \mathrm{keV}$ with a beam size of $(0.025\ \mathrm{x}\ 0.6)\ \mathrm{mm}^2$ (v $\times$ h). For the GID experiments, an incident angle of $0.045°$ was used. The custom made Langmuir trough of the beamline ID10B was used during the experiments. The X-ray reflectivity measurements were performed up to a wave vector transfer of q_z=$0.8\ \mathrm{\AA}^{-1}$ and the GID experiments were performed in the angular regime from $2\theta = 7°$ to $2\theta = 9°$.

3.6. Beamline BL9, DELTA

The beamline BL9 is located at the synchrotron radiation source DELTA, Dortmund, using synchrotron radiation emitted from a superconducting asymmetric wiggler.[135] At the experimental end-station, GID experiments on the solution-air interface were performed. The beamline is equipped with a silicon (311) double crystal monochromator providing an energy range from 5 keV up to 30 keV. For measurements at liquid interfaces, an additional silicon mirror is mounted into the beam path utilizing total external reflection for the beam deflection. The experiments were carried out using a two-dimensional MAR345 detector with a sample to detector distance

of $350\ \mathrm{mm}$.[136] An X-ray energy of 13 keV was used for the GID experiments. The incident angle of the X-ray beam was fixed to $0.076°$ and a beam size of (0.2 x 2) mm^2 (v $\times$ h) was chosen. A sample cell containing a KSV mini trough was installed to the experimental end-station. An angular regime from $2\theta = 2°$ to $2\theta = 30°$ was accessible by these experimental conditions.

3.7. Beamline BL8, DELTA

At the beamline BL8 of the synchrotron radiation source DELTA, Dortmund, XAS experiments were performed. The beamline uses the synchrotron radiation emitted by the same superconducting wiggler as beamline BL9. The beamline is equipped with different monochromator crystals allowing an accessible energy range from $1\ \mathrm{keV}$ up to $30\ \mathrm{keV}$. Because the iron K-edge onset lies at an energy of 7.112 keV, the Si(111) double crystal monochromator was used. The beam was bent down by a mirror. The X-ray beam was adjusted to hit the sample under an angle of $0.1°$. The size of the incident X-ray beam was defined by slits to a size of (1 x 3) mm^2 (v $\times$ h). The energy range from 7.05 keV to 7.21 keV was scanned for XANES spectra. EXAFS measurements were performed in the energy range of 6.9 keV to 7.6 keV.

3.8. Laboratory diffractometer D8

Two different laboratory diffractometers D8 Advanced built by Bruker AXS were employed during the experiments. The diffractometers are differing in optical components and available detectors. Both diffractometers use the radiation emitted by a copper anode resulting in an X-ray wavelength of λ= 1.54 Å. Whereas one diffractometer is optimized for XRR measurements the other one is optimal for diffraction experiments.

The XRR setup utilizes a Göbel mirror for beam monochromatization and parallelization. The beam is further defined by a slit system to a spot size of (0.1 x 10) mm^2 (v $\times$ h). The diffractometer is equipped with a single point detector with an vertical opening of 0.2 mm.

The second diffractometer utilizes a so called “Montel Optic“ focusing the X-rays horizontally and vertically to a single spot. The beam size is defined by a slit system to an area of (1 x 1) mm^2 (v $\times$ h) and the scattered intensity is monitored by a PSD detector.

3.9. Sample system and preparation

Liquid solutions were prepared by using ultra pure water (ρ =$18.2\ \Omega/\mathrm{m}$, specific resistivity) right before the measurements. The Langmuir trough was cleaned with chloroform and ultra pure water in order to remove organic and water soluble deposits. A small stripe of filter paper was used as Wilhelmy plate. For every sample a new stripe was prepared. In the following, the balance was calibrated and amphiphilic molecules dissolved in chloroform were spread by gently dropping the solution with a syringe over the subphase. The sample cell was closed and

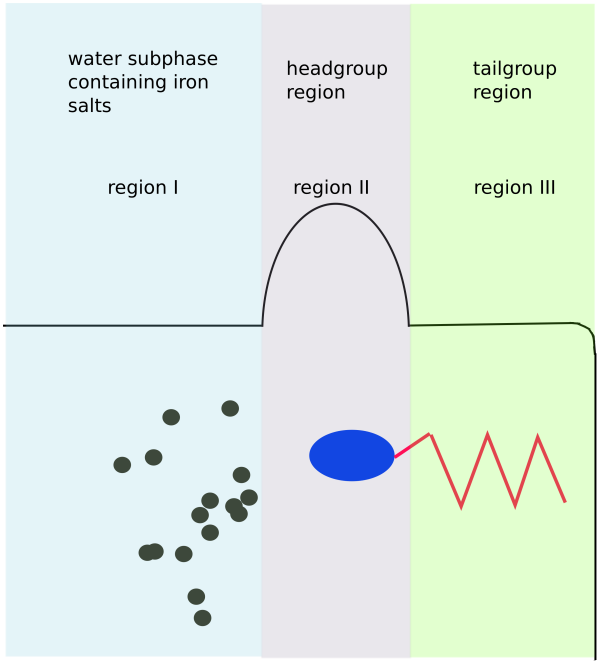

Figure 3.4.: Sketch of an electron density originating from a Langmuir layer on a subphase. Region I denotes the subphase containing different ions. The headgroup of the Langmuir layer is present in region II whereas the alkyl group is in region III.

the films were left for 20 minutes to allow evaporation of chloroform. Afterwards, the films were compressed to the target pressure by using a surface barrier speed of $4\ \mathrm{mm/min}$. After the initial state was monitored, the sample cell was opened and 4 vials with a $3\ \mathrm{wt\%}$ ammonia solution were placed inside to trigger the formation process. These vials were equally distributed in the sample cell around the Langmuir trough and the sample cell was sealed again. The ammonia diffused from the gas phase into the interfacial region thus increasing the pH value. By this, the precipitation reaction was induced in the interfacial region.

It has to be mentioned that a critical point in these experiments is the determination of the surface pressure. As solid material forms at the interface, the surface pressure has to be reviewed with precaution. Under this condition not only the surface pressure has an influence on the balance also the solid material exerting an additional weight due to gravitational forces might virtually increase the value recorded by the balance.

3.10. Data handling

The analysis of the obtained data is similar throughout the thesis. Therefore, a short description of the general data handling will be given here.

XRR data For measurements at the laboratory diffractometer and the beamline ID10B the diffusely scattered background was obtained by tilting the detector by $0.1°$ from the specular condition and recording the longitudinal diffusely scattered intensity. This scan was afterwards subtracted from the XRR data. All reflectivity curves which will be shown in this thesis are

formula	water H_2O (T = 0°)	carbon (graphite) C	iron Fe	gold Au
density $[\mathrm{g/cm^{-3}}]$	0.998	2.26	7.874	19.32
dispersion $\delta \cdot 10^6$	4.55	5.06	16.75	33.36
absorption $\beta \cdot 10^6$	$3.72 \cdot 10^{-4}$	$5.57 \cdot 10^{-3}$	1.59	2.65

Table 3.1.: Constants of different materials at an X-ray energy of 9.5 keV. The dispersion and absorption values were calculated via [137]

normalized by the Fresnel reflectivity. By this, the strong decay in the intensity is accounted for and also slight changes in the obtained data are visible. For the analysis of the XRR data, the recursive Parratt algorithm along with the effective density model to account for interfacial roughness was used.[109, 112] For Langmuir layers, it is sufficient to use a model consisting of two layers. Thereby one layer represents the headgroup and the other one the tailgroup. A sketch of the electron density profile, originating from a Langmuir monolayer, is shown in figure 3.4. If the data showed the growth of a layer at the interface, additional layers were added. The absorption and dispersion values of different elements are given in table 3.1. It can be seen that for water or carbon the absorption is low. This changes for metals with a large atomic number Z. Thus, the absorption is in the same regime as the dispersion and can no longer neglected. In a first step the layer thickness and dispersion of the layers were adjusted. This was necessary as the dispersion is a function of the electron density at the interface and the value is proportional to the amount of adsorbed material. The formation of a not fully closed layer results in an effective decrease of the layer dispersion. After these factors were adjusted, the roughness and the absorption parameters of the layer system were optimized.

GID data The GID patterns were collected by a PSD which was oriented perpendicular to the scan direction. By this, two dimensional scattering patterns were obtained. The data was summed up along the vertical scattering direction yielding one dimensional scattering curves as function of the lateral wave vector transfer $q_{||}$. The data was corrected for the background by using an area of the two dimensional map where no reflection was observed. For some cases, this was not possible. Here, a polynomial was fitted to the data and was subtracted afterwards. All diffraction patterns were normalized by the intensity of the incoming X-rays. For a qualitative analysis, Voigt profiles were fitted to the Bragg reflections. Voigt profiles are obtained by a convolution of a Gaussian function and a Lorentzian function. In X-ray scattering experiments, peak broadening has different origins. Broadening due to experimental resolution has a Gaussian character whereas peak broadening due to crystalline size effects has a Lorentzian shape.[138] By applying this function, peak broadening due to the experimental resolution and size effects can be considered. For the Voigt profile, no analytical expression exists which made the use of numerical approximations necessary.[139] At the beginning of the experiments, the primary beam was scanned in the direction parallel to the interface and a Gaussian function was fitted to it in order to estimate peak broadening due to resolution. This width was used for the Voigt profiles in the data analysis throughout one experimental run. By this, only the width of the Lorentzian part had to be adjusted.

From the lateral position $q_{||}$ the distance of the lattice planes d_{hk} can be calculated via equation

lattice type	hexagonal	centered rectangular	oblique
unit cell size A_{xy}	$a^2 \sin(\frac{2\pi}{3})$	$a \cdot b$	$a \cdot b \sin \gamma_d$
molecules per unit cell	1	2	1
area per molecule A_0	A_{xy}	$A_{xy}/2$	A_{xy}
lattice constant a	$\frac{4\pi}{\sqrt{3}}d$	$\sqrt{\frac{d_{1\bar{1}}^2 \cdot b^2}{d_{1\bar{1}}^2 - b^2}}$	d_{10}
lattice constant b		$2 \cdot d_{02}$	d_{01}

Table 3.2.: Formulas used to calculate the unit cell size and molecular areas of the amphiphiles.

(2.49). If these d-spacings are known the lattice constants and unit cell area can be calculated. The formulas for the relevant lattice types are summarized in table 3.2.

A two dimensional diffraction pattern of a DPPC monolayer is shown in figure 3.5a. Figure 3.5b shows the summarized profile along the q_z direction as function of the lateral wave vector transfer $q_{||}$. At the maxima of the lateral diffraction profile, the Bragg rods were extracted, which are depicted in figure 3.5c and 3.5d. The positions of the diffraction maxima were determined yielding a position of $q_{||} = 1.453$ Å^{-1} and $q_z = 0.533$ Å^{-1} for the first reflection and a position of $q_{||} = 1.503$ Å^{-1} and $q_z = 0$ Å^{-1} for the second reflection. By using equations (2.57),(2.72) and (2.74) the tilt angle can be deduced to be $23.16°$ with respect to the surface normal. Afterwards, the Bragg rods were simulated using equations (2.67) and (2.67). These were than compared to the experimental data. Such simulated Bragg rods are also drawn in figure 3.5c and 3.5d.

It has to be mentioned that for oblique or rectangular lattices in some cases the position of maximum intensity of the first Bragg rod was close to $q_z = 0$. In such a case, no reliable determination of the position was possible due to the shading of the sample and an overlap by the Vineyard peak, see figure 3.6. In these cases no valid statement about the tilt angle could be made.

Because Langmuir layers are sensitive to radiation damage the Langmuir trough was translated vertically during the measurement. By this the X-ray exposure of the surface was distributed over a bigger area and the risk for beam damage was reduced.

XAFS data The XAS data was analyzed by the usage of the program package ATHENA.[140] With the aid of this program, the background contributions were subtracted and the EXAFS data was further analyzed by performing a Fourier transformation. A k value of 2 was used as weight for data evaluation throughout the analysis. The phase shift correction implemented in ATHENA was not used as it can only account for phase pure materials. Analysis of the coordination shell composition and distribution for non crystalline samples was performed with the program package ARTEMIS.[140] First, the s_0^2 was determined by analyzing a magnetite reference sample. Afterwards, a model composed of one or two coordination shells was fitted. By this, the distance and the number of atoms in the coordination shell could be determined.

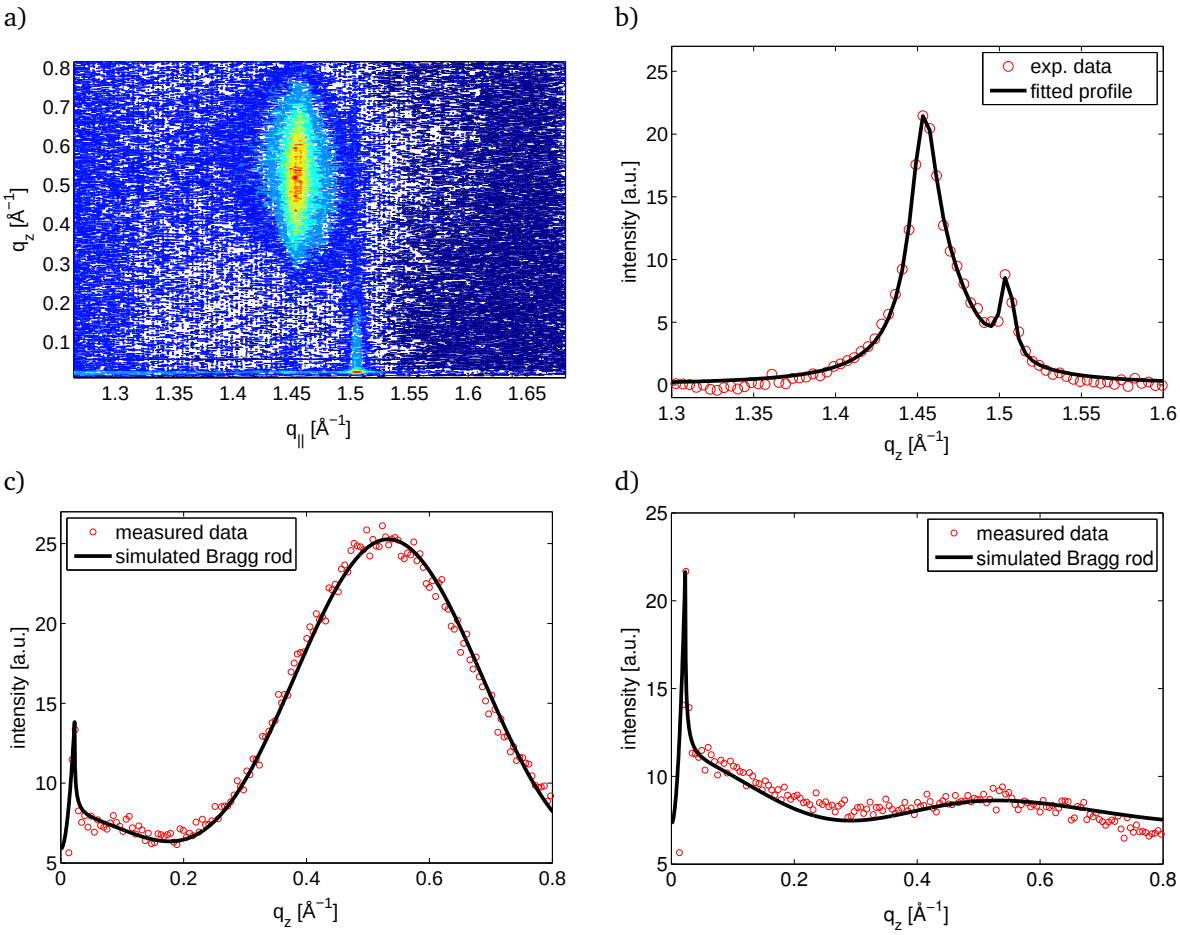

Figure 3.5.: Diffraction patterns of a DPPC monolayer compressed to a surface pressure $\Pi = 40\ \mathrm{mN/m}$ in the presence of ammonia. a) Contour plot of the two dimensional diffraction pattern. b) Diffraction pattern summarized along the q_z direction. c) extracted Bragg rod at the $q_{||} = 1.453\ \mathrm{Å}^{-1}$ c) extracted Bragg rod at the $q_{||} = 1.503\ \mathrm{Å}^{-1}$.

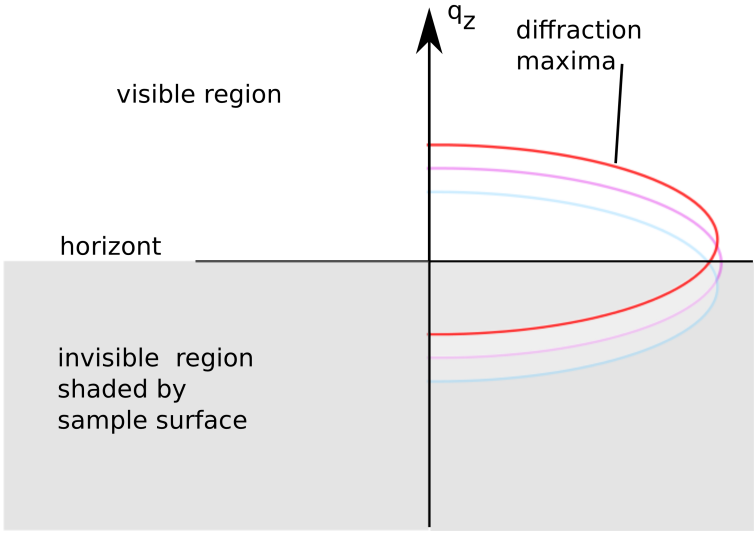

Figure 3.6.: Schematic drawing of Bragg rods along the q_z direction. The maximum of the rod is at different q_z positions. Because of the shading by the sample only half of the curve can be seen rendering problems to determine the position reliably.

4. Influence of the pH value on monolayer films

In the following chapter the results of a study on the influence of ammonia on different Langmuir layers is reported. It is known that the structure of Langmuir layers is influenced by the pH value of the subphase.[141, 142] Therefore, the structural changes appearing in an already assembled monolayer upon the change of the subphase pH value were investigated systematically. The aim of this study was to gain knowledge on the structural changes induced by ammonia diffusing from the gas phase into the interfacial region. Thus, the observations reported herein serve as groundwork for the investigation on iron salt solutions presented in chapter 5.

The amphiphiles which were examined can be divided in different classes which differ in the interaction between the amphiphilic molecules. The lateral structure of polysiloxane layers is determined by the covalent bond which is formed between the single monomers. Thus, highly stable membranes can be formed. The other class is composed of amphiphiles whose interaction is only determined by van der Waals forces and electrostatic interactions, e.g. stearic acid.

4.1. The network structure of polysiloxane membranes

The lateral structure of membranes formed by polysiloxane networks was investigated for different pH values of the subphase and furthermore as a function of ammonia present in the gas phase. Deposition of octadecyltrichlorosilane (OTS) monomers at the liquid-air interface induces the formation of the two-dimensional network with pronounced viscoelastic properties resulting in an increased stability against deformation. Such networks can undergo elastic contortion exerted by external forces. These membranes are used as model systems for membranes [143], as directing templates for nanoparticle aggregation [144–146] and as wall material for capsules.[147, 148] The structure of such a molecule is similar to amphiphiles like fatty acids which can be described by a hydrophobic tailgroup and a hydrophilic headgroup. The OTS molecules polymerize by the condensation of the silane headgroups under the separation of hydrochloric acid (HCl). The reaction pathway is shown in figure 4.1. Since this process can only proceed in the presence of water, membranes can be formed e.g. at the water/air or water/oil interface. Polysiloxane networks are the subject of different investigations, in which their properties at different interfaces were explored.[148, 149] Such membranes are semipermeable, exhibit special rubber-elastic properties and have controllable pore size.[150–152]

The kinetics of the condensation reaction of the silane network is known to depend on the pH value of the water subphase.[153–157] Furthermore ammonia (NH_3) can disturb the network

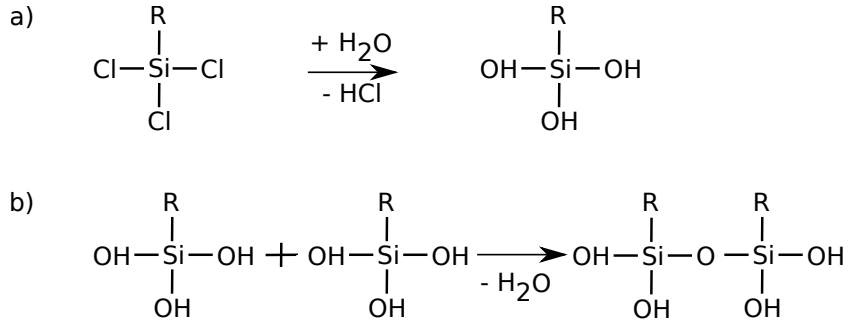

Figure 4.1.: a) Hydrolysis reaction of the OTS monomers. b) Condensation reaction of the OTS monomers.

structure by breaking SiO bonds.[158] In order to investigate if the homogeneity of the lateral structure is influenced by the pH value, X-ray scattering experiments on polysiloxane networks at the water-air interface were performed at the beamline BW1, DORIS III,Hamburg, Germany. To this end polysiloxane membranes were prepared on subphases with different pH value. In the case of acidic (pH $= 3$) and neutral (pH $= 7$) subphases ammonia was added afterwards in order to investigate if a subsequent manipulation could be achieved. For the alkaline water phase (pH $= 12$) polysiloxane networks were prepared on solutions of sodium hydroxide (NaOH). All measurements were performed with a constant surface pressure of $\Pi = 20\ \mathrm{mN/m}$.

The investigations on the pH dependence of the lateral homogeneity of polysiloxane networks were performed within the collaboration with the group of Prof. Metin Tolan (TU-Dortmund) and Prof. Heinz Rehage (TU-Dortmund). Part of the presented results were published as: D. C. Florian Wieland, Patrick Degen, Michael Paulus, Martin A. Schroer, Heinz Rehage and Metin Tolan (2011). *Manipulating thin polymer films by changing the pH value*. Journal of Applied Physics 110:102221-102224.

In the first part of this chapter the influence of ammonia on polysiloxane networks prepared on a water subphase with a pH value of 7 is presented. The adjacent section deals with the influence of acidic subphases (pH $= 3$) on the lateral polysiloxane network structure. Subsequent the investigation on alkaline solution is discussed. The chapter ends with a summary of the results.

4.1.1. Experimental Data

The GID data integrated along the q_z direction of an OTS layer on a neutral water subphase (pH $= 7$) are shown in figure 4.2 as a function of the wave vector transfer parallel to the water surface. The data was collected before and after the addition of ammonia.

OTS monomers form a monolayer with a hexagonal unit cell indicated by the presence of one Bragg reflection at $q_{||} = 1.540\ \text{Å}^{-1}$. The intensity of this Bragg reflection increases by a factor of 9 after ammonia is added to the gas phase. The scans were refined using a Voigt function. The obtained parameters are shown in table 4.1. The position of the Bragg reflection and the width of the Voigt function keep constant within the error-bars indicating no change of the size of the unit cell. The domain size of the polycrystalline film is 91 Å and the lattice constant is

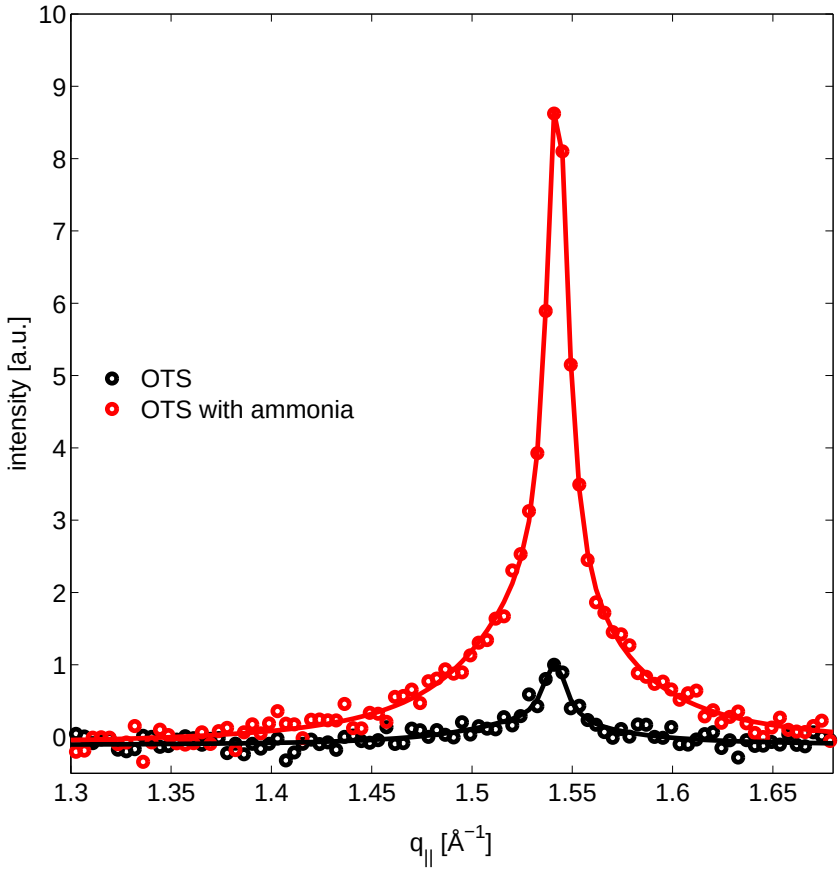

Figure 4.2.: GID scans of an OTS monolayer on a water subphase with a pH value of 7; native state (black), after the addition of ammonia (red). The refinements to the data are shown as solid lines.

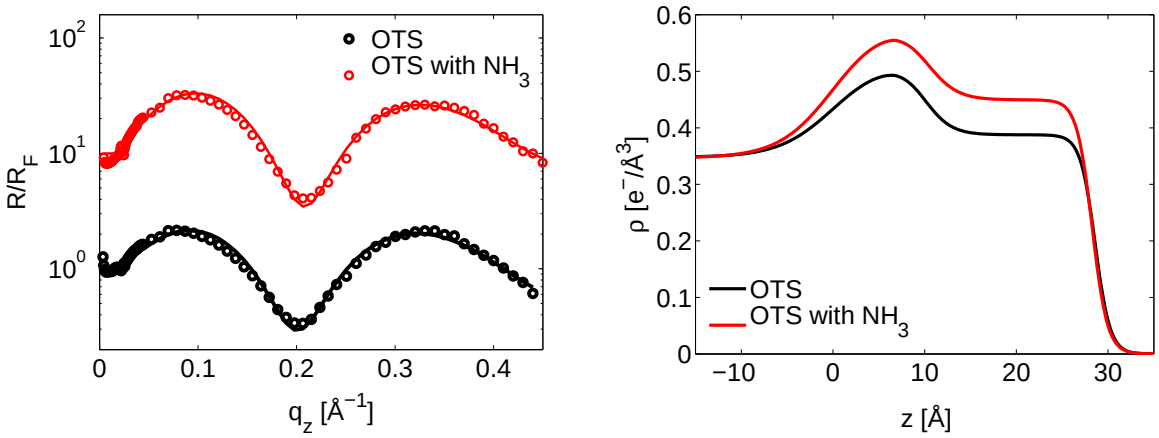

Figure 4.3.: Left: XRR data of an OTS layer on a water subphase with a pH value of 7 (circles) and refinement (lines) normalized by Fresnel-reflectivity R_F. For a better visibility the curves are shifted by a factor of 10 against each other. Right: Electron density profiles obtained by the refinement of the reflectivity data.

	without NH_3	with NH_3
FWHM [Å^{-1}]	0.09 ± 0.02	0.085 ± 0.006
domain size [Å]	91 ± 22	96 ± 6
$q_{\|\|}$ [Å^{-1}]	1.540 ± 0.005	1.535 ± 0.005
lattice constant a[Å]	4.70 ± 0.04	4.72 ± 0.04
I_{norm} [a.u.]	1.00 ± 0.12	8.84 ± 0.06

Table 4.1.: Parameters of the Voigt function fitted to the GID scans recorded on OTS membranes on neutral water subphases, full width of half maximum (FWHM), lateral position of the reflection $q_{||}$, intensity I_{norm} of the peak normalized to the maximum of the first measurement without ammonia.

a=4.71 Å. From this it can be concluded that the increased intensity is due to enrichment of scattering material in the illuminated area.

The XRR curves normalized by the Fresnel reflectivity are shown in figure 4.3. The polysiloxane monolayer was refined a model consisting of two layers, whereat the first layer represents the headgroup and the second layer the tailgroup of the molecule. The electron density profiles obtained by the refinement procedure are shown in figure 4.3. The overall electron density of the Langmuir layer increases in the presence of ammonia but the initial structure is preserved.

The behavior of the polysiloxane network was further investigated on acidic solutions with a pH value of 3 Hydrochloric acid was used to adjust the pH value of the water subphase. After the polysiloxane membrane was formed and characterized by GID experiments ammonia was added to the gas phase above the sample. The evolution of the system was then monitored until stable conditions were reached. The two-dimensional scattering maps of the OTS film after deposition and in the presence of ammonia are shown in figure 4.4 together with integrated scattering curves along the vertical scattering direction q_z.

The polysiloxane network deposited on the acidic subphase exhibits a Bragg rod with a curved shape indicating tilted tailgroups. Since the intensity distribution along the arc shaped rod exhibits no maximum it can be concluded that different tilt angles are present in this phase. The lateral position of the Bragg reflection is shifted to a smaller q-value of $q_{||} = 1.506$ Å^{-1} compared to the position of a neutral water subphase at $q_{||} = 1.540$ Å^{-1}. This reveals that the membrane has a larger unit cell constant of (4.81 ± 0.04)Å.

Figures 4.4b-c show the Bragg reflection of the polysiloxane membrane for different times after the addition of ammonia. Directly after the addition of ammonia the intensity of the Bragg

	t = 33 min	t = 100 min	t = 157 min	t = 212 min
domain size [Å]	298 ± 20	103 ± 12	88 ± 13	100 ± 23
FWHM [Å^{-1}]	0.027 ± 0.002	0.078 ± 0.006	$0{,}092 \pm 0.003$	0.081 ± 0.008
$q_{\|\|}$ [Å^{-1}]	1.506 ± 0.005	1.550 ± 0.005	1.555 ± 0.005	1.545 ± 0.005
a [Å]	4.81 ± 0.04	4.67 ± 0.04	4.66 ± 0.04	4.69 ± 0.04
A_0 [Å^2 molecule^{-1}]	20.0 ± 0.1	18.9 ± 0.1	18.8 ± 0.1	19.0 ± 0.1

Table 4.2.: Structural parameters of a polysiloxane membrane determined by evaluation of the GID data. Area per molecular (A_0), full width at half maximum (FWHM), parallel wave vector transfer $q_{||}$, lattice constant a.

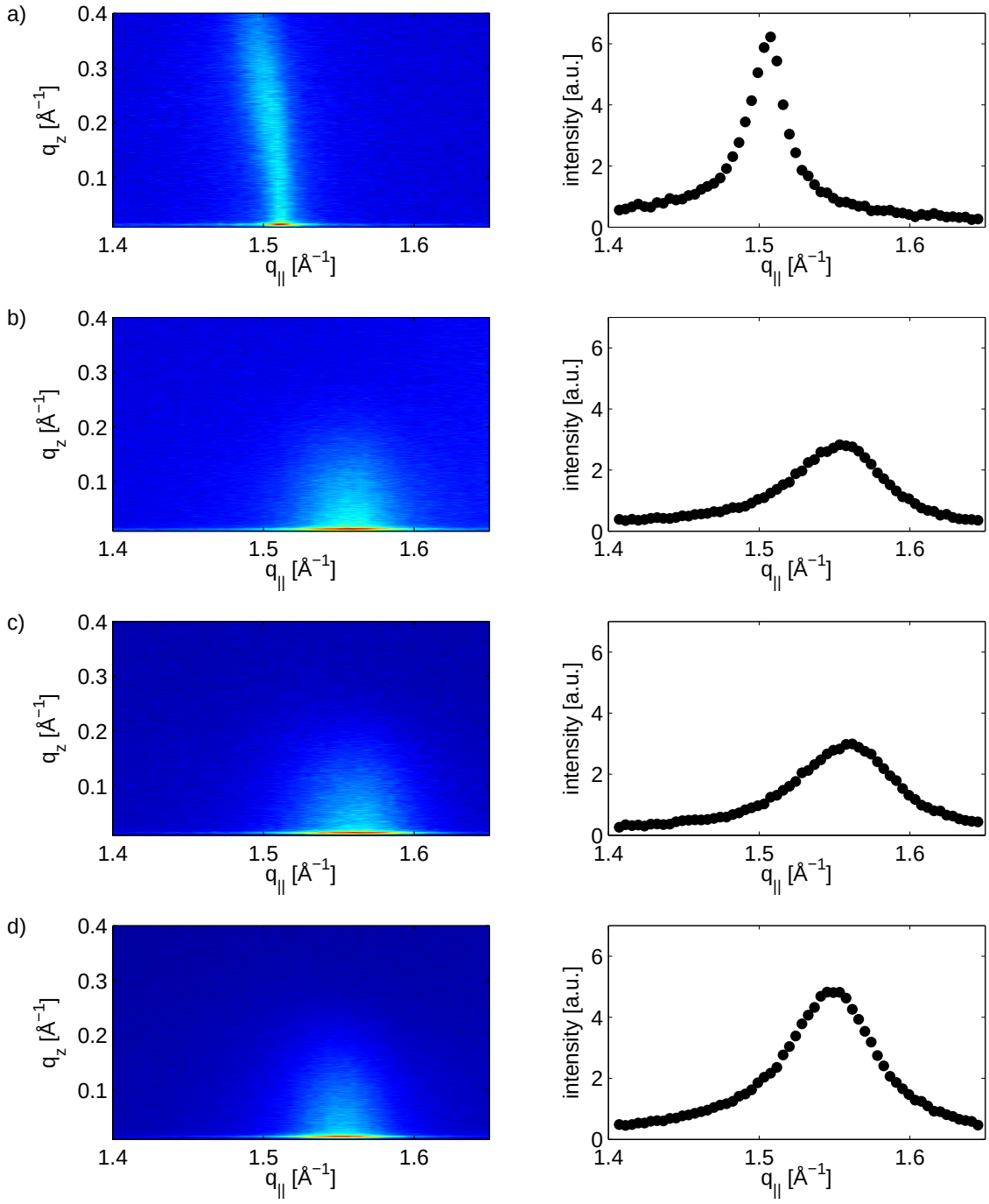

Figure 4.4.: GID data of polysiloxane networks on acidic subphases. Left: Two-dimensional diffraction pattern. Right: Integrated scattering intensity along the q_z direction. a) Without ammonia. b) Ammonia added. c) 57 minutes after addition of ammonia. c) 112 minutes after addition of ammonia.

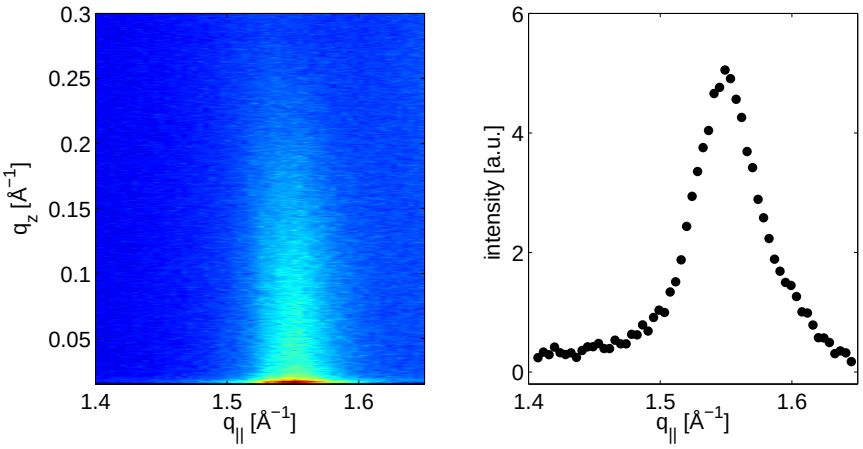

Figure 4.5.: GID scan of an OTS membrane on an alkaline subphase (pH = 12). Left: Two dimensional diffraction pattern. Right: Scattering curve integrated along the q_z direction.

reflection drops significantly accompanied by a shift of the position to $q_{||} = 1.550$ Å^{-1}. In the following 180 minutes the intensity of the Bragg reflection recovers again. The evaluated parameters are summarized in table 4.2. Within the error-bars the position of the Bragg reflection as ammonia is present is the same as for the neutral subphase. Furthermore the crystalline domain size coincides with the value observed for a pure water subphase.

The reason for these observations might be a hindered hydrolysis reaction of the single monomers due to the low pH value of the solution, see Figure 4.1. The network formation proceeds via two steps being first a hydrolysis reaction of the silane group and a subsequent condensation of single monomers. The hydrolysis reaction is a nucleophilic substitution of the type S_n2 which is slowed down under acidic conditions.[81, 158] As a consequence the single monomers are not able to condensate and the monolayer might consist of single OTS monomers which are not joined by covalent bonds. Bond length calculations of the Si-O-Si bond yield a distance of 4.3 Å.[154] By assuming an interaction of the hydrocarbon chains via van der Waals forces the distance between the chains would be 4.8 Å.[154] These calculations of the bond length show that the hydrocarbon chains had to be compressed during the condensation reaction which requires an elastic energy of 40 meV. This amount is smaller than 8 eV which will be gained by formation of the covalent bond between the single monomers.[154] Insofar, it can be concluded that on the acidic subphase the OTS is not polymerized in the beginning. The distance of the hydrocarbon tails is governed by the van der Waals interaction which results in a larger unit cell size. When ammonia is added to the system the condensation reaction is enabled and the polysiloxane network forms. This is indicated by the collapse of the intensity of the Bragg reflection due to a reorganization of the monolayer and by the shift of the Bragg reflection. With ongoing time the intensity of the reflection recovers but does not reach the initial state. The size of the crystalline domains drops by a factor of 2 after ammonia is added. Thereafter the domain size keeps constant.

Langmuir layers of OTS were also studied on an alkaline subphase. Therefore a sodium hydroxide subphase was used with a pH value of 12. The GID scan is shown in figure 4.5. By comparing the position of the Bragg reflection with the position found for a water subphase no

domain size [Å]	126 ± 20
FWHM [Å^{-1}]	0.064 ± 0.02
$q_{\|\|}$ [Å^{-1}]	1.548 ± 0.005
lattice constant a [Å]	4.68 ± 0.04
area per molecule A_0[Å^2 molecule^{-1}]	19.0 ± 0.1

Table 4.3.: Properties of the polysiloxane membranes on alkaline subphases determined by evaluation of the GID scans. Area per amphiphilic molecule (A_0), full width at half maximum (FWHM), parallel wave vector transfer $q_{||}$, lattice constant a.

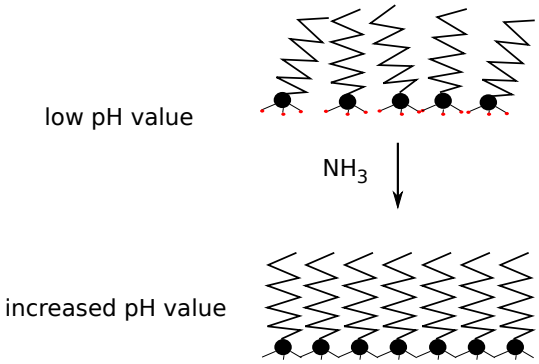

Figure 4.6.: Sketch of the restructuring in the polysiloxane membrane on the addition of ammonia. The membrane was formed on acidic subphases.

change can be observed. The structural parameters of the film obtained are summarized in table 4.3. Due to the high pH value the condensation reaction is terminated after the deposition of the monomers at the interface.

4.1.2. Discussion and conclusion

The initial state of the polysiloxane networks is influenced by the subphase's pH value. Under acidic conditions a layer composed of single OTS monomers is formed which exhibit a tilt of the hydrocarbon chain, see figure 4.6 top. The distance between the single monomers is controlled by van der Waals forces between the hydrocarbon groups resulting in an increased unit cell size. After ammonia is added the pH value in the interfacial region of the subphase increases which enables the formation of a two-dimensional network by covalent bonding of the monomers thus reducing the distance between the hydrocarbon tails and decreasing the tilt of the hydrocarbon chain a shown in figure 4.6 bottom.[153, 157] The polysiloxane network structure is the same as on a neutral subphase in the end. The size of the crystalline domains observed also coincides with the patch sizes on neutral subphases. Thus, the homogeneity of the network after polymerization is the same. The results are reasonable as the hydrolysis reaction is slowed down under acidic conditions and the single monomers are not able to polymerize. [81, 158] Thus, the membrane formation process is controlled by the hydrolysis equilibrium. As the pH value increases the silane group is hydrolyzed and the condensation reaction can take place. The kinetics of the membrane formation process are thus controlled by the hydrolysis reaction.

On neutral subphases the polymerization is not hindered. The OTS molecules spontaneously polymerize forming polysiloxane patches with voids between them.[159] After ammonia is

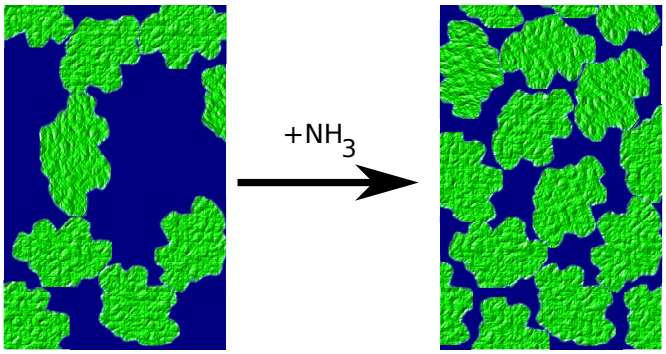

Figure 4.7.: Sketch of the lateral restructuring in the polysiloxane membrane on the addition of ammonia. The membranes was formed on neutral subphases.

added the XRR data show an increase of the electron density without an alteration of the film structure. The crystalline structure of the polysiloxane patches is not influenced by the ammonia as the GID measurements show a constant crystalline domain size and a constant unit cell size. However the scattering amplitude increases indicating an increase of scattering material in the illuminated area. Surface pressure measurements performed in the context of these experiments by P. Degen, Physikalische Chemie II, TU Dortmund, show a decrease of the surface pressure in the presence of ammonia.[160] This can be explained by a reorientation of macroscopic polysiloxane patches induced by ammonia. Furthermore, surface potential measurements in the presence of ammonia indicate a distortion of the film structure which recovers with time.[160] The observations can be explained by the break up of siloxane bonds in the network by ammonia.[158] The flexibility of the film is increased and a rearrangement of the film can take place. This rearrangement of the OTS patches is sketched in figure 4.7.

4.2. Influence of ammonia on Langmuir layers

In the following chapter the influence of ammonia on lipids forming a Langmuir layer is investigated. The samples were prepared as described in chapter 3.9. Amphiphiles were spread onto subphases consisting of ultra pure water (specific resistivity ρ=18.2 Ωm) and the formed layers were compressed to a surface pressure of $\Pi = 20\ \mathrm{mN/m}$. After characterizing the initial state vials containing an ammonia solution were placed in the sample cell. XRR and GID measurements were conducted at the beamline BW1, DORIS III, Hamburg, Germany and at the beamline ID10B, ESRF, Grenoble, France.

4.2.1. Stearic acid

The XRR data recorded from Langmuir layers consisting of stearic acid are shown in figure 4.8 and are normalized by the Fresnel reflectivity. The data show oscillations indicating the

	as deposited	ammonia added
FWHM [Å^{-1}]	0.013 ± 0.001	0.020 ± 0.006
$q_{\|\|}$ [Å^{-1}]	1.526 ± 0.005	1.522 ± 0.005
I_{norm} [a.u.]	68 ± 4	16 ± 1
lattice constant a [Å]	4.75 ± 0.3	4.7 ± 0.3
unit cell size A_{xy} [Å^2]	19.5 ± 0.3	19.6 ± 0.7
area per molecule A_0 [Å^2]	19.5 ± 0.3	19.6 ± 0.7

Table 4.4.: Properties of the stearic acid films on water subphases estimated by evaluation of the GID scans, full width of half maximum (FWHM), lateral position of the reflection $q_{||}$, intensity I_{norm} of the Bragg reflection.

presence of a thin film at the interface. The subsequent addition of ammonia has no effect on the reflectivity. The electron density profiles obtained by refinement are shown in figure 4.8. This data show no significant change in the vertical density profile.

The GID data obtained from this sample are shown in figure 4.9. In the native state a Bragg reflection at $q_{||} = 1.526$ Å^{-1} can be observed. The stearic acid molecules organize in a hexagonal lattice with the hydrophobic carbon tails oriented perpendicular to the sample surface indicated by the existence of one single reflection. After the vials containing the ammonia had been placed inside the sample chamber the diffraction signal lost intensity by a factor of 4.25. The lateral position of the diffraction peak was stable at $q_{||} = 1.526$ Å^{-1}. The increase of the width of the reflections indicates a decrease in crystalline domain size. It can be concluded that ammonia reduces the lateral order but has no effect on the crystal lattice of the Langmuir film. The fitted parameters are summarized in table 4.4 and are in agreement with values from literature.[161]

In order to keep the surface pressure stable the area covered by the Langmuir film had to be reduced by reducing the geometrical size of the trough by the surface barrier as ammonia was added. This indicates a loss of amphiphilic material from the interface which can be explained by the formation of ammonia stearate, which is soluble in water.[162] By this formation amphiphilic molecules are removed from the interface which results in a decline of surface pressure. This might also provoke disorder in the lateral structure reducing the size of the crystalline patches.

4.2.2. Stearyl alcohol

Fresnel normalized XRR data of stearyl alcohol layers are shown in figure 4.10. In the beginning the reflected signal shows an oscillation with a small amplitude which is damped when ammonia is added. The electron density profiles obtained from the experimental data are also shown in figure 4.10. The headgroup of the film has an electron density which is slightly higher than the electron density of water. After the addition of ammonia the overall electron density of the film is reduced.

The GID scans of the stearyl alcohol layer are shown in figure 4.11. In the beginning a single reflection originating from the Langmuir layer can be observed. Voigt profiles were fitted to the

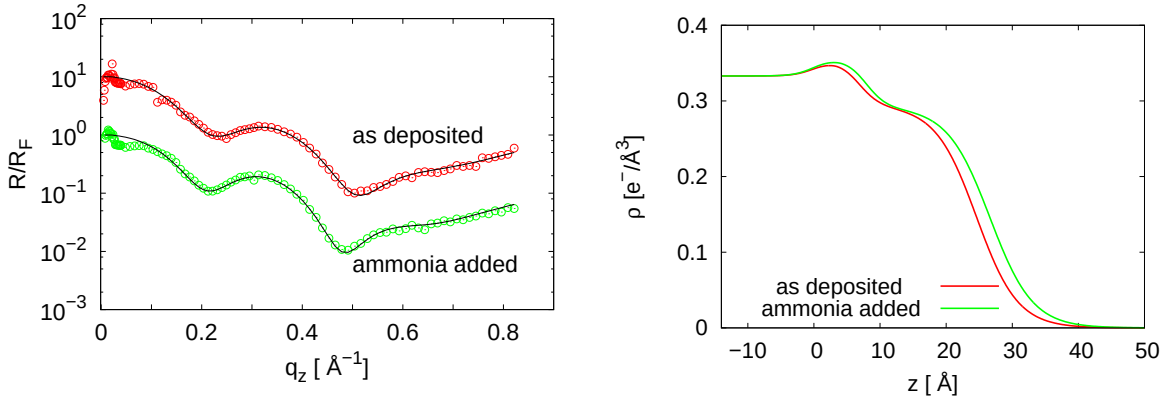

Figure 4.8.: Left: XRR data of stearic acid on a water subphase. Right: Electron density profiles of stearic acid on a water subphase.

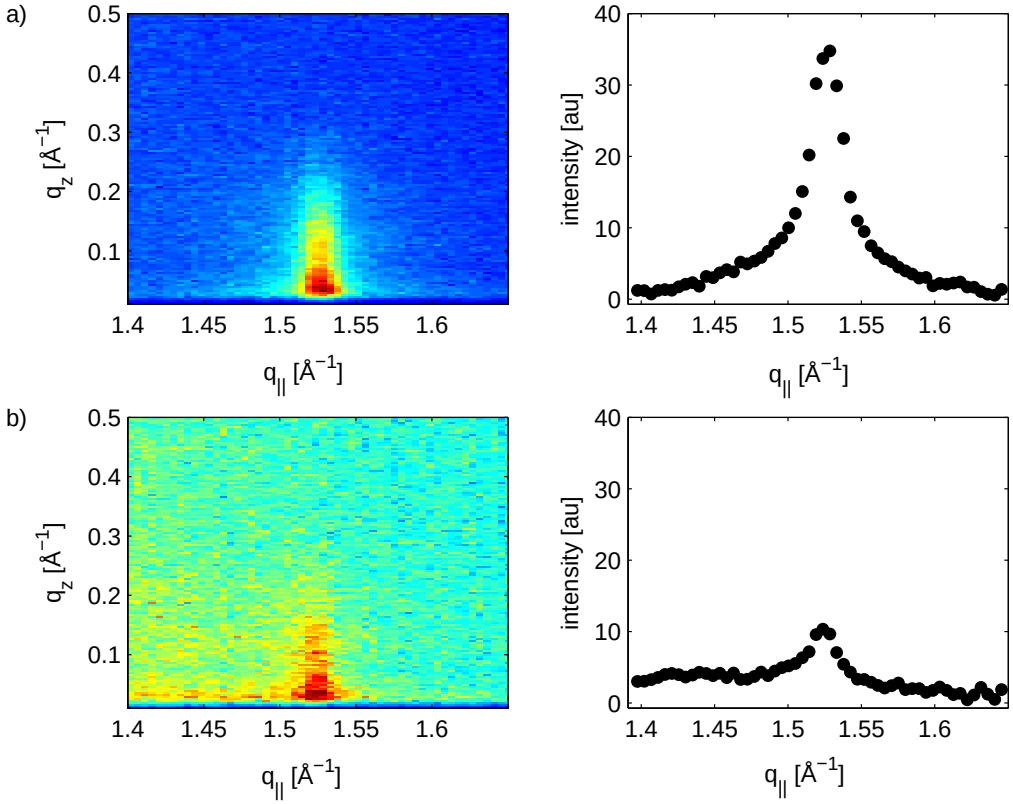

Figure 4.9.: GID measurements of stearic acid on a) water subphase and b) in the presence of ammonia.

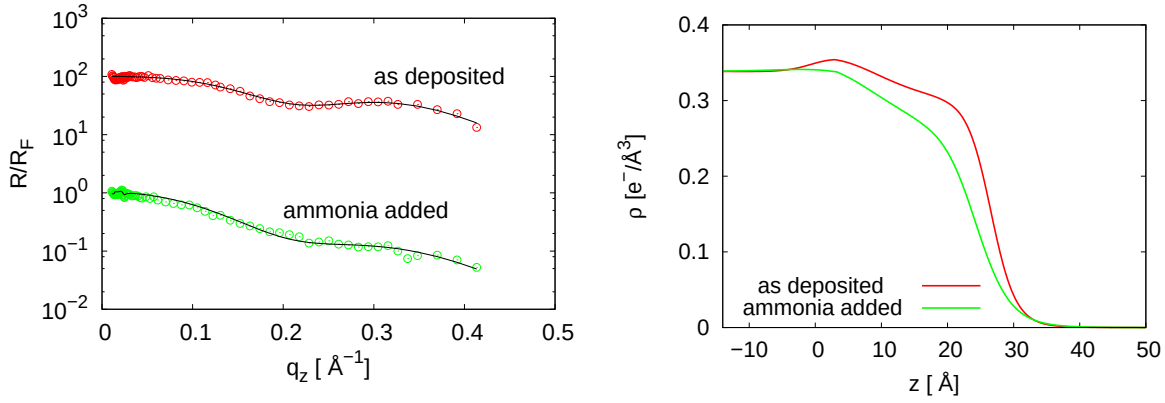

Figure 4.10.: Left: XRR data of stearyl alcohol on a water subphase. Right: Electron density profiles of stearyl alcohol on a water subphase.

Bragg reflections and a satisfactory result was achieved by using two Voigt profiles simultaneously. This indicates a distortion of the alkyl chain packing with a slight tilt of the alkyl chains. Although the reflections are not clearly distinguishable making a clear structure determination impossible, the unit cell of the Langmuir layer is supposed to be centered rectangular. The peak with the smallest $q_{||}$ value is attributed to be the (1,1) and$(1,\bar{1})$ reflections whereas the peak at high $q_{||}$ is the (0,2) reflection. After ammonia was added the intensity of the Bragg reflections decreased. The parameters of the Langmuir layer with and without ammonia show that the (1,1) and $(1,\bar{1})$ reflections gain in intensity upon addition of ammonia (see table 4.5). This process is accompanied by a change in the size of the crystalline domains. The most plausible reason for the observations is change in the tilt of the hydrocarbon tailgroup. However from the experimental data no exact conclusion can be drawn. The overlapping of the Bragg rods and the proximity to the horizon make a reliable evaluation of the q_z position impossible.[1] Shih et al. report on a size of 19.9 Å^2 for the headgroup area of Langmuir monolayers of heneicosanol which has a slightly longer hydrocarbon chain but the same hydrophilic headgroup structure.[163]

As ammonia is added the scattering intensity decreases whereas the width of the reflections increase. This indicates a decrease in the size of the crystalline domains due to ammonia.

4.2.3. Stearyl amide

The Fresnel normalized reflectivity data obtained on stearyl amide are shown in figure 4.12 as well as the electron density profiles. The electron density profiles resemble each other showing the same vertical film structure.

In contrast the GID scans show an alteration when ammonia is added, see figure 4.13. In the initial state the stearyl amide Langmuir layer shows two Bragg reflections. This already implies that the layer is organized in a centered rectangular unit cell. Further, the appearance of a reflection at $q_z \neq 0$ indicates a tilt of the Langmuir layer hydrocarbon chains.

[1] See chapter 3.10, a determination of the q_z position of the maximum in a Bragg rod would have a high error. A reliable conclusion is thus not possible.

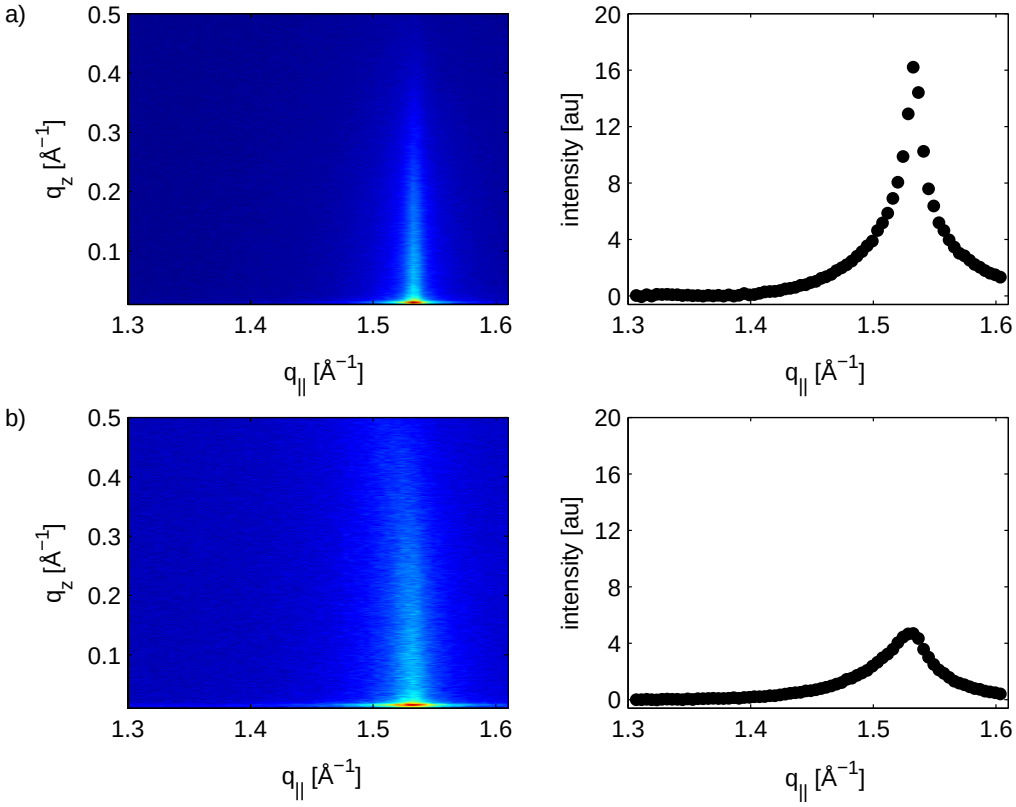

Figure 4.11.: GID measurements of stearyl alcohol a) on a water subphase and b) in the presence of ammonia. The left row shows the two-dimensional scattering pattern and the right shows the summarized scattering pattern along the vertical scattering direction.

(1,1) and (1,$\bar{1}$) reflections	as deposited	ammonia added
FWHM [Å^{-1}]	0.088 ± 0.006	0.10 ± 0.01
$q_{\|\|}$ [Å^{-1}]	1.528 ± 0.005	1.512 ± 0.005
I_{norm} [a.u.]	10.2 ± 0.3	3.75 ± 0.1
(0,2) reflection		
FWHM [Å^{-1}]	0.015 ± 0.005	0.037 ± 0.004
$q_{\|\|}$ [Å^{-1}]	1.530 ± 0.005	1.530 ± 0.005
I_{norm} [a.u.]	18.2 ± 0.3	4.99 ± 0.07
lattice constant a [Å]	4.7 ± 0.1	4.8 ± 0.2
lattice constant b [Å]	8.2 ± 0.4	8.2 ± 0.5
unit cell size A_{xy}[Å^2]	39.4 ± 0.5	39.4 ± 0.7
area per molecule A_0 [Å^2]	19.7 ± 0.5	19.7 ± 0.7

Table 4.5.: Properties of the stearyl alcohol film on water subphases estimated by evaluation of the GID scans, full width of half maximum (FWHM), lateral position of the reflection $q_{||}$, intensity I_{norm} of the Bragg reflection.

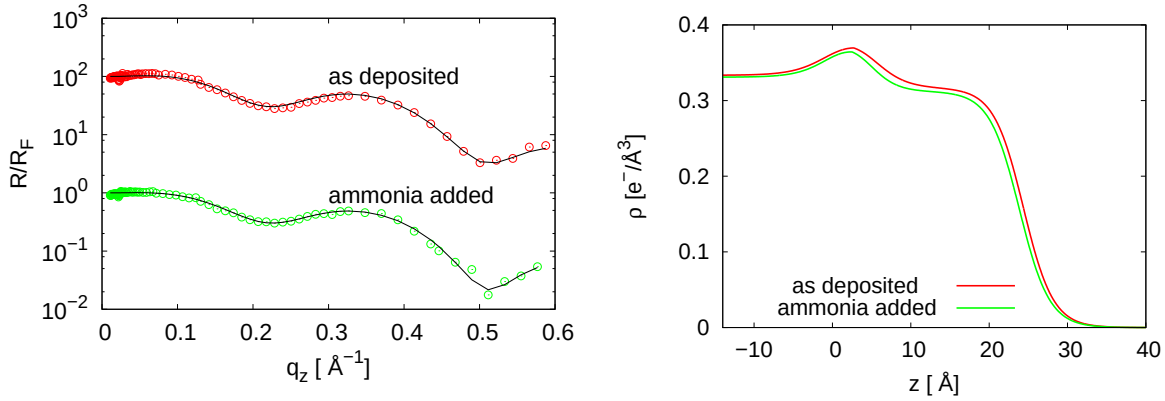

Figure 4.12.: Left: XRR data of stearyl amide on a water subphase. Right: Electron density profiles of stearyl amide on a water subphase.

(1,1) and (1,$\bar{1}$) reflections	as deposited	ammonia added
FWHM [Å^{-1}]	0.064 ± 0.005	0.062 ± 0.004
$q_{\|\|}$ [Å^{-1}]	1.415 ± 0.005	1.398 ± 0.005
q_z [Å^{-1}]	0.165 ± 0.003	0.0716 ± 0.010
I_{norm} [a.u.]	21.2 ± 0.3	22.3 ± 0.07
(0,2) reflection		
FWHM [Å^{-1}]	0.177 ± 0.006	0.173 ± 0.01
$q_{\|\|}$ [Å^{-1}]	1.538 ± 0.005	1.541 ± 0.005
I_{norm} [a.u.]	23.7 ± 0.3	27.5 ± 0.1
lattice constant a [Å]	5.2 ± 0.3	5.3 ± 0.3
lattice constant b [Å]	8.1 ± 0.4	8.1 ± 0.3
unit cell size A_{xy}	43.2 ± 0.6	43.8 ± 0.5
area per molecule A_0 [Å^2]	21.6 ± 0.4	21.9 ± 0.8
tilt angle τ [°]	7 ± 0.4	3.5 ± 0.3

Table 4.6.: Properties of the stearyl amide film on water subphases estimated by evaluation of the GID scans, full width of half maximum (FWHM), lateral position of the reflection $q_{||}$, intensity I_{norm} of the Bragg reflection.

The reflection at $q_{||}$ =1.415 Å is the degenerated (1,1) and (1,$\bar{1}$) reflection and the peak at $q_{||}$ =1.538 Å is indexed as the (0,2) reflection. The unit cell has dimensions of a = 5.2 Å and b = 8.1 Å. A tilt of the hydrocarbon tails of $\tau = 7°$ was calculated in the direction of the nearest neighbor (NN-tilt), see figure 2.16. After ammonia is added the unit cell of the stearyl amide layer changes. The (1,1) and (1,$\bar{1}$) reflection, which in the beginning have a q_z value of 0.165 Å^{-1} shifts to a q_z value of 0.0716 Å^{-1}. In addition the position of the Bragg reflection changes to $q_{||}$= 1.398 Å^{-1}. The analysis shows that the tilt of the tail groups is reduced to τ = 3.5°. The calculated parameters are summarized in table 4.6.

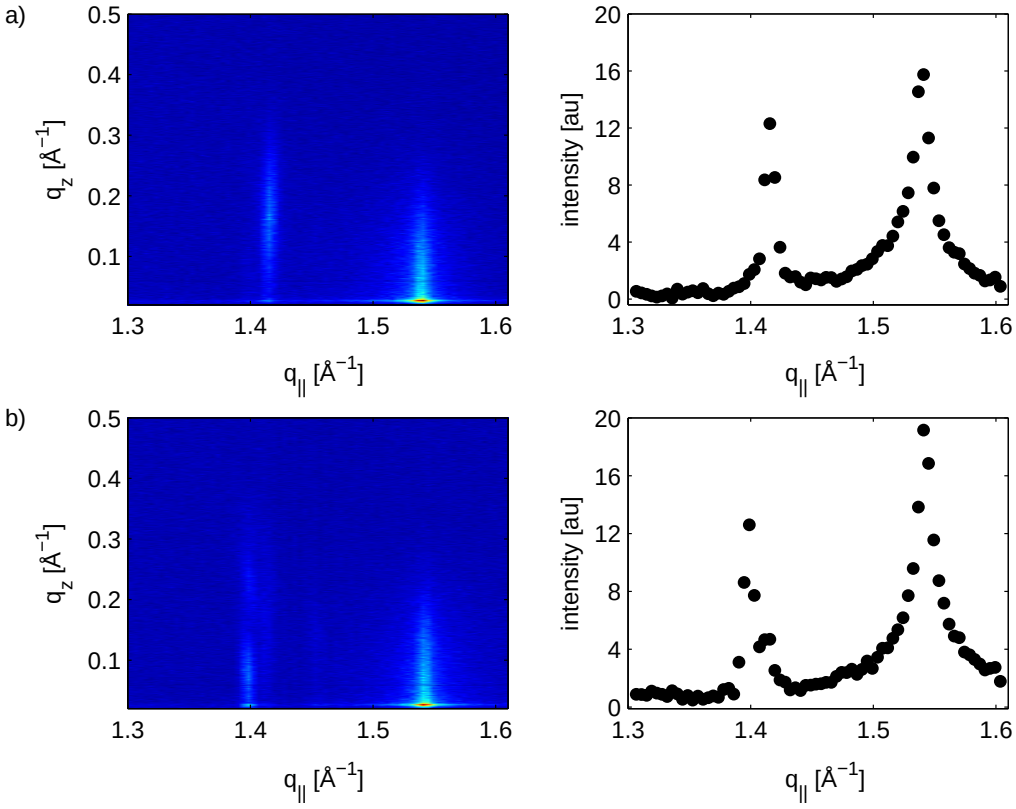

Figure 4.13.: GID measurements of stearyl amide a) on a water subphase and b) in the presence of ammonia. The left row shows the two-dimensional scattering pattern and the right shows the summarized scattering pattern along the vertical scattering direction.

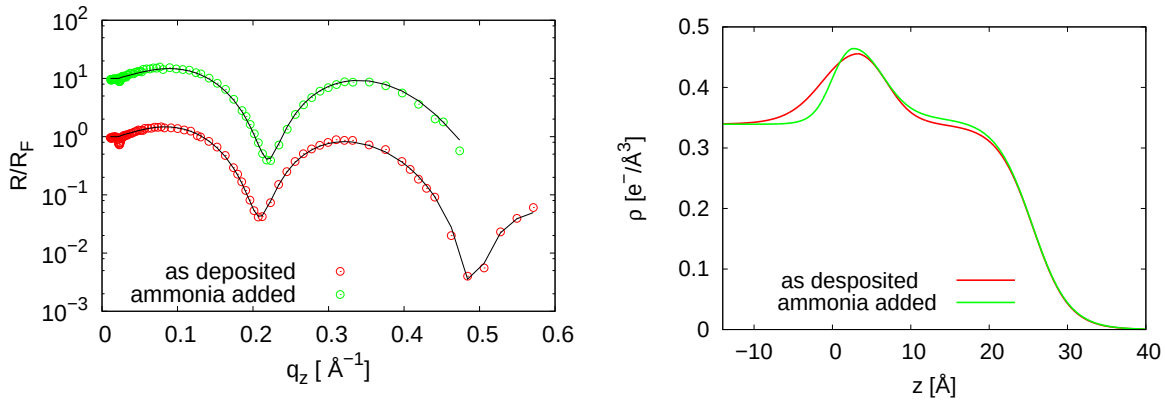

Figure 4.14.: Left: XRR data of DPPA on a water subphase. Right: Electron density profiles of DPPA on a water subphase.

4.2.4. DPPA

The Fresnel normalized XRR data obtained on Langmuir layers of the phospholipid DPPA are shown in figure 4.14. The data show strong oscillations originating from the Langmuir layer. After ammonia is added the first minimum shifts to a slightly smaller q_z value. The electron density profiles reveal a slightly smaller headgroup with an increased electron density, see figure 4.14.

The GID scans show strong variations upon ammonia addition, see figure 4.15. In the beginning a single Bragg reflection can be observed indicating a hexagonal crystal lattice. After ammonia is added a second reflection appears. This indicates a transformation of the hexagonal lattice to a centered rectangular lattice accompanied with a tilting of the tailgroup. When ammonia is added the available molecular area of the DPPA amphiphiles is enlarged. The observation is attributed to the changed pH value which has direct influence on the electrostatic repulsion of the headgroups of the DPPA molecules. As the pH value increases the repulsion between the single headgroups gets stronger thus enlarging the distance between them and increasing the effectively occupied area. The evaluated parameters of the DPPA film are summarized in table 4.7. The values observed by Estela-Lopis et al. for the pure water subphase are the same within the error.[164] The Bragg rod analysis is shown in appendix A.

4.2.5. DPPC

The XRR data obtained on Langmuir layers composed of DPPC are shown in figure 4.16. After addition of ammonia no changes can be identified in the data. In agreement to this the electron density profiles obtained from the XRR data show no significant changes of the film structure only a slight decrease of the overall electron density, see figure 4.16.

The GID data is shown in figure 4.17. The diffraction pattern shows two peaks indicating that the layer can be described by a centered rectangular unit cell. By this the first peak at $q_{||} = 1.414\,\text{Å}^{-1}$ can be ascribed to be the degenerated (1,1) and ($\bar{1}$,1). The second peak at $q_{||} = 1.479\,\text{Å}^{-1}$ is the (0,2) reflection. After ammonia is added the intensity of the diffraction

	as deposited six fold degenerate	ammonia added (1,1) and (1,$\bar{1}$) reflections
FWHM [Å^{-1}]	0.088 ± 0.003	0.044 ± 0.004
$q_{\|\|}$ [Å^{-1}]	1.530 ± 0.003	1.439 ± 0.005
q_z [Å^{-1}]	0 ± 0.002	0.586 ± 0.002
I_{norm} [a.u.]	55.6 ± 0.3	33.8 ± 0.2
		(0,2) reflection
FWHM [Å^{-1}]	-	0.041 ± 0.02
$q_{\|\|}$ [Å^{-1}]	-	1.500± 0.005
q_z [Å^{-1}]	-	0 ± 0.002
I_{norm} [a.u.]	-	10.2 ± 0.1
lattice constant a [Å]	4.7 ± 0.1	5.1 ± 0.3
lattice constant b [Å]	-	8.3 ± 0.4
unit cell size A_{xy}[Å^2]	38.8 ± 0.6	42.8 ± 0.6
area per molecule A_0[Å^2 molecule^{-1}]	19.4 ± 0.6	19.3 ± 0.6
tilt angle τ [°]	-	25.5 ± 0.3

Table 4.7.: Properties of the DPPA film on water subphases estimated by evaluation of the GID scans, full width of half maximum (FWHM), lateral position of the reflection $q_{||}$, intensity I_{norm} of the Bragg reflection.

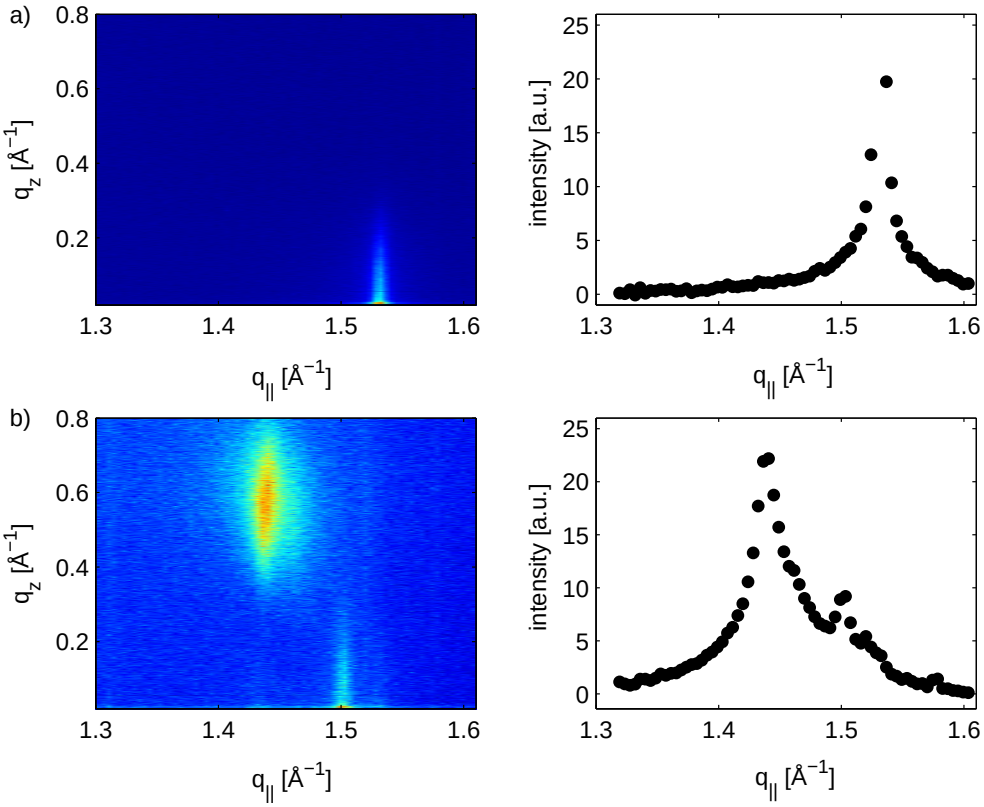

Figure 4.15.: GID measurements of DPPA a) on a water subphase and b) in the presence of ammonia. The left row shows the two-dimensional scattering pattern and the right side shows the summarized scattering pattern along the vertical scattering direction.

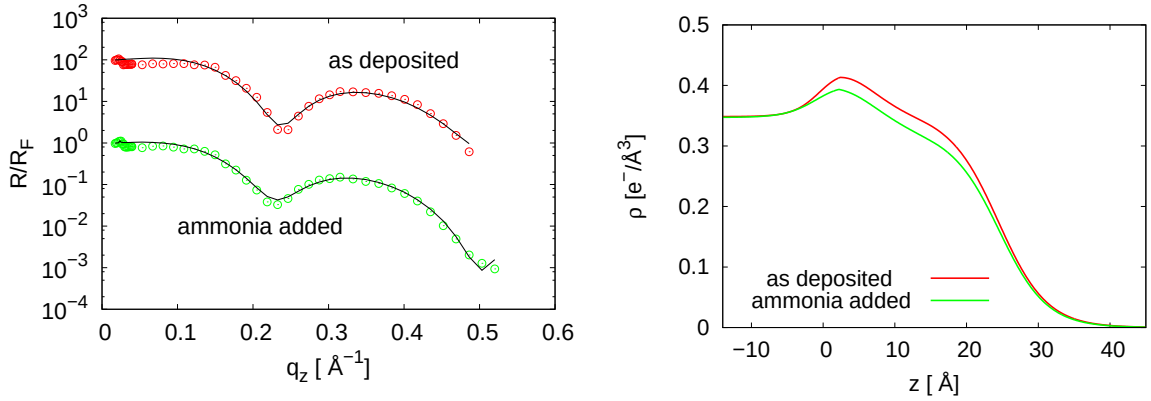

Figure 4.16.: Left: XXR data of DPPC on a water subphase. Right: Electron density profiles of DPPC on a water subphase.

(1,1) and (1,$\bar{1}$) reflections	as deposited	ammonia added
FWHM [Å^{-1}]	0.054 $\pm$ 0.003	0.031 $\pm$ 0.008
$q_{\|\|}$ [Å^{-1}]	1.414 $\pm$ 0.003	1.405$\pm$ 0.005
q_z [Å^{-1}]	0.637 $\pm$ 0.003	0.605$\pm$ 0.005
I_{norm} [a.u.]	4.5 $\pm$ 0.3	3.2 $\pm$ 0.1
(0,2) reflection		
FWHM [Å^{-1}]	0.008 $\pm$ 0.004	0.020 $\pm$ 0.005
$q_{\|\|}$ [Å^{-1}]	1.479 $\pm$ 0.003	1.476 $\pm$ 0.005
I_{norm} [a.u.]	7.2 $\pm$ 0.3	6.6 $\pm$ 0.1
lattice constant a [Å]	5.21 $\pm$ 0.4	5.23 $\pm$ 0.1
lattice constant b [Å]	8.48$\pm$ 0.04	8.50 $\pm$ 0.04
unit cell size A_{xy} [Å^2]	44.2 $\pm$ 0.7	44.5 $\pm$ 0.8
area per molecule A_0 [Å^2]	22.1 $\pm$ 0.7	22.2 $\pm$ 0.8
tilt angle τ	27.9 $\pm$ 0.3	26.8 $\pm$ 0.8

Table 4.8.: Properties of a DPPC film on water subphases estimated by evaluation of the GID scans, full width of half maximum (FWHM), lateral position of the reflection $q_{||}$, intensity I_{norm} of the Bragg reflection.

peaks decreases slightly, however the peak positions and the width change only hardly indicating minor changes in crystal lattice. The obtained unit cell parameters show a slight deviation to data reported in literature. Estela-Lopis et al. observed for DPPC a slightly larger area per molecule of 23.7 Å^2 at a surface pressure of 20 mN/m.[164] This difference might be explained by the presence of calcium and natrium ions in the solution subphase of the mentioned study influencing the interaction between the DPPC headgroups. The Bragg rod analysis is shown in appendix A.

4.2.6. EPC

The XRR data on Langmuir layers of EPC are shown in figure 4.18. The oscillations in the obtained curve indicate the presence of a surfactant layer. After ammonia is added the amplitude

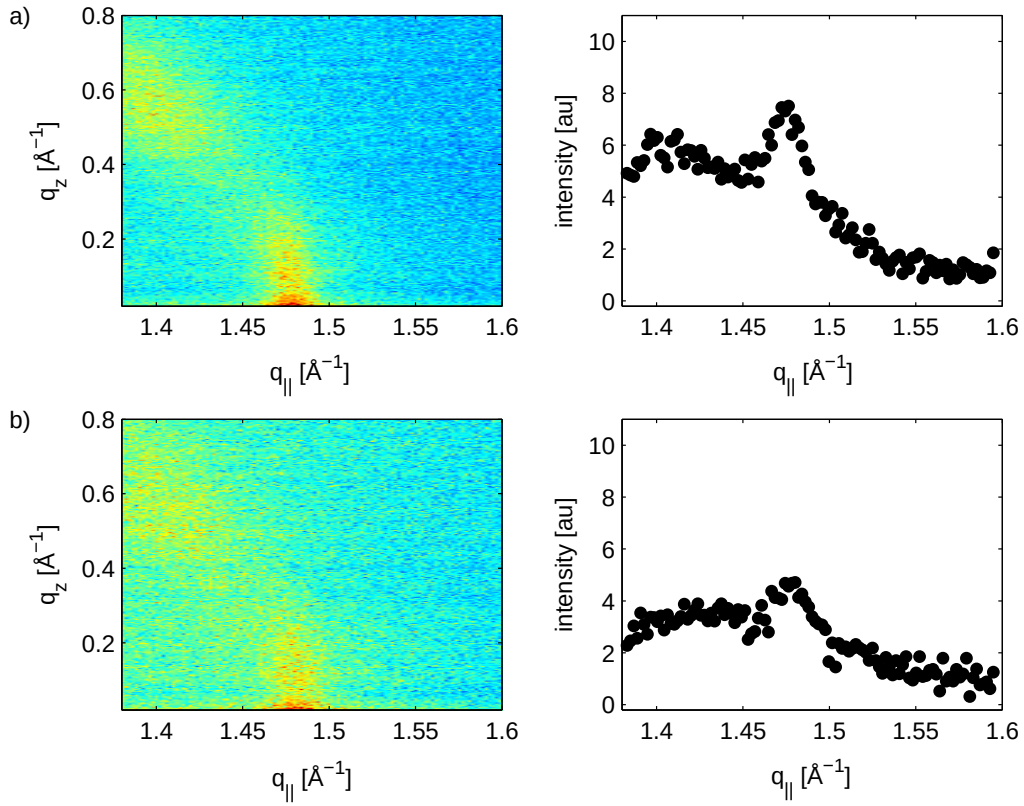

Figure 4.17.: GID measurements of DPPC a) on a water subphase and b) in the presence of ammonia. The left row shows the two-dimensional scattering pattern and the right row shows the summarized scattering pattern along the vertical scattering direction.

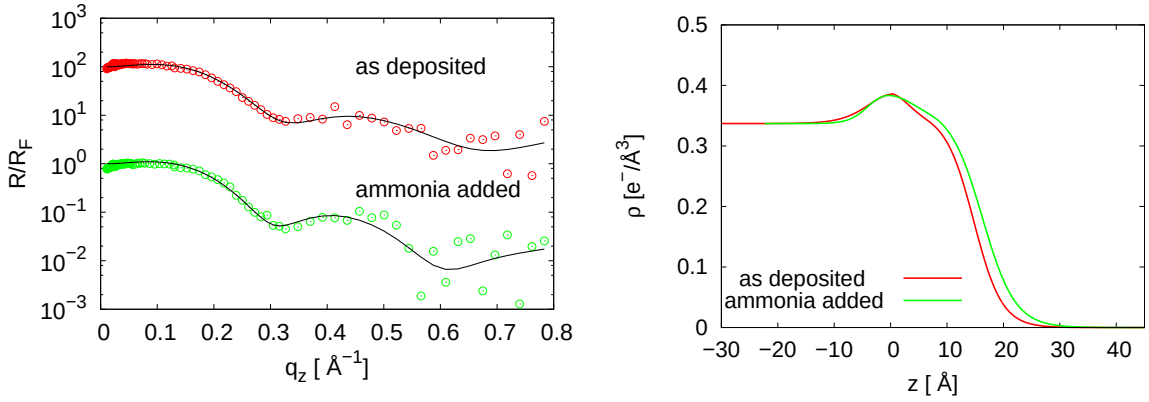

Figure 4.18.: Right: XRR data of EPC on a water subphase. Left: Electron density profiles of EPC on a water subphase.

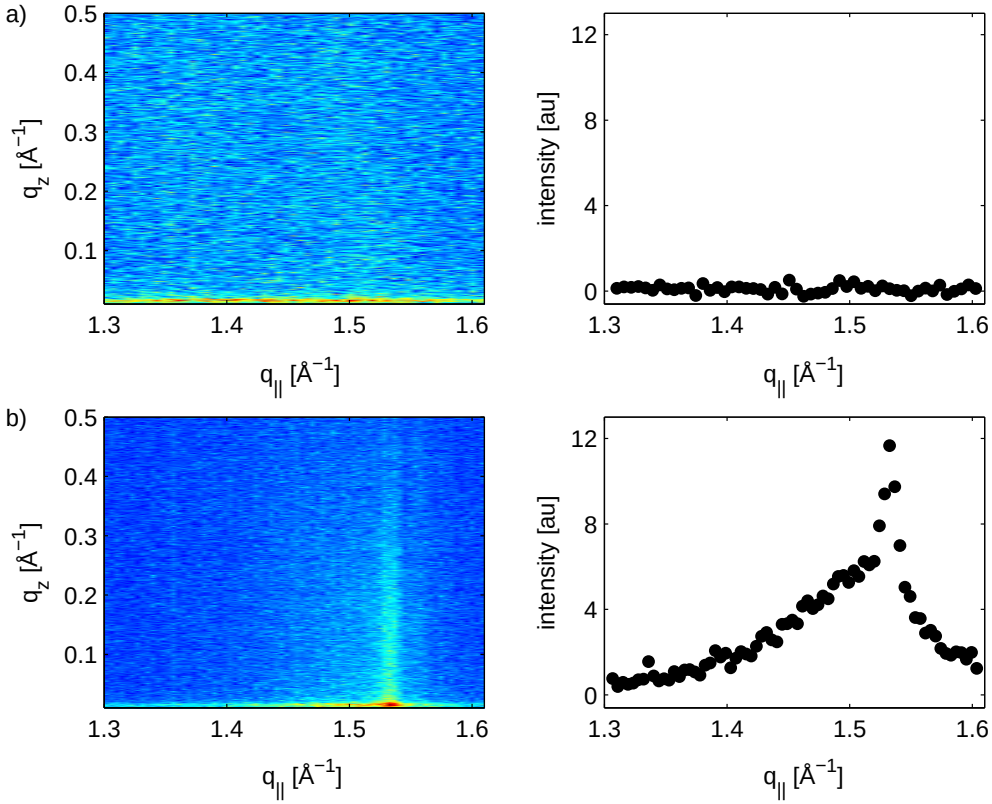

Figure 4.19.: GID measurements of EPC a) on a water subphase and b) in the presence of ammonia. The left row shows the two-dimensional scattering pattern and the right row shows the summarized scattering pattern along the vertical scattering direction.

of the oscillation is enhanced. The electron density profiles are shown in figure 4.18. The data indicate an enlarged tail group length upon addition of ammonia which can be explained by a more upright and ordered state of the tailgroup.

The GID data is shown in figure 4.19. In the initial state no Bragg reflection can be observed. This shows that the tail groups are not ordered even though the surface pressure is $20\ \mathrm{mN/m}$. When ammonia is added a broad Bragg reflection occurs. The reflection shows a maximum at $q_z = 0\ \text{Å}^{-1}$. Two Voigt profiles were fitted to the data for a satisfactory result. The obtained parameters are summarized in table 4.9. The XRR and GID data indicates that in the presence of ammonia the Langmuir layer might undergo a transition from a liquid expanded to a condensed state.

4.3. Summary

The experiments on the influence of ammonia on the Langmuir layer structure show significant changes of the lateral film structure at a constant surface pressure. The non-ionic Langmuir films (stearyl amide, stearyl alcohol) show in general a reduction in the tilt angle of the hydrocarbon tailgroup. As the pH value in the interfacial region increases the amphiphilic molecules are pushed closer together thus reducing the molecular area and the tilt of the tailgroup. This

	as deposited	ammonia added
FWHM [Å^{-1}]	-	0.012 ± 0.001
$q_{\|\|}$ [Å^{-1}]	-	1.532 ± 0.005
I_{norm} [a.u.]	-	13.2 ± 0.1
FWHM [Å^{-1}]	-	0.152 ± 0.001
$q_{\|\|}$ [Å^{-1}]	-	1.498± 0.005
I_{norm} [a.u.]	-	8.8 ± 0.1
lattice constant a [Å]	-	4.7 ± 0.1
lattice constant b [Å]	-	8.3 ± 0.2
unit cell size A_{xy} [Å^2]	-	39.4 ± 0.9
area per molecule A_0 [Å^2]	-	19.7 ± 0.9

Table 4.9.: Properties of a EPC film on water subphases estimated by evaluation of the GID scans, full width of half maximum (FWHM), lateral position of the reflection $q_{||}$, intensity I_{norm} of the Bragg reflection.

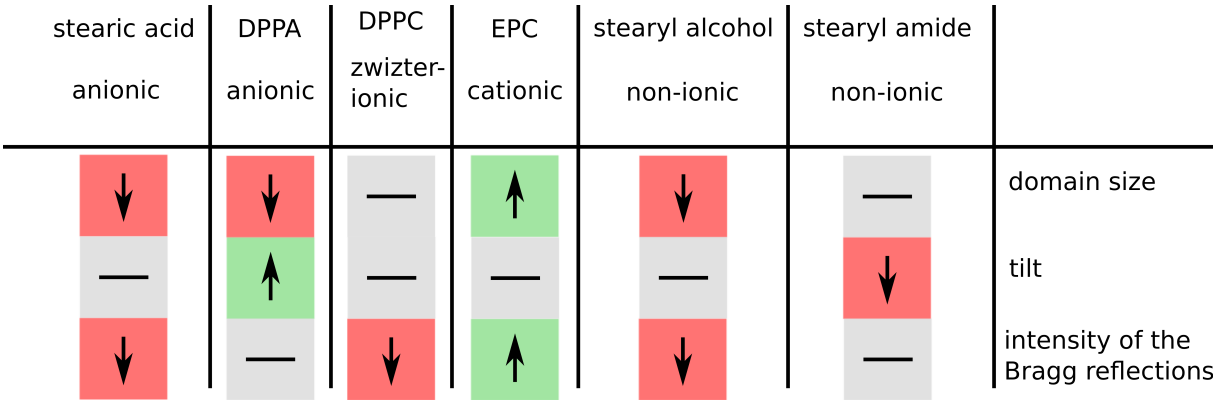

Figure 4.20.: Graphical representation of the observed changes in the different Langmuir layers upon the addition of ammonia.

effect is not observed for the cationic amphiphil of DPPA showing a transition to a more tilted phase. The lateral structure of stearic acid Langmuir layers shows no change on the addition of ammonia. Further the zwitter-ionic DPPC Langmuir layer structure is influenced only slightly. In contrast the Langmuir film of the cationic amphiphile EPC shows a transition to an untilted phase as the subphase is more alkaline. An observation which can be made for all Langmuir films independent on the type of headgroup is a reduction in scattering intensity of the Bragg reflections. The results are summarized graphically in figure 4.20.

The experiments illustrate that ammonia is not destroying the lateral structure as all amphiphiles show a Bragg reflection up to the end.

Damage induced by the X-ray beam normally gets visible by the formation of thick film in a XRR experiment. The vertical structure was only slightly disturbed which shows that the stability against beam damage is not reduced as ammonia is present.

5. Membrane mediated growth of thin films at the aqueous solution-air interface

As mentioned in chapter 2.1, in nature the formation of organic-inorganic compound materials is controlled by different processes like macromolecular or interface mediated growth. [5, 30, 31] These materials, grown in organisms, exhibit properties which are optimized for special needs.[13–16] Getting insight into the interface controlled growth could yield knowledge important for thin film applications. For instance, the controlled nucleation of iron oxide at interfaces could help to develop membranes with magnetic properties by choosing a distinct iron oxide polymorph. Further, adjusting the film thickness or its lateral homogeneity allows to influence the elastic properties of the membranes.[165]

In order to learn about the important factors which govern the interfacial growth of inorganic thin films, the formation of iron containing aggregates is investigated at Langmuir layers. These layers are regarded as model systems for membranes of living organisms although these amphiphilic molecules form only monolayers at the water air interface.[166, 167] In order to vary the interfacial properties, Langmuir layers with different types of headgroups were used and the influence on the film formation process was studied. In addition, the influence of the oxidation state of iron ions on the film growth was investigated by using different subphases. It is known for different ion species with oxidation states ranging from 1^+ up to 3^+ that they interact differently with Langmuir layers.[35, 36, 168–170] The condensed phase of a Langmuir layer can be observed even at larger areas per molecule. The surface potential and the layer transferability to solid substrates are also affected by the metal ions in the subphase.[171–176] X-ray absorption spectroscopy measurements on water air interfaces of solutions containing Pb^{2+} ions revealed the binding of this metal ions by a polynuclear complex to Langmuir layers having carboxylate headgroups.[37] Supplementary ions of different elements with the same oxidation state exhibit a varying interaction with Langmuir layers which cannot be explained by the pure charge showing the configuration of the electronic shell has to be considered.[168, 171, 177] In order to investigate if the formation process is altered as the oxidation state of the ions in solution is changed, subphases containing either iron(II) chloride or iron(III) chloride were used, respectively. But also the concentration of the single reactants will have great influence on the formation process as this parameter directly influences supersaturation levels needed for the nucleation together with pH value in the solutions. Further the sample preparation is crucial as it is not clear if the spreading of a monolayer film on an iron salt solution is different to the addition of an iron solution under an already assembled monolayer. The mentioned aspects show the extent of the parameter space which makes this system very complex. The line of action in this study was to make a comprehensive survey on the controllable parameters which

might influence the nucleation process. Most studies on this field of science make use of ex-situ techniques like e.g. scanning electron microscopy and transmission electron microscopy. These techniques are critical since an influence of the sample preparation e.g. drying or heat treatment can not be ruled out. The X-ray techniques permits to investigate the sample system in its real environment without disturbing the interface.

In the first part of this chapter, the film growth using an iron(III) chloride solution in combination with different types of Langmuir layers is discussed. Following this, studies on diluted solutions containing iron(II) chloride in combination with different Langmuir layers are reported. This part is continued by the investigation of the formation of aggregates using higher iron(II) chloride salt concentrations. In the following, the results of the investigations of the thin film growth under membranes composed of polysiloxane networks are shown. The chapter is closed by a summery of the results obtained on the different sample systems.

5.1. Subphases containing iron(III) chloride

In the following chapter, the investigations on iron(III) chloride solutions will be presented. The sample system was investigated by XRR, GID and XAFS measurements. These experiments were performed at different beamlines of the synchrotron light sources ESRF, Grenoble and DORIS III, Hamburg. The experimental end-stations along with the available techniques are summarized in table 5.1 and the setups were described in chapter 3. The sample preparation and the experimental procedure is described in chapter 3.9. As mentioned in chapter 2.1 by solving iron(III) chloride in aqueous solution the Fe^{3+} ions form different compounds and are not present as sole ions at the pH regime used in the investigations. A detailed description is given in chapter 2.1.

5.1.1. Experimental Results

In a first step the iron(III) chloride concentration of the subphase was varied in order to find ideal parameters for the experiments. Subphases with a concentration of $8\ \mathrm{mmol/L}$ were prepared and the initial state was characterized by XRR experiments. Four vials containing a $3\ \mathrm{wt\%}$ ammonia solution were placed inside the sample cell in order to trigger the precipitation reaction. This resulted in a fast formation process of a rough layer, which could be seen by the bare eye. The concentration of iron(III) chloride was then lowered to $1\ \mathrm{mmol/L}$. Using this concentration, the formation process was slowed down and the increase of the interfacial roughness was not too strong during the formation process. As a consequence XRR and GID measurements reported in this chapter were performed at an iron(III) chloride concentration of $1\ \mathrm{mmol/L}$. The concentration of ammonia in the air was measured by diffusion tubes (ISO 9001 purchased from Dräger) yielding a maximal concentration of 100 ppm during the experiments.

In a next step the influence of the surface pressure on the film formation process was probed. Since experiments on the growth of calcite single crystals showed the need for a sufficient surface pressure for a successful nucleation.[56] Stearic acid monolayers were spread on the interface

experimental end station	synchrotron light source	technique
A1	DORIS III	XANES/EXAFS
BW1	DORIS III	XRR/GID
ID10B	ESRF	XRR/GID

Table 5.1.: Experimental end-stations used for the investigation of solution containing iron(III) chloride with a concentration $1\ \mathrm{mmol/L}$ and $100\ \mathrm{mmol/L}$

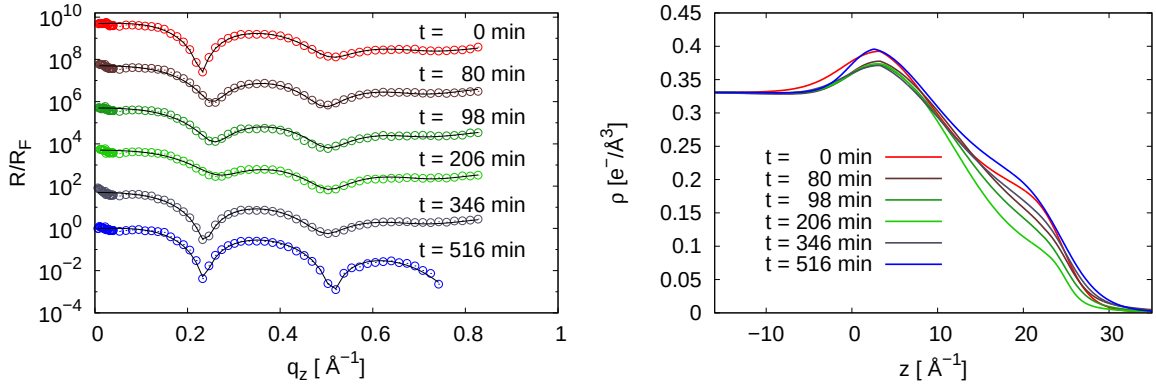

Figure 5.1.: Left: Fresnel normalized XRR curves obtained on stearic acid spread on an iron(III) chloride surface. The surface pressure was adjusted to $\Pi = 10\ \mathrm{mN/m}$. Right: Electron densities obtained by the refinement of the XRR data. After a time of 80 minutes ammonia was added.

of an iron(III) chloride solution having a concentration of $1\ \mathrm{mmol/L}$. The film was compressed to a surface pressure of $\Pi = 10\ \mathrm{mN/m}$ which was maintained constant during the experiment. After the initial state was characterized, ammonia was added (80 minutes after preparation). The Fresnel normalized XRR data are shown in figure 5.1 and were refined using a density model consisting of two layers. The obtained electron density profiles are shown in figure 5.1 as a function of evolution time. The profiles show a decrease of the electron density predominantly in the tailgroup region upon addition of ammonia. This process stops after 206 minutes and the electron density recovers. The data show no evidence of an aggregation of additional material at the interface.

The next experimental series was conducted with a surface pressure of $\Pi = 20\ \mathrm{mN/m}$. After the initial state was characterized by XRR ammonia was added to the gas phase. In the following, the evolution of the system was monitored. The Fresnel normalized reflectivities along with the refined theoretical curves and the obtained electron density profiles are shown in figure 5.2. After addition of ammonia an increase of the electron density in the headgroup region can be identified. With ongoing time, this effect becomes more pronounced accompanied by a growth of the layer towards the subphase. The data reflects the penetration of the Langmuir film by additional material thereby disturbing its structure. These experiments indicate the need for a surface pressure of $\Pi = 20\ \mathrm{mN/m}$ for a successful aggregation of iron containing aggregates. As a result of these observations a surface pressure of $\Pi = 20\ \mathrm{mN/m}$ was chosen for all following experiments.

Figure 5.3 shows the Fresnel normalized XRR data recorded at different times after preparing a DPPA film having an anionic headgroup on a subphase of an iron(III) chloride solution with

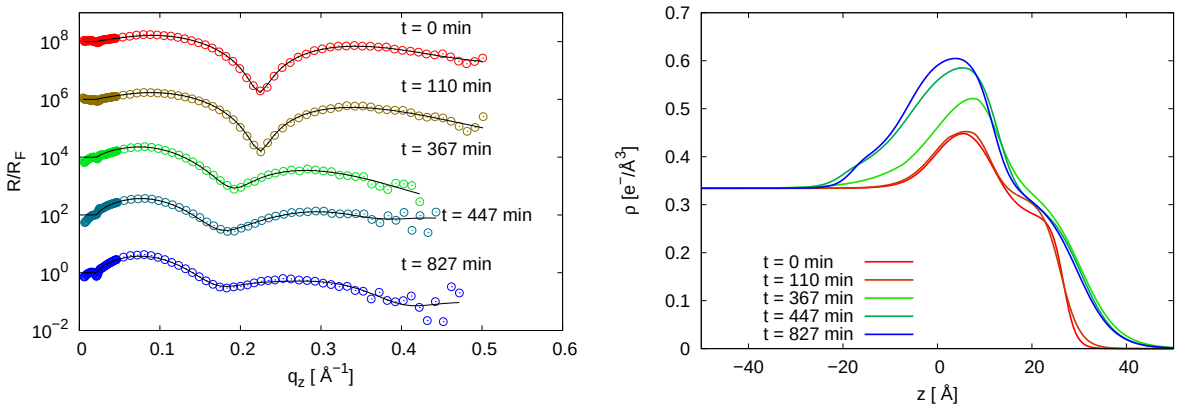

Figure 5.2.: Left: Fresnel normalized reflectivities from monolayers of stearic acid on iron(III)chloride subphases with a concentration of 1 mmol/L. Ammonia was added after a time of t = 55 min. The reflectivities are shifted vertically for clarity. Right: Electron density profiles.

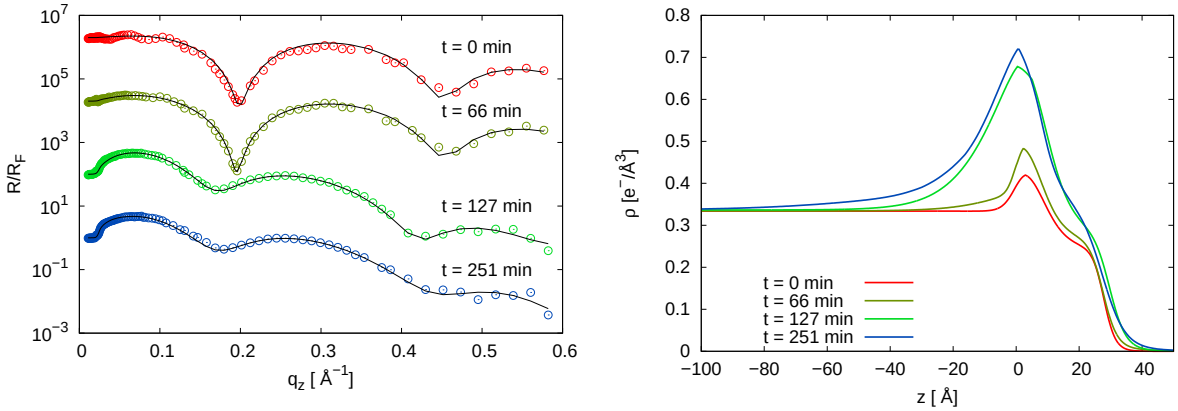

Figure 5.3.: Left: Fresnel normalized reflectivities from monolayers of DPPA on iron(III)chloride subphases with a concentration of 1 mmol/L. Ammonia was added after a time of t = 64 min. The reflectivities are shifted vertically for clarity. Right: Electron density profiles.

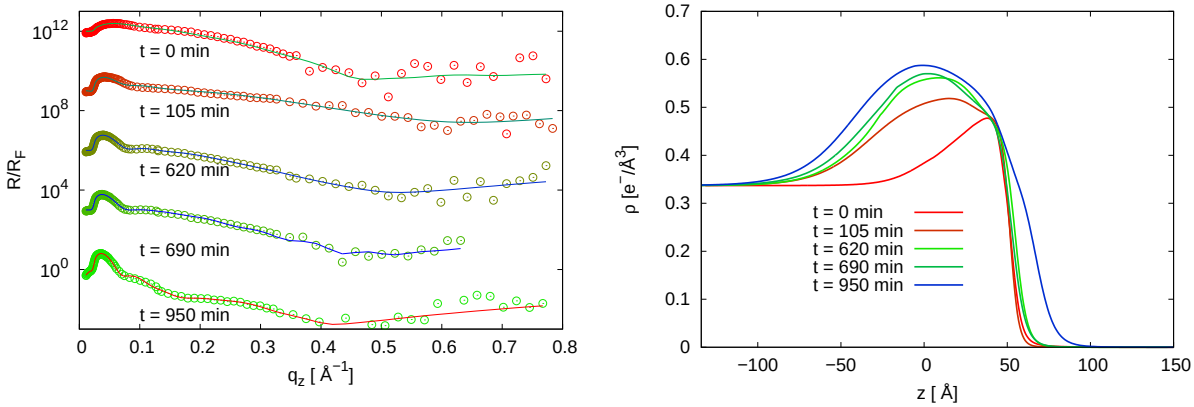

Figure 5.4.: Left: Fresnel normalized reflectivities from monolayers of EPC on iron(III)chloride subphases with a concentration of 1 mmol/L. Ammonia was added after a time of t = 693 min. The reflectivities are shifted vertically for clarity. Right: Electron density profiles.

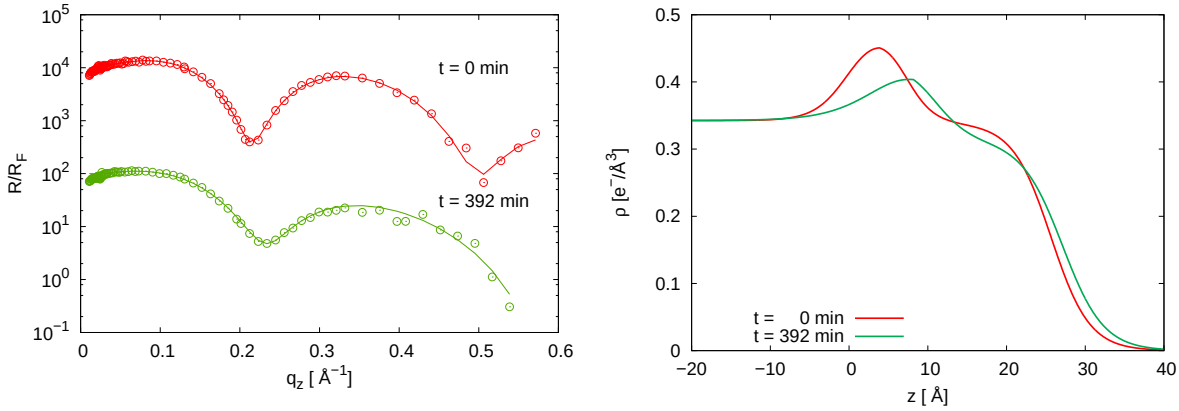

Figure 5.5.: Left: Fresnel normalized reflectivities from monolayers of DPPC on iron(III)chloride subphases with a concentration of $1\ \mathrm{mmol/L}$. Ammonia was added after a time of t = 50 min. The reflectivities are shifted vertically for clarity. Right: Electron density profiles.

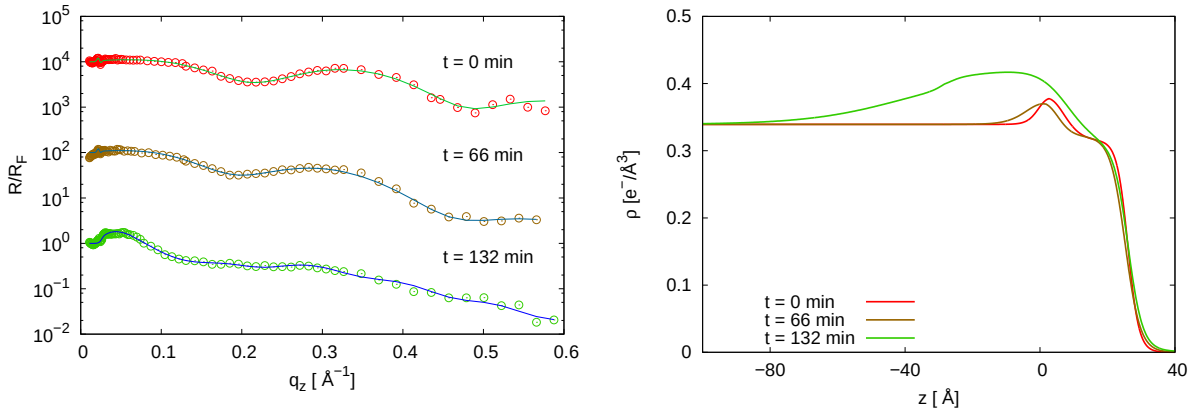

Figure 5.6.: Left: Fresnel normalized reflectivities from monolayers of stearyl alcohol on iron(III)chloride subphases with a concentration of $1\ \mathrm{mmol/L}$. Ammonia was added after a time of t = 110 min. The reflectivities are shifted vertically for clarity. Right: Electron density profiles.

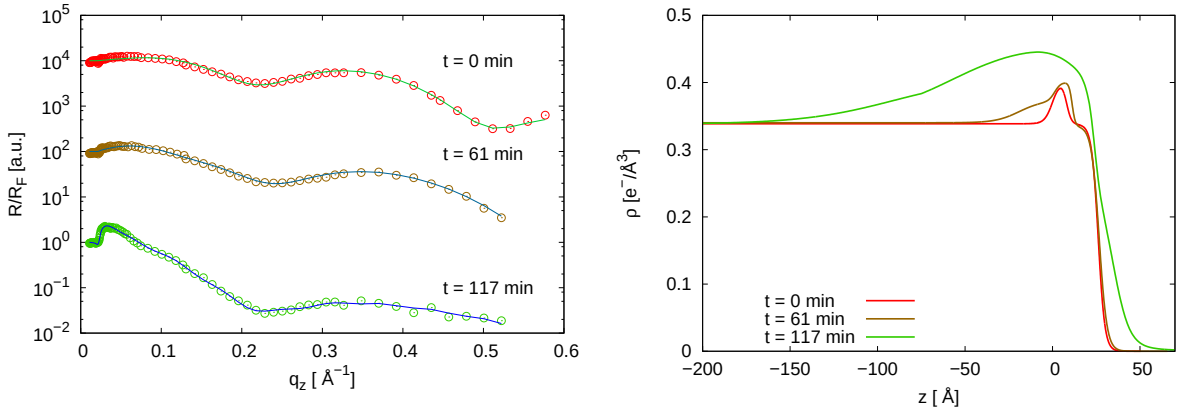

Figure 5.7.: Left: Fresnel normalized reflectivities from monolayers of stearyl amide on iron(III)chloride subphases with a concentration of $1\ \mathrm{mmol/L}$. Ammonia was added after a time of t = 60 min. The reflectivities are shifted vertically for clarity. Right: Electron density profiles.

a concentration of $1\ \mathrm{mmol/L}$. Ammonia was added after 64 minutes. After 127 minutes a change in the reflectivities can be observed as the intensity for low q_z increases. This process is accompanied by a change in the oscillation period. Figure 5.3 shows the electron density profiles obtained by the refinement of the XRR data. The data show the evolution of a 40 Å thick layer at the liquid-gas interface. It should be noted that the DPPA layer is still present at this stage. Nevertheless, no clear distinction can be made between the Langmuir layer and the material aggregating at the interface. Thus, additional material penetrates the Langmuir layer. This effect is most pronounced in the region of the anionic headgroups.

Further, the phospholipid EPC was employed as a Langmuir film possessing a cationic headgroup. The Fresnel normalized reflectivity curves shown in figure 5.4 exhibit already in the beginning (t = 0) an increase of intensity for low q_z. This indicates an enrichment of material with a high electron density just after the deposition of the amphiphiles. This can be better seen in the electron density profiles obtained by the refinement of the XRR data shown in figure 5.4. The layer has a thickness of 50 Å without the addition of ammonia. Thus, an electrostatic repulsion of the iron ions by the headgroups is not observed. The aggregation dies down after 620 minutes where a layer with a thickness of 160 Å has been formed. Hence, after 693 minutes ammonia was added in order to check if the film growth process can be continued by increasing the pH value in the subphase. The surface pressure up to this point was constant and as ammonia was added a strong decrease of the pressure happened. In order to maintain the surface pressure at $\Pi = 20\ \mathrm{mN/m}$ the accessible area for the amphiphiles had to be decreased by $18\ \%$. The electron density profile of this final state shows an increase of the interfacial roughness and thickness.

In contrast to this, the zwitter-ionic DPPC Langmuir layer deposited on iron(III) chloride solution exhibits no film formation. Figure 5.5 shows the electron densities and XRR data. Only the disturbance of the monolayer structure is visible. The observations made in relation to stearic acid hinted that the used surface pressure of $\Pi = 20\ \mathrm{mN/m}$ might be too low to induce aggregation of iron compounds at the DPPC Langmuir film. Therefore experiments with an elevated surface pressure of $\Pi = 40\ \mathrm{mN/m}$ were performed. These experiments also showed no aggregation at the liquid-air interface, see appendix figure B.1. Accordingly, the zwitter-ionic layer seems to suppress the enrichment of material at the interface but precipitates could be observed after the experiment.

Two further investigated Langmuir layers of stearyl alcohol and stearyl amide both having non-ionic headgroups show layer formation at the liquid-gas interface as ammonia is added, see figure 5.6 and figure 5.7. The respective Langmuir film structure is indistinguishable in the end state from the grown film.

In the case of stearyl amide in the beginning an aggregation of additional material at the headgroups is observed without disturbing the vertical layer structure. With ongoing time a progressively growth towards the subphase can be viewed as well as a blurring of the Langmuir layer structure by the penetration of aggregates.

Figure 5.8 shows the GID scans from Langmuir layers on top of iron(III) chloride solutions. All scans were performed in between the XRR experiments at a surface pressure of $\Pi = 20$ mN/m.

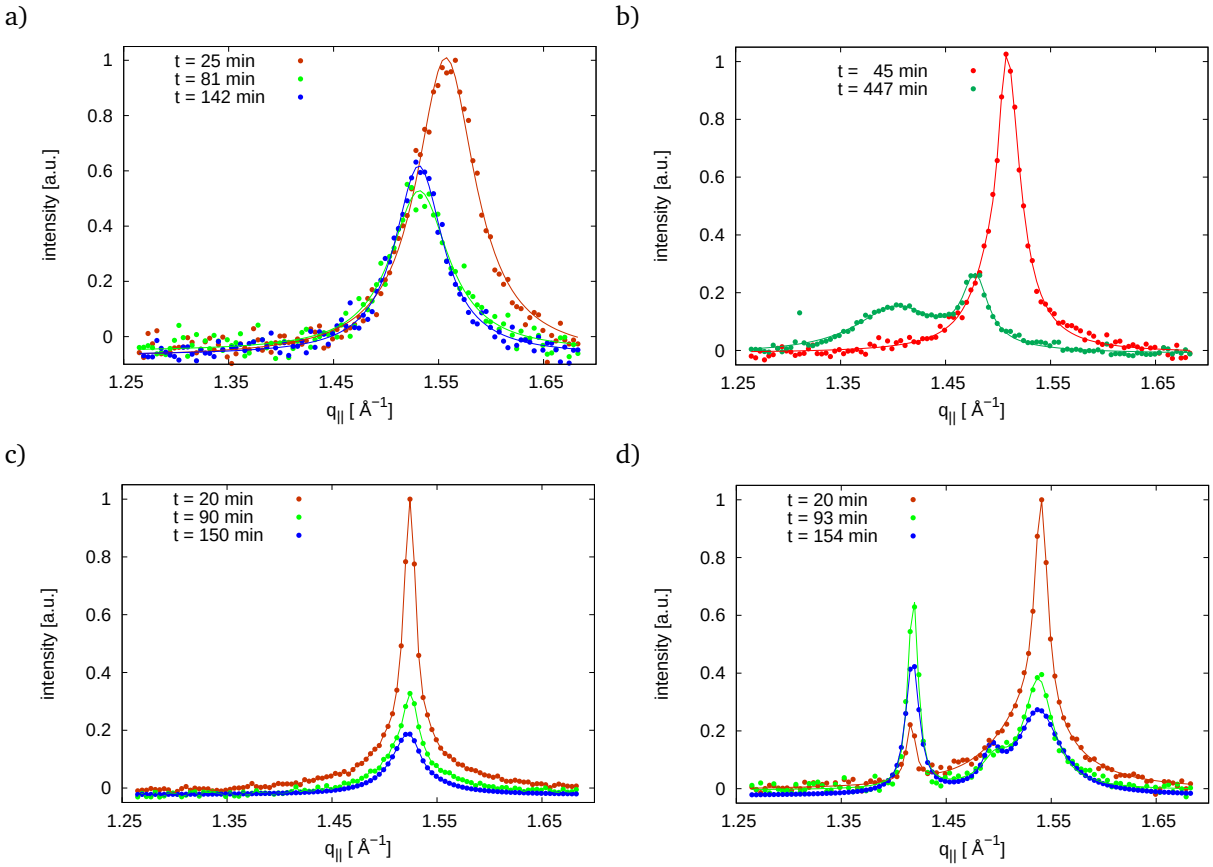

Figure 5.8.: Grazing incidence diffraction measurements from monolayers on iron(III) chloride solutions. The surface pressure for all measurements was $\Pi = 20$ mN/m. Points represent the measured data, lines are the corresponding refinements. a) DPPA, ammonia was added after a time of t = 64 min. b) DPPC, ammonia was added after a time of t = 50 min. c) stearyl alcohol, ammonia was added after a time of t = 60 min. d) stearyl amide, ammonia was added after a time of t = 60 min.

The structural parameters of the films extracted from GID scans are summarized in table 5.2. The GID data for the EPC is not shown due to the lack of any Bragg reflection.

The diffraction patterns acquired from Langmuir layers of DPPA are shown in 5.8a. The data suggests the organization of the Langmuir layer in a hexagonal unit cell. Upon the addition of ammonia, the lateral reflection shifts to a lower wave vector of $q_{||} = 1.531$ Å^{-1} accompanied by a decrease of the intensity. The slight shift of the Bragg reflection shows the change of the lattice constant from (4.66 ± 0.01)Å to (4.73 ± 0.01)Å. The size of the crystalline domains is about 150 Å. By comparing the obtained data with the reference measurements (chapter 4.2.4) a different behavior can be observed. The increased tilt of the tailgroup induced by ammonia observed for the water subphase is suppressed on an iron(III) chloride subphase. In principle two different mechanisms can explain this observation. The iron(III) chloride subphase has a lower pH value compared to the pure water subphase thus, the pH value of the solution, which increases due to ammonia diffusing from the air phase towards the solution, could be too low to induce the tilting. Another explanation is the interaction of the iron species with the Langmuir layer stabilizing the lateral structure. An interaction between an anionic phospholipid or anionic fatty acid with complexes formed by Fe^{3+} ions was observed at pH values above 2.[168, 177] Due to the presence of the iron complexes, the surface pressure needed to reach a phase were

the hydrocarbon tails were not tilted was significantly lowered.

In the case of the DPPC monolayer, where no film growth was observed, the GID scan shows a change in the tilt angle of the Langmuir layer tailgroup after addition of ammonia, see figure 5.8b. The Langmuir layer structure can be described in the beginning by a hexagonal unit cell. After ammonia is added a transition to a centered rectangular cell can be observed. The repulsion between the headgroups increases and the distance between the single amphiphiles increases. The area per molecule increases from 19.58 Å^2 to 22.3 Å^2. Due to this, the tail groups are able to tilt towards the water surface. The full width of half maximum of the reflection at $q_{||} = 1.508$ Å^{-1} slightly decreases indicating an increasing size of the crystalline domains from (339 ± 6)Å) to (364 ± 7)Å). From this data the tilt angle of the tailgroup of the amphiphiles can be extracted. The analysis of the Bragg rods is shown in the appendix paragraph A. In the beginning the tails are in the upright position with a tilt angle of $\tau = 0°$ which increases by the addition of ammonia to $\tau = (28.0 \pm 0.2)°$. The reference measurements described in chapter 4.2.5 show significant difference to this data prior to the addition of ammonia. The observed final states for DPPC on pure water subphases and subphases containing iron(III) chloride are the same within the errors. In the case of pure water subphases the tails are tilted right from the beginning. The difference can be ascribed to the pH value in the subphase.[178] Due to the low pH value of the iron(III) chloride solutions the repulsion between the headgroups is diminished leading to a closer arrangement of the amphiphilic molecules. Ammonia diffusing from the air phase into the interfacial region increases the pH value, thus, resulting in an increased repulsion and expansion of the layer. By this the repulsion is increased and the layer expands. As a consequence the hydrocarbon tailgroup tilts towards the solution surface.

The lateral structure of the stearyl alcohol Langmuir film shows only minor changes as ammonia is added. Only the intensity of the reflection decreases. This behavior is similar to the reference measurements on pure water subphases. By this it can be concluded that the observed slight changes in the lateral structure are a result of ammonia.

The GID measurements from the stearyl amide monolayer are shown in 5.8d. Here, a continuous change of the film from a centered rectangular phase towards an oblique lattice is observable with the ongoing growth process. In the initial state an orthorhombic phase can be seen as indicated by the two reflections at $q_{||} = 1.416$ Å^{-1}, $q_z = 0.174$ Å^{-1} and $q_{||} = 1.530$ Å^{-1}, $q_z = 0$ Å^{-1} which can be indexed as the degenerated (1,1),(1,$\bar{1}$) and the non degenerated (0,2) reflections. The hydrocarbon tails are tilted by $8.3°$ from the surface normal. The Bragg rod analysis is shown in the appendix in paragraph A. After the film formation is induced, a third reflection appears at $q_{||} = 1.497$ Å^{-1}, $q_z = 0.9$ Å^{-1} showing the transformation of the unit cell towards an oblique phase. Starting at low $q_{||}$ the reflections can be indexed in the following order (0,1), (1,0) and (1,1). In case of an oblique unit cell all reflections are moved out of the horizontal plane having an $q_z \neq 0$ component. The determination of the q_z position of the maximum in the single Bragg rods for this sample system was not possible. The maxima of the Bragg rods lie very close to the horizontal plane and therefore the calculation of the tilt was not possible with reliable results.[1] However, the area per molecule can be deduced from the $q_{||}$ position to be A_{xy}

[1] See chapter 3.10, a determination of the q_z position of maximum in Bragg rod would have a high error. A reliable conclusion is thus not possible.

DPPA (anionic)	t = 25 min	t = 81 min	t = 142 min
lattice type	hexagonal	hexagonal	hexagonal
lattice constant a[Å]	4.66 ± 0.05	4.73 ± 0.05	4.73 ± 0.05
lattice constant b [Å]	-	-	-
unit cell size A_{xy} [Å^2]	18.8 ± 0.3	19.3 ± 0.2	19.3 ± 0.2
area per molecule A_0 [Å^2]	18.8 ± 0.3	19.3 ± 0.2	
tilt τ[°]	0	0	0
DPPC (zwitter-ionic)	t = 45 min	t = 447 min	
lattice type	hexagonal	centered rectangular	
lattice constant a [Å]	4.65 ± 0.05	8.50 ± 0.05	
lattice constant b [Å]	5.25 ± 0.05	-	
unit cell size A_{xy} [Å^2]	19.58 ± 0.3	45.6 ± 0.2	
area per molecule A_0 [Å^2]	19.58 ± 0.3	22.8 ± 0.2	
tilt τ[°]	0	28 ± 0.2	
stearyl alcohol (non-ionic)	t = 20 min	t = 90 min	t = 150 min
lattice type	hexagonal	hexagonal	hexagonal
lattice constant a[Å]	4.76 ± 0.05	4.76 ± 0.05	4.77 ± 0.05
lattice constant b[Å]	-	-	-
unit cell size A_{xy} [Å^2]	19.6 ± 0.3	19.6 ± 0.2	19.7 ± 0.2
area per molecule A_0 [Å^2]	21.4 ± 0.3	21.4 ± 0.2	21.3 ± 0.4
tilt τ[°]	0	0	0
stearyl amide (non-ionic)	t = 20 min	t = 93 min	t = 154 min
lattice type	centered rectangular	oblique	oblique
lattice constant a[Å]	8.14 ± 0.05	4.22 ± 0.05	4.21 ± 0.05
lattice constant b[Å]	4.43 ± 0.05	4.43 ± 0.05	4.42 ± 0.05
unit cell size A_{xy} [Å^2]	42.8 ± 0.3	20.4 ± 0.8	20.8 ± 0.5
area per molecule A_0 [Å^2]	21.4 ± 0.3	20.4 ± 0.8	20.8 ± 0.5
tilt τ[°]	8.3 ±0.4	-	-

Table 5.2.: Properties of Langmuir films on iron(III) chloride subphases determined by evaluation of the GID scans.

$= 20.8$ Å.

Nevertheless the reference measurement on water subphases showed no transition of the crystal lattice from the centered rectangular phase towards an oblique phase. It can be concluded that the iron(III) chloride subphase is responsible for this behavior.

For all these systems studied no reflections from crystalline iron oxide or hydroxide species were observable indicating the formation of amorphous aggregates. A decrease of the scattered intensity of the reflection originating from the lateral Langmuir layer structure was visible in all measurements showing that the aggregation process goes simultaneously with the degeneration of the Langmuir films.

In order to gain insight into the structure of the forming layers in-situ XAFS experiments at the iron K-edge were performed at the beamline A1, DORIS III, Germany. The experiments investigated the thin film growth at stearyl alcohol and stearic acid layers with iron(III) chloride concentrations ranging from $1\ \mathrm{mmol/L}$ up to $100\ \mathrm{mmol/L}$. In the first step XAFS data were acquired at bare interfaces of $1\ \mathrm{mmol/L}$ and $100\ \mathrm{mmol/L}$ iron(III) chloride solutions as references. The data show no change in the structure of the iron K-edge upon the addition of ammonia, see appendix figure B.2 and figure B.3, respectively. In the next step samples were prepared with stearyl alcohol present at the interface. As already pointed out XRR measurements proved the formation of 150 Å thick layers using $1\ \mathrm{mmol/L}$ iron(III) chloride solutions. The XANES spectra obtained on this sample system showed no change in the near-edge structure in the presence of ammonia neither for concentrations of $1\ \mathrm{mmol/L}$ nor for concentrations of $100\ \mathrm{mmol/L}$, see appendix figure B.4 and figure B.6. Nevertheless EXAFS scans were performed on these samples and were processed with the program package ATHENA.[140] The Fourier transformed EXAFS signal χ(R) is displayed in figure 5.10. The obtained data showed the existence of only one coordination shell in a distance of 1.5 Å for both concentrations. After ammonia is added the coordination shell does not change. By considering XAFS data obtained by Suzuki et al. the first shell of iron hydroxides (lepidocrocite and goethite) can be found at a distance of roughly 2 Å hosting six oxygen atoms.[179, 180] The different value of the distance of the first coordination shell is due to the fact that no phase correction was performed. This phase correction was not performed because in a mixture of elements with unknown composition the phase shift is determined by the chemical element which scatters the photo electron. This is not taken into account by ATHENA. The program is only capable to do a phase correction for materials composed of one single atom type. However, comparing the obtained data to literature the peak at 1.5 Å is a common feature of iron compounds showing the first coordination shell with oxygen atoms.[94, 179, 181–183]

The investigations of subphases of $1\ \mathrm{mmol/L}$ iron(III) chloride solutions in combination with stearic acid monolayers show no change in the structure of the absorption edge during the aggregation, see appendix figure B.5. In the following the experiment was repeated with an elevated concentration of $100\ \mathrm{mmol/L}$. These spectra are depicted in figure 5.11 showing a change in the near-edge structure of the iron K-edge. A further feature develops at 7.14 keV and the intensity of the pre-edge at 7.11 keV increases. This indicates a change in the type of coordination of the iron atom.

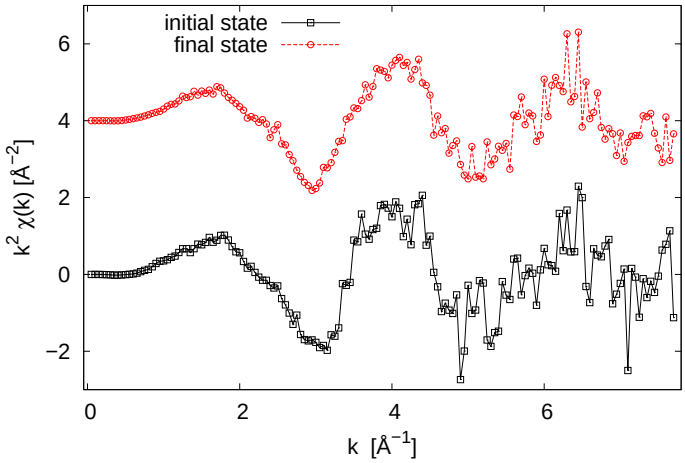

Figure 5.9.: EXAFS signal of the iron K-edge from samples of an iron(III) chloride subphase with a concentration of $100\ \mathrm{mmol/L}$ with stearyl alcohol monolayers present at the interface.

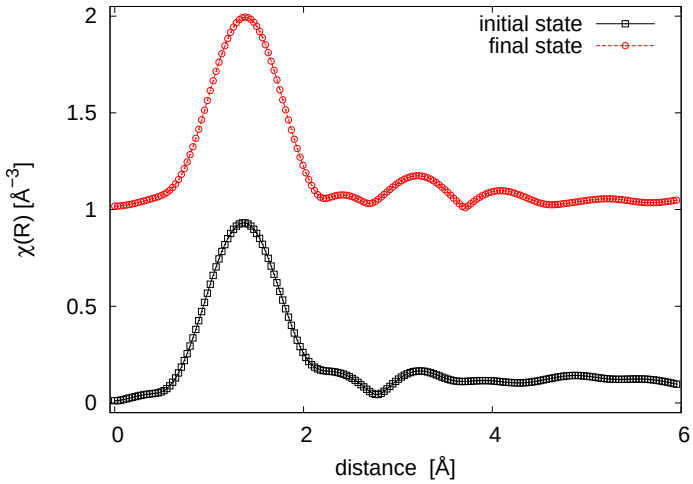

Figure 5.10.: Fourier transformed EXAFS signal of the iron K-edge at samples of an iron(III) chloride subphase with a concentration of $100\ \mathrm{mmol/L}$ with stearyl alcohol monolayers present at the interface.

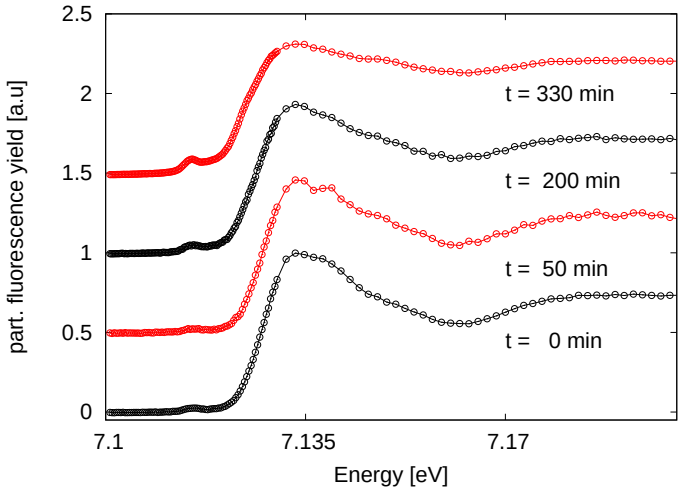

Figure 5.11.: Near-edge structure of the iron K-edge at samples of iron(III) chloride subphases with stearic acid monolayers present at the interface.

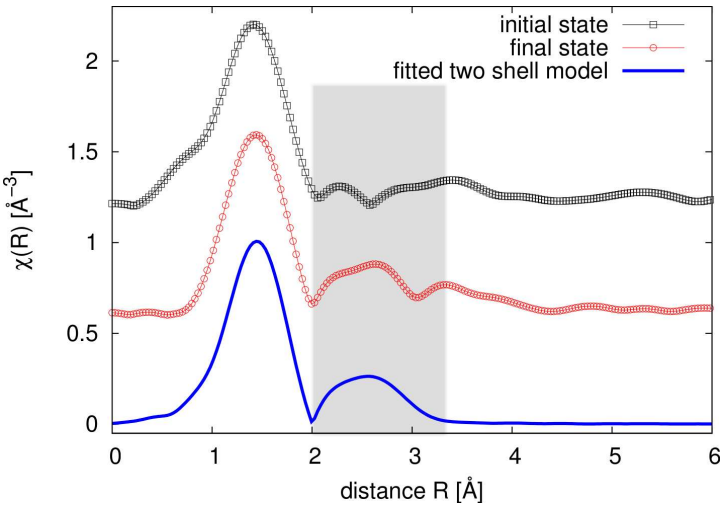

Figure 5.12.: Fourier transformed EXAFS signal of the iron K-edge on samples of a $100\ \mathrm{mmol/L}$ iron(III) chloride subphases with stearic acid monolayers present at the interface. Furthermore the $\chi(K)$ of a fitted model is plotted. This curve is plotted without the phase correction performed by ARTEMIS.

The pre-edge is determined by a 1s-3d transition.[94] The increase of the intensity shows a mixing of the 4p and 3d states due to a non centrosymmetric coordination resulting in an increased possibility for this transition. This hints at an increased amount of non centrosymmetric coordinated iron atoms.

The Fourier transformed EXAFS signals χ(R) extracted from the spectra acquired on the sample system in the initial state (directly after deposition) and the final state (after addition of ammonia) are shown in figure 5.12. By using a stearic acid monolayer in combination with a $100\ \mathrm{mmol/L}$ iron(III) chloride solution the development of a second coordination shell can be observed, indicating an increased order around the iron atom. In order to gain qualitative information a model consisting of two coordination shells was fitted to the data by using the program package ARTEMIS.[140] The model consists of two coordination shells, the first is occupied by oxygen the second by iron atoms. First only the coordination shell hosting the oxygen was fitted. After satisfactory agreement was achieved in the R-range from 0 Å to 2 Å a second coordination

shell was added with iron atoms. The resulting fit is depicted in figure 5.12 showing still a difference compared to the experimental curve. The s_0^2 was estimated by reference measurements of magnetite to be 0.68. The first coordination shell was determined to be at a phase corrected distance of 1.92 Å. The distance of the second coordination shell was determined to be 3.03 Å and the value of the mean iron content to be 2 ± 0.3 iron atoms. For comparison in the hematite structure 5 iron atoms are present in the second coordination shell.[179]

5.1.2. Conclusion

XRR measurements revealed the layer formation of aggregates containing iron under different interfaces which are modified with cationic, anionic and non-ionic amphiphiles. The film growth is only inhibited at the interface of the zwitter-ionic amphiphil DPPC. The observed changes for this sample can be attributed to a change in the pH value. The XRR measurements hint at an aggregation of small particles at the liquid air interface as the observed electron densities are lower than closed layers of common iron hydroxides or oxides. Indications for such a behavior were also observed by optical ex-situ studies where the growth of small particles at the interface was reported.[184]

The GID measurements show stable Langmuir layers at the interfaces during the aggregation process. Especially for DPPA, a stabilizing effect on the structure of the Langmuir layer was observed during the growth process if ammonia was present. On iron(III) chloride solutions, the DPPA film changes the unit cell parameters only slightly. Because the pK_A value for DPPA is 2.1 it can be concluded that the headgroup is fully deprotonated on the iron(III) chloride solution (pH 3) leading to a negatively charged interface attracting positively charged ions and complexes.[185] This leads to the assumption that the iron complexes nucleate at the interface and interact with the Langmuir layer. This is in agreement to the reports of Wang et al. on the interaction of iron(III) complexes with negatively charged Langmuir monolayers.[168, 177] In these experiments, a pH dependence of the interaction was observed which was explained by the formation of iron complexes forming covalent bonds with the carboxylate headgroups influencing the Langmuir layer structure.

For DPPC, a transition from an untilted phase towards a tilted phase is visible. This effect is caused by the change of the pH value in the subphase which was also observed for other Langmuir layers e.g. fatty acids.[178] No effect of the iron(III) chloride solution on the Langmuir layer was observed as the lateral structure after the addition of ammonia is similar to the structure on water. For stearyl amide a structural change of the monolayer caused by the aggregation process could be seen. The transformation from an orthorhombic towards an oblique unit cell is influenced by the presence of an evolving inorganic layer leading to a different lateral structure. This effect is clearly induced by the presence of iron species because reference measurements of this amphiphile on pure water subphases did not show this effect. The lateral structure of Langmuir layers of stearyl alcohol seem to be unaffected by the presence of iron(III) chloride solutions. The decrease in the intensity can be attributed to ammonia disturbing the lateral layer structure.

For all measurements no diffraction signals from any crystal were observed. This might indicate the formation of amorphous material. In order to gain more insight into the structure of the forming inorganic films, in-situ XAS experiments were performed at the solution air interface. These data show that for low iron(III) chloride concentrations the iron atom has only one coordination shell which can be attributed to an iron oxygen coordination.[179] Boyanov et al. have investigated the interaction of Pb^{2+} ions with the carboxylate headgroup of Langmuir layers by XAS.[37] The authors state a covalent binding of polynuclei complexes to the carboxylate headgroup. The insufficient k-range and high noise level in the data presented in this chapter prevent an analysis similar to Boyanov et al.[37] Also, Boyanov at al. used much lower concentrations of 10^{-2} mmol/L decreasing the contribution to the signal from unbound ions in the proximity of the interface. Nevertheless by comparing the data sets of Boyanov and the data presented in this chapter such features as observed in the report are not visible indicating that the scenario proposed for Pb^{2+} is not congruent for iron containing solutions.

As the concentration in the subphase is increased, an ordering occurs in the presence of stearic acid as hinted by the EXAFS data. A second coordination shell evolves indicating an increased order. Further, the XANES data show a change in the coordination of the iron atom as the intensity of the pre-edge increases showing a change to a non centrosymmetric coordination. A qualitative analysis of the EXAFS data shows that the second coordination shell is occupied by 2 ± 0.2 iron atoms in average. Structural data from iron hydroxides show that normally 6 iron atoms can be found in the second coordination shell. This underlines the presence of small aggregates with lacking long range order. Such an effect was not observed for stearyl alcohol where no increase in order occurred. It is speculative that a differing saturation level of iron complexes in the vicinity of the Langmuir layer is responsible for this. Comparing the electron density profiles of stearic acid and stearyl alcohol, the electron density of stearic acid is higher than for stearyl alcohol. By this, a higher saturation level could be achieved enabling a partial crystallization which increases the order around the iron atoms. Nevertheless, this is supported by the fact that the process only occurs in higher iron(III) chloride solutions and cannot be observed by using 1 mmol/L iron(III) chloride solutions.

It might be speculated that in the case of the non-ionic and anionic amphiphiles different aggregation processes are present compared for the cationic Langmuir layers. This can be concluded by the fact that the shape of the layer structures observed by the XRR experiments differs significantly for the different headgroup structures. In case of DPPA and stearic acid, having cationic headgroups, thin films with a high electron density in the vicinity of the Langmuir film are observed, whereas for non-ionic headgroups the thickness of the film is much larger and the electron density is much lower. Furthermore, the XAFS experiments show no second coordination shell by using stearyl alcohol films. For the explanation of this behavior, the iron complexes present in the subphase have to be considered, see chapter 2.1. At anionic Langmuir layers the aggregation of negatively charged iron complex $Fe(OH)_4^{-1}$ might happen forming an inorganic layer where as under cationic Langmuir layers the positively charged complexes might aggregate.

To summarize, the formation of amorphous layers was observed under Langmuir layers with different types of headgroups. Although Mann et al. stated the formation of magnetite from

hydrated iron(III) oxide species in magnetotactic bacteria this process was not observed in this ex-vitro experiments.[24] A surface pressure of $\Pi = 20\ \mathrm{mN/m}$ was necessary to achieve a successful layer formation. Subphases having an iron(III) chloride concentration which is higher than $1\ \mathrm{mmol/L}$ show the growth of macroscopically rough films. Structures without any crystalline character were observed to form at the interfaces. An increase in the short range order of the aggregate structure could be induced by increasing the subphase concentration to $100\ \mathrm{mmol/L}$. Nevertheless, this structure is still far away from a long range ordering. It is reasonable that a much higher iron(III) chloride concentration is needed to induce a successful growth of crystalline structures. However, investigations of such highly concentrated solutions by XRR and XAFS will be complicated by enhanced roughness of the interface.

5.2. Subphases with low iron(II) chloride concentrations

In this chapter the investigation of the aggregation process at Langmuir layers using solutions with a $0.1\ \mathrm{mmol/L}$ concentration of iron(II) chloride is reported. The experiments were performed at the beamline BW1, DORIS III, using the liquid scattering setup described in chapter 3. The Langmuir layers were prepared as described in chapter 3.9. The experiments were performed at a constant surface pressure of $\Pi = 20\ \mathrm{mN/m}$. The phospholipid DPPC (zwitter-ionic), DPPA (cationic) and EPC (anionic) were employed for the investigations, see chapter 2.5.

Water free iron(II) chloride (purity $\geq$ 99 %, Sigma-Aldrich) was applied for the preparation of the solutions using ultra pure water (specific resistance 18.2 MΩ cm). Because the solutions containing the iron(II) chloride are subjected to aging the samples were prepared shortly before the measurements.[186] The subphase pH of the $0.1\ \mathrm{mmol/L}$ iron(II) chloride solution was 4. As mentioned in chapter 2.4 iron(II) ions can form water insoluble iron hydroxide ($Fe(OH_2)$). The amount of $Fe(OH)_2$ formed at this subphase conditions was calculated to be $10^{-8}\ \mathrm{mmol/L}$ by using the solubility product.[187] It can be concluded that mainly positively charged iron(II) ions are present in solution and water insoluble complexes can be ignored.

The study on the investigation of the formation of inorganic films using low concentrations of iron(II) chloride were performed within the collaboration with the group of Prof. Metin Tolan (TU Dortmund) and Prof. Heinz Rehage (TU Dortmund).

5.2.1. Experimental data

In a first step the aggregation of inorganic compounds at the aqueous solution-air interface was studied without a monolayer. The XRR and GID measurements in the presence of ammonia are depicted in figure 5.13. The GID experiments performed on this sample show no diffraction signal from crystalline material. The obtained XRR data can be modeled without a layer yielding an interface roughness of σ =(3.37 $\pm$ 0.09)Å. By comparing this data to values found in literature for the roughness of a water interface of σ = (3.24 $\pm$ 0.05)Å no significant deviation can be observed.[188] Formation of aggregates would result in an increase of the interfacial

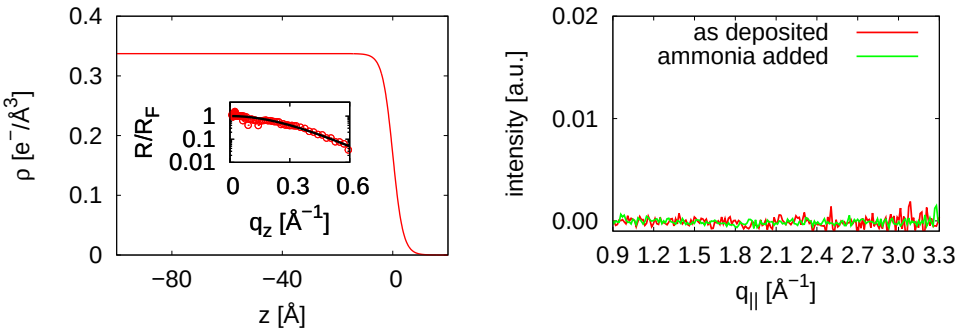

Figure 5.13.: Left: XRR measurements and electron density profile of an iron(II) chloride subphases with a concentration of $0.1\ \mathrm{mmol/L}$ after the addition of ammonia. Right: GID measurements of the iron(II) chloride subphase with a concentration of $0.1\ \mathrm{mmol/L}$.

roughness, thus this data demonstrates that no formation of aggregates occurs at the solution-air interface by using this subphase concentration.

In the next step the interface was modified by different types of Langmuir layers. Figure 5.14 shows the XRR data recorded from the samples. The XRR data obtained on EPC show a shift of the first minimum to lower q_z values upon addition of ammonia (figure 5.14a). The electron density profiles which are obtained from the data are given in figure 5.15a and show an increase of the length of the tailgroup of 2 Å after 619 minutes. These observations are in agreement with measurements on a pure water subphase after the addition of ammonia. Thus, the changes in the electron density curves can be attributed to ammonia. No influence due to the iron(II) chloride solution can be noticed.

The XRR data and electron density profiles obtained from DPPC monolayers are shown in 5.14b and 5.15b. These data reflect the disturbance of the Langmuir layer upon addition of ammonia which is in agreement to the reference measurements (see chapter 4.2.5). In the beginning the electron density profiles show the characteristics of a DPPC layer. After ammonia is added the structure gets smeared out.

A completely different behavior can be observed when using DPPA Langmuir layers. The XRR curves are depicted in figure 5.14c and show an increase of the reflected intensity for small q_z values indicating the enrichment of material with a higher electron density at the interface upon the addition of ammonia (t = 64 min). Furthermore a slight shift to larger q_z values of the minima can be seen. In order to keep the surface pressure constant at Π=$20\ \mathrm{mN/m}$ the accessible area of the amphiphiles had to be reduced during the experiment. The minimal area was reached during the third XRR measurement and the surface pressure decreased to Π= $12.7\ \mathrm{mN/m}$. Nevertheless a fourth reflectivity was recorded still showing oscillations. The decrease of the surface pressure Π can be attributed to a loss of amphihpiles from the interface. The electron density profiles are depicted in figure 5.15c. In the initial state the structure of the Langmuir layer can be seen. After ammonia is added an increase of the electron density can be observed. In this state the structure of the Langmuir layer is clearly evident. With ongoing time the growing inorganic film and the Langmuir layer can not be distinguished anymore (t = 98 min). The tails of the DPPA layer can only be seen as a shoulder at z = 25 Å.

After the XRR measurements a GID scan was performed on the DPPA sample shown in figure

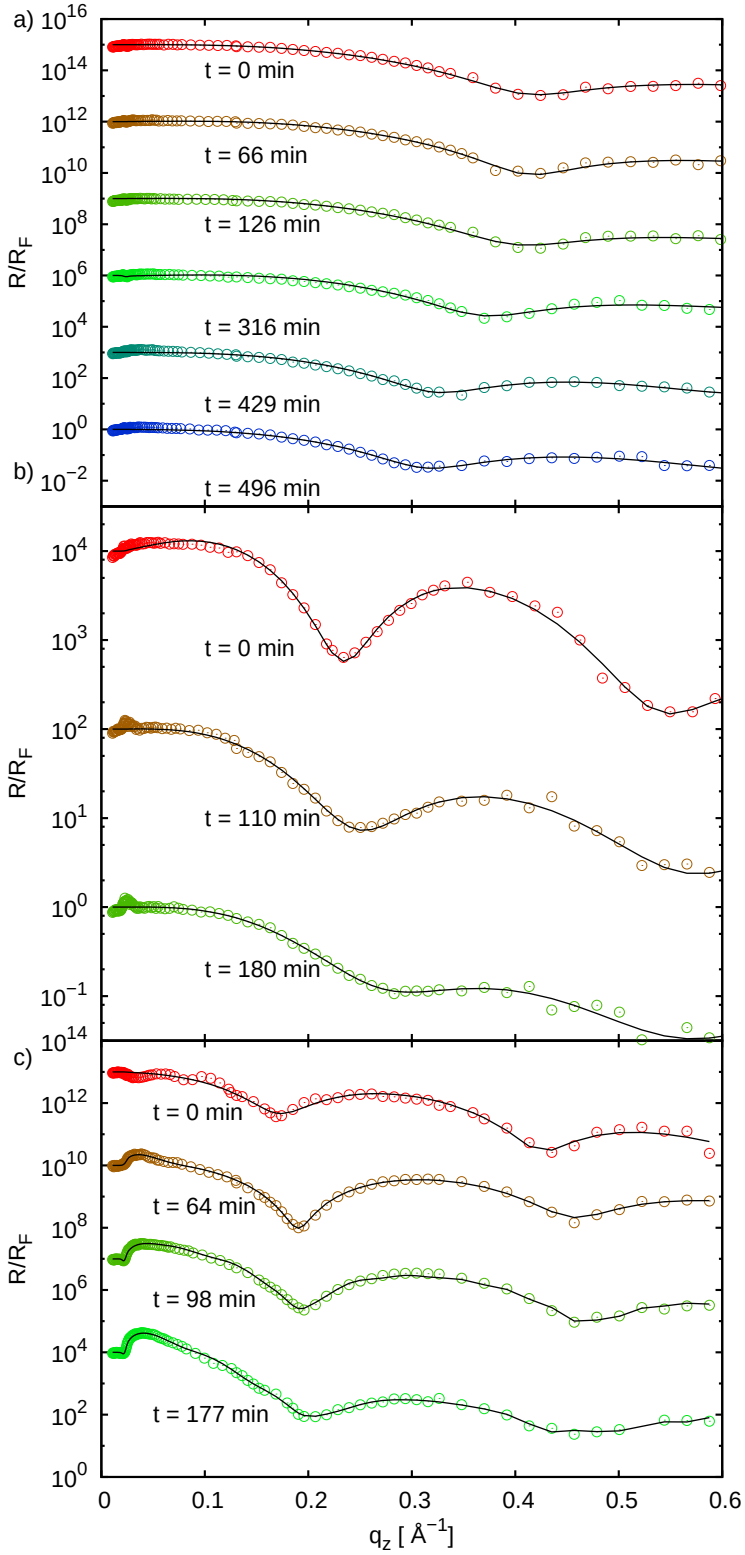

Figure 5.14.: XRR data acquired on subphases of iron(II) chloride solutions with different phospholipid Langmuir layers. a) EPC, ammonia added after t = 66 min. b) DPPC, ammonia added after t = 100 min. c) DPPA, ammonia added after t = 64 min.

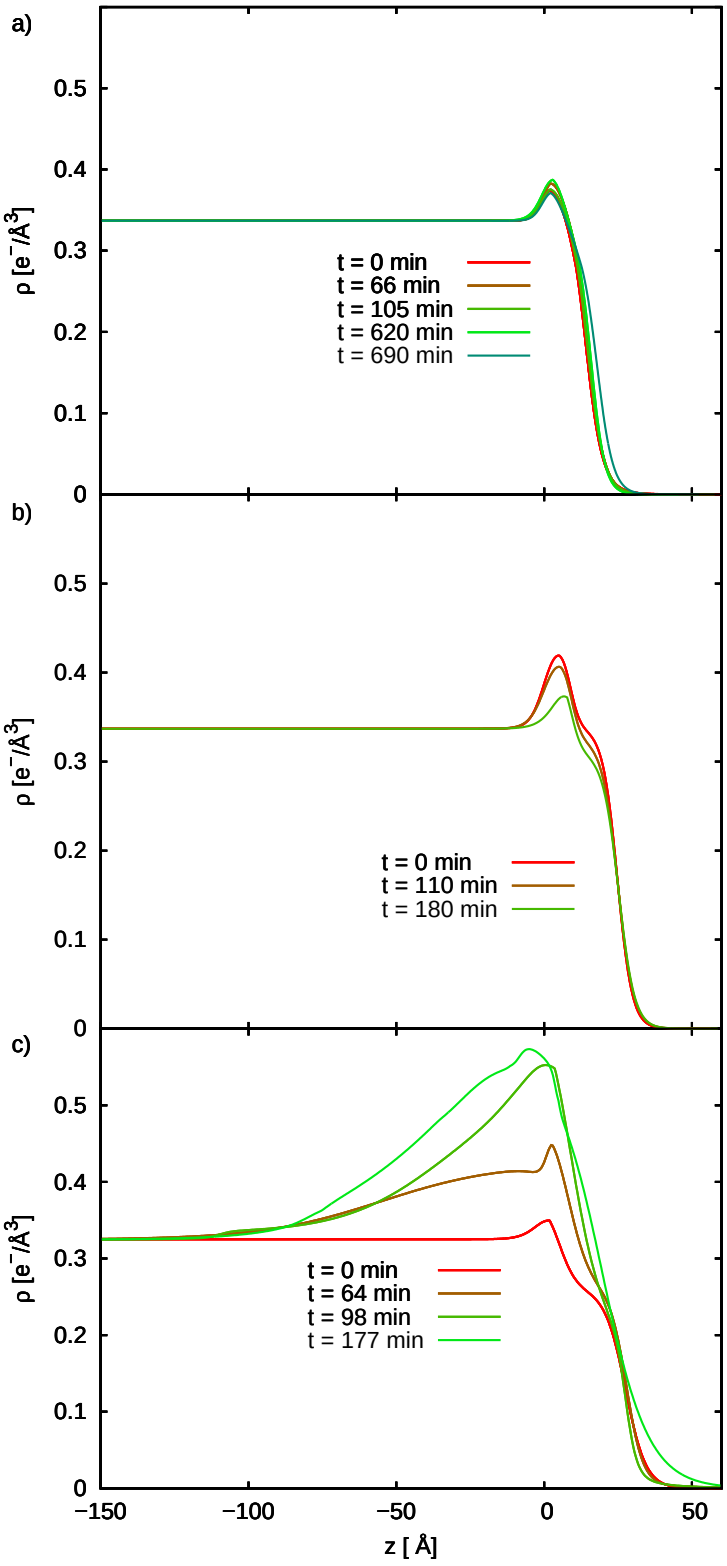

Figure 5.15.: Electron density profiles from an iron(II) chloride subphase with varying monolayers. a) DPPA, ammonia added after t = 64 min b) DPPC, ammonia added after 60 min c) EPC, ammonia added after t = 64 min.

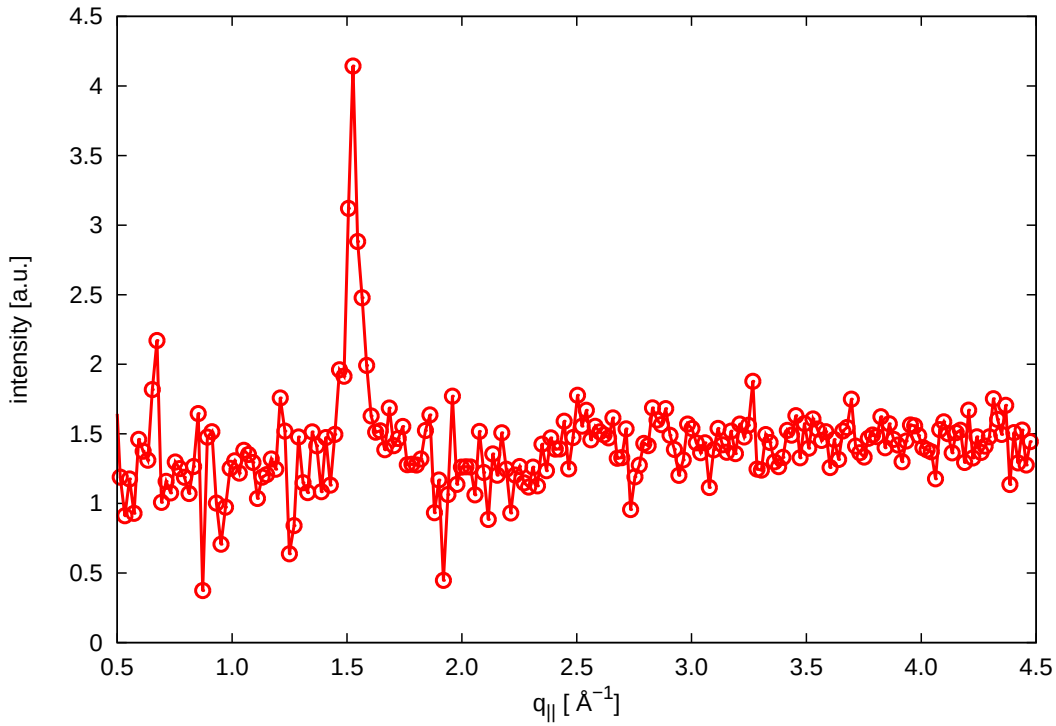

Figure 5.16.: GID data of a DPPA layer on an iron(II) chloride subphase showing the diffraction peak originating from the Langmuir layer at q_z = 1.527 Å^{-1}.

5.16. Even though the surface pressure decreased to $12.7\ \mathrm{mN/m}$ a diffraction signal can be seen at $q_{||}$ =$(1.527\ \pm 0.003\ )$Å^{-1}, which can be attributed to a Langmuir layer organized in a hexagonal unit cell with a lattice constant of $(4.75\ \pm 0.01\ )$Å. Langmuir layers of DPPA on pure water subphases exhibit a unit cell constant of 4.79 Å.[164] Although a loss of amphiphilic molecules is observed in the experiments the structure of the Langmuir layer is still in a crystalline state. It is likely that the Langmuir layer is in a phase witch is similar to the so called X-phase.[189] This phase is observed at Langmuir monolayers where divalent ions are present in the subphase. The ions begin to condensate at the headgroup under the monolayer structure.[35] This process not only depends on the protonation state of the headgroup but also depends on the divalent ion concentration in the subphase. Due to this an effective electrostatic force may appear between headgroups with and without condensated ion. In this phase the amphiphiles organize in an untilted lattice even at low surface pressure. However, in the X-phase the layer adopts a centered rectangular unit cell where the maximum in the intensity of the Bragg rod has a position of q_z =0 Å^{-1}. This is not observed for the DPPA layer showing only a single reflection at q_z = 0 Å^{-1}. Diffraction signals from crystalline iron oxides or hydroxides were absent.

The final state of the DPPA sample was examined more closely by scanning electron microscopy (SEM) images. A Stereo Scan 360 SEM by Leica, (Cambridge Ltd., Cambridge, UK) electron microscope was employed. The Langmuir Blodgett (LB) technique was used to prepare thin films of the final product of the DPPA sample on silica. The obtained image is shown in figure 5.17. Irregularly shaped agglomerates can be identified spread at the interface. The smallest structures are roundly shaped with a diameter of 17 nm. This shows that no closed film is formed but small aggregates form all along at the interface.

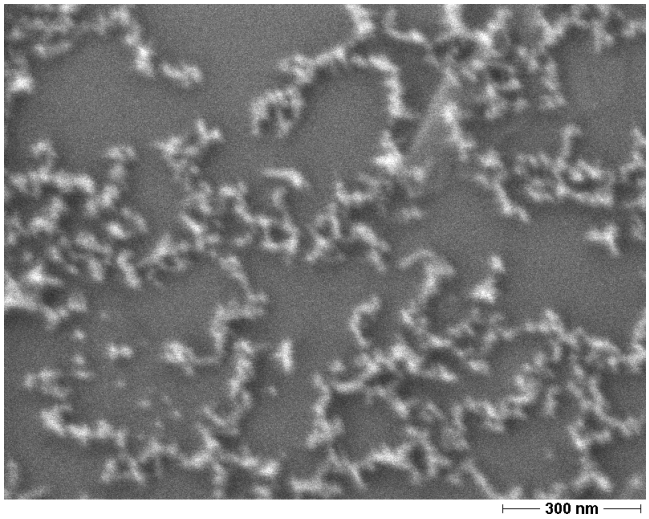

Figure 5.17.: SEM image of the film formed at interfaces modified with DPPA in the final state.

5.2.2. Discussion and conclusion

In the framework of the collaboration, dynamic light scattering experiments were performed by P. Degen, Physikalische Chemie II, TU Dortmund, on $0.1\ \mathrm{mmol/L}$ bulk solutions of iron(II) chloride. These measurements show the presence of objects with a diameter of $248\ \mathrm{nm} \pm 21\ \mathrm{nm}$ with a very high polydispersity of $0.8\ \pm 1$. Due to the low count rates a low concentration of the objects can be assumed. After addition of ammonia particles with a diameter of $64\ \mathrm{nm}$ were detected which grow to a diameter of $250\ \mathrm{nm}$ with ongoing time. This growth is accompanied by a decrease of the polydispersity to $0.4\ \pm 0.1$ and an increases of the counts by a factor of 10. This hints at the formation of nanoparticles floating in the solution.

In order to gain more information on the influence of the ions on the Langmuir layer, surface pressure/area (Π/A) isotherms were recorded by P. Degen, Physikalische Chemie II, TU Dortmund. The isotherms were measured on $0.1\ \mathrm{mmol/L}$ iron(II) chloride solutions and on pure water for comparison. The data of the three phospholipids are depicted in figure 5.18. For the zwitter-ionic DPPC, the characteristic shape of the phospholipid on water can be seen(see figure 5.18).[190] No change in the isotherms can be observed as iron(II) chloride is present. The isotherm of the positively charged EPC shows a steady increase (no plateau) of the surface pressure on both subphases. Nevertheless, the isotherm measured on an iron(II) chloride subphase shows a shift to smaller areas which might be due to a reduced repulsion of the headgroups, because of the presence of chloride ions. The isotherms of the negatively charged DPPA also reflect a reduced repulsion of the headgroup. The area needed for the transition from liquid expanded to the liquid condensed state is shifted to lower values. This might be due to the presence of positively charged iron(II) ions screening the electrostatic repulsion.

Additional Brewster angle microscopy (BAM) images were recorded by P. Degen, Physikalische Chemie II, TU Dortmund. DPPA monolayers were spread on iron(II) chloride solutions and ammonia was added. The sample system was monitored in absence and presence of ammonia at different times. The images show already in the beginning an inhomogeneous film (see figure 5.19a). Similar inhomogeneities were observed in other studies investigating the interaction of

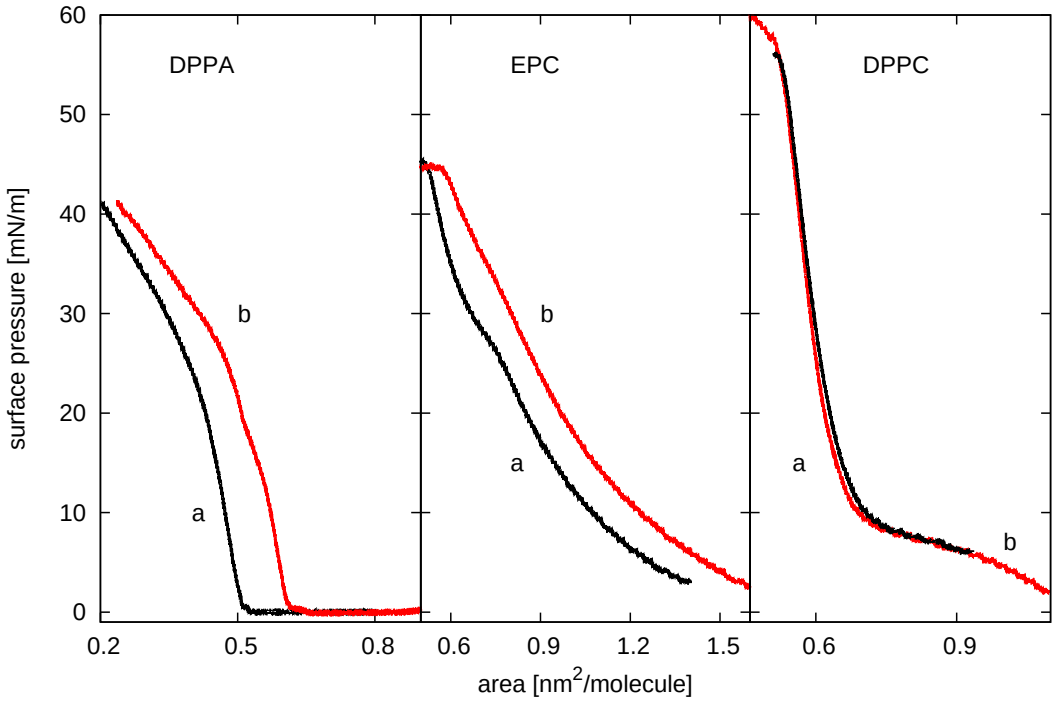

Figure 5.18.: II/A isotherms of DPPA, EPC, and DPPC on a) iron(II) chloride (green) and b) water (red). The isotherms were measured by P. Degen, Physikalische Chemie II, TU Dortmund.

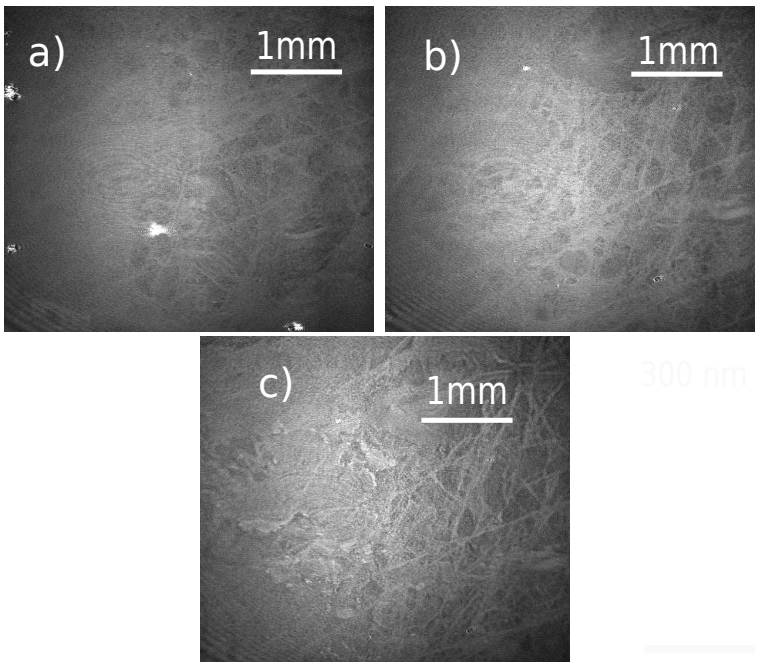

Figure 5.19.: a-c: BAM images of DPPA on iron(II) chloride solution (0.1 mmol/L), before (a), 10 min after addition of NH_3 (b) and 60 minutes after addition of NH_3 (c). The images were recorded by P. Degen, Physikalische Chemie II, TU Dortmund.

copper ions in solution with Langmuir layers.[189] The intensity of the images is increases after ammonia is added indicating the enrichment of material at the interface (see figure 5.19b). Figure 5.19c shows a later state of the Langmuir layer with a higher structuring. In these measurements, no structures which could be identified as crystals could be seen.

The experiments on phospholipid monolayers of DPPC and EPC show no film formation. This is in contradiction to the study of Maas et al., who report the formation of iron containing aggregates independent of the lipid headgroup using iron(II) chloride concentrations of $8\ \mathrm{mmol/L}$.[184] This discrepancy can be explained by the lower iron(II) chloride concentrations of $0.1\ \mathrm{mmol/L}$ used in these experiments.

The obtained surface pressure-area isotherms on the DPPA monolayer show an increase of the screening due to the presence of iron(II) ions in the interfacial region. Similar observations were reported for studies investigating the condensation of multivalent ions at carboxylate headgroups. Here, a reduced headgroup area could be found due to the condensation of counter ions inverting the sign of the headgroup charge.[141, 191] By varying the pH value of the subphase, the degree of deprotonation could be controlled and by this, the degree of the condensed ions. Due to the condensation an effective attractive force evolves between the amphiphiles.[35, 141]

The experiments exhibit no evidence for crystalline iron oxide at the liquid interface. Due to this the micro structure of the compound can not be determined. The formed aggregates might exhibit a complete amorphous structure or are made of ferrihydrid. This polymorph can be synthesized by a fast deprotonation of iron solutions.[103] Because ferrihydrid often exhibits a very weak crystalline order, a diffraction signal is hard to detect and could be indistinguishable from the background.[192]

The investigations show the nucleation of aggregates in the bulk solution without adsorption taking place at the bare interface. If the interface is covered by a DPPA monolayer, a successful heterogeneous nucleation can be observed. The Langmuir layer acts as a heterogeneous nucleation side for the iron containing aggregates. The DPPA amphiphiles have a pK_A value of 2.1. Thus, the monolayer is fully deprotonated because the solution has a pH value of 4.[185, 187] Consequently the Langmuir film is negatively charged and iron ions are attracted. Accumulation of the nanoparticles, observed in the solution, can be ruled out since the size of the nanoparticles in the solution (d = 64 nm) is much bigger than the thickness of the growing layer (d = 10 nm). The surface pressure-area isotherms of DPPA hint at an increase of the iron ions in the interfacial region. For comparison, the surface pressure-area isotherms on EPC monolayers indicate an increase of the chloride ion concentration in the vicinity of the interface explaining the hampered aggregation. A similar conclusion can be made for DPPC monolayers, where the surface pressure-area isotherms indicate no interaction of the ions in solution with the Langmuir layer at all.

5.3. Subphases containing high iron(II) chloride concentration

The investigations reported in chapter 5.2 showed a discrepancy to the findings of Maas et al. where much higher iron(II) chloride concentrations were used.[184] In order to gain more in-

sight into the influence of this concentration dependency, experiments with elevated iron(II) chloride concentrations were performed. The concentration in the subphase was raised to $1\ \mathrm{mmol/L}$, $8\ \mathrm{mmol/L}$ and $100\ \mathrm{mmol/L}$. Test XRR experiments showed the formation of rough interface and made the use of XRR experiments inapplicable. Hence, the main techniques which were used to probe these samples were XRD and XAFS. These experiments were performed at different beamlines of the synchrotron light sources DELTA, Dortmund and DORIS III, Hamburg. The experimental end-stations along with the available techniques are summarized in table 5.3. The sample preparation and the experimental procedure is described in chapter 3.9.

Solutions were prepared by using water-free iron(II) chloride (purity $\geq$ 99 %, Sigma-Aldrich) for the XRD measurements with ultra-pure water (specific resistance 18.2 MΩ cm). For the XAS experiments iron(II) chloride tetra-hydrate (purity $\geq$ 99 %, Sigma-Aldrich) was used. Because these solutions are subject to aging samples were prepared shortly before the measurements.

5.3.1. Experimental data

Iron(II) chloride subphases were prepared with a concentration of $8\ \mathrm{mmol/L}$ and the bare surface of these solutions was investigated by XRD. The integrated XRD data are shown in figure 5.20 as a function of the wave vector transfer. In the initial state only scattering from the water subphase can be seen as indicated by the presence of the water structure factor. After the initial state was characterized, $30\ \mathrm{mL}$ of a $3\ \mathrm{wt\%}$ ammonia solution were placed inside the sample cell. In the following Bragg reflections could be observed. The intensity of these reflections increased as a function of time. This process stops after 142 minutes. From the two-dimensional scattering pattern (data not shown) an unoriented growth can be proposed as the diffraction pattern was circularly shaped. By comparing this data to theoretically simulated scattering signals an agreement with iron hydroxide lepidocrocite could be found. The data clearly shows the growth of crystalline iron hydroxide (lepidocrocite) even without monolayers.

XAFS measurements at the iron K-edge on interfaces of a $1\ \mathrm{mmol/L}$ iron(II) chloride solution were performed at the beamline A1, DORIS III and BL8, DELTA. The evolution of the system was monitored by XANES measurements (data not shown). The XANES spectra show no significant deviations as ammonia is present indicating no change in the local structure of the iron atom within the surface region.

Figure 5.21 shows the extracted EXAFS signal of the iron K-edge and figure 5.22 the Fourier transformed EXAFS signals χ(R) of the $1\ \mathrm{mmol/L}$ iron(II) chloride solution with and without ammonia. The EXAFS measurements were performed on the as deposited sample (initial state) and after the addition of ammonia (final state). By comparing the extracted data sets from the

experimental station	synchrotron light source	technique
A1	DORIS III	XANES/EXAFS
Bl8	DELTA	XANES/EXAFS
Bl9	DELTA	XRD

Table 5.3.: Experimental station used for the investigation of the interface at solution with iron(II) chloride solution exceeding $1\ \mathrm{mmol/L}$.

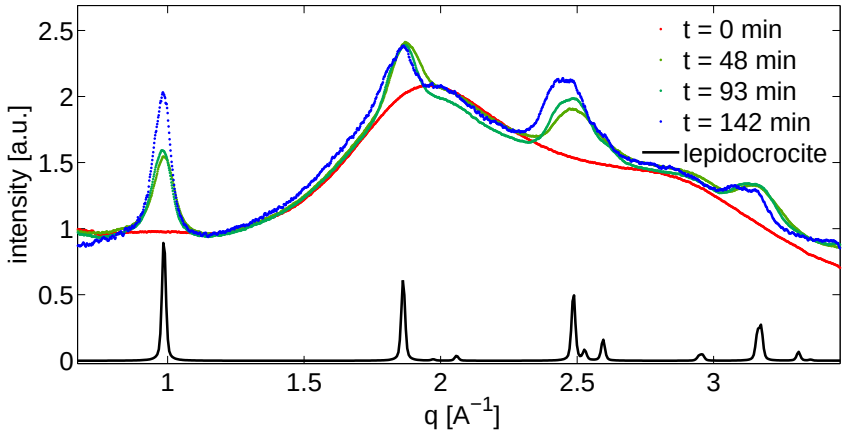

Figure 5.20.: GID data on an iron(II) chloride subphase with a concentration of $8\ \mathrm{mmol/L}$. Ammonia was added after 26 minutes. The black line shows the calculated diffraction pattern of lepidocrocite.

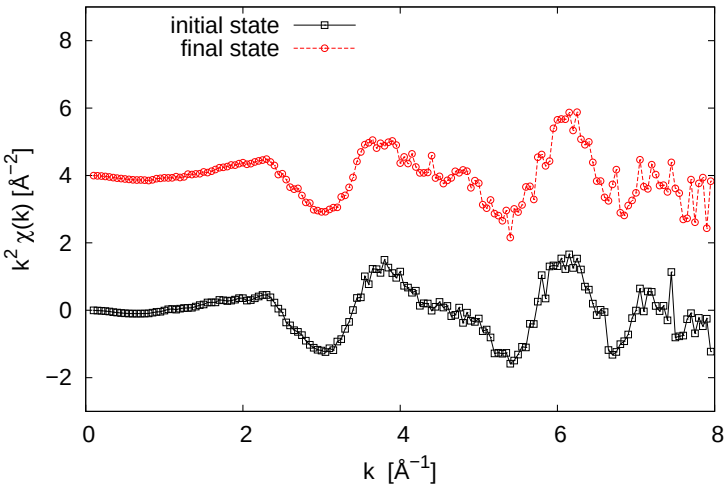

Figure 5.21.: Extracted EXAFS signal of the initial and end state of a $1\ \mathrm{mmol/L}$ iron(II) chloride subphase with a concentration of 1 mmol. The measurement of the final state was performed after 240 minutes.

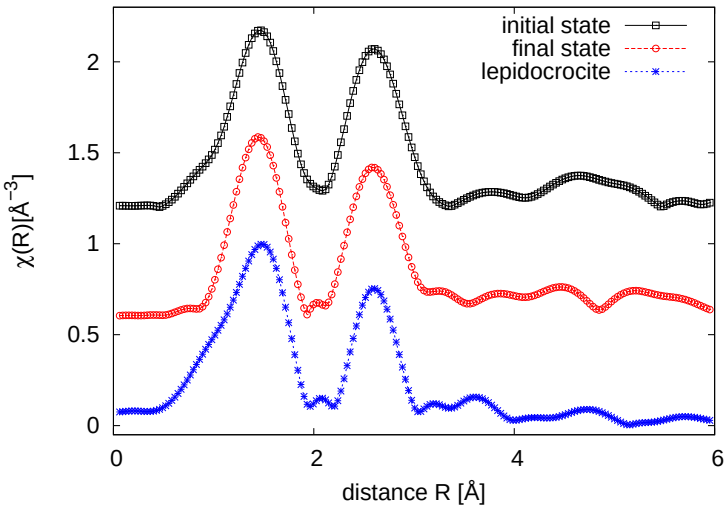

Figure 5.22.: Fourier transformed EXAFS signals χ(R) on 1 mmol iron(II) chloride solutions with and without ammonia. An experimentally obtained reference of lepidocrocite taken from [193] is shown.

initial and final state to reference data taken from [193] the formation of a lepidocrocite like structure can be observed even without the presence of ammonia.[180, 180] However, this is not in contradiction to the XRD data as XAS is only sensitive to the short range order.[125]

Combining the information gained by the GID and XAFS experiments the following picture can be drawn. In the initial state small seeds with a local structure similar to lepidocrocite can be observed at the interface as indicated by the EXAFS data. The addition of ammonia induces an aggregation whereby the degree of crystallinity and the size of the particles increase as shown by the GID experiments.

In further experiments the iron(II) chloride concentration in the subphase was raised to $100\ \mathrm{mmol/L}$. The initial state was again monitored by XANES and EXAFS before adding ammonia. The changes in the sample were monitored by XANES measurements until the process stopped. The extracted and k weighted EXAFS signal of the initial and final state of the sample are shown in figure 5.23. These data show an increase of the number of oscillations in the EXAFS signal accompanied by a damping of the amplitudes. The damping can be attributed to an enhanced self-absorption decreasing the fluorescence signal coming out of the sample. The spectra were Fourier transformed and are shown in figure 5.24. In the initial state only one coordination shell is present as indicated by the presence of one single maximum. This maximum can be attributed to a Fe-O distance indicating the coordination of oxygen to the iron ions as already mentioned in the foregoing chapter.[94, 179, 181–183] After ammonia is added an increase in the local order around the iron atom can be observed as indicated by the appearance of a second maximum. This maximum can be assigned to be a Fe-Fe scattering path showing the formation of a further coordination shell. The experimentally obtained data was compared to reference data.[180, 180, 193] An agreement to lepidocrocite can be found.

Influence of Langmuir layers on the nucleation process

So far only bare interfaces were investigated. The observations made in chapter 5.2 demonstrate the influence of anionic lipid membranes on the formation process. Therefore, studies on the aggregation of inorganic films with elevated iron(II) chloride concentration were conducted with the amphiphiles stearic acid (anionic headgroup) and further stearyl alcohol (non-ionic) for comparison. XAFS experiments were performed on subphases with $1\ \mathrm{mmol/L}$ and $100\ \mathrm{mmol/L}$ iron(II) chloride concentration. The experiments on iron(II) chloride solution with a concentration of $1\ \mathrm{mmol/L}$ (data not shown) show no difference to the experiments at the bare interfaces. The data offer the presence of small seeds in the beginning with a lepidocrocite like structure independent of the monolayer and presence of ammonia. It can be concluded that these monolayers have only minor influence on the crystallization of iron oxide using iron(II) chloride subphases with a concentration of $1\ \mathrm{mmol/L}$.

The extracted and k-weighted EXAFS signal from interfaces of $100\ \mathrm{mmol/L}$ iron(II) chloride solutions with a Langmuir layer of stearyl alcohol are displayed in figure 5.25 and the Fourier transformation χ(R) is depicted in figure 5.26. The data show the evolution of further coordination shells between a distance of 2 Å and 4 Å as ammonia is added. The comparison to reference data of different iron oxides yielded no agreement.

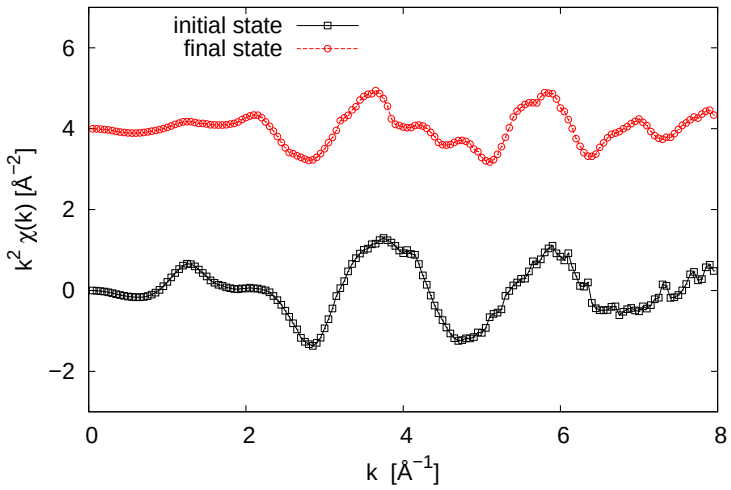

Figure 5.23.: Extracted EXAFS signal of the initial and end state of an iron(II) chloride subphase with a concentration of $100\ \mathrm{mmol/L}$. The measurement of the final state was performed after 220 minutes.

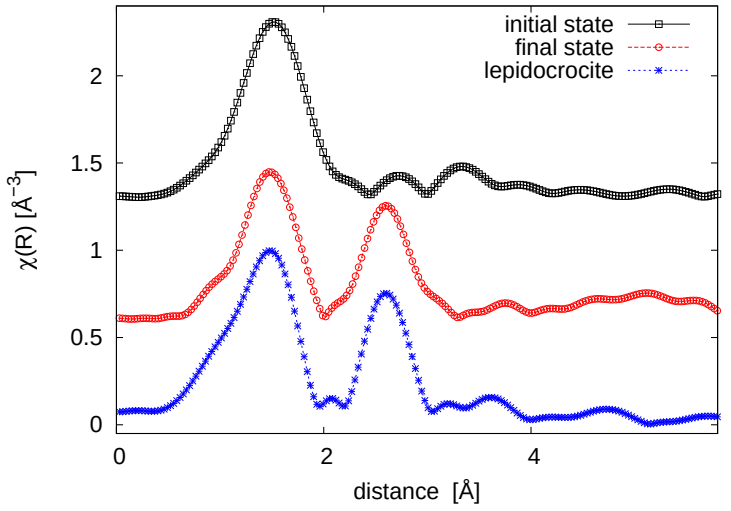

Figure 5.24.: Fourier transformed EXAFS signals χ(R) on $100\ \mathrm{mmol/L}$ iron(II) chloride solutions with and without ammonia. A reference of lepidocrocite taken from [193] is also shown.

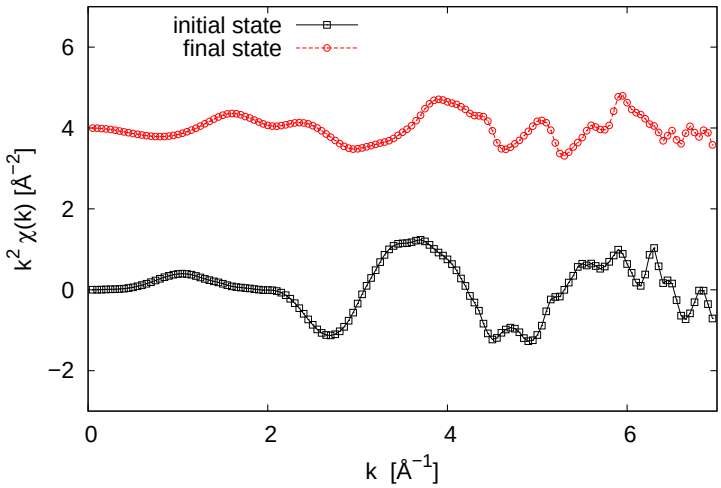

Figure 5.25.: Extracted EXAFS signal of the initial and end state of an iron(II) chloride subphase with a concentration of $100\ \mathrm{mmol/L}$ and a stearyl alcohol monolayer. The measurement of the final state was performed after 220 minutes. The measurement of the final state was performed after 216 minutes.

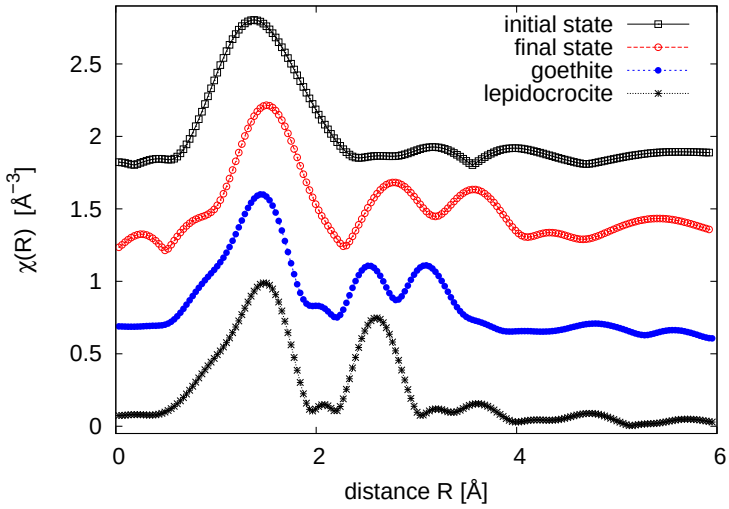

Figure 5.26.: Fourier transformed EXAFS signals χ(R) on $100\ \mathrm{mmol/L}$ iron(II) chloride solutions with and without ammonia and a stearyl alcohol monolayer. The references of lepidocrocite and goethite taken from [193] are also shown.

Because the extracted EXAFS data show no agreement with the reference data a combined XRD and SEM experiment was performed. For this the ammonia concentration was lowered to stop the thin film formation after some time. Then the sample was investigated by XRD and afterwards a fragment of the film was deposited on a silicon wafer to investigate it by SEM. 6 hours after the initial addition of ammonia a layer had formed which could be seen by the naked eye. Nevertheless no diffraction signal could be obtained (data not shown). A part of the layer was then transferred via the Langmuir-Blodgett technique onto a silicon wafer for ex-situ investigation. The formation process was then continued by adding ammonia a second time. This resulted in the formation of crystalline iron hydroxide as shown by XRD. The obtained scattering pattern along with simulated scattering data are shown in figure 5.27. The observed scattering curve can be described by lepidocrocite alone indicting only a single crystalline phase. Again, a part of the sample was transferred to a silicon wafer for ex-situ characterization by SEM. This images are shown in figure 5.28.

The SEM image made from the top of the sample after the first application of ammonia is shown in figure 5.28a. This picture shows the formation of a thick layer with small holes in the surface. A more detailed view of the composition can be seen in image 5.28b showing a side view of the sample. It seems that the layer was formed by the aggregation of small particles. Because the XRD experiments showed no diffraction signal the observed structures exhibit no long range ordering. After ammonia was applied for a second time the layer has grown further into the subphase. In this state the layer can be divided in three parts. The first part can be identified as the initial nucleation layer observed in the pictures of the top row. This part is followed by a layer with darker color indicating a layer with higher electron density. The middle layer seems to be composed of small crystallites indicating a starting mineralization. The part of the layer being in contact with the water phase is composed of long needle-like structures with random orientation. The crystalline structures are composed of lepidocrocite as proven by XRD.

Further the influence of stearic acid monolayers on the formation process was investigated. XANES spectra were recorded from solutions with a concentration of $100\ \mathrm{mmol/L}$ and are shown in figure 5.29. In the beginning the typical structureless curve can be seen as in the other investigated samples. On addition of ammonia a decrease of the white line accompanied by an increase in the structure can be observed. Furthermore the absorption edge shifts by 2 eV to lower energies. The EXAFS data obtained on this sample system is shown in figure 5.30 and the Fourier transformed χ(R) is shown in figure 5.31. The data indicates the presence of two coordination shells just in the beginning. After ammonia is added the second coordination shell becomes more pronounced indicating an increased order around the iron atom. The highest accordance of these spectra can be found to that of magnetite. Nevertheless the agreement is not satisfactory.

Subphases with an iron(II) chloride concentration of $100\ \mathrm{mmol/L}$ and stearic acid monolayers present at the interface were further subject of XRD experiments. The obtained scattering pattern is depicted in figure 5.32. The data shows the formation of crystalline structures at the interface after the addition of ammonia. By comparing the so obtained pattern to simulated scattering signals the data can be best described by a combination of lepidocrocite and magnetite. The presence of magnetite is in agreement to the EXAFS data.

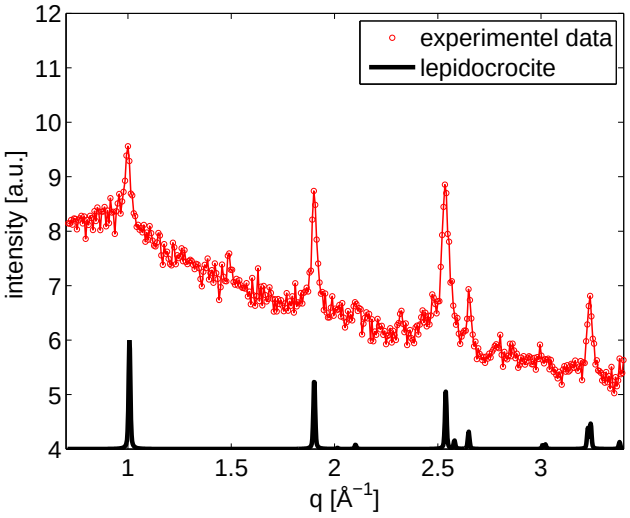

Figure 5.27.: XRD curves of a samples of iron(II) chloride with a concentration of $100\ \mathrm{mmol/L}$ with stearyl alcohol monolayers.

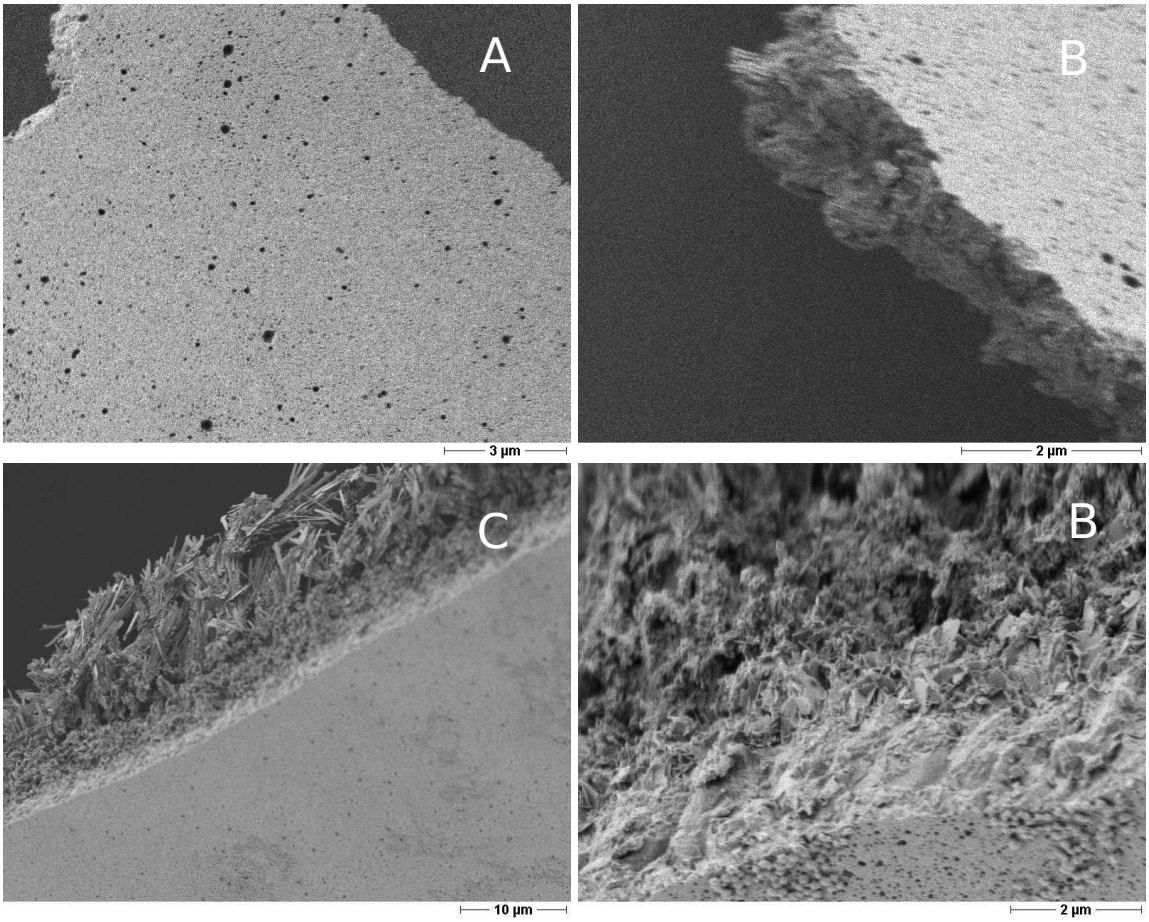

Figure 5.28.: SEM images taken on films grown on iron(II) chloride solutions with a concentration of $100\ \mathrm{mmol/L}$ and stearyl alcohol monolayers present at the interface. The images show different states of the film evolution. A) Top view, ammonia added. B) Side view, ammonia added. C) Side view, second addition of ammonia. D) Side view higher magnification, second addition of ammonia.

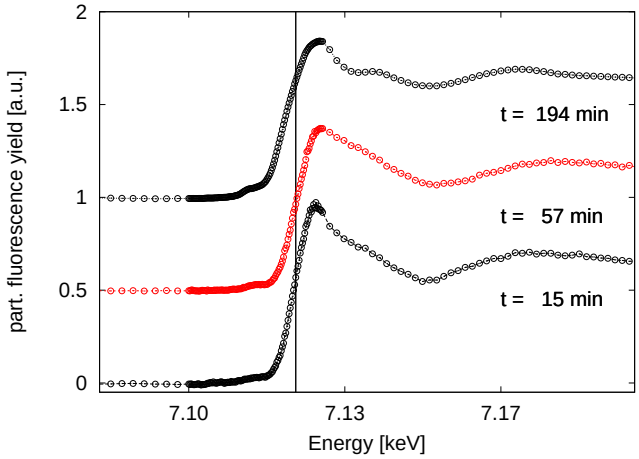

Figure 5.29.: XANES spectra obtained on iron(II) chloride subphases with a concentration of $1\ \mathrm{mmol/L}$ and a stearic acid monolayer showing the time evolution of the sample. Ammonia was added after 30 minutes. The data is shifted vertically for clarity.

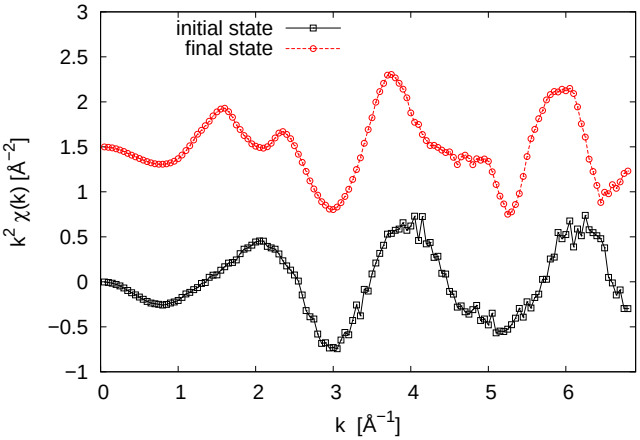

Figure 5.30.: Extracted EXAFS signal of the initial and end state of an iron(II) chloride subphase with a concentration of $100\ \mathrm{mmol/L}$ and a stearic acid monolayer showing the evolution of the near edge structure. The measurement of the final state was performed after 200 minutes.

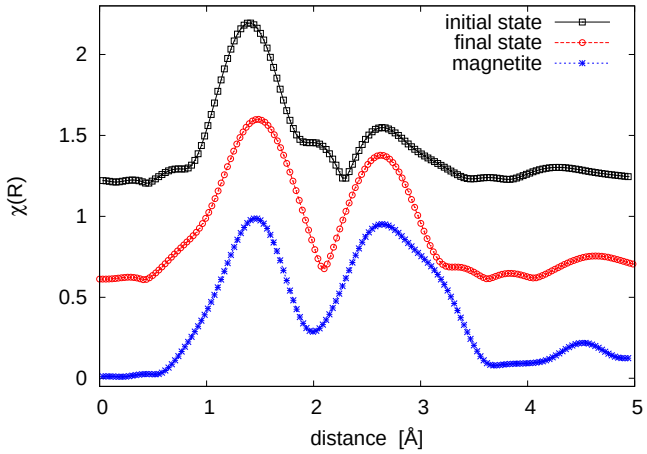

Figure 5.31.: Fourier transformed EXAFS signals χ(R) of $100\ \mathrm{mmol/L}$ iron(II) chloride solution with and without ammonia and a stearic acid monolayer. A reference of lepidocrocite taken from [193] is also shown.

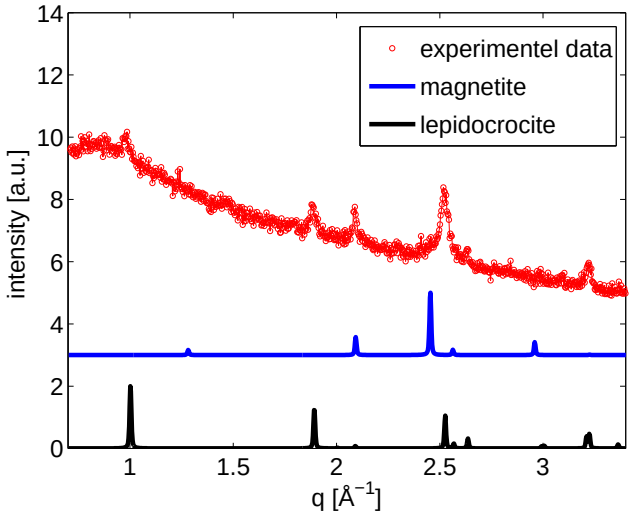

Figure 5.32.: XRD curves on sample of iron(II) chloride with a concentration of $100\ \mathrm{mmol/L}$ with stearic acid monolayers.

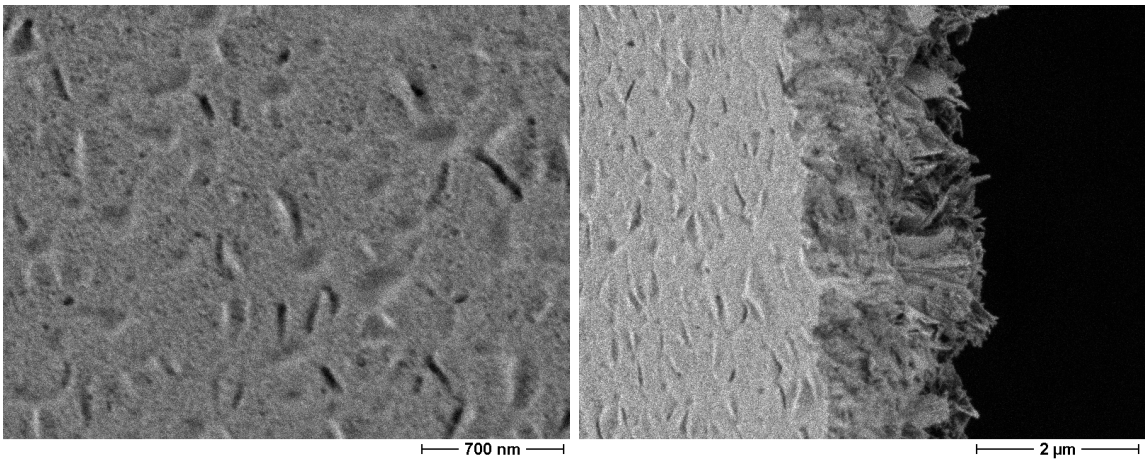

Figure 5.33.: SEM images taken on films grown on iron(II) chloride solutions with a concentration of $100\ \mathrm{mmol/L}$ and stearic acid monolayers present at the interface. The images show the final state of the film. A) Top view, B) side view.

Although the magnetite (113) reflection at q=2.45 Å^{-1} can not be observed in the measured diffraction curve, the diffraction peak at q=2.09 Å^{-1} can only be explained by taking the (202) magnetite reflection into account. The flank of the (301) lepidocrocite reflection at q=2.51 Å^{-1} seems to have an increased intensity indicating the existence of the (331) magnetite reflection. The observation might hint at a growth with a preferred orientation at the interface.

The final product was again a brittle film which could be seen by the bare eye. A piece of the formed film was again transferred via the Langmuir Blodgett technique to a silicon substrate and SEM images were recorded. The images are depicted in figure 5.33 showing the formation of a structured layer. The top side of the sample is nearly closed and almost no holes can be seen in it. The first part seems to persist of an unordered structure quite similar to the layers observed for amphiphiles of stearyl alcohol. This layer is followed by sharp structures which are supposed to be composed of crystals.

5.3.2. Discussion and Conclusion

The experiment on subphases containing iron(II) chloride with a concentration greater than $1\ \mathrm{mmol/L}$ show the formation of lepidocrocite crystals at the interface upon the addition of ammonia. Furthermore, the XAFS experiments demonstrate that in solutions with $1\ \mathrm{mmol/L}$ iron(II) chloride concentration, aggregates with a lepidocrocite structure can be observed even without a monolayer. In this state XRD experiments show no diffraction signal indicating a weak crystalline order or very small structures which are not detectable by the experimental setup. After the addition of ammonia, these seeds grow, as seen by the XRD experiments, yielding lepidocrocite crystals with random orientation at the interface. By keeping the results of chapter 5.2 in mind, the following model can be postulated: Upon the addition of ammonia, aggregates form in the bulk solution. As the concentration in the bulk solution increases, particles start to accumulate to the interface. The same behavior could be observed for nanoparticles, where also a sufficient bulk concentration is needed to induce adsorption at the surface.[91]

XAFS experiments on iron(II) chloride solutions with $100\ \mathrm{mmol/L}$ concentration showed only the existence of one coordination shell around the iron atom in the beginning. No second coordination shell can be observed, as found for $1\ \mathrm{mmol/L}$ iron(II) chloride solutions. Because the precipitation reaction is pH dependent, this observation can be explained by the higher pH value of the $1\ \mathrm{mmol/L}$ solution. In this case the pH is high enough to enable a small fraction of iron ions to nucleate adapting a lepidocrocite like structure. If ammonia is introduced to the sample system the precipitation reaction is triggered as observed by the evolution of a second coordination shell. The analysis shows that the obtained χ(R) can be best described by lepidocrocite. X-ray diffraction experiments performed in the framework of the diploma thesis of F. Wirkert showed the growth of lepidocrocite crystals at the interface after the addition of ammonia.[194] The width of the observed scattering reflections decreased with time indicating the growth of the crystals.

The XAFS and XRD data obtained on $1\ \mathrm{mmol/L}$ iron(II) chloride solution showed the formation of lepidocrocite without any contribution from other phases.

Langmuir monolayers seem to have no influence on the crystalline structures forming in $1\ \mathrm{mmol/L}$ iron(II) chloride solutions. In all cases, the obtained data show a signal originating from lepidocrocite structures.

This changes as the concentration is raised to $100\ \mathrm{mmol/L}$, in the presence of stearic acid magnetite crystals start to form aside of lepidocrocite as proved by the XRD experiments. These changes are supported by the XAFS experiments which also show the existence of magnetite. Prior to the addition of ammonia, the local structure around the iron atoms seem also more ordered than without monolayer which is indicated by the presence of a weak maximum in the χ(R). The SEM image revealed the formation of a closed surface layer. The formation starts with an unstructured layer which is likely to be amorphous. With time, sharp structures are formed at the face of the layer oriented towards the aqueous solution. It is supposed that these structures have a crystalline character. The formation of such composite films was also observed by Maas et al.[184]

Langmuir layers of stearyl alcohol seem to have no influence on the polymorph of the formed crystals as seen in the XRD experiments showing the growth of lepidocrocite. The deviation observed in the XAFS experiments from the bare interface can be explained by the formation of a composite structure as proven by the SEM images. As this is no phase pure material EXAFS signal from iron atoms with a varying environment are obtained. In a first step a composite structure forms without crystalline order by the fusion of small aggregates. As the growth of the layer continues the formation of lepidocrocite crystals takes place. The fact that the EXAFS data can be described not by lepidocrocite alone is due to the different coordinations of the iron atoms. All iron atoms in the illuminated area are probed and not only the crystalline part alone. These observations are in clear contrast to the measurements performed by Lin et al.[195] These studies report on the formation of magnetite by using stearyl alcohol. The discrepancy can be attributed to varying sample treatment as Lin et. al. deposited the sample on glass substrates via the Langmuir-Blodgett technique. Due to this, the samples dried which might result in a phase transformation.

From the data the following picture of the nucleation of inorganic film from subphases containing iron(II) chloride can be drawn. In the case of charged interfaces, iron containing aggregates nucleate at the interface as revealed by the experiments on low iron(II) concentrations. Parallel to this interfacial nucleation, aggregates start to form in the bulk solution which can adsorb at the interface if a critical subphase concentration is passed. Thus, the iron hydroxide aggregation at the interface can be achieved without monolayers by adjusting the subphase concentration alone. At iron(II) chloride concentrations of $100\ \mathrm{mmol/L}$, the formation of a composite structure is observed which seems to have an amorphous character. It is likely that the roundly shaped aggregates, which form the first layer, are the same as observed for low iron(II) chloride concentrations in combination with DPPA Langmuir layers. These aggregates show no long range order. As the pH value drops, which results in an enhanced formation of lepidocrocite particles in the bulk solution, a competitive adsorption at the interface takes place.

5.4. Growth of inorganic thin films at polysiloxane membranes

In this chapter the growth of thin films at solution-air interfaces modified with polysiloxane networks is discussed. In a first step subphases containing iron(III) chloride were studied. The iron(III) complexes present in the subphase have the affinity to accumulate in the interface region.[168] By this a seeding layer could be formed from which the nucleation starts.

Synthesis protocols for iron oxide nanoparticles (magnetite or maghemite) make use of iron salt solutions composed of a mixture of salts with varying oxidation states.[196] In order to investigate how the presence of different ions with varying oxidation states influence the growth process aqueous solutions containing a mixture of iron(II) chloride and iron(III) chloride were used.

In the first part of the following chapter the aggregation of inorganic films under polysiloxane networks is presented using an iron(III) chloride. After this, the study of thin film growth

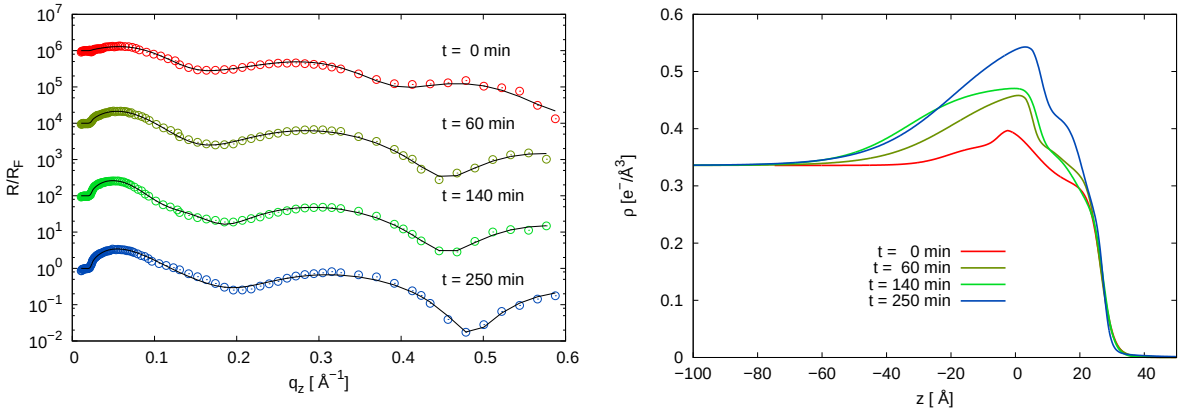

Figure 5.34.: Polysiloxane membranes on iron(III) chloride solutions with a concentration of $1\ \mathrm{mmol/L}$. The samples were investigated at different evolution times. Left: Fresnel normalized reflectivities. Right: Electron density profiles.

at polysiloxane membranes using solutions with a mixture of iron(II) chloride and iron(III) chloride is represented. The chapter closes with a conclusion of the observations.

5.4.1. Subphases containing iron(III) chloride

X-ray reflectivity and grazing incidence diffraction measurements were performed on polysiloxane networks using subphases of iron(III) chloride solution. The concentration of the iron(III) chloride was chosen to be $1\ \mathrm{mmol/L}$ resulting in a pH value of 3 for the solution. The experiments were performed using the liquid scattering setup of the beamline BW1, DORIS III, Hamburg, Germany. The Langmuir layers were prepared as described in chapter 3.9 using a $1\ \mathrm{mmol/L}$ solution of OTS in chloroform. In the following the film was compressed to a surface pressure of $\Pi = 20\ \mathrm{mN/m}$ and was kept constant.

The Fresnel normalized XRR curves are depicted in figure 5.34 as a function of the wave vector transfer perpendicular to the surface. The reflectivities were measured at different time of the evolution of the system. The curve marked with t = 0 min denotes the time when the first measurement was started. The reflectivities show an increase of intensity in the low q_z range around $0.05\ \mathrm{Å}^{-1}$. This indicates an enrichment of material with high electron density at the interface. By closer inspection of the obtained data also changes in the characteristics of the curves can be observed.

The XRR curves were analyzed in order to obtain the electron density profile perpendicular to the surface. For the actual sample system a model consisting of 3 layers was used. The obtained profiles are shown in figure 5.34. The electron density profile obtained directly after compression of the monolayer show already a slight increase in the region beneath the headgroup. A gradient with a length of 20 Å from the water towards the headgroup can be observed. During the following time a further increase of the electron density takes place in a region of 60 Å below the headgroup of the polysiloxane network. In the later evolution states the headgroup of the polysiloxane networks can not be distinguished anymore from the growing layer. However, the tail group can be clearly identified until the end of the growth process although the elec-

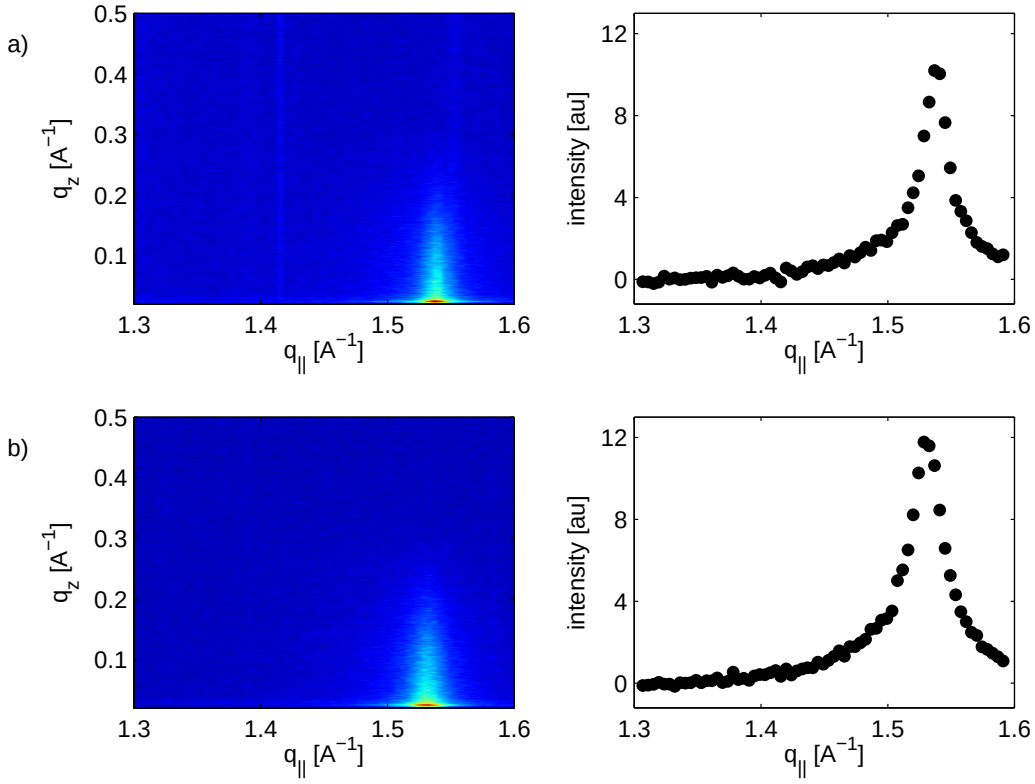

Figure 5.35.: GID data obtained from polysiloxane networks on top of iron(III) chloride solutions. The left side shows the two dimensional scattering pattern and the right side depicts the scattering signal integrated along the q_z direction. a) 36 min after the first measurement b) 174 min after the first measurement.

tron density in the tailgroup region increases as well. In fact an absorption throughout the film structure takes place. It has to be pointed out that in this state no ammonia was present yet.

In order to investigate the lateral structure of the polysiloxane network GID experiments were performed in between the reflectivity scans. The two dimensional GID data along with the integrated data along the q_z direction is shown in figure 5.35. In the beginning a single diffraction peak can be observed at $q_{||} = 1.537\,\text{Å}^{-1}$. The two-dimensional crystal lattice can be described by a hexagonal unit cell. The resulting parameters are summarized in table 5.4. The tails of the polysiloxane network are in an upright position. By comparing the unit cell parameters of polysiloxane networks on iron(III) chloride subphases with values obtained on a water subphase no change can be observed (see chapter 4.1). From this it can be concluded that the iron(III) chloride has no influence on the lateral polysiloxane network structure.

The ongoing aggregation process seems to disturb the lateral order thereby decreasing the size of the crystalline patches as indicated by the increase of width of the Bragg reflections, see table 5.4. GID scans covering a larger q range were performed in order to search for reflections from crystalline iron oxide or hydroxide species. In these scans no reflections could be found indicating the formation of an amorphous layer.

	t = 34 min	t = 174 min
FWHM [Å^{-1}]	0.026 ± 0.003	0.039 ± 0.006
$q_{\|\|}$ [Å^{-1}]	1.536 ± 0.005	1.528 ± 0.005
lattice constant a [Å]	4.72 ± 0.3	4.75 ± 0.3
unit cell size A_{xy} [Å^2]	19.1 ± 0.3	19.3 ± 0.2
I [a.u.]	16.1 ± 0.4	14.3 ± 0.1

Table 5.4.: Parameters of the Voigt function fitted to GID scans of the polysiloxane networks on iron(III) chloride subphases, full width of half maximum (FWHM), $q_{||}$ lateral position of the reflection, I intensity of the diffraction peak. Properties were estimated by evaluation of the GID scans using Voigt profiles.

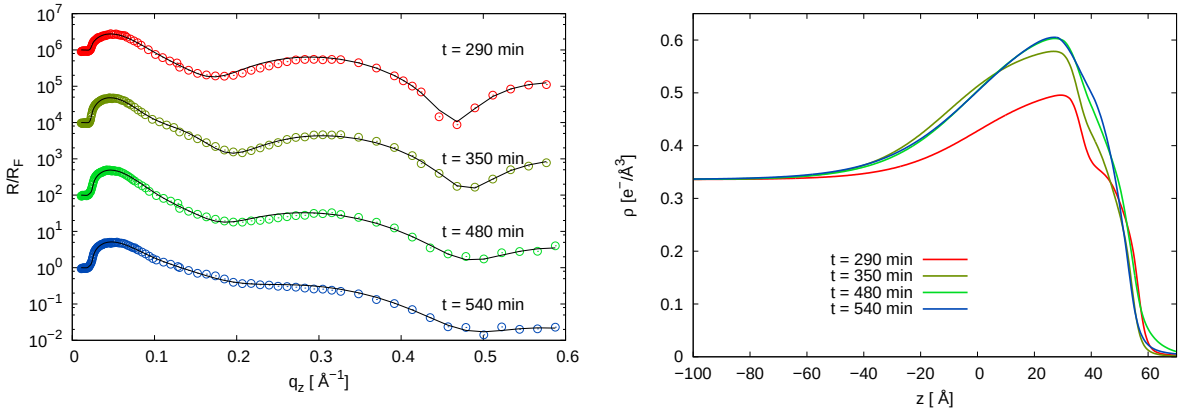

Figure 5.36.: Polysiloxane membranes on iron(III) chloride solutions with a concentration of $1\ \mathrm{mmol/L}$ in the presence of ammonia. The samples were investigated at different evolution times. Left: Fresnel normalized reflectivities. Right: Electron density profiles.

In the following ammonia was added to the system to investigate if a phase transformation could be induced. Four vials containing in total $30\ \mathrm{mL}$ of a $3\ \mathrm{wt\%}$ ammonia solution were placed inside. After this XRR and GID measurements were performed again. The Fresnel normalized XRR data are shown in figure 5.36. After ammonia was added the oscillation in the reflected signal was damped. Additionally a further increase in the intensity around $q_z = 0.05$ Å^{-1} can be seen. The corresponding electron density profiles are shown in figure 5.36 reflecting a further increase of the electron density as ammonia is present. During this process the vertical structure of the polysiloxane network is completely destroyed. The final state of the system is reached after a time of t = 480 min. At the end a GID measurement was performed in order to examine the lateral structure of the polysiloxane network again and to search for reflections from crystalline material (data not shown). No scattering signal at all could be detected. From this it can be concluded that no crystalline iron compound was present in the sample and the lateral order of the polysiloxane was completely destroyed. This is in contrast to the reference measurements presented in chapter 4.1. During these experiments the homogeneity of the membrane increased as ammonia was added.

5.4.2. Subphases containing a mixture of iron(III)- and iron(II) chloride

The growth of inorganic films at polysiloxane monolayers was studied for mixtures of iron salts. A stock solution with a mixture of iron(II) chloride and iron(III) chloride in the ratio of 2:3 was

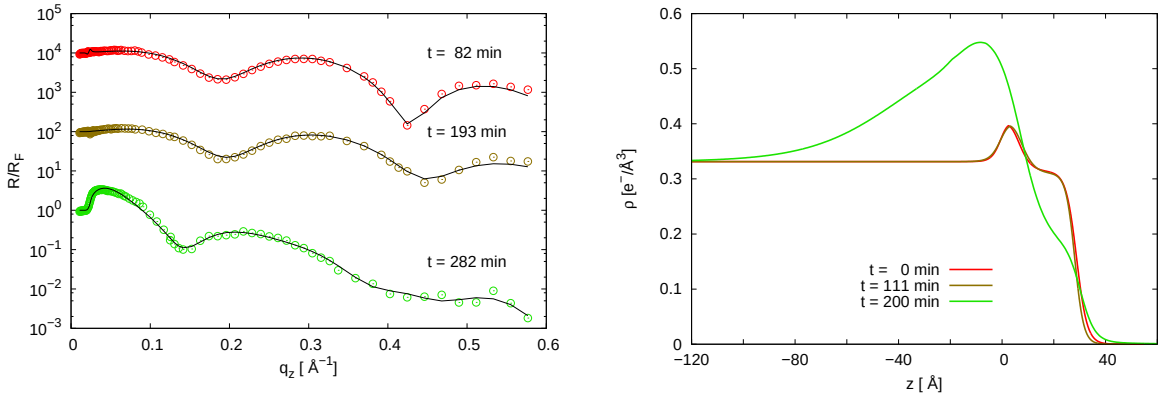

Figure 5.37.: Polysiloxane membranes on solutions containing an iron(II):iron(III) chloride mixture with a concentration of $1\ \mathrm{mmol/L}$ in the presence of ammonia. The samples were investigated at different evolution times. Left: Fresnel normalized reflectivities. Right: Electron density profiles.

prepared. The overall iron concentration in solution was adjusted to $1\ \mathrm{mmol/L}$. X-ray reflectivity measurements and grazing incidence diffraction measurements were performed at the beamline BW1, DORIS III, Hamburg. Polysiloxane layers were prepared as mentioned in chapter 3.9 using a $1\ \mathrm{mmol/L}$ solution of OTS in chloroform. The film was compressed to a surface pressure of $\Pi = 20\ \mathrm{mN/m}$ which was kept constant during the measurements.

The Fresnel normalized XRR data measured on this system is shown in figure 5.37. Because of the observation made in chapter 5.4.1 two reflectivity measurements were performed one after another in order to investigate if aggregation also occurs without ammonia (data not shown). Both curves show no deviation indicating no aggregation of inorganic material at the interface. After this ammonia was added to the gas phase above the sample. The first scan (t=195 min) after the addition of ammonia shows only minor changes. Whereas the scan started after 282 minutes shows a strong increase in the reflected intensity of the low q_z range.

The electron density profiles obtained from the XRR data are shown in figure 5.37. The electron density profiles show only a small increase of the layer roughness as ammonia is added (t = 193 min) implying a hindered aggregation. After a further waiting period of 200 minutes a 100 Å thick layer was observed at the interface. The electron density increases gradually from the water subphase towards the headgroup which is merged with the growing layer. By comparing the electron density of the tailgroup in the initial state with the later one a decrease can be observed. This might be due to the aggregation of an inorganic film at the headgroup whereas the polysiloxane patches are pushed apart. By this the electron density of the polysiloxane network decreases accompanied with a decrease of the electron density of the tailgroup.

GID experiments performed on these polysiloxane network are shown in figure 5.38. After the polysiloxane network is deposited at the interface a Bragg reflection at $q_{||} = 1.538\ \mathrm{Å}^{-1}$ can be observed. This indicates the organization of the hydrocarbon chains in a hexagonal unit cell. After ammonia was added to the gas phase the intensity of the diffraction peak dropped. The width of the reflection increased implying a shrunk lateral size of the crystalline patches. The structural parameters are summarized in table 5.5. Bragg reflections originating from crystalline material were not present in the GID experiments covering a larger q range (data not shown). This hints at the formation of amorphous aggregates at the polysiloxane interface.

	t = 32 min	t = 129 min	226 min
FWHM [Å^{-1}]	0.025 ± 0.002	0.035 ± 0.006	0.048 ± 0.009
$q_{\|\|}$ [Å^{-1}]	1.538 ± 0.005	1.540 ± 0.005	1.532 ± 0.009
lattice constant a [Å]	4.72 ± 0.09	4.71 ± 0.08	4.7 ± 0.2
unit cell size A_{xy} [Å^2]	19.3 ± 0.2	19.2 ± 0.2	19 ± 1
I [a.u.]	36.3 ± 0.4	23.6 ± 0.4	8.4 ± 0.9

Table 5.5.: Parameters of the Voigt function fitted to GID scans of the polysiloxane networks on a mixture of a iron(III):iron(II) chloride subphases, full width of half maximum (FWHM), $q_{||}$ lateral position of the reflection, I intensity of the diffraction peak. Properties were estimated by evaluation of the GID scans using Voigt profiles.

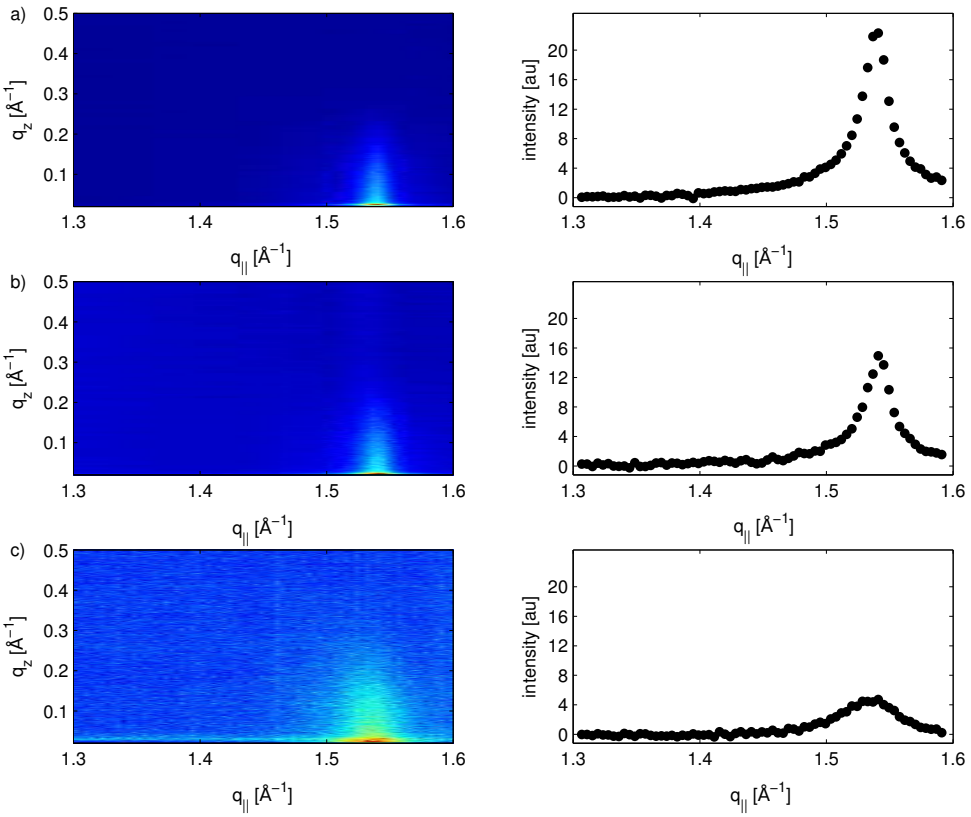

Figure 5.38.: GID data obtained from polysiloxane networks on solutions containing an iron(II):iron(III) chloride mixtures. The left side shows the two dimensional scattering pattern and the right depicts the scattering signal integrated along the q_z direction. a) 32 min after the first measurement b) 129 min after the first measurement c) 226 min after the first measurement.

5.4.3. Conclusion

The experiments utilizing iron(III) chloride subphases show a formation of inorganic films without the presence of ammonia in a region of 60 Å below the interface. During the formation process, the iron species penetrates the polysiloxane layer completely. These experiments show no sole adsorption at the headgroup. The lateral structure of the polysiloxane network is not influenced by the formation process, although the vertical layer structure is penetrated. The fact that no Bragg reflection from crystalline material could be observed, implies the formation of an amorphous layer at the interface.

If ammonia is added, a further increase of the electron density can be observed which goes in hand with the destruction of the lateral layer structure, although the reference measurements discussed in chapter 4.1 show an increase of the homogeneity of the polysiloxane layer. This effect seems to be blocked in the presence of iron(III) chloride solutions, in fact, the layer structure is disturbed as ammonia is present. As an inorganic film formation is observed even without ammonia another nucleation pathway might be present in this sample system. Because the exact composition of the inorganic films is unknown, no statement can be made about the restructuring of the inorganic film, which might induce the collapse of the lateral film structure. Nevertheless, ammonia is not responsible for this phenomena.

By using solutions which contain a mixture of iron salts, a growth of an inorganic film at the interface could be observed without iron penetrating the tailgroup of the monolayer. This is in contrast to subphases containing iron(III) chloride. The small particles formed in the headgroup region grow in the following progressively into the subphase. This process is accompanied by an increase of the width of the diffraction peaks showing a reduction in the lateral patch size.

Additional measurements, performed by P. Degen, Physikalische Chemie II, TU Dortmund, show a strong dependence of the crystallization kinetics on the iron salt and ammonia concentration. Since the measurements presented here are performed at very low concentrations, it is reasonable that only the initial stage is observed. The obtained data suggest that in the beginning iron containing aggregates are formed at the headgroup structure which is incorporated into the growing layer. By this, a composite structure is formed and the polysiloxane layer is disrupted. The formation of a composite structure was also observed by SEM images on samples using higher iron concentrations showing sponge like structures that form at the membrane. Ex-situ XRD measurements reveal the formation of maghemite by using higher subphases concentrations. This also supports the observation of a precursor phase which nucleates the interface and transforms to a crystalline structure at sufficient supersaturation levels.

5.5. Summary

The experiments on iron chloride solutions, performed in the framework of this thesis, observed the growth of inorganic films using different iron salt solutions and concentrations. Different nucleation and growth behavior are observed depending on the experimental conditions. The investigations reveal clearly, that not only pure electrostatic effects are responsible, but rather

more complex mechanisms have to be accounted. These mechanisms are quite difficult to identify as the system is very complex.

Low iron(II) chloride solutions showed the formation of amorphous aggregates at the negatively charged interface. For zwitter-ionic or cationic Langmuir layers, no growth was observed. Although the formation of aggregates was observed in the bulk solution for these concentrations no influence on the thin film forming at the interface was obvious. An attachment from the bulk phase to the interface can be ruled out due to the different sizes of the aggregates observed in the bulk solution and the inorganic layer formed at the interface.

If the concentration of iron(II) chloride was increased and with this, the number of aggregates forming in the solution, an accumulation of crystalline iron hydroxide (lepidocrocite) even without monolayers was observed at the interface. This was accompanied by a dramatical increase of the interfacial roughness. By modification of the interface with neutral amphiphile stearyl alcohol, no change in the growing polymorph could be induced. The formation of an amorphous structure with a subsequent growth of lepidocrocite could be seen. As stearic acid is used the formation of magnetite and lepidocrocite could be proven by XRD and XAFS measurements. The layer formation is, thus, not only a function of the amphiphiles, but also depends strongly on the subphase concentration. The structures formed at the interface might be produced by a combined adsorption of lepidocrocite crystals and an interfacial aggregation process.

By using iron(III) chloride solutions, a different behavior could be observed. This system showed only in the presence of Langmuir layers a formation of inorganic films. For bare interfaces, no adsorption could be achieved. Also, a critical surface pressure of $\Pi = 20\ \mathrm{mN/m}$ was a requirement for the interfacial adsorption. The layers forming at the interface in the presence of amphiphiles were amorphous with no long range ordering. The formation of thin films was proven to happen at anionic, cationic and non-ionic Langmuir layers. Only for the zwitter-ionic Layer the formation process was suppressed.

By the right choice of the sample parameters (concentration of $100\ \mathrm{mmol/L}$ and a stearic acid monolayer) an ordering, which is still far away from a crystalline phase, could be observed by XAFS measurements. These samples showed the formation of a second coordination shell with less iron content than for crystals of bulk iron hydroxides. The investigations showed no formation of closed inorganic films suggesting the formation of small particles at the interface.

During the aggregation process the Langmuir layer structure was recognized to be disturbed. This effect can mainly be attributed to ammonia as seen in the reference measurements. The presence of iron(III) chloride in the subphase influenced the properties of DPPA monolayers, which can be attributed to iron complexes interacting with the phosphate headgroup, thus, stabilizing the lateral structure.[168, 177]

The experiments utilizing polysiloxane layers showed the formation of amorphous aggregates even without ammonia. The membrane structure is penetrated by the aggregates adsorbing into the tailgroup and headgroup region. During this process the lateral structure keeps stable and only a decrease of the intensity of the diffraction peak can be observed. A further addition of ammonia increases the electron density more and leads to the destruction of the layer. The

healing effect of ammonia discussed in chapter 4.1 seems to be suppressed in the presence of iron(III) chloride which might be caused by iron complexes aggregating at the polysiloxane membrane.

A penetration can be avoided by using a mixture of ion(II) and iron(III) chloride solutions as subphases. The nucleation takes place at the headgroup region without the penetration of the tailgroup. The headgroup is still influenced by the aggregates which grow in the direction of the subphase. During these measurements, again no crystalline material could be found to form at the interface. In analogy to the observations made for iron(II) chloride, crystal structures could be observed to form in case of elevated iron concentrations as observed by P. Degen, Physikalische Chemie II, TU Dortmund. This again shows the strong dependence on the subphase concentration of the iron chlorides.

The results present a survey of the parameters influencing the formation of inorganic films at interfaces from iron salt solutions. The results discussed above clearly show the complexity of the system. The concentration of the iron salt solution has a differing influence for the two salts and also the Langmuir layers. The studies on the low iron(II) chloride solution hint predominately at the influence of electrostatic forces on the formation process as only interfacial growth was observed for DPPA amphiphiles. For solutions containing trivalent ions this is not true any more as the in solution formed complexes seem to have a greater influence on the formation of the inorganic films.

6. Surface adsorption of nanoparticles controlled by surfactants

Control over the properties of fluid interfaces is of great interest for applications utilizing systems with high specific surface areas. The stability of e.g. foams or emulsions can be influenced by adding ionic or non-ionic surfactants or colloidal particles.[8, 89, 197] Moreover, the research on the combination of surfactants and particles shows great opportunities due to synergetic effects highlighting the relevance of this research field.[198, 199]

On the one hand, in systems where only surfactants are present the properties of the fluid interface depend on the thermal equilibrium and dynamics of the adsorption and desorption of the surfactants. However, if colloids are accumulating at fluid interfaces the inter particle interaction can cause self assembly or aggregation altering the interfacial properties significantly.[200] But also the size of the adsorbing particles is crucial. The particles must have a sufficient size for a successful stabilization of the fluid interface.[201] Consequential the mixing of different types of systems could induce changes in the adsorption process at the interface thus resulting in unique interfacial properties. The most important factors controlling the fluid interface in this context are the adsorption of the surfactant to the surface of the particles, the influence of the surfactant on the interaction of the particles in solution, and the effect of the particles surfactant interaction on the interface properties.[202]

Rheological measurements on the composite system of iron oxide nanoparticles (maghemite, γ-Fe_2O_3) in the presence of sodiumdodecylsulfate (SDS) showed an increased adsorption of the nanoparticles at the interface which depends on the ratio of the surfactant and nanoparticles in solution.[203] Surface shear rheological measurements showed increased elastic properties pointing to the formation of a film at the surface.[203] During these measurements the film was stressed until rapture. Subsequently, the measurements were repeated with the same sample showing again a film formation at the interface. By this it can be concluded that after the film was teared a reformation occurred. The enhanced surface activity is attributed to synergetic effects between the nanoparticles and surfactants. The surfactant is bound to the nanoparticle by electrostatic forces and the nanoparticle surface gets hydrophobic. As a consequence the nanoparticles are more likely to adsorb to the interface forming nanoparticle thin films. Further, the formation of aggregates was observed in bulk solutions of the nanoparticle surfactant mixture.[203] By adjusting the interaction of the surfactant nanoparticles composites the size of the aggregates can be influenced.

In order to gain information on the microscopic structure on the forming films XRR experiments on solution mixtures of surfactant and nanoparticles were performed. In these measurements the adsorption behavior of electrostatically stabilized iron oxide (maghemite, γ-Fe_2O_3)

and gold nanoparticles was studied which are charged positively and negatively, respectively. These particles were combined systemically with aqueous solutions of sodiumdodecylsulfate (SDS), cetyl trimethylammonium bromide (CTAB), and 2-dodecoxyethanol (Brij 35), being anionic, cationic and non-ionic surfactants, respectively.

The experiments were performed at the D8 laboratory diffractometer using a wavelength of 1.54 Å. The samples were prepared by mixing solutions of nanoparticles with solutions of the surfactants. The concentrations mentioned in the following are the resulting concentrations in the final solution. The samples were placed in a sample cell which was flushed with helium in order to suppress air scattering and evaporation.

The study on the nanoparticle solutions was performed within the collaboration with the group of Prof. Metin Tolan (TU Dortmund) and Prof. Heinz Rehage (TU Dortmund). Part of the presented results were published as: Patrick Degen, D. C. Florian Wieland, Sabine Leick, Michael Paulus, Heinz Rehage and Metin Tolan *Effect of magnetic nanoparticles on the surface rheology of surfactant films at the water surface*. Soft Matter 2011, **7**, 7655.

In following chapter the adsorption behavior of iron oxide nanoparticles is investigated in the presence of different surfactants. This part is followed by the study of the adsorption behavior of gold nanoparticles under varying surfactant additives. The chapter is finished by the conclusion and discussion of the observations made.

6.1. Iron oxide nanoparticles

The XRR experiments were performed using solutions of nanoparticles with a solid fraction of iron oxide of 0.05 wt%. The concentration of SDS was adjusted to $0.01\ \mathrm{mmol/L}$ and $20\ \mathrm{mmol/L}$, respectively. These concentrations were chosen because the surface rheological measurements showed a strong increase of the elastic moduli at a SDS concentration of $0.01\ \mathrm{mmol/L}$. In contrast to this at a SDS concentration of $20\ \mathrm{mmol/L}$ no increase was monitored.

First experiments of pure nanoparticle solution without the presence of surfactants showed no adsorption at the interface. The obtained XRR data on solution of SDS with a concentration of $0.01\ \mathrm{mmol/L}$ together with reference data of a pure SDS solution were normalized by the Fresnel reflectivity and are shown in the appendix figure C.4. The electron densities acquired by refinement of the data are depicted in figure 6.1. The time t denotes the point between preparation of the sample and the end of the measurement. The data show a strong increase of the electron density in a region of 90 Å below the interface after the first reflectivity measurements. By comparing these data to the results of a pure SDS solution the adsorption of the nanoparticles to the interface is obvious. In order to extract the size of the particles an electron density profile was modeled theoretically. Because the size of the nanoparticles is logarithmic-normal (log-normal) distributed a model was constructed consisting of spheres being weighted by a

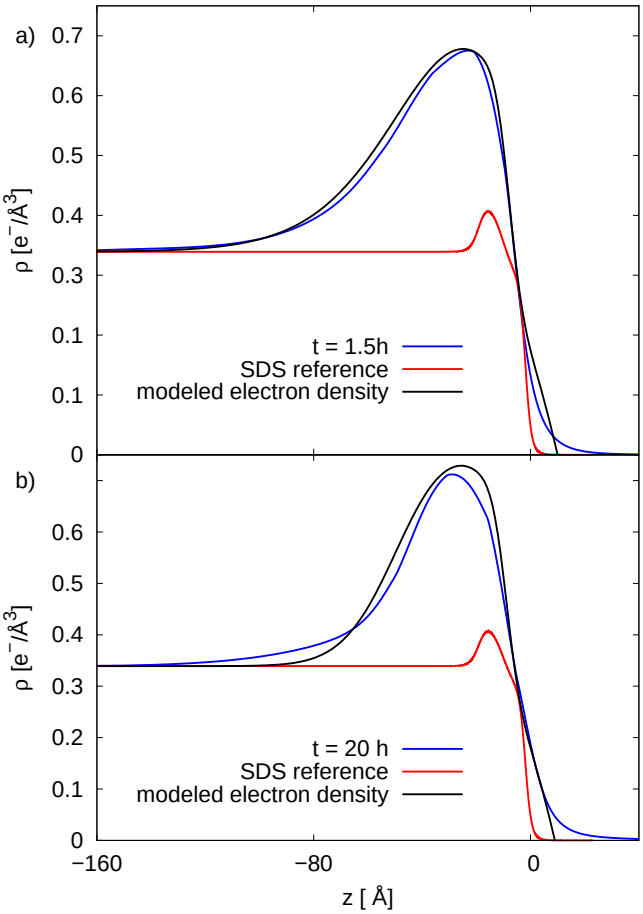

Figure 6.1.: Electron density profiles on solutions of 0.05 wt% γ-Fe_2O_3 and 0.01 mmol/L SDS solution obtained by the refinement of the reflectivity. The data was recored at different times after the preparation. Additional the electron density profile of spheres with log-normal distribution is drawn. a) t = 1.5h b) t = 20h.

log-normal distribution function.[204] This distribution is defined by

$$\xi(\Delta\mu, \mu, r_i) = \frac{u}{\sqrt{2\pi}\ln(\Delta\mu) r_i} \exp\left(-\frac{1}{2}\left(\frac{\ln(\frac{r_i}{\mu})}{\ln(\Delta\mu)}\right)^2\right), \tag{6.1}$$

with the most probable particle radius μ, the scaling amplitude u, and the width of the particle distribution $\Delta\mu$. The electron density profile $ED(z)$ was calculated via

$$ED(z) = \sum_i [(2\pi r_i z - \pi z^2)\xi(r_i)] \tag{6.2}$$

with $z \leq r_i$. The parameters obtained by refining equation 6.2 to the data are summarized in table 6.1. The resulting electron density is shown in the figure 6.1a. The sample was left for 18.5 hours and a second reflectivity was recorded afterwards. The resulting electron density is shown in figure 6.1b. By comparing the obtained profiles it gets obvious that the electron density increases further accompanied by a decrease of the width of the adsorbed layer. This density profile was again modeled by a log-normal weighted sphere distribution. The obtained

parameters are given in table 6.1 as well.

The data suggest an enhancement of adsorbed nanoparticles at the interface with time as the electron density of the layer increases. A side effect seems to be a decrease of the width of the adsorbed nanoparticle layer. But these results have to be reviewed with precaution. For a successful modeling of the electron density profile 6 slabs had to be used resulting in 25 parameters which had to be adjusted. Further the q range was only accessible up to 0.2 Å^{-1}. The reason for this is the high fluorescence emission from the sample. The absorption edge of iron lies at 7.9 keV which is only 0.1 keV beneath the X-ray energy used. As a result the background is enlarged in these experiments reducing the accessible q range.

	t = 1.5 h	t = 20.0 h
$\Delta\mu$	1.35 ± 0.02	1.2 ± 0.03
μ [Å]	32 ± 0.5	32 ± 0.5

Table 6.1.: Parameters of the log-normal distribution used for simulating the electron density profiles of iron oxide nanoparticles for different adsorption times.

Further experiments were performed for a solution of nanoparticles and increased SDS concentration of $20\ \text{mmol/L}$. The electron density profiles show the adsorption of SDS to the interface alone. No thin film composed of nanoparticles forms at these conditions, see figure appendix C.1(b). Similar observations were made when using CTAB and Brij solutions. Figure C.2(b) and figure C.2(b) of the appendix show the formation of a sole surfactant adsorption layer independent on the presence of nanoparticles.

6.2. Gold nanoparticles

The experiments on the gold nanoparticles utilized aqueous solutions with different concentrations. The electron density profiles obtained on solutions with a solid fraction of 0.05 wt% gold combined with $0.5\ \mu\text{mol/L}$ CTAB solutions are shown in the appendix figure C.6(b). The obtained data show no film formation at the interface. If the concentration of the nanoparticles and surfactant is changed by using 0.1 wt% solution and $1\ \mu\text{mol/L}$ CTAB solution a formation of a film can be observed. The obtained electron density profiles are depicted in figure 6.2. The electron density at the interface region increases with ongoing time until the process stops after 12.5 hours. For comparison an electron density originating from a pure CTAB layer is shown. The final state was again modeled by a log-normal distributed sphere ensemble using equation 6.2 and the obtained parameters are summarized in table 6.2.[204]

Similar experiments utilizing gold nanoparticle concentrations of 0.2 wt% and a CTAB con-

	t = 26.5 h
$\Delta\mu$	1.42 ± 0.02
μ [Å]	63.0 ± 0.5

Table 6.2.: Parameters of the log-normal distribution used for simulating the electron density profiles of the gold nanoparticles after 26.5 hours of adsorption.

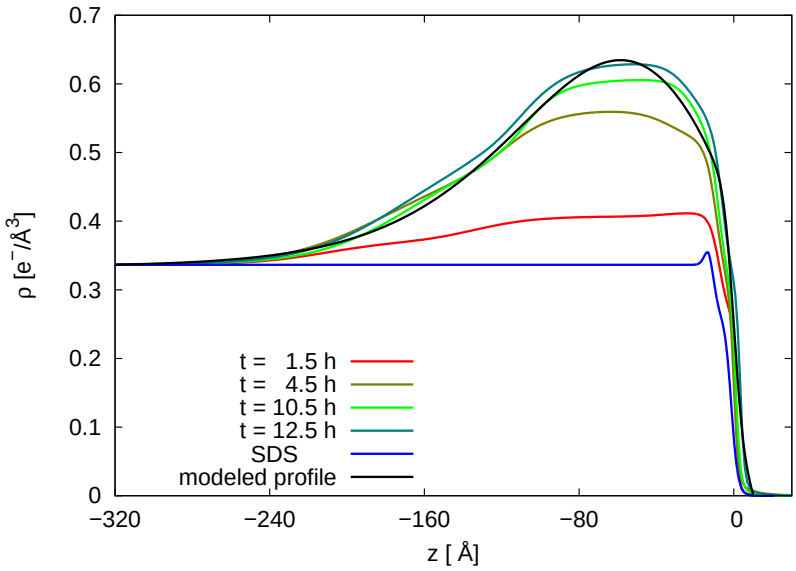

Figure 6.2.: Electron density profiles of the interface of 0.1 wt% gold nanoparticle solution and $1\ \mu\mathrm{mol/L}$ CTAB solution obtained by the refinement of the reflectivity data. As reference a density profile of a pure SDS solution is drawn. Additionally an electron density profile generated by summing log-normal weighted spheres distribution is shown.

centration of $1\ \mu\mathrm{mol/L}$ showed a faster adsorption. The process was completed after 4.5 h, see figure C.6(b). Subsequent experiments were performed using nanoparticle solution in combination with SDS and without surfactant, see appendix figure C.9(a) - C.12(a). The data show no formation of nanoparticles thin films as expected.

6.3. Discussion and Conclusion

The adsorption of nanoparticle thin films can be controlled by surfactants in the solution as shown by the experiments. By adjusting the concentrations of the surfactant the adsorption behavior of nanoparticles can be tuned. The observations made can be explained by an electrostatic interaction of the ionic surfactant molecules with the oppositely charged nanoparticles. As a result the composite system tends to a stronger interfacial adsorption. The interaction of the surfactant and nanoparticles leads to the formation of surfactant nanoparticles composites with increased hydrophobic interaction at the particle surface.

The surface of the iron oxide nanoparticle is positively charged which explains the adsorption behavior by using negatively ionic surfactants of SDS. In this system a nanoparticle layer can be observed at the interface. The experiments showed a dependence on the ratio of the number of SDS molecules to those of the number of nanoparticles in solution. If the amount of SDS is low in the solution only few molecules bind to the nanoparticles thus increasing the interfacial adsorption only slightly, see figure 6.3. As a result no film formation can be induced. Vice versa a too high concentration of the SDS solution also prevents a film formation. At this point a double layer of SDS is formed around the nanoparticle as shown in the right of figure 6.3. A SDS layer forms at the nanoparticles surface. But SDS molecules which are still in solution continue to

adsorb to the surface due to the interaction of the hydrophobic groups. By this the hydrophobic forces are neutralized.

The system offers the unique possibility to tune the wettability of the nanoparticles by adjusting the surfactant concentration. This is highly important for the stabilization of liquid-liquid interfaces. At these interfaces an optimal stabilization is observed if the particles are wetted each with 50 % of the organic and 50 % of the inorganic phase.[201]

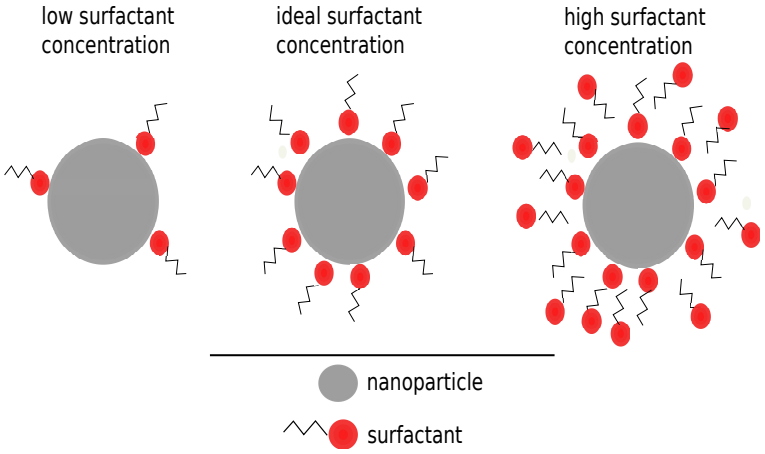

Figure 6.3.: Sketch of the composite nanoparticle structure under different solution conditions.

The diameter of the iron oxide nanoparticles was determined by DLS measurements to be 16 nm.[203] A transmission electron microscopy (TEM) image was taken by P. Degen, Physikalische Chemie II, TU Dortmund, of samples of the nanoparticles and is shown in figure 6.4. The particle size can be determined by evaluation of the image yielding a radius of 6.6 nm $\pm$ 1.5 nm. By comparing this radius with the size of 6.3 nm $\pm$ 0.5 obtained by modeling a log-normal weighted sphere distribution to the obtained data it can be concluded that only a monolayer of nanoparticles forms at the interface. The experiments show a deviation from the particles radius determined by DLS in comparison to the TEM data. The deviation of the DLS data can be attributed to an ion and hydration shell surrounding the nanoparticle and affecting its diameter thus enhancing virtually the particle radius. This happens because in DLS experiments the diameter is determined indirectly by measuring the diffusion speed of the particles under consideration.

If the positively charged nanoparticles were combined with CTAB and Brij solutions no film formation was observed. For CTAB the Coulomb repulsion of the equally charged nanoparticles and surfactants prevented the formation of composite particles and therefore the film formation at the liquid-air interface. For the non-ionic Brij the same explanation can be applied. Because of the absence of electrostatic interactions between the nanoparticles and surfactant no nanoparticle composite forms.

The gold nanoparticles, in contrast to the iron oxide nanoparticles, exhibit a negative surface charge. This explains the adsorption behavior of the sample system by using cationic CTAB. The experiments showed the formation of thin films during a period of hours depending on the gold concentration. No film formation was observed when using SDS. The same explanation holds for

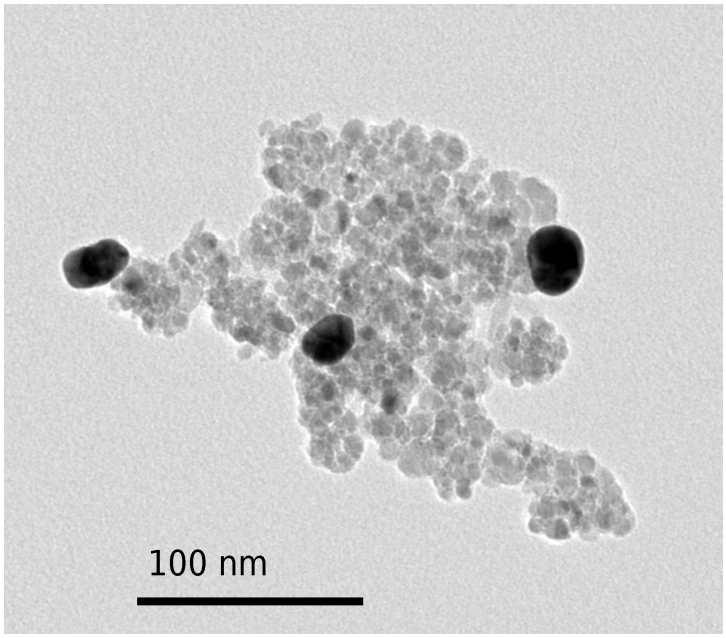

Figure 6.4.: TEM picture of iron oxide nanoparticles.

this composite system as for the iron oxide nanoparticle solution. The electrostatic interactions between the positively charged CTAB and the negatively charged gold nanoparticles induces the formation of a nanoparticle composite which adsorbs in the following to the interface. The thin film was modeled by a log-normal weighted sphere distribution yielding a diameter of 13.0 nm $\pm$ 0.1 nm. The particle diameter was determined by DLS experiments to 23 nm. The obtained size by the XRR experiments is smaller than the DLS data. Nevertheless the experiments on the iron oxide nanoparticles already showed that the particles diameter determined by DLS are too large. It can also be stated that in the gold-surfactant composite system a monolayer of nanoparticles forms.

The slower film formation rate for gold nanoparticles can be attributed to a low nanoparticle concentration. As mentioned, a finished film formation was achieved in 4.5 hours by using higher gold nanoparticle concentrations. The concentrations denoted above belong to the total amount of gold in solution but give no clue about the actual number of nanoparticles. An estimation of the number can be made by using the radii of the nanoparticles obtained by the XRR data. The volume of a nanoparticle is calculated on the basis of the most proper radius μ by neglecting the radii distribution. The concentration of gold nanoparticles can be calculated to be $1.25 \cdot 10^{20}$ L^{-1}. By doing this for the iron oxide nanoparticles a concentration of $5.47 \cdot 10^{20}$ L^{-1} is obtained. The concentration of the iron oxide particle is roughly a factor 5 higher as for the gold nanoparticles which might explain the faster kinetics. Further the adsorption of the gold nanoparticles might be slowed down due to the larger diameter of the nanoparticles as the film formation process is controlled by diffusion. The Stokes-Einstein diffusion constant is proportional to the inverse particle radius.[1] [205] As a consequence the diffusion kinetics of the gold nanoparticles is slowed down by a factor of 1.7 in comparison to the iron nanoparticles because of the higher diameter.

[1] $D = \frac{k_b T}{6\pi\nu R_0}$; k_b Boltzmann constant, T temperature, ν viscosity, R_0 hydrodynamic radius

7. Summary & Outlook

Aqueous solution-gas interfaces were investigated by means of in-situ X-ray scattering techniques concerning structural changes through adsorption processes. Different parameters like the subphase composition or the solution's pH value were changed in order to modify basic conditions of the film growth processes. Further, an approach combining XRR, GID, XAS and ex-situ techniques was made in order to obtain a comprehensive picture of the samples on different length scales. By this, a class of parameters influencing the growth process were obtained.

The structure of polysiloxane membranes at the liquid-air interface was studied regarding the influence of the subphase's pH value. The lateral cross linking of the polysiloxane network is inhibited under acidic conditions and the presence of loose monomers forming a Langmuir layer was observed. It can be concluded that the hydrolysis reaction of the trichlorosilane group, which is slowed down under these subphase constitutions, controls the network formation. If the subphase's pH value of such a sample system is increased by adding ammonia to the gas phase, the hydrolysis equilibrium is shifted, thus, increasing the amount of reactive monomers enabling the membrane formation process. The micro crystalline structure of the polysiloxane network in the final state is similar to the structure observed on neutral or alkaline subphases. Under neutral subphase conditions the membranes are composed of patches with voids between them. A subsequent addition of ammonia causes a reduction of these voids resulting in a better arrangement of the single patches. However, the micro crystalline structure of the patches does not alter. The GID experiments on acidic subphases showed that the tailgroups of the single OTS monomers are not well aligned parallel to each other and that they still posses still some degree of disorder. An increase of the surface pressure could decrease this disorder and align the tailgroups parallelly. Enabling the lateral cross-linking in this state could lead to the formation of a membrane with larger patch size.

Films of amphiphiles which are not joined by covalent bonds, were subject to investigations regarding the influence of the interfacial pH value on their film structure. These experiments showed that ammonia has mainly a destructive impact on the film arrangement. Only for EPC a different behavior was observed as this amphiphile showed a phase transition to a condensed state.

The formation of inorganic thin films from solutions containing iron chloride salts, either iron(II) chloride or iron(III) chloride, showed a differing growth process depending on the oxidation state of the iron species present in solution.

By using subphase solutions containing iron(III) chloride, the growth of inorganic films composed of small aggregates was observed under cationic and anionic as well as under non-ionic monolayers reflecting little influence of the headgroup charge or composition. This observation

can be understood by the different iron species which are formed in aqueous media offering a variety of possible interactions of the iron species with the Langmuir layers. A hint for different nucleation and growth process at the Langmuir layers can be identified from the differing shape of the electron density profiles. However, all layers forming lack long range order as shown by XAS and XRD experiments. An increase in the local order around the iron atom could be proven by XAS experiments under Langmuir layers of stearic acid and iron(III) chloride concentrations of $100\ \mathrm{mmol/L}$. Under these experimental conditions the evolution of a second coordination shell possessing 2 iron atoms in average could be identified.

At interfaces of iron(II) chloride solutions with a concentration of $0.1\ \mathrm{mmol/L}$ the formation of amorphous aggregates could be induced by employing negatively charged Langmuir layers of DPPA. Although aggregates forming in the bulk solution could be seen by DLS measurements. An accumulation of these aggregates at the interface can be ruled out due to the different sizes of the aggregates observed in the solution and the structures nucleating at the interface. At zwitter-ionic as well as at the cationic Langmuir layers no formation of inorganic films was seen. This indicates mainly an electrostatic interaction. A major impact on the film growth was identified being the iron(II) chloride concentration. The formation of lepidocrocite crystals was observed at the bare interface of iron(II) chloride solutions with a concentration of $1\ \mathrm{mmol/L}$. The modification of the solution interfaces with Langmuir layers induced no change in the growing polymorph resulting still in the formation of lepidocrocite. For iron(II) chloride solutions with a concentration of $100\ \mathrm{mmol/L}$ the formation of a composite structure was observed when Langmuir layers of stearyl alcohol were employed. The XRD and SEM data of this sample system indicate a growth mechanism where first an amorphous structure is formed and a subsequent transition to the growth of lepidocrocite occurs. However, when Langmuir layers of stearic acid were employed the growth of magnetite along with lepidocrocite could be detected. Thus, a competitive adsorption of lepidocrocite, which is formed in the bulk phase, with the nucleation of magnetite at the interface can be proposed for this sample system.

Further studies are needed to get a more detailed view on the single aspects of the nucleation and growth process. No optimal parameters are known for the growth of crystalline films from iron(III) chloride solutions. As the saturation level in the vicinity of interface could be one critical factor as indicated by the XAS data, experiments on higher iron(III) chloride solutions or the use of Langmuir layers having a higher surface charge, thus, increasing the concentration highly at the interface, could shed light on the aspect whether the formation of crystals can be induced for this sample system. Furthermore, for the controlled growth of crystalline films from iron(II) chloride solutions, the formation of lepidocrocite has to be suppressed in the bulk solution. Investigations using either buffer solutions or solutions with a higher pH value could, thus, inhibit the formation of lepidocrocite in bulk solution. By this, it could be clarified in which way the magnetite accumulates under stearic acid as the data hinted to the oriented growth of this polymorph.

Thin films of nanoparticles could be generated at the liquid-air interface by using solutions containing nanoparticles and surfactants. The adsorption of the nanoparticles to the interface was proven to depend on the ratio of the nanoparticle and the surfactant concentration and on the charge states of the components. If nanoparticles with a positive surface potential are em-

ployed the adsorption to the interface occurs by using anionic surfactants whereby for nanoparticles with a negative surface potential cationic surfactants are needed. These experiments illustrate that the wettability of the nanoparticles can be tuned by the surfactant-nanoparticle ratio, thus, changing the adsorption properties of the particles. This adsorption process is further controlled by diffusional processes and the time for the film formation depend on the solution concentration and with this on the nanoparticle concentration.

The experiments give only insight into the vertical density profile and no conclusion on the lateral order can be made. As rheological measurements showed a reversible network formation for these films after stress load the lateral structure on a microscopic scale is of great interest. This could help to understand the process by which the film encounters the stress and reforms. These measurements can be best performed at the solution-air interface by in-situ grazing incidence small angle scattering measurements. Here the lateral order of the nanoparticles can be probed in-situ even when the film is stressed giving information on the deformation and reformation of the film structure.

8. Concomitantly performed projects

Besides the investigations which were performed in the framework of this thesis, a further project was continued collaterally, which was started during the author's Diploma thesis. This work was conducted in the collaboration of the groups of Prof. Fischer (Ruhr-Universität Bochum) and Prof. Wöll (Karlsruher Institut für Technik) and investigated structural properties of metal-organic frameworks (MOF). These hybrid structures are a fast developing field in material sciences as they offer exciting properties for advanced applications. Key features of these structures are their high porosity and the channels in the framework which opens the possibility for the application as molecular sieves or for gas purification. These crystalline compounds gained attention due to their possibilities for modification which are found in their principle design. The network of these structures is composed of two parts being an organic ligand and an inorganic metal node. The crystal is, thus, formed by joining the metal nodes through the organic ligands by coordination bonds. The properties of the so formed network can be influenced by the modification of the organic ligand without changing the three dimensional structure. The other way around these building blocks offer the opportunity to fabricate crystals with a desired structure. The controlled fabrication of MOFs as coatings is, thus, a key ability for advanced materials like membranes and detailed knowledge of the process parameters leading to high quality coatings is essential. A special class of these MOFs exhibit structural flexibility upon external stimuli like the adsorption of guest molecules to the network. The integration of such flexible MOF structures into coatings is of great interest as it might lead to the fabrication of sensing devices and smart membranes.

In a first step of this project samples were investigated in order to get insight into the quality of the MOF coatings in general and to examine if oriented growth could be achieved. This step is crucial as for membrane applications the control over the channel direction is needed. In the course of this project a newly developed MOF [Zn_2 (BME-bdc)$_2$(dabco)](n) was first characterized as a powder sample regarding the structural transition and flexibility upon adsorption of CO_2 at $195\ \mathrm{K}$. After the successful characterization, this flexible MOF was grown as coating onto substrates. Different aspects were investigated concerning the control of the growth direction along a distinct crystal axis and the CO_2 adsorption behavior. It could be shown that depending on the nucleation conditions the crystal axis which changes upon CO_2 adsorption could be either grown parallel to the interface or perpendicular, respectively, without losing the structural flexibility.

Intercalation in Layered Metal-Organic Frameworks: Reversible Inclusion of an Extended pi-System

Arslan, H.K., Shekhah, O., Wieland, D.C.F., Paulus, M., Sternemann, C., Schroer, M.A., Tiemeyer, S., Tolan, M., Fischer, R.A., Wöll, C.

Journal of the American Chemical Society Volume: 133 Issue: 21 Pages: 8158-8161

Step-by-step growth of highly oriented and continuous seeding layers of [Cu_2(ndc)$_2$(dabco)] on bare oxide and nitride substrates

Yusenko, K.,Meilikhov, M., Zacher, D., Wieland, F., Sternemann, C., Stammer, X., Ladnorg, T., Wöll, C. and Fischer, R.A.

Crystal Engineering Communications Volume: 12 Issue: 7 Pages: 2086-2090

Multiple phase-transitions upon selective CO_2 adsorption in an alkyl ether functionalized metal-organic framework-an in situ X-ray diffraction study

Henke, S., Wieland, D.C.F., Meilikhov, M., Paulus, M., Sternemann, C., Yusenko, K., Fischer, R.A.

Crystal Engineering Communications Volume: 13 Issue: 21 Pages: 6399-6404

A. Bragg rod analysis

Bragg rod analysis of the DPPA Langmuir layer

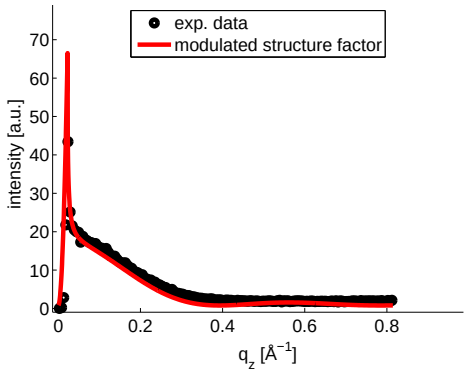

Figure A.1.: Bragg rod of a DPPA Langmuir layer on a pure water subphase at a lateral wavevector transfer of $q_{||} = 1.530\ \text{Å}^{-1}$. The circles denote the measured data, lines represent the fitted structure factor.

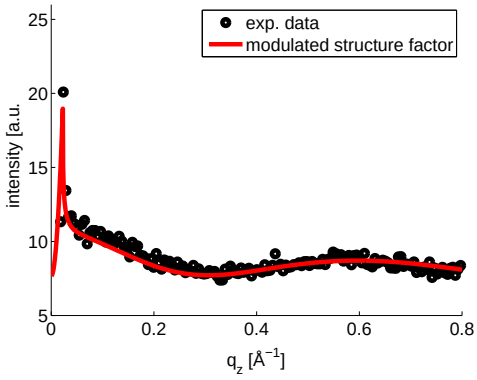

Figure A.2.: Bragg rod of a DPPA Langmuir layer on a pure water subphase at a lateral wavevector transfer of $q_{||} = 1.500\ \text{Å}^{-1}$ after addition of ammonia. The circles denote the measured data, lines represent the fitted structure factor.

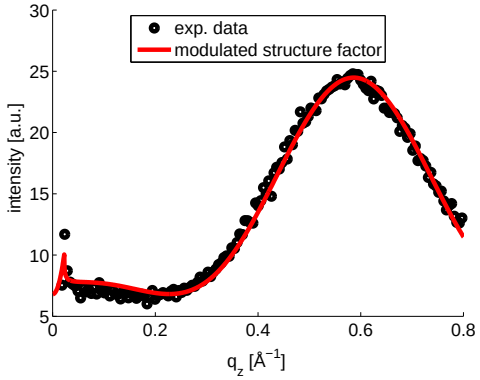

Figure A.3.: Bragg rod of a DPPA Langmuir layer on a pure water subphase at a lateral wavevector transfer of $q_{||} = 1.439\ \text{Å}^{-1}$ after addition of ammonia. The circles denote the measured data, lines represent the fitted structure factor.

Bragg rod analysis of the DPPC Langmuir layer

The deviations in the fitted structure factor can be explained as the approximation for the structure factor hold only for lipids in the free rotator phase.[119, 120] DPPC amphiphiles at an surface pressure of Π =20 mN/m are not in the free rotator phase. This could also induces changes in the intensity distribution along the rod explaining the difference.[124]

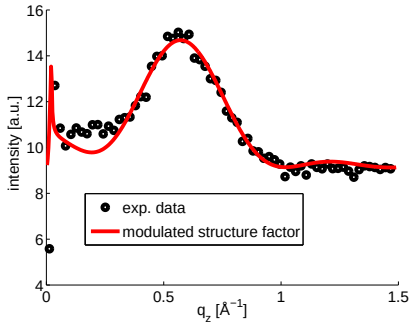

Figure A.4.: Bragg rod analysis of a DPPC Langmuir layer at a lateral wavevector transfer of $q_{||}$ = 1.414 Å. The circles denote the measured data, lines represent the fitted structure factor.

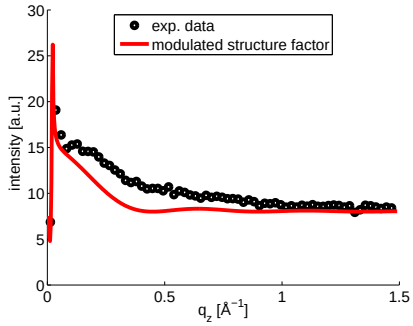

Figure A.5.: Bragg rod analysis of a DPPC Langmuir layer at a lateral wavevector transfer of $q_{||}$ =1.479 Å. The circles denote the measured data, lines represent the fitted structure factor.

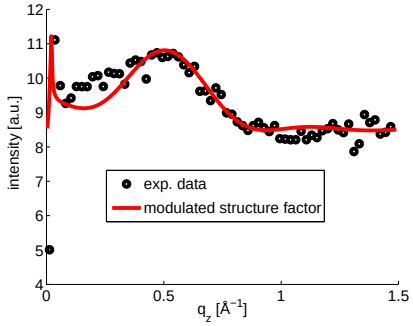

Figure A.6.: Bragg rod analysis of a DPPA Langmuir layer at a lateral wavevector transfer of $q_{||}$ = 1.405 Å after addition of ammonia. The circles denote the measured data, lines represent the fitted structure factor.

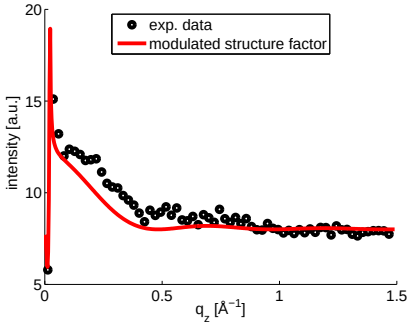

Figure A.7.: Bragg rod analysis of a DPPA Langmuir layer at a lateral wavevector transfer of $q_{||}$ = 1.476 Å after addition of ammonia. The circles denote the measured data, lines represent the fitted structure factor.

Bragg rod analysis of DPPC Langmuir layers deposited on iron(III) chloride solutions

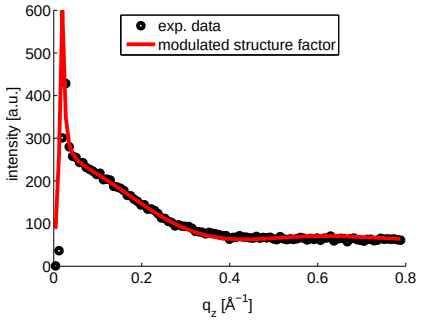

Figure A.8.: Bragg rod analysis of a DPPC Langmuir layer at a lateral wavevector transfer of $q_{||}$ =1.508 Å^{-1} on iron(III) chloride solutions. The circles denote the measured data, lines represent the fitted structure factor.

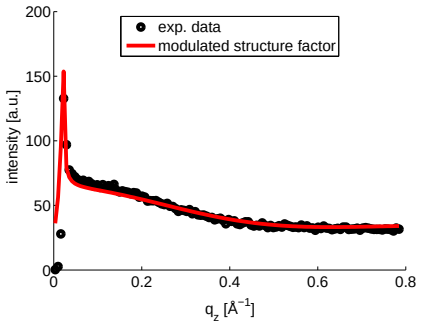

Figure A.9.: Bragg rod analysis of a DPPA Langmuir layer at a lateral wavevector transfer of $q_{||} = 1.407$ Å^{-1} on iron(III) chloride solutions after addition of ammonia. The circles denote the measured data, lines represent the fitted structure factor.

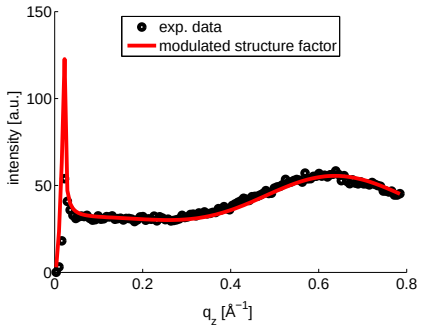

Figure A.10.: Bragg rod analysis of a DPPA Langmuir layer at a lateral wavevector transfer of $q_{||} = 1.478$ Å^{-1} on iron(III) chloride solutions after addition of ammonia. The circles denote the measured data, lines represent the fitted structure factor.

Bragg rod analysis of stearyl amide Langmuir layers deposited on iron(III) chloride solutions

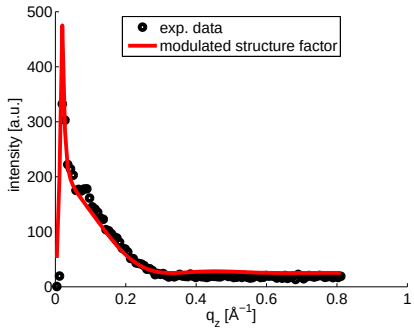

Figure A.11.: Bragg rod analysis of a stearyl amide Langmuir layer at a lateral wavevector transfer of $q_{||} = 1.416\,\text{Å}^{-1}$ on iron(III) chloride solutions. The circles denote the measured data, lines represent the fitted structure factor.

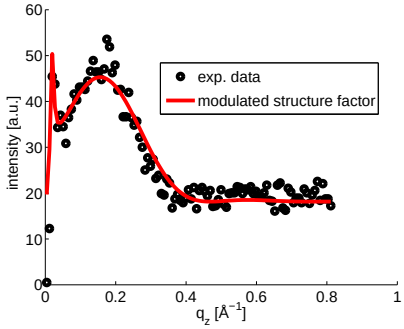

Figure A.12.: Bragg rod analysis of a DPPA Langmuir layer at a lateral wavevector transfer of $q_{||} = 1.537\,\text{Å}^{-1}$ on iron(III) chloride solutions. The circles denote the measured data, lines represent the fitted structure factor.

B. Iron(III) chloride solutions

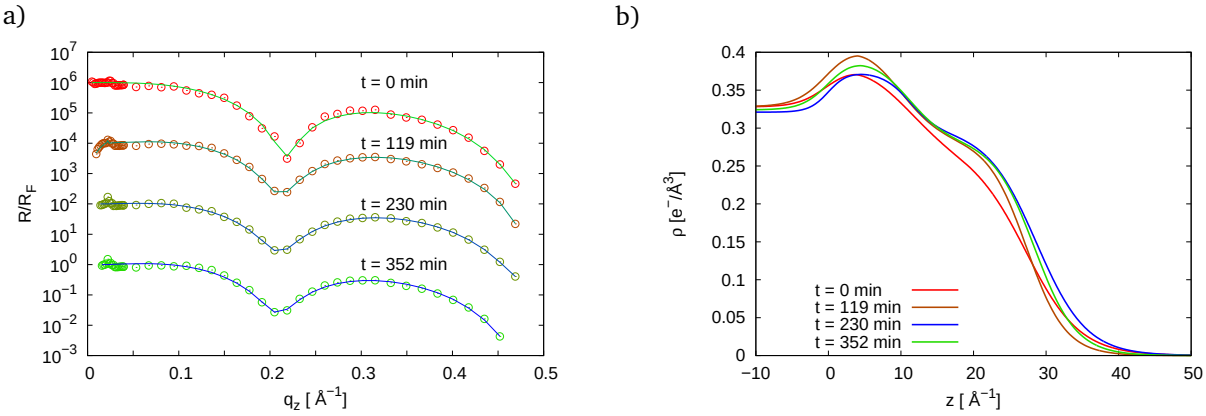

Figure B.1.: a) Fresnel normalized reflectivities of DPPC monolayers at a surface pressure of Π=40 mN/m on an iron(III)chloride subphase. b) Electron density profiles obtained by refining the reflectivity data.

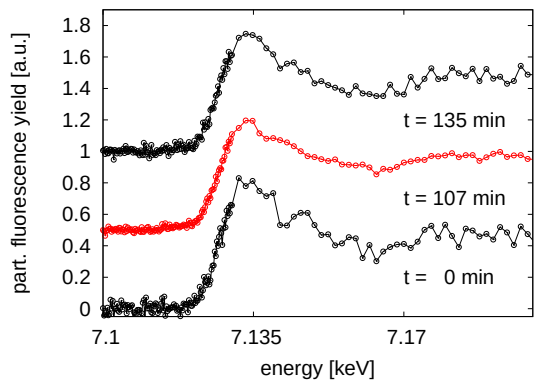

Figure B.2.: Near edge structure of the iron K-edge of an iron(III) chloride subphase with a concentration of 1 mmol/L .

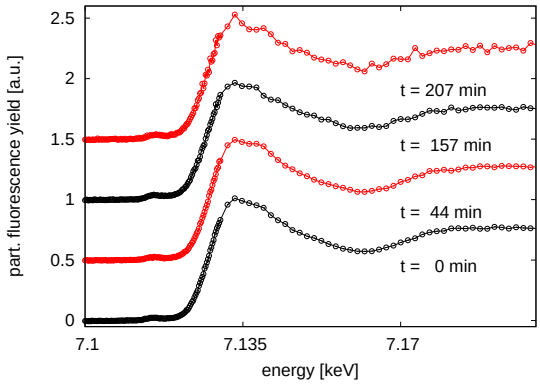

Figure B.3.: Near edge structure of the iron K-edge of an iron(III) chloride subphase with a concentration of 100 mmol/L .

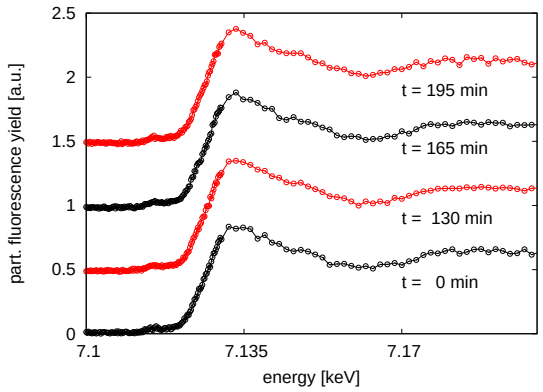

Figure B.4.: Near edge structure of the iron K-edge of an iron(III) chloride subphase with a concentration of $1\ \mathrm{mmol/L}$ and a stearyl alcohol monolayer present at the interface.

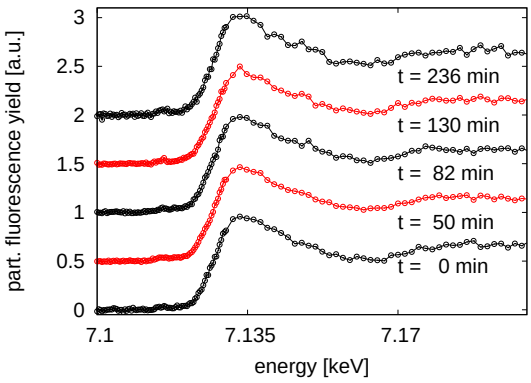

Figure B.5.: Near edge structure of the iron K-edge of an iron(III) chloride subphase with a concentration of $1\ \mathrm{mmol/L}$ and a stearic acid monolayer present at the interface.

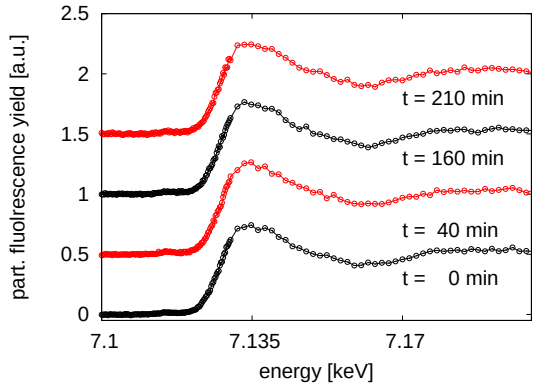

Figure B.6.: Near edge structure of the iron K-edge of an iron(III) chloride subphases with a concentration of $100\ \mathrm{mmol/L}$ and a stearic acid monolayer present at the interface.

C. Nanoparticles

Iron oxide nanoparticles

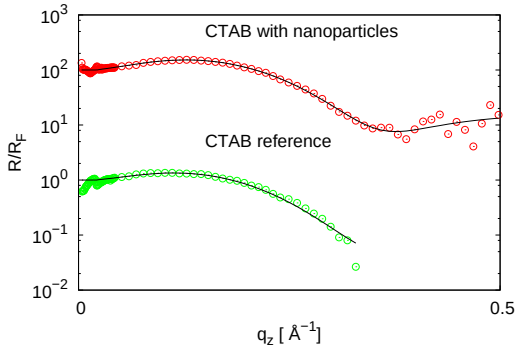

(a) Fresnel normalized XRR data.

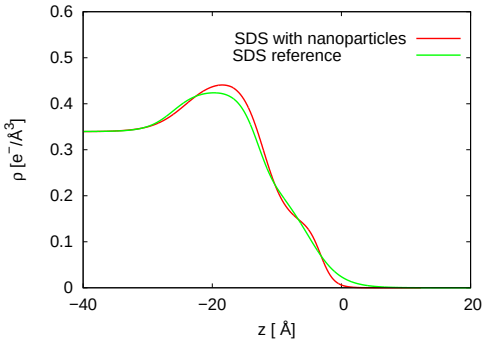

(b) Electron density profiles obtained by the refinement of the reflectivity data.

Figure C.1.: Experiments on solutions containing iron oxide (γ-Fe2O3) nanoparticles with a concentration of 0.05 wt% and SDS with a concentration of $20\ \mathrm{mmol/L}$.

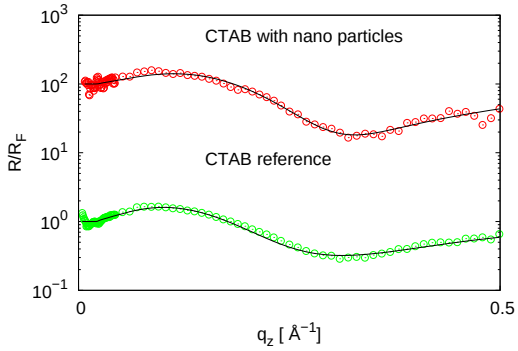

(a) Fresnel normalized XRR data.

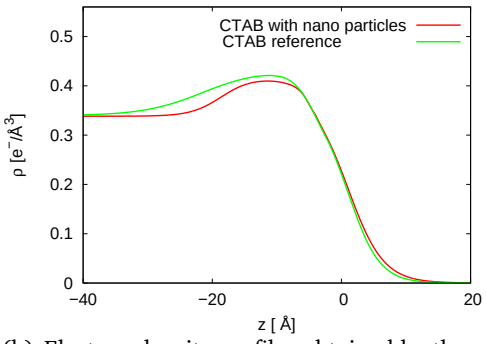

(b) Electron density profiles obtained by the refinement of the reflectivity data.

Figure C.2.: Experiments on solutions containing iron oxide (γ-Fe_2O_3) nanoparticles with a concentration of 0.05 wt% and a CTAB concentration of $2.5\ \mathrm{mmol/L}$.

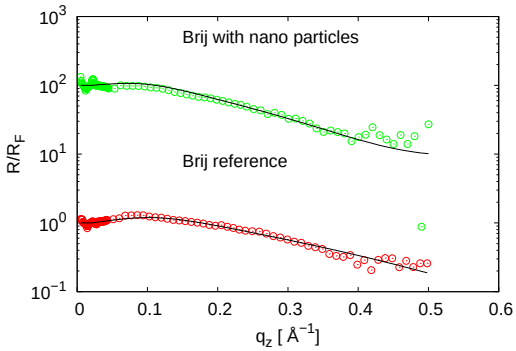

(a) Fresnel normalized XRR data.

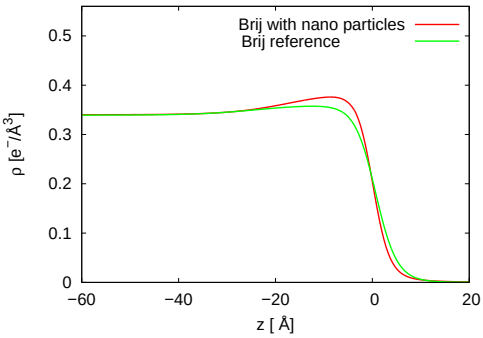

(b) Electron density profiles obtained by the refinement of the reflectivity data.

Figure C.3.: Experiments on solutions containing iron oxide (γ-Fe_2O_3) nanoparticles with a concentration of 0.05 wt% and a Brij concentration of $2.5\ \mathrm{mmol/L}$.

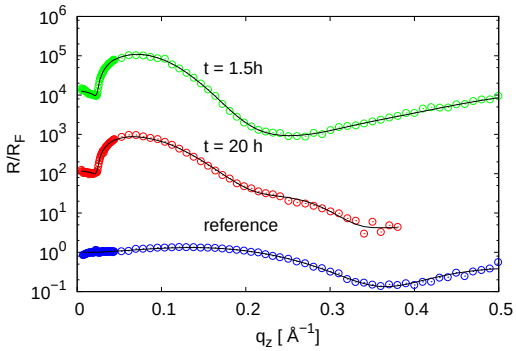

Figure C.4.: XRR data from the interface of an aqueous iron oxide nanoparticle (γ-Fe_2O_3) solution with a concentration of 0.05 wt%. The concentration of SDS was $0.01\ \mathrm{mmol/L}$.

Gold Nanoparticles

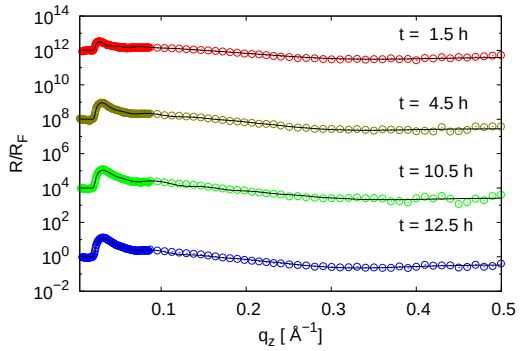

Figure C.5.: XRR data from the interface of an aqueous gold nanoparticle solution with a concentration of 0.1wt% and a CTAB concentration of $1\ \mu\mathrm{mol/L}$.

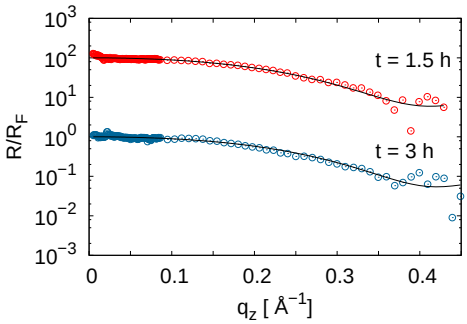

(a) Fresnel normalized XRR data.

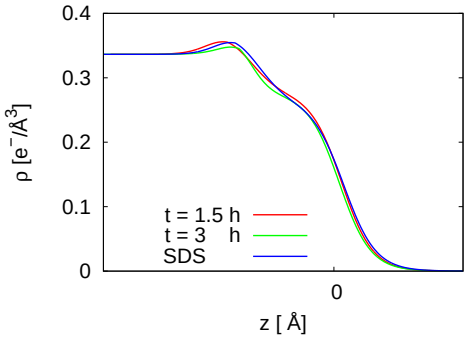

(b) Electron density profiles obtained by the refinement of the reflectivity data. The electron density profile of the interface of a pure CTAB solution is shown for comparison.

Figure C.6.: Experiments on solutions containing gold nanoparticles with a concentration of 0.05 wt% and a CTAB concentration of $1\ \mathrm{mmol/L}$.

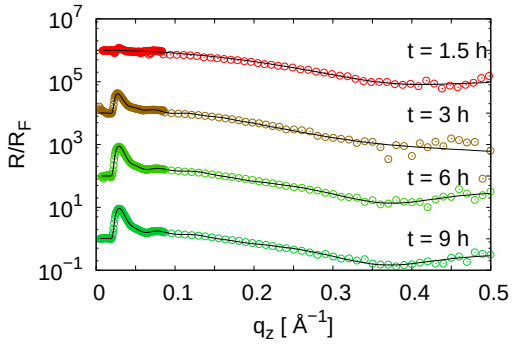

(a) Fresnel normalized XRR data.

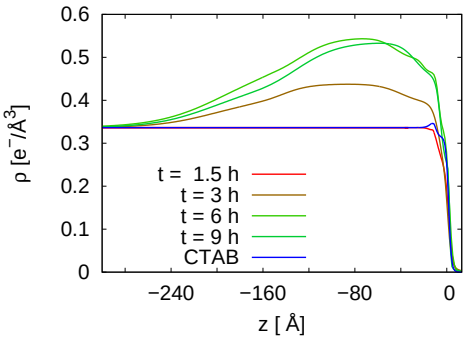

(b) Electron density profiles obtained by the refinement of the reflectivity data. The electron density profile of the interface of a pure CTAB solution is shown for comparison.

Figure C.7.: Experiments on solutions containing gold nanoparticles with a concentration of 0.1 wt% and a CTAB concentration of $1\ \mathrm{mmol/L}$.

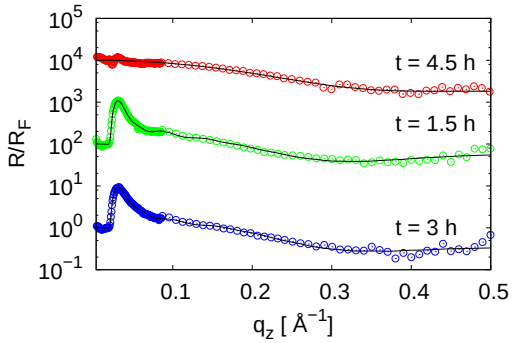

(a) Fresnel normalized XRR data.

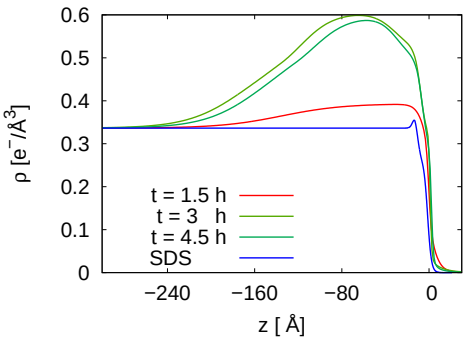

(b) Electron density profiles obtained by the refinement of the reflectivity data. The electron density profile of the interface of a pure CTAB solution is shown for comparison.

Figure C.8.: Experiments on solutions containing gold nanoparticles with a concentration of 0.1 wt% and a CTAB concentration of $1\ \mathrm{mmol/L}$.

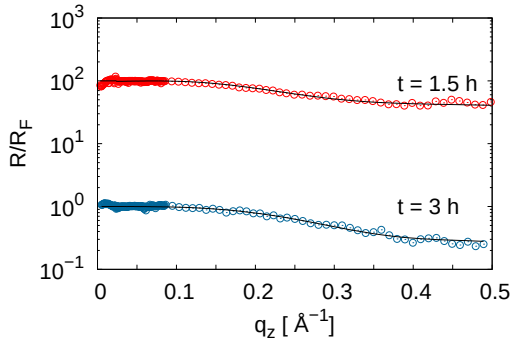

(a) Fresnel normalized XRR data.

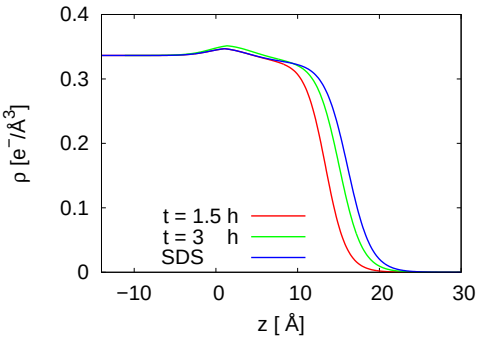

(b) Electron density profiles obtained by the refinement of the reflectivity data. The electron density profile of the interface of a pure SDS solution is shown for comparison.

Figure C.9.: Experiments on solutions containing gold nanoparticles with a concentration of 0.1 wt% and a SDS concentration of $0.01\ \mathrm{mmol/L}$.

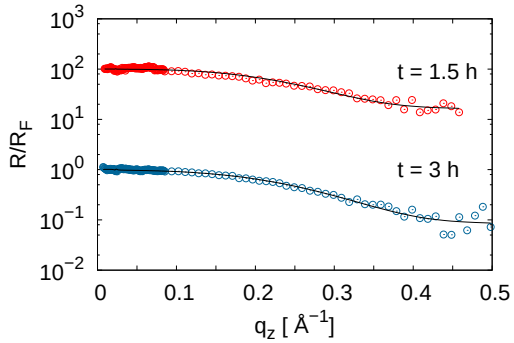

(a) Fresnel normalized XRR data.

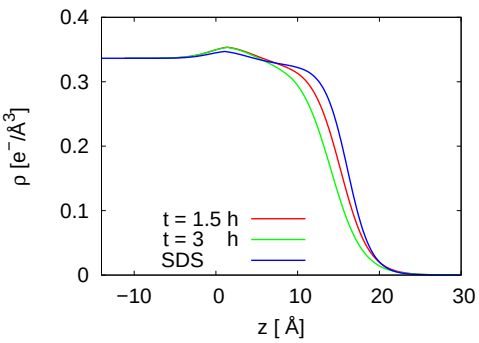

(b) Electron density profiles obtained by the refinement of the reflectivity data.

Figure C.10.: Experiments on solutions containing gold nanoparticles with a concentration of 0.1 wt% and a SDS concentration of $1\ \mathrm{mmol/L}$.

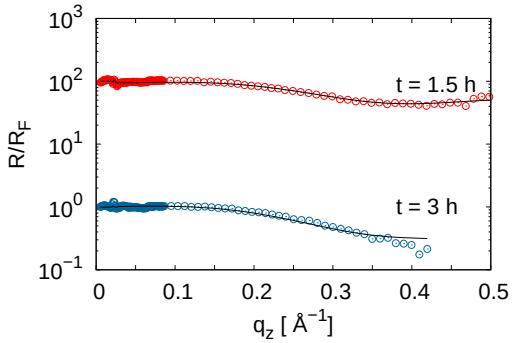

(a) Fresnel normalized XRR data.

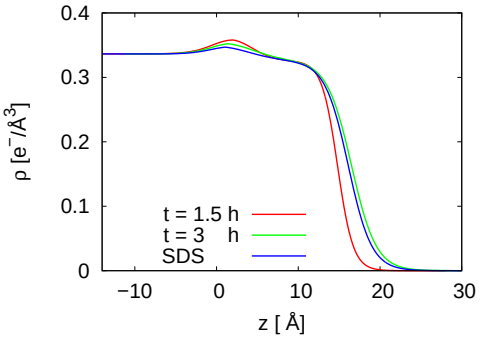

(b) Electron density profiles obtained by the refinement of the reflectivity data.

Figure C.11.: Experiments on solutions containing gold nanoparticles with a concentration of 0.2 wt% and a SDS concentration of $1\ \mathrm{mmol/L}$.

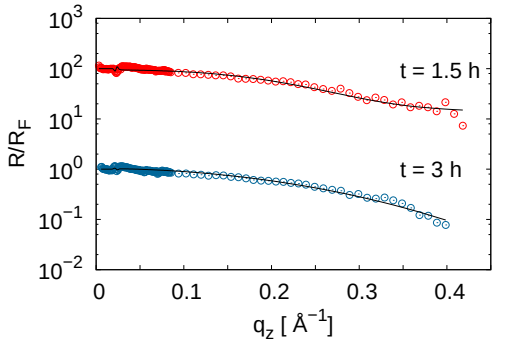

(a) Fresnel normalized XRR data.

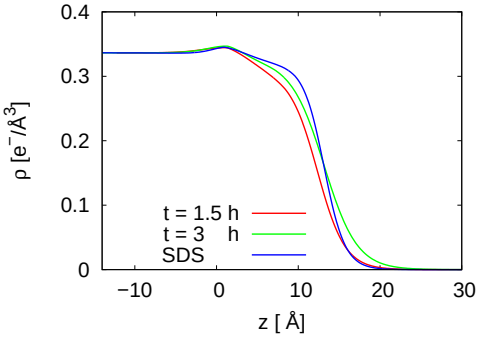

(b) Electron density profiles obtained by the refinement of the reflectivity data.

Figure C.12.: Experiments on solutions containing gold nanoparticles with a concentration of 0.1 wt% and a SDS concentration of $2\ \mathrm{mmol/L}$.

Bibliography

[1] M. Paulus. *Röntgenstreuung an Flüssigkeits-Gas Grenzflächen*. PhD Thesis. Universität Dortmund, 2006.

[2] J. Als-Nielsen and D. McMorrow. *Elemts of Modern X-Ray Physics*. Wiley, Weinheim, 2004.

[3] D.C. Koningsberger and R. Prins, editors. *X-ray absorption -Principles, Applications, Techniques of EXAFS, SEXAFS and XANES*. John Wiley and Sons, New York, 1988.

[4] S. Mann. *Biomineralisation; Principles and Concepts in Bioinorganic Materials Chemistry*. Oxford University Press, Oxford, 2001.

[5] An-Wu Xu, Yurong Ma, and Helmut Coelfen. Biomimetic mineralization. *Journal of Materials Chemistry*, 17:415–449, 2007.

[6] D. Marsh. Lateral pressure in membranes. *Biochimica et Biophysica Acta*, 4:1286, 1996.

[7] A. Rössler, G. Skillas, and S.E. Pratsinis. Nanopartikel — materialien der zukunft: Maßgeschneiderte werkstoffe. *Chemie in unserer Zeit*, 35:32, 2001.

[8] B.P. Binks and C.P. Whitby. Nanoparticle silica-stabilised oil-in-water emulsions: improving emulsion stability. *Colloids and Surfaces A-Physicochemical and Engenering Aspects*, 253:105–115, 2005.

[9] M.A. Schroer, J. Markgraf, D.C.F. Wieland, C.J. Sahle, J. Moeller, M. Paulus, M. Tolan, and R. Winter. Nonlinear pressure dependence of the interaction potential of dense protein solutions. *Physical Review Letters*, 106:178102–178105, 2011.

[10] P. Wernet, D. Testemale, J.L. Hazemann, R. Argoud, P. Glatzel, L.G.M. Pettersson, A. Nilsson, and U. Bergmann. Spectroscopic characterization of microscopic hydrogen-bonding disparities in supercritical water. *Journal of Chemical Physics*, 123:154503 154509, 2005.

[11] H. Lowenstam and S. Weiner. *On Biomineralization*. Oxford University Press, Oxford, 1989.

[12] F.C. Meldrum. Calcium carbonate in biomineralisation and biomimetic chemistry. *International Materials Reviews*, 48(3):187–224, 2003.

[13] N.A.J.M. Sommerdijk and G. de With. Biomimetic caco3 mineralization using designer molecules and interfaces. *Chemical Reviews*, 108:4499–4550, 2008.

[14] F. Brudevold, L.T. Steadman, and F.A. smith. Inorganic and organic components of tooth strucuture. *Annals of the New York Academy of Science*, 85:110–132, 1960.

[15] H.E. Harper and A.H. Knoll. Silica, diatoms, and cenozoic radiolarian evolution. *Geology*, 3:175–177, 1975.

[16] J. Miot, K. Benzerara, G. Morin, A. Kappler, M. Obst, G. E. Brown, Jr., and F. Guyot. Iron biomineralization by neutrophilic nitrate-reducing iron-oxidizing bacteria. *Geochimica et Cosmochimica Acta*, 73:A884, 2009.

[17] D.D. Archibald and S. Mann. Template minrealization of self assembled anisotropic lipid microstructures. *Nature*, 364:430–433, 1993.

[18] S. Mann, J.P. Hannington, and R.J.P. Williams. Phospholipid-vesicles as a model system for biomiernalization. *Nature*, 324:565–567, 1986.

[19] V.J. Wade, S. Levi, P. Arosio, A. Treffry, P.M. Harrison, and S. Mann. Influcce of site-directed modificatons on the formation of iron cores in ferritin. *Journal of molecular Biologie*, 221:1443–1452, 1991.

[20] L. Addadi and S. Weiner. Control and design principles in biological mineralization. *Angewandte Chemie- International Edition*, 31:153–169, 1992.

[21] F.C. Meldrum, B.R. Heywood, and S. Mann. Magnetoferritin - invitro synthesis of a novel magnetic protein. *Science*, 257:522–523, 1992.

[22] G. Falkenberg, G. Fleissner, K. Schuchardt, M. Kuehbacher, P. Thalau, H. Mouritsen, D. Heyers, G. Wellenreuther, and G. Fleissner. Avian magnetoreception: elaborate iron mineral containing dendrites in the upper beak seem to be a common feature of birds. *PloS one*, 5:e9231, 2010.

[23] S. Mann, N.H.C. Sparks, R.B. Frankel, D.A. Bazylinski, and H.W. Jannasch. Biomineralization of ferrimagnetic greigite (fe3s4) and iron pyrite (fes2) in a magnetotactic bacterium. *Nature*, 343:258–261, 1990.

[24] S. Mann, R.B. Frankel, and R.P. Blakemore. Structure, morphology and crystal-growth of bacterial magnetite. *Nature*, 310:405–407, 1984.

[25] S.G. Benner, C.M. Hansel, B.W. Wielinga, T.M. Barber, and S. Fendorf. Reductive dissolution and biomineralization of iron hydroxide under dynamic flow conditions. *Environmental Science & Technolgy*, 36:1705–1711, 2002.

[26] P. Wolber and G. Warren. Bacterial ice-nucleation proteins. *Trends in Biochemical Science*, 14:179–182, 1989.

[27] J.C. Weaver, Q. Wang, A. Miserez, A. Tantuccio, R. Stromberg, K.N. Bozhilov, P. Maxwell, R. Nay, S.T. Heier, E. DiMasi, and D. Kisailus. Analysis of an ultra hard magnetic biomineral in chiton radular teeth. *Materials Today*, 13:42–52, 2010.

[28] K.M. Towe and Lowenstam.H.A. Ultrastructure and develpment of iron mineralization in radular teeth of cryptochiton stelleri (mollusca). *Journal of Ultrastructure Research*, 17:1–17, 1967.

[29] A. Tsortos, S. Ohki, A. Zieba, R.E. Baier, and G.H. Nancollas. The dual role of fibrinogen as inhibitor and nucleator of calcium phosphate phases: The importance of structure. *Journal of Colloid and Interface Science*, 177:257–262, 1996.

[30] S. Mann, D.D. Archribald, J.M. Didymus, T. Douglas, B.R. Heywood, F.C. Meldrum, and N.J. Reeves. Crystallization at inorganic-organic interfaces - biominerals and biomemetic synthesis. *Science*, 261:1286–1292, 1993.

[31] S. Weiner and H. Lowenstam. Organization of extracellularly mineralized tissues: A comparative study of biological crystal growth. *Critical Reviews in Biochemistry*, 20:365–408, 1986.

[32] G. Falini, S. Albeck, S. Weiner, and L. Addadi. Control of aragonite or calcite polymorphism by mollusk shell macromolecules. *Science*, 271:67–69, 1996.

[33] AM Belcher, XH Wu, RJ Christensen, PK Hansma, GD Stucky, and DE Morse. Control of crystal phase switching and orientation by soluble mollusc-shell proteins. *Nature*, 381:56–58, 1996.

[34] J. Seelig. Interaction of phyospholipids with ca-2+ ions - on the role of the phospholipid head group. *Cell Biology International Reports*, 14(4):353–360, APR 1990.

[35] J. Kmetko, A. Datta, G. Evmenenko, and P. Dutta. The effects of divalent ions on langmuir monolayer and subphase structure: A grazing-incidence diffraction and bragg rod study. *Journal of Physical Chemistry B*, 105:10818–10825, 2001.

[36] V. Dupres, S. Cantin, F. Benhabib, F. Perrot, P. Fontaine, M. Goldmann, J. Daillant, and O. Konovalov. Superlattice formation in fatty acid monolayers on a divalent ion subphase: Role of chain length, temperature, and subphase concentration. *Langmuir*, 19:10808–10815, 2003.

[37] M.I. Boyanov, J. Kmetko, T. Shibata, A. Datta, P. Dutta, and B.A. Bunker. Mechanism of pb adsorption to fatty acid langmuir monolayers studied by x-ray absorption fine structure spectroscopy. *Journal of Physical Chemistry B*, 107(36):9780–9788, 2003.

[38] C.Y. Tang, Z. Huang, and H.C. Allen. Binding of mg(2+) and ca(2+) to palmitic acid and deprotonation of the cooh headgroup studied by vibrational sum frequency generation spectroscopy. *Journal of Physical Chemistry B*, 114:17068–17076, 2010.

[39] A. Gericke and H. Huhnerfuss. In-situ investigatin of saturated long-chain fatty-acids at the air-water-interface by extternal infrared reflection-absorption spectrometry. *Journal of Physical Chemistry*, 97:12899–12908, 1993.

[40] S. Whipps, S.R. Khan, F.J. O'Palko, R. Backov, and D.R. Talham. Growth of calcium oxalate monohydrate at phospholipid langmuir monolayers. *Journal of Crystal Growth*, 192:243–249, 1998.

[41] B. Heywood and S. Mann. Molecular construction of orinted inorganic materials: Controlled nucleation of calcite and aragonite under compressed langmuir monolayers. *Chemistry of Materials*, 6:311–318, 1994.

[42] X.K. Zhao, J. Yang, L.D. McCormik, and J.H. Fendler. Epitaxial formation of pbs crystals under arachidic acid monolayers. *Journal of OPhysical Chemistry*, 96:9933–9939, 1992.

[43] E. DiMasi, V.M. Patel, M. Sivakumar, M.J. Olszta, Y.P. Yang, and L.B. Gower. Polymer-controlled growth rate of an amorphous mineral film nucleated at a fatty acid monolayer. *Langmuir*, 18:8902–8909, 2002.

[44] S. Mann, B.R. Heywood, S. Rajam, and J.D. Birchall. Controlled crystallization of $caco_3$ unter steric-acid monolayers. *Nature*, 334:692–695, 1988.

[45] M. Fricke, D. Volkmer, C.E. Krill, M. Kellermann, and A. Hirsch. Vaterite polymorph switching controlled by surface charge density of an amphiphilic dendron-calix[4]arene. *Crstystal Growth and Design*, 6:1120–1123, 2006.

[46] K.K. Sand, M. Yang, E. Makovicky, D.J. Cooke, T. Hassenkam, K. Bechgaard, and S.L.S. Stipp. Binding of ethanol on calcite: the role of the oh bond and its relevance to biomineralization. *Langmuir*, 26(19):15239–15247, October 2010.

[47] S. Mann, editor. *Biomimetic Materials Chemistry*. John Wiley and Sons, Weihheim, 1996.

[48] E.M. Landau, M. Levanon, L. Leiserowitz, M. Lahav, EM Sagiv, L. LANDAU, M LEVANON, L LEISEROWITZ, M LAHAV, and J SAGIV. Transfer of structural information from langmuir monolayers to 3-dimensional growing-crystals. *Nature*, 318:353–356, 1985.

[49] S. Mann, B.R. Heywood, S. Rajam, and J.B.A. Walker. Structural and stereochemical relationships between langmuir monolayers and calcium-carbonte nucleation. *Journal of Physics D - Applied Physics*, 24:154–164, 1991.

[50] G. K. Hunter, Ja. O'Young, B. Grohe, M. Karttunen, and H. A. Goldberg. The flexible polyelectrolyte hypothesis of protein-biomineral interaction. *Langmuir*, 26:18639–18646, 2010.

[51] Y. Yang, Q. Cui, and N. Sahai. How does bone sialoprotein promote the nucleation of hydroxyapatite? a molecular dynamics study using model peptides of different conformations. *Langmuir*, 26:9848–9859, 2010.

[52] David L. Masica, Sarah B. Schrier, Elizabeth A. Specht, and Jeffrey J. Gray. De novo design of peptide-calcite biomineralization systems. *Journal of the American Chemical Society*, 132:12252–12262, 2010.

[53] G.A. Tribello, F. Bruneval, C. Liew, and M. Parrinello. A molecular dynamics study of the early stages of calcium carbonate growth. *Journal of Physical Chemistry B*, 113:11680–11687, 2009.

[54] J. Xiao, Z. Wang, Y. Tang, and S. Yang. Biomimetic mineralization of caco3 on a phospholipid monolayer: from an amorphous calcium carbonate precursor to calcite via vaterite. *Langmuir*, 26:4977–83, 2010.

[55] E. DiMasi, M.J. Olszta, , V.M. Patel, and L.B. Gowe. When is directed mineralization really template directed? *Crystal Engineering Communications*, 5:346–350, 2003.

[56] D Volkmer and M Fricke. Growth of calcite single crystals underneath monolayers of 5,11,17,23-tetra-t-butyl-25,26,27,28-tetrakis(earboxymethoxy)calix[4]a rene. *Zeitschrift für Anorganische und Allgemeine Chemie*, 629(12-13):2381–2390, NOV 2003.

[57] L. Addadi, S. Raz, and S. Weiner. Taking advantage of disorder: Amorphous calcium carbonate and its roles in biomineralization. *Advanced Materials*, 15:959–970, 2003.

[58] B.P. Pichon, P.H.H. Bomans, P.M. Frederik, and N. J. M. Sommerdijk. A quasi-time-resolved cryotem study of the nucleation of caco3 under langmuir monolayers. *Journal of the American Chemical Society*, 130:4034–4040, 2008.

[59] E.M. Pouget, P.H.H. Bomans, A. Dey, P.M. F, G. de With, and N.A.J.M. Sommerdijk. The development of morphology and structure in hexagonal vaterite. *Journal of the American Chemical Society*, 132:11560–11565, 2010.

[60] Y. Chen, J. Xiao, Z. Wang, and S. Yang. Observation of an amorphous calcium carbonate precursor on a stearic acid monolayer formed during the biomimetic mineralization of caco(3). *Langmuir*, 25:1054–1059, 2009.

[61] B. Hasse, H. Ehrenberg, J.C. Marxen, W. Becker, and M. Epple. Calcium carbonate modifications in the mineralized shell of the freshwater snail biomphalaria glabrata. *Chemistry*, 6:3679–3685, 2000.

[62] Y. Levi-Kalisman, S. Raz, S. Weiner, L. Addadi, and I. Sagi. X-ray absorption spectroscopy studies on the structure of a biogenic amorphous calcium carbonate phase. *Journal of the Chemical Society, Dalton Transactions*, pages 3977–3982, 2000.

[63] Y. Levi-Kalisman, S. Raz, S. Weiner, L. Addadi, and I. Sagi. Structural differences between biogenic amorphous calcium carbonate phases using x-ray absorption spectroscopy. *Advanced Functional Materials*, 12:43–48, 2002.

[64] M.G. Taylor, K. Simkiss, G.N. Greaves, M. Okazaki, and S. Mann. An x-ray-absorption spectroscopy study of the strucutre and transformation of amorphous calcium-carbonte from plant cystoliths. *Proceedings of the Royal Society of London Series B-Biological Science*, 252(1333):75–80, APR 22 1993.

[65] J.D. Rodriguez-Blanco, S. Shaw, P. Bots, and L.G. Roncal-Herrero T. Benning. The role of ph and mg on the stability and crystallization of amorphous calcium carbonate. *Journal of Alloys and Compounds*, in press, 2012.

[66] X. Wang, R. Kong, X. Pan, H. Xu, D. Xia, H. Shan, and J.R. Lu. Role of ovalbumin in the stabilization of metastable vaterite in calcium carbonate biomineralization. *Journal of Physical Chemistry B*, 113:8975–8982, 2009.

[67] D Braga. From amorphous to crystalline by design: Bio-inspired fabrication of large micropatterned single crystals. *Angewandte Chemie- International Edition*, 42:5544–5546, 2003.

[68] J.W. Mullin. *Crystalizastion*. Butterworth-Heinemann, Boston, 1992.

[69] M. Takeo. *Disperse Systems*. Wiley-VCH, Weinheim, 1999.

[70] J. Schmelzer, G. Röpke, and R. Mahnke. *Aggregation Phenomena in Complex Systems*. Wiley-VCH, Weinheim, 1992.

[71] P.G. Debenedetti. *Metastable Liquids*. Princtopn University Press, Princton, 1996.

[72] G. Wulff. *Zeitschrift für Kristallographie*, 34:449, 1991.

[73] J.H. Adair and E. Suvaci. Morphological control of particles. *Current Opinion in Colloid & Interface Science*, 5:160–167, 2000.

[74] B.J. Brisdon, B.R. Heywood, A.G.W. Hodson, S. Mann, and W.K.W. Wong. Polymer-mediated crystallization of inorganic solids - calcite nucleation on poly(organosiloxane) surfaces polymer-mediated crystallization of inorganic solids - calcite nucleation on poly(organosiloxane) surfaces. *Advanced Materials*, 5:49–51, 1993.

[75] G. Widawski, M. Rawiso, and B. Francois. Self-organized honeycomb morphology of star-polymer polystyrene films. *Nature*, 369:387–389, 1994.

[76] J. Lin, E. Cates, and P.A. Bionconi. Am synthetic analog of the biomineralization process - controlled crystallization of an inorganic phase by a polymer matrix. *Journal of the American Chemical Society*, 116:4738–4745, 1994.

[77] S.M. D'Souza, C. ALexander, S.W. Carr, A.M. Waller, M.J. Whitecombe, and E.N. Vulfson. Directed nucleation of calcite at a crystal-imprinted polymer surface. *Nature*, 398:312–316, 1999.

[78] T. Kato, T. Suzuki, and T. Irie. Layered thin-film composite consisting of polymers and calcium carbonate: A novel organic/inorganic material with an organized structure. *Chemistry Letters*, 2:186–187, 2000.

[79] N. Hosoda and T. Kato. Thin-film formation of calcium carbonate crystals: Effects of functional groups of matrix polymers. *Chemistry of Materials*, 13:688–693, 2001.

[80] S.H. Yu and H. Cölfen. Bio-inspired crystal morphogenesis by hydrophilic polymers. *Journal of Materials Chemistry*, 14:2124–2147, 2004.

[81] W. A. Peter and A Höpfner. *Physikalische Chemie*. Wiley-VCH, 2002.

[82] E. Beniash, J. Aizenberg, L. Addadi, and S. Weiner. Amorphous calcium carbonate transforms into calcite during sea urchin larval spicule growth. *Proceedings of the Royal Society of London Series B, Biological Science*, 264:461–465, 1997.

[83] Y. Politi, T. Arad, S. Klein, E. Weiner, and L. Addadi. Sea urchin spine calcite forms via a transient amorphous calcium carbonate phase. *Science*, 306:1161–1164, 2004.

[84] J.C. Marxen, W. Becker, D. Finke, B. Hasse, and M. Epple. Early mineralization in biomphalaria glabrata: Microscopic and structural results. *Journal of Molluscan Studies*, 69:113–121, 2003.

[85] I.M. Weiss and S. Addadi, L. Weiner. Mollusc larval shell formation: Amorphous calcium carbonate is a precursor phase for aragonite. *Journal of Experimental Zoology*, 293:478–491, 2002.

[86] H.A. Lowenstam and S. Weiner. Transformation of amorphous calcium-phosphate to crystalline dahllite in the radular teeth of chitons. *Science*, 227:51–53, 1985.

[87] D. Pontoni, J. Bolze, N. Dingenouts, T. Narayanan, and M. Ballauff. Crystallization of calcium carbonate observed in-situ by combined small- and wide-angle x-ray scattering. *Journal of Physical Chemistry B*, 107:5123–5125, 2003.

[88] M. Maas. *Biomimetische Bildung von Dünnfilmen an Lipid-Monoschichten*. PhD thesis, Universität Dortmund, 2008.

[89] R. Aveyard, B.P. Binks, and J.H. Clint. Emulsions stabilised solely by colloidal particles. *Advances in Colloid and Interface Science*, 100:503–546, 2003.

[90] H.S. Wi, S. Cingarapu, K.J. Klabunde, and B.M. Law. Nanoparticle adsorption at liquid-vapor surfaces: Influence of nanoparticle thermodynamics, wettability, and line tension. *Langmuir*, 27:9979–9984, 2011.

[91] M. Paulus, P. Degen, S. Schmacke, M. Maas, R. Kahner, B. Struth, M. Tolan, and H. Rehage. In situ observation of maghemite nanoparticle adsorption at the water/gas interface. *European Physical Jorunal - Special Topics*, 167:133–136, 2009.

[92] A. Stefansson. Iron(iii) hydrolysis and solubility at 25 degrees c. *Enviromental Sciene & Technology*, 41:6117–6123, 2007.

[93] R.H. Byrne, Y.R. Luo, and RW.. Young. Iron hydrolysis and solubility revisited: observations and comments on iron hydrolysis characterizations. *Marine Chemistry*, 70:23–35, 2000.

[94] W. Liu, B. Etschmann, J. Brugger, L. Spiccia, G. Foran, and B. McInnes. Uv-vis spectrophotometric and xafs studies of ferric chloride complexes in hyper-saline licl solutions at 25-90 degrees c. *Chemical Geology*, 231:326–349, 2006.

[95] B.R. Tagirov, I.I. Diakonov, O.A. Devina, and A.V. Zotov. Standard ferric-ferrous potential and stability of fecl2+ to 90 degrees c. thermodynamic properties of fe-(aq)(3+) and ferric-chloride species. *Chemical Geology*, 162:193–219, 2000.

[96] R.H. Byrne and D.R. Kester. Ultraviolet spectroscopic study of ferric equilibria at high chloride concentrations. *Journal of Solution Chemistry*, 10:51–67, 1981.

[97] F.J. Millero, W.S. Yao, and J. Aicher. The specitation of fe(ii) and fe(iii) in natural-waters. *Marine Chemistry*, 50:21–39, 1995.

[98] W. Davison. Soluble inorganic ferrous complexes in natural waters. *Geochimica et Cosmochimica Acta*, 43:1693–1696, 1979.

[99] D. Langmuir and D.O. Whittemo. Variations in stability of precipitated ferric oxyhydroxides. *Advances in Chemistry Series*, 106:209, 1971.

[100] T. Grundl and J. Delwiche. Kinetics of ferric oxyhydroxide precipitation. *Journal of Contaminant Hydrology*, 14:71–87, 1993.

[101] J. Dousma, D.D. Ottelander, and P.L.D. Bruyn. Influence of sulfate-ions on the formation of iron(iii) oxides. *Journal of Inorganic Nucleation Chemistry*, 41:1565–1568, 1979.

[102] D. Macalady, D a.nd Langmuir, T. GrundlL, and A. Elzerman. Use if nodel generated fe-3+ ion activities to compute eh and ferric oxyhydroxide solubilities in anaerobic systems. *ACS Symposium Series*, 416:350–367, 1990.

[103] U. Schwertmann and R.M. Cornell. *Ironoxides in the Laboratory*. VCH Publischers, New York, 2001.

[104] G.L. Gaines. *Insoluble monolayers at the liquid-gas interface*. Wiley-Interscience, New York, 1966.

[105] L. Wiegert. *Thermodynamic and structural properties of lipid monolayers on sol surfaces*. Diploma Thesis. Universität Dortmund, (unpublished), 2004.

[106] V.M. Kaganer, H. Möhwald, and P. Dutta. Structure and phase transitions in langmuir monolayers. *Reviews of moderen Physics*, 71:779–819, 1999.

[107] G. Adam, P. Läuger, and G. Stark. *Physikalische Chemie und Biophysik*. Springer, 2003.

[108] H. Möhwald. *Phospholipid Monolayers*, chapter 4. Amsterdam, Elsevier, 1995.

[109] M. Tolan. *X-ray Scattering from Soft-matter thin Films - Material Science and Basic Research, Springer Tracts in Modern Physics 148*. Springer, Berlin, 1999.

[110] J.D. Jackson. *Klassiche Elektrodynamik, 2. Auflage*. de Gruyter, Berlin, 1985.

[111] Y. Yoneda. Anomalous surface reflection of x-rays. *Physical Review*, 131:2010, 1963.

[112] L.G. Parratt. Surface studies of solids by total reflection of x-rays. *Physical Review*, 95:359–369, 1954.

[113] H. Kiesing. Interferenz von röntgenstrahlung an dünnen schichten. *Annalen der Physik*, 10:769–788, 1917.

[114] T. Hahn, editor. *International Tables For Crystallograpgy*. Dordrecht, Holland / Boston, USA, D. Reichel Publishing Company, 1983.

[115] B.E. Warren. *X-Ray Diffraction*. Addison-Wesley Publishing Company, 1969.

[116] A. T. D'Agostino. Determination of thin metal film thickness by x-ray diffractometry using the scherrer equation, atomic absorption analysis and transmission/reflection visible spectroscopy. *Analytica Chimica Acta*, 262:269–275, 1991.

[117] L.A. Patterson. The scherrer formula for x-ray particle size determination. *Physical Review*, 56:978–982, 1939.

[118] J. Als-Nielsen and K. Kjaer. *Phase Transitions in Soft-Condensed Matter*. New York, Plenum Press, 2001.

[119] E. B. Sirota. Remarks concerning the relation between rotator phases of bulk n- alkanes and those of langmuir monolayers of alkyl-chain surfactants on water. *Langmuir*, 13:3849, 1997.

[120] E. B. Sirota. Supercooling, nucleation, rotator phases, and surface crystallization of n-alkane melts. *Langmuir*, 14:3133, 1998.

[121] G. Porod. *Small Angle X-ray Scattering*. London, Aca- demic Press Inc. Ltd, 1982.

[122] V.M. Kaganer, M.A. Osipov, and I.R. Peterson. A molecular-model for tiliting phase-transitions between condensed phases of langmuir monolayers. *Journal of Chemical Physics*, 98:3512–3527, 1993.

[123] B. Struth, E. Scalas, G. Brezesinski, H. Möhwald, F. Bringezu, and Kjaer K. Bouwman, W. G. Influence of a hydrophilic spacer on the structure of a phospholipid monolayer. *Nuovo Cimento*, 16:3133, 1994.

[124] K. Kjaer. Some simple ideas on x-ray reflection and grazing-incidence diffraction from thin surfactant films. *Physica B*, 198:100–109, 1994.

[125] M. Newville. Fundamentals of xafs, 2004.

[126] J.A. Victoreen. The absorption of incident quanta by atoms as defined by the mass photoelectric absorption coefficient and the mass scattering coefficient. *Journal of Applied Physics*, 19:855–860, 1948.

[127] J.J. Rehr and R.C. Albers. Theoretical approcahes to x-ray absorption finde strucutre. *Rev. of Mod. Phys.*, 72:621, 2000.

[128] D.E. Sayers and B.A. Bunker. *X-ray absorption: Principles, Applications, Techniques of EXAFS, SEXAFS and XANES*, chapter 6. John Wiley and Sons, 1988.

[129] E.A. Stern. Theory of extended x-ray-absorption fine strucutre. *Physical Review B*, 10:3027, 1974.

[130] H. Dosch, B.W. Batterman, and D.C. Wack. Depth-controlled grazing incidence diffraction of synchrotron x-radiation. *Physical Review Letters*, 56:1144–1147, 1986.

[131] H. Dosch. Evanescent absorption in kinematic surface bragg-diffraction. *Physical Review B*, 35:2137–2143, 1987.

[132] R. Frahm, J. Weigelt, G. Meyer, and G. Materlik. X-ray undulator beamline bw1 at doris-iii. *Review of Scientific Instruments*, 66:1677, 1995.

[133] E. Welter. Set up of an xafs beamline for measurements between 2.4 8 kev at doris iii. *AIP Conference Proceedings*, 1234:955, 2009.

[134] D.M. Smilgies, N. Boudet, B. Struth, and O. Konovalov. Troika ii: a versatile beamline for the study of liquid and solid interfaces. *Journal of Synchrotron Radiation*, 12:329–339, 2005.

[135] C. Krywka, M. Paulus, C. Sternemann, M. Volmer, A. Remhof, G. Nowak, A. Nefedov, B. Poter, and M. Spiegel, M .and Tolan. The new diffractometer for surface x-ray diffraction at beamline bl9 of delta. *Journal of Synchrotron Radiation*, 13:8–13, 2006.

[136] C. Krywka, C. Sternemann, M. Paulus, N. Javid, R. Winter, A. Al-Sawalmih, S. Yi, D. Raabe, and M. Tolan. The small-angle and wide-angle x-ray scattering set-up at beamline bl9 of delta. *Journal of Synchrotron Radiation*, 14:244–251, 2007.

[137] B-L Henke and J.C. Gullikson, E.M. ad Davis. X-ray interactions: photoabsorption, scattering, transmission, and reflection at e=50-30000 ev, z=1-92. *Atomic Data and Nuclear Data Tables*, 54:181–342, 1993.

[138] D.E. Cox. High resolution powder diffraction and strucutre determination. In P. Coppens, editor, *Synchrotron radiation crystallography*. Academic Press, London, 1992.

[139] A.B. McLean, C.E.J. Mitchell, and D.M. Swanston. Implementation of an efficeint analytical approximation to the voigt function for photoemission lineshape analysis. *Journal of the Electron Spectroscopy and Related Phenomena*, 69:125–132, 1994.

[140] B. Ravel and M. Newville. *ATHENA*, *ARTEMIS*, *HEPHAESTUS*: data analysis for X-ray absorption spectroscopy using *IFEFFIT*. *Journal of Synchrotron Radiation*, 12:537–541, 2005.

[141] R. Johann, D. Vollhardt, and H. Mohwald. Shifting of fatty acid monolayer phases due to ionization of the headgroups. *Langmuir*, 17:4569–4580, 2001.

[142] L.V.N. Avila, S.M. Saraiva, and J.F. Oliveira. Stability and collapse of monolayers of stearic acid and the effect of electrolytes in the subphase. *Colloids and Surfaces A-Physicochemical and Engenering Aspects*, 154:209–217, 1999.

[143] G. Pieper, H. Rehage, and D. Barthas-Biesel. Deformation of a capsule in a spinning drop apparatus. *J. Coll. Int. Sci.*, 202:293, 1998.

[144] P. Degen, M. Paulus, S. Leick, M. Tolan, and H. Rehage. gamma-fe2o3 nanoparticle adsorption at an ots langmuir monolayer. *Colloid and Polymer Science*, 288:643–651, 2010.

[145] P. Degen, M. Paulus, M. Maas, R. Kahner, S. Schmacke, B. Struth, M. Tolan, and H. Rehage. In situ observation of gamma-fe2o3 nanoparticle adsorption under different monolayers at the air/water interface. *Langmuir*, 24:12958–62, 2008.

[146] J.W. Hu, G.b. Han, B. Ren, Sg. Sun, and Zq. Tian. Theoretical consideration on preparing silver particle films by adsorbing nanoparticles from bulk colloids to an air-water interface. *Langmuir*, 20:8831, 2004.

[147] M. Husmann, H. Rehage, E. Dhenin, and D. Barthes-Biesel. Deformation and bursting of nonspherical polysiloxane microcapsules in a spinning-drop apparatus. *Journal of Colloid and Interface Science*, 282:109, 2005.

[148] S.J. Yao and M.G. Cho. Diffusion characteristics in microcapsules. *Chinese Journal Of Chemical Engineering*, 2:116, 1998.

[149] H. Rehage, M. Husmann, and Walter A. From two-dimensional model networks to microcapsules. *Rheologica Acta*, 41:292, 2002.

[150] M. Husmann, B. Achenbach, and Rehage H. Ultrathin cross-linked networks at interfaces between fluids: Structure, properties and preparative prospectives. In B. T. Stokke and A. Elgsaeter, editors, *The Wiley polymer network review series, 2 ed.*, pages 444–459. John Wiley and Sons: Chichester, Weinheim, New York,, 1999.

[151] V. Bergeron and D. Langevin. Monolayer films of poly(dimethylsiloxane) on aqueous surfactant solutions. *Macromolecules*, 29:306, 1996.

[152] H. Rehage, B. Achenbach, and F.G. Klaerner. Ultrathin cross-linked networks at the interface between oil and water: Structure, properties, and preparative perspectives. *Langmuir*, 18:7115, 2002.

[153] M. Husmann. *Polyorganosiloxan-Filme zwischen fluiden Phase*. Dissertation (*in german*), Univesität, Essen, Deutschland, 2001.

[154] P. Fontaine, M. Goldmann, and F. Rondelez. Influence of headgroup cross-linking on chain packing in langmuir monolayers of n-alkyltrialkoxysilanes. *Langmuir*, 15:1348–1352, 1999.

[155] S.W. Barton, A Goudot, SW Rondelez, F. BARTON, A GOUDOT, and F RONDELEZ. X-ray structural study of polymerized octyldecyltrichorosilane on water. *Langmuir*, 7:1029–1030, 1991.

[156] D. Blaudez, M. Bonnier, B. Desbat, and F. Rondelez. Two-dimensional polymerization in langmuir films: A pm-irras study of octadecyltrimethoxysilane monolayers. *Langmuir*, 18:9158–9163, 2002.

[157] M. Linden, J.P. Slotte, and J.B. Rosenholm. Two-dimensional gelation: Octadecyltrimethoxysilane at the air/water interface. *Langmuir*, 12:4449–4454, 1996.

[158] A.F. Hollemann and E. Wiberg. *Lehrbuch der Anorganischen Chemie*. deGyuter, Berlin, 1994.

[159] K. Kojio, S.R. Ge, A. Takahara, and T. Kajiyama. Molecular aggregation state of n-octadecyltrichlorosilane monolayer prepared at an air/water interface. *Langmuir*, 14:971–974, 1998.

[160] D.C. Florian Wieland, Patrick Degen, Michael Paulus, Martin A. Schroer, Heinz Rehage, and Metin Tolan. Manipulating thin polymer films by changing the ph value. *Journal of Applied Physics*, 110:1022211–1022214, 2011.

[161] I.R. Peterson, G. Brezesinski, B. Struth, and E. Scalas. Grazing-incidence x-ray diffraction study of octadecanoic acid monolayers. *Journal of Physical Chemistry B*, 102:9437–9442, 1998.

[162] T.V. Bukreeva, V.V. Arslanov, and I.A. Gagina. Langmuir-blodgett films of fatty acid salts of bi- and trivalent metals: Y, ba, and cu stearates. *Colloid Journal*, 65:134–140, 2003.

[163] M.C. Shih, M.K. Durbin, A. Malik, P. Zschak, and P Dutta. Lattice structures and molecular tilts in langmuir monolayers of saturated fatty acid-alcohol mixtures. *Journal of Chemical Physics*, 101(10):9132–9136, NOV 15 1994.

[164] I. Estrela-Lopis, G. Brezesinski, and H. Mohwald. Miscibility of dppc and dppa in monolayers at the air/water interface. *Chemistry and Physics of Lipids*, 131:71–80, 2004.

[165] P. Degen, S. Peschel, and H. Rehage. Stimulated aggregation, rotation, and deformation of magnetite-filled microcapsules in external magnetic fields. *Colloid and Polymer Science*, 286:865, 2008.

[166] G. Brezesinski and H. Möhwald. Langmuir monolayers to study interactions at model membrane surfaces. *Advances in Colloid and Interface Science*, 100:563–584, 2003.

[167] C. Dietrich, L.A. Bagatolli, Z.N. Volovyk, N.L. Thompson, M. Levi, K. Jacobson, and E. Gratton. Lipid rafts reconstituted in model membranes. *Biophysical Journal*, 80:1417–1428, 2001.

[168] W. Wang, R.Y. Park, A. Travesset, and D. Vaknin. Ion-specific induced charges at aqueous soft interfaces. *Physical Review Letters*, 106:56102– 56105, 2011.

[169] F. Leveiller, C. Bohm, D. Jacquemain, L. Möwald, H.and Leiserowitz, Kjaer K., and J Als-Nielsen. 2-dimensional crystal-strucutre of cadmium arachidate studied by synchrotron x-ray-diffraction and reflectivity. *Langmuir*, 10:819–829, 1994.

[170] S. Kewalramani, H. Hlaing, B.M. Ocko, I. Kuzmenko, and M. Fukuto. Effects of divalent cations on phase behavior and structure of a zwitterionic phospholipid (dmpc) mono layer at the air-water interface. *Journal of Physical Chemistry Letters*, 1:489–495, 2010.

[171] H. Yazdanian, M. abd Yu, G. Zografi, and M.W. Kim. Divalent-cations steric-acid monolayer interactions at the air-water-interface. *Langmuir*, 8:630–636, 1992.

[172] H. Yazdanian, M. abd Yu and G. Zografi. ionic interactions of fatty-acid monolayers at the air-water-interface. *Langmuir*, 6:1093–1098, 1990.

[173] S Bettarini, F. Bonosi, G. Gabrielli, and G. Martini. Characterization of the monolayer as the basis of langmuir-blodgett-film formation - metal derivatives of behenic acid. *Langmuir*, 7:1082–1087, 1991.

[174] R.S. Ghaskadvi, S. Carr, and M. Dennin. Effect of subphase ca++ ions on the viscoelastic properties of langmuir monolayers. *Journal of Chemical Physics*, 111:3675–3678, 1999.

[175] J.A. Zasadzinsk, R. Viswanathan, L. Madsen, and D.K. Garnaes, J. Schwartz. Langmuir-blodgett-films. *Science*, 263:1726–1733, 1994.

[176] M.W. Kim, B.B. Sauer, H. Yu, M. Yzadanian, and G. Zografi. Ionic interactions of fatty-aid monolayers studied by ellipsometry. *Langmuir*, 6:236–240, 1990.

[177] W. Wang, R.Y. Park, D.H. Meyer, A. Travesset, and D. Vaknin. Ionic specificity in ph regulated charged interfaces: Fe(3+) versus la(3+). *Langmuir*, 27:11917–11924, 2011.

[178] A. Datta, J. Kmetko, A.G. Richter, C.J. Yu, P. Dutta, K.S. Chung, and J.M. Bai. Effect of headgroup dissociation on the structure of langmuir monolayers. *Langmuir*, 16:1239–1242, 2000.

[179] S Suzuki, T Suzuki, M Kimura, Y Takagi, K Shinoda, K Tohji, and Y Waseda. Exafs characterization of ferric oxyhydroxides. *Applied Surface Science*, 169:109–112, 2001.

[180] S.L. Heath, J.M. Charnock, C.D. Garner, and A.K. Powell. Extended x-ray absorption fine structure (exafs) studies of hydroxo(oxo)iron aggregates and minerals, and a critique of their use as models for ferritin. *Chemistry*, 2:634–639, 1996.

[181] S. Trudel, E.D. Crozier, R.A. Gordon, P.S. Budnik, and R.H. Hill. X-ray absorption fine structure study of amorphous metal oxide thin films prepared by photochemical metalorganic deposition. *Journal of Solid State Chemistry*, 184:1025–1035, 2011.

[182] L. Nagy, T. Yamaguchi, M. Nomura, and H. Ohtaki. Exafs study of iron(iii) complexes of sugar type ligands. *Magyar Kemiai Folyoirat*, 95:8–15, 1989.

[183] M.J. Apted, G.A. Waychunas, and G.E. Brown. Structure and specification of iron complexes in aqueous-solutions derermined by x-ray absorption-spectroscopy. *Geochimica et Cosmochimica Acta*, 49:2081–2089, 1985.

[184] M. Maas, P. Degen, H. Rehage, H. Nebel, and M. Epple. Biomimetic formation of thin, coherent iron oxide films under langmuir monolayer. *Colloids and Surfaces A*, 354:149–155, 2010.

[185] W. Bu, D. Vaknin, and A. Travesset. Monovalent counterion distributions at highly charged water interfaces: Proton-transfer and poisson-boltzmann theory. *Physical Review E*, 72:605011–605014, 2005.

[186] K.H. Gayer and L. Wootner. The hydrolysis of ferrous chloride at 25-degrees. *Journal of the American Chemical Society*, 78:3944–3946, 1956.

[187] A. E. Martell and R. M. Smith. *Critical Stability Constants*. Plenum, New York, 1977.

[188] A. Braslau, M. Deutsch, P. S. Pershan, A. H. Weiss, J. Als-Nielsen, and J. Bohr. Surface roughness of water measured by x-ray reflectivity. *Physical Review Letters*, 54:114–117, 1985.

[189] S. Cantin, S. Peralta, P. Fontaine, M. Goldmann, and F. Perrot. Evolution toward the x phase of fatty acid langmuir monolayers on a divalent cation solution. *Langmuir*, 26:830–837, 2010.

[190] D. Vaknin, K. Kjaer, J. Als-Nielsen, and M. Losche. Structural-properties of phosphatidylcholine in a monolayer at the air-water-interface - neutron reflectivity study and reeaxamination of x-ray reflection measurements. *Biophysicak Journal*, 59:1325–1332, 1991.

[191] R. Johann, G. Brezesinski, D. Vollhardt, and H. Mohwald. The effect of headgroup interactions on structure and morphology of arachidic acid monolayers. *Journal of Physical Chemistry B*, 105:2957–2965, 2001.

[192] F. M. Michel, L. Ehm, S.M. Antao, P.L. Lee, P. J. Chupas, G. Liu, D.R. Strongin, M.A.A. Schoonen, B.L. Phillips, and J.B. Parise. The structure of ferrihydrite, a nanocrystalline material. *Science*, 316:1726–1729, 2007.

[193] S. Calvin. Scott calvin's xafs divination set. Website, 2011. `http://www.xafs.org/EXAFS_Divination_Set`.

[194] F. Wirkert. *Aufbau einer Apparatur zur Streuung unter streifendem Einfall an Strahllinie BL9 bei DELTA*. Diploma Thesis. Universität Dortmund, (unpublished), 2010.

[195] H. Lin, H. Sakamoto, W.S. Seo, K. Kuwabara, and K. Koumoto. Crystal growth of lepidocrocite and magnetite under langmuir monolayers. *Journal of Crystal Growth*, 192:250–256, 1998.

[196] N.A. abd Fendler J.H. Meldrum, F.C. abd Kotov. Preparation of particulate monolayers and multilayers from surfactant-stabilized, nonosized magnetite crystallites. *Journal of Physical Chemistry*, 98:4506–4510, 1994.

[197] B. J. Park, J.P. Pantina, E.M. Furst, M. Oettel, S. Reynaert, and J. Vermant. Direct measurements of the effects of salt and surfactant on interaction forces between colloidal particles at water-oil interfaces. *Langmuir*, 24:1686–1694, 2008.

[198] R. Miller, V. B. Fainerman, V. I. Kovalchuk, D. O. Grigoriev, M. E. Leser, and M. Michel. Composite interfacial layers containing micro-size and nano-size particles. *Advances in Colloid and Interface Science*, 128:17–26, 2006.

[199] T.N. Hunter, R.J. Pugh, G.V. Franks, and G.J. Jameson. The role of particles in stabilising foams and emulsions. *Advances in Colloid and Interface Science*, 137:57–81, 2008.

[200] O.D. Velev, A.M. Lenhoff, and E.W. Kaler. A class of microstructured particles through colloidal crystallization. *Science*, 287:2240–2243, 2000.

[201] B.P. Binks and S.O. Lumsdon. Pickering emulsions stabilized by monodisperse latex particles: Effects of particle size. *Langmuir*, 17:4540–4547, 2001.

[202] T.N. Hunter, E.J. Wanless, G.J. Jameson, and R.J. Pugh. Non-ionic surfactant interactions with hydrophobic nanoparticles: Impact on foam stability. *Colloids and Surfaces A*, 347:81–89, 2009.

[203] P. Degen, D.C.F. Wieland, S. Leick, M. Paulus, H. Rehage, and M. Tolan. Effect of magnetic nanoparticles on the surface rheology of surfactant films at the water surface. *Soft Matter*, 7:7655–7662, 2011.

[204] M. Paulus, P. Degen, T. Brenner, S. Tiemeyer, B. Struth, M. Tolan, and H. Rehage. Sticking polydisperse hydrophobic magnetite nanoparticles to lipid membranes. *Langmuir*, 26:15945–15947, 2010.

[205] P.A. Tipler. *Physik*. Spektrum, 1994.

Publications

- D.C.F. Wieland, M. Paulus, M.A. Schroer, M. Tolan, P. Degen, H. Rehage. Manipulating thin polymer films by change of pH. *J. Appl. Phys.* **110**, 102221 (2011).
- P. Degen,D.C.F. Wieland, S. Leick, M. Paulus, H. Rehage, and M. Tolan. Effect of magnetic nanoparticles on the surface rheology of surfactant films at the water surface . *Soft Matter* **7**, 7655 (2011).
- S. Henke,D.C.F. Wieland, M. Meilikhov, M. Paulus, C. Sternemann, K. Yusenko, and R.A. Fischer. Multiple phase-transitions upon selective CO_2 adsorption in an alkyl ether functionalized metal-organic framework – An in situ x-ray diffraction study . *Cryst. Eng. Com,* **13**, 6399 (2011).
- K. Yusenko, M. Meilikhov, D. Zacher,F. Wieland, C. Sternemann, X. Stammer, T. Ladnorg, C. Wöll, R.A. Fischer. Step-by-step growth of highly oriented and continuous seeding layers of $[Cu_2(ndc)_2(dabco)_n]$ on bare oxide and nitride substrates. *Cryst. Eng. Com,* **12**, 2086 (2010).
- H.K. Arslan, O.I. Shekhah, D.C.F. Wieland, M. Paulus, C. Sternemann, M.A. Schroer, S. Tiemeyer, M. Tolan, R.A. Fischer, C. Wöll. Intercalation in Layered Metal-Organic Frameworks: Reversible Inclusion of an Extended π-System. *J. Am. Chem. Soc.* **133**, 8158-8161 (2011).
- M.A. Schroer, Y. Zhai., D.C.F. Wieland, Ch.J. Sahle, J. Nase, M. Paulus, M. Tolan, R. Winter. Exploring the Piezophilic Behavior of Natural Cosolvent Mixtures. *Ang. Chem. Int. Ed.* **50**, 11413-11416 (2011).
- M.A. Schroer, J. Markgraf, D.C.F. Wieland, Ch.J. Sahle, J. Möller, M. Paulus, M. Tolan, R. Winter. Nonlinear Pressure Dependence of the Interaction Potential of Dense Protein Solutions. *Phys. Rev. Lett.* **106**, 178102 (2011).
- M.A. Schroer, M. Paulus, C. Jeworrek, C. Krywka, S. Schmacke, Y. Zhai, D.C.F. Wieland, Ch.J. Sahle, M. Chimenti, C.A. Royer, B. Garcia-Moreno, M. Tolan, R. Winter. High-Pressure SAXS Study of Folded and Unfolded Ensembles of Proteins. *Biophys. J.* **99**, 3430-3437 (2010).
- J. Möller, M. Cebi, M.A. Schroer, M. Paulus, P. Degen, Ch.J. Sahle, D.C.F. Wieland, S. Leick, A. Nyrow, H. Rehage, M. Tolan. Dissolution of iron oxide nanoparticles inside polymer nanocapsules. *Phys. Chem. Chem. Phys.* **13**, 20354-20360 (2011).
- A. Steffen, C. Kronholz, M. Paulus, F. Wieland, S. Bieder, P. Degen, C.J. Sahle, M. Ferreira, R. Wagner, W. Tillmann and M. Tolan. Predicting properties of materials with x-rays: The

application of synchrotron radiation in materials science. *st International Conference on Product Property Prediction* , ISBN 978-3-9808718-6-0 , 203 (2010).

- W. Tillmann, L. Hagen, I. Baumann, M. Tolan, M. Paulus and D.C.F. Wieland. Correlation of the particle behavior, microstructure and phase evolution during the optimization of HVOF sprayed WC-12Co coatings by means of DoE. *DVS-Berichte* **276**, ISBN 978-3-87155-268 (2011).

Acknowledgments

I would like to thank Dr. Michael Paulus and Dr. Patrick Degen for many discussions and ideas which helped to make the right decisions for a successful accomplishment of this project.

I also acknowledge Prof. Metin Tolan for the opportunity to be part of his group and to work self-contained on interesting research topic. I am also grateful for the possibility to attend different conference and beam times around the world. And I am also thankful to Prof. Heinz Rehage for co-supervising this work.

Experiments at synchrotron light sources can never be performed alone and always need a lot of man power. For his help and company during reams of night shifts I would like to thank Martin A. Schroer, without him the nights would have been extremely tedious. I am also grateful to Dr. Michael Paulus and Dr. Patrick Degen for a lot of enjoyable discussions during these experiments.

I also would like to thank Christoph J. Sahle, Steffen Bieder, Sabine Leick, Johannes Möller and Jens Benecken for their help during the beam times and all other persons who I might have forgotten.

Further are Dr. Bernd Struth for his help at the beamline BW1 and Dr. Alexei Vorobiev for the support at the ID10B acknowledged.

I also enjoyed the time with my cubicle neighbor Christoph J. Sahle, the dark and busy hours in our office were always a pleasure for me. But it was also wonderful to have Martin A. Schroer and Sabrina Hoffmann in the office next door which I could phone if there were some problems.

Further I like to thank Martin A. Schroer, Dr. Michael Paulus, Sabrina Hoffmann, Christoph J. Sahle and Dr. Julia Nase for proof reading my thesis and for their advice. I hope they have not obtained to much gray hairs.

The work group E1 consist of many nice and sympathetic people, therefore it was always a happiness to be part of this group even when science was not the topic.

For funding I like to acknowledge the NRW Forschungsschule "Forschung mit Synchrotronstrahlung".

I also want to thank Jessica for her encouragement and for taking ventures when I ran the risk to be overwrought.

The last lines I like to dedicate to thank my beloved parents Bernd and Gisela Wieland, who supported me under every condition and were a backing in every situation of my live.

Eidesstattliche Erklärung

Ich versichere hiermit an Eides statt, dass ich die vorliegende Dissertation mit dem Titel ”Formation of organic and inorganic thin films at the aqueous solution-gas interface” selbständig und ohne unzulässige Hilfe erbracht habe. Ich habe keine anderen als die angegebenen Quellen und Hilfsmittel benutzt sowie wörtliche und sinngemäße Zitate kenntlich gemacht. Die Arbeit hat in gleicher oder ähnlicher Form noch keiner Prüfungsbehörde vorgelegen.

Dortmund, den

_____

(D.C. Florian Wieland)